A Data-Driven Understanding of Plasma Transport in Saturn's Magnetic Environment

by

Abigail R. Azari

A dissertation submitted in partial fulfillment
of the requirements for the degree of
Doctor of Philosophy
(Atmospheric, Oceanic and Space Sciences)
in the University of Michigan
2020

Doctoral Committee:

Associate Professor Xianzhe Jia, Co-Chair
Professor Michael W. Liemohn, Co-Chair
Assistant Professor Yang Chen
Associate Professor Carolyn C. Kuranz
Senior Scientist Michelle Thomsen, Planetary Sciences Institute

Abigail R. Azari
azari@umich.edu
ORCID iD: 0000-0002-8665-5459

To my family, and those who arrive with empty hands.

–

"I'm going to go unbuild walls."
The Dispossessed by Ursula K. Le Guin

ACKNOWLEDGEMENTS

The Cassini-Huygens mission left Earth to start its long journey to Saturn when I just started to wonder which light in the sky was Saturn. By the time it arrived and took its first pictures of Saturn, I had entered high school. When I finished college, Cassini had taken its arguably most famous picture of Saturn. This photo showed, in stark detail, Saturn's rings shining brightly, illuminated by the sun. Cassini transformed Saturn into a tangible object, not just a softly shining dot in the night sky. I like to think that the Cassini mission and my own journey of looking at the stars grew up together. I find it fitting that I'm finishing my PhD by looking over the entirety of the data Cassini collected throughout my life. Without the thousands of people across the world in Cassini's family, working for over multiple decades to launch this extremely ambitious mission, Cassini would have not existed and the research in this thesis would be very different. But without my family's unwavering support, my PhD would not exist at all.

I want to express my gratitude to my family who believed in my future even when others did not. I would like to recognize my parents who persisted in this belief, and worked with me to unbuild barriers in my early education. You have taught me the value of empty hands, how to unbuild walls, and that sometimes the best places to study the universe are outside the classroom. I want to also thank my brothers and sisters who spent years alongside and cheered me on. To Timothy, thank you for making absolutely sure I know that coffee is not from space. To the new members of my family, Nils and Nova, thank you for bringing your excitement and light into my life. Your work and support, enabled me to reach this point in my education, and persist in my own PhD.

In my PhD, I found a welcoming and collaborative place within the research groups of my co-advisors: Dr. Michael Liemohn and Dr. Xianzhe Jia. Thank you to you both, for providing a wonderful introduction to the community of scholars in planetary space physics. Your leadership and excellence in computational modeling provided a lofty example of the potential future of machine learning in space physics. I look forward to seeing the community of machine learning advance to the same research excellence as that which you showed me in physics based modeling.

To the members of the Liemohn, Jia, and (as of recently) Pulkinnen research

groups, thank you for being wonderful office mates, travel companions, and advocates. I look forward to seeing the convergence of your hard work on models of the moons of Jupiter, the celebration of your first accepted papers and your own PhD defenses, your implementation of new computational courses, your advocacy and raising of voices often unheard, and finally your next steps from post-doc and beyond. I have learned so much from each and every one of you and I'm so excited to see what you will do. To Rickey Shackelford, thank you for working with us on Cassini magnetic field data analysis and I'm excited to see you thrive in your next steps after the University of Michigan.

I also want to thank Dr. Michael Liemohn for taking a leap of faith in trying novel ways of teaching and learning by working together to create a new course. Your guidance and mentorship enabled us to create a course that builds on the lessons I learned in my early education. Even more importantly, I want to thank the students of CLaSP 405-002 2018 and 2019, Data Visualization and Statistics in the Geosciences for striving with us in this effort. In creating this course, I was fortunate to benefit from the lessons of my education mentors across multiple fields. Thank you Dr. Cynthia Howell, for introducing me to the world of building community in climate and renewable education. Your work and my other education mentors Dr. Aileen Huang-Saad and Dr. Susan Montgomery helped inspire this course.

Along my path several teachers, research advisors, and instructors encouraged my interests. I want to express gratitude to my early education teacher Mrs. Campbell for providing a classroom in which students can focus on learning. I want to thank Professors Doreen Weinberger at Smith College who took extra time out of your day to provide new ways of looking at classical physics problems. Thank you to my undergraduate research advisors, who were willing to take a chance on undergraduate research in climate change education, astrophysics, and fusion. You all provided unique insights that I have taken into my graduate education.

My own path in STEM was shaped strongly by my experience at Smith College, where I found a fantastic community of support in physics and other scientific and technical fields (STEM). Through the years at Smith I want to thank my fellow physics and astronomy majors, as well as housemates. Michaela Gonzales, Audra Macie, Lucy Chikwetu, Carissa Misch, and Kristina Fedorenko, thank you for providing at Smith and beyond, a cohort of fellow ladies in STEM to collaborate through the highs and the lows. Thank you to my other colleagues of Smith, who are all pursuing wonderful lives after graduating. To Rosaline Martinez, Julia Reed, Will Saladin, and Elizabeth Davis and even more numerous amazing people who I met at Smith and after, thank

you for providing a community of scholars and support beyond as you continue on your amazing paths. You all provided a unique perspective on higher education, and from you I was inspired by your commitment to both your studies and your communities. I continue to learn from you all even now many years afterwards.

I want to thank my former colleagues at the IDA Science and Technology Policy Institute who provided insights and unique perspective on STEM for people in the world beyond academia. To my office mates and cohort of STPI Fellows, Ryan Whelan, Mitch Ambrose, Jessica Brooks, Emma Tran, and Eoin McCarron, thank you for the years we worked together and community we built. You are all striving now to bring STEM into policy discourse, and vice versa through becoming experts in your own rights. I am grateful we were able to spend those brief years learning and working with each other. To all the other staff, and years of STPI Fellows, thank you for providing a collaborative and inclusive workplace. STPI is a unique place and I am grateful to have spent time learning from you all.

Throughout my graduate education I found similarly supportive communities through my fellow students. You are all amazing researchers and educators, working passionately to improve graduate education. To my office mates through the years Dr. Lois Smith, Dr. Doga Ozturk, and Dr. Shaosui Xu thank you for providing an ear during my first years of the PhD and beyond. To my fellow women in graduate education, Alicia Petersen, Camilla Harris, Dr. Meghan Burleigh, Kali Roeten, Jenna Zink, Dr. Samantha Basile, and Marissa Torres - thank you for making a place where we can share our stories with each other. To the wonderful community and officers of the Graduate Society of Women Engineers (GradSWE), thank you for sharing your knowledge and working to tear down walls in higher education with myself and my fellow GradSWE co-director Dr. Stephanie Crocker-Ross. Finally, thank you to the Rackham Graduate School and the Rackham Merit Fellows program for introducing me to a wonderful lifelong community of professionals committed to diversity and leadership in higher education.

I have been fortunate to find this community, as it exists only due to the striving of previous leaders in the field through research, and advocacy. I want to thank Dr. Fran Bagenal and Dr. Margaret Kivelson for your example, your interest, for providing essential advice on careers, interchange injections, and the planetary science regarding the outer planets. Similarly I want to recognize my thesis committee members, Dr. Michelle Thomsen, Dr. Yang Chen, and Dr. Carolyn Kuranz for their time, detailed review, and interest in this body of work and their exemplary leadership in their respective fields.

To my co-authors and mentors on these works across the world, thank you for providing guidance in Cassini science, instrumentation, and data science. Thank you for hosting my visits, hours of phone calls together to understand mass transport around Saturn, painstaking calculation comparisons, discussions of survey methodology, and deciphering of rotating coordinate systems. These works would not be possible without your willingness, interest, and time. To my soon to be fellow PhD holders, Ryan Dewey and Jeffrey Lockhart, thank you for taking time out of your own graduate studies in Mercury science and computational social science to work with me and trade lessons learned. I have enjoyed my discussions with you and I look forward to continuing learning with you.

Bridging machine learning and planetary science could only be done with the advice and mentorship of cross field experts. I want to thank the willingness of several data science experts for taking steps outside of their respective application fields to discuss both data limitations, and applications. Thank you Monica Bobra, Dr. Frank Crary, Dr. Robert Wilson, Garret Limon, Brian Swiger, and Dr. Jenna Wiens for discussing machine learning, complex space physics instrumentation, and large-scale statistics with me.

Thank you to the wonderful I.T. department of CLaSP and Dr. Faye Ogasawara, for enabling all my last minute requests including, most recently, a hard drive to move all my work remotely for the current work from home policies shuttering the world.

This PhD was supported through a range of funding sources. The first year of this thesis was supported by the NASA Earth and Space Science Fellowship under Grant No. NNX15AQ63H. Subsequent years of this thesis were supported by the National Science Foundation Graduate Research Fellowship Program under Grant No. DGE 1256260 and the University of Michigan's Rackham Merit Fellowship Program. Additional costs were funded by the Michigan Space Grant Consortium under NNX15AJ20H and the Michigan Institute for Plasma Science and Engineering. Conference travel in this PhD was supported through various funding including the American Astronomical Society Thomas Metcalf Travel Award, the AGU Student Travel Grant, the Rackham Conference Travel Grant, the Rackham Pre-Candidate Grant, the Notre Dame American Association for Women in Science, the conference organizers for the Magnetospheres of the Outer Planets at Tohoku University in Sendai, Japan, and a NASA travel grant for the Magnetospheres of the Outer Planets at Uppsala, Sweden.

In my thesis, and in my life, I have learned so much from each and every one of you. To accomplish this PhD I've had to look outside my primary field and its been such a

rewarding experience. I've found your interest and engagement extremely welcoming to your communities. To my colleagues across all fields of STEM, in policy, and working in data science your talents astound me. As I write this, the world is going to look very different in the next few weeks. Each day is bringing new challenges, and is upending our expectations. The next few weeks, and beyond, will be extremely challenging, but from my experience in my PhD I believe that we can learn, and work together. I look forward to bridging the divides between fields and people, to stretch our imaginations in exploring new worlds once again.

Thank you -

PREFACE

This dissertation contains previously published and presented material. Chapters II and III are first-author publications within the Journal of Geophysical Research: Space Physics in 2018 and 2019 (Azari et al., 2018; Azari, Jia, et al., 2019). Chapter IV has been presented at the American Geophysical Union Fall Meeting in 2018 and is a manuscript in preparation for submission (Azari, Allen, et al., 2020). Chapter V has been presented at the first ever Machine Learning in Heliophysics conference in Amsterdam, the Netherlands and is submitted to the special issue of Machine Learning in Heliophysics in Frontiers in Astronomy and Space Sciences (Azari, Lockhart, et al., 2020). The appendix is summarized from developed course materials which can be accessed on Github (Azari, Liemohn, & Swiger, 2019a), and was presented at the American Geophysical Union 2019 Fall Meeting session on Jupyter (Azari, Liemohn, & Swiger, 2019b). Published and submitted works are presented with minor formatting changes and there will be minor duplication of material between sections.

Interchange events identified in this thesis can be obtained through on the Deep Blue Data Repository under doi:10.7302/Z2WM1BMN (Azari, 2018). Data used in this work can be found on the NASA Planetary Data System (PDS). The most recent datasets can be found on the Cassini-Huygens Archive page at the PDS Planetary Plasma Interactions node at (https://pds-ppi.igpp.ucla.edu/mission/Cassini-Huygens).

Several computational tools were used in this PhD. For the relevant references I direct the readers attention to the usage within the subsequent chapters and appendix. Certain figures and images are used in this PhD which were not produced by the author. They are credited appropriately in the figure caption, or the figure itself.

TABLE OF CONTENTS

LIST OF FIGURES

Figure

ABSTRACT

In 2004 the Cassini-Huygens mission arrived at Saturn. As the first ever Saturn orbiter, Cassini collected data reaching from the largest moon, Titan, at 20 Saturn radii (R_S), to the atmosphere during its death plunge in 2017. This mission drastically shifted our understanding of the Saturn system by providing insights of complex dynamics for over a decade. One of the major findings was of cryovolcanic geysers on Enceladus at 4 R_S, deep in the region dominated by Saturn's magnetic field, or magnetosphere. The water from Enceladus is one of the major factors leading to an instability of charged particles, or plasma, called interchange. Interchange is most similar to a Rayleigh-Taylor instability, in which the rapid rotation of Saturn drives dense plasma into less dense H^+, resulting in inward moving high-energy plasma, and outward moving dense plasma. Interchange has long been expected as a process of plasma transport throughout planetary magnetospheres and due to Cassini, statistical studies are now able to answer in new detail questions about interchange's role in magnetospheric dynamics including plasma transport, energization, and loss.

In this thesis I present a supervised physics-based classification of interchange from high-energy (3-220 keV) ions using methods commonly employed in machine learning merged with physical knowledge of Saturn's environment. With this standardized list, subsequent work can be broken into four advancements toward understanding Saturn's plasma dynamics. First, this thesis developed estimations of event size, location, and severity, painting interchange as a complex instability sensitive to in-situ plasma dynamics. Second, an investigation of ionospheric influence on injections demonstrated limited control, opening up questions on the ionosphere's role in interchange. Third, interchange was shown to be adiabatically energizing plasma around Saturn and long-standing observations of energetic regions of Saturn were explained through quantification of plasma-neutral interactions. Fourth, the original physics-based classification was used to propose a framework toward applications of machine learning to gain physical understanding benefiting from the surge of planetary space physics data available. This work provides a data-rich perspective on mass transport in planetary magnetospheres through characterizing Saturn's complex environment and details a path for integrating physics into machine learning.

CHAPTER I

Introduction

1.1 Exploration of Saturn's Complex System

In 2004, the Cassini-Huygens mission arrived at Saturn. For the next 13 years, this mission collected 635 gigabytes (GB) of scientific data about Saturn and its complex system of rings and moons (NASA Jet Propulsion Laboratory, 2017a). The previous missions to Saturn, Pioneer 11, Voyager I and II, provided only brief fly bys of the planet in the late 1970s and early 1980s. In comparison, Voyager I and II, each had a 70 kilobyte (kB) or 8-track tape machine to fill with observations before transmitting these data to Earth (NASA Headquarters, 1980). This means that as the first orbiter around Saturn, Cassini offers a new data rich perspective of the planet (see Figure 1.1). Saturn now has the second most observed near-space magnetic environment, or magnetosphere, after that of Earth (Gombosi et al., 2009). These data allow for the first measurements to disentangle spatio-temporal dynamics and enable large scale statistical methods.

From Cassini, many of our previous expectations about the Saturn space environment have been overturned. One such example is the primary source of mass throughout the magnetosphere. Previously this was thought to be the largest moon of Saturn, Titan, near 20 Saturn Radii (R_S) from the planet. Instead, Enceladus, a small and unassuming moon deep within the magnetosphere at 4 R_S, was observed outgassing plumes of icy particles and vapor from the southern region of its pole (see Figure 1.2) (Porco et al., 2006; Dougherty et al., 2006). Enceladus alone is estimated to be contributing 150-350 kg/s of material (Hansen et al., 2006). The plumes are thought to be sourced from liquid water under Enceladus' icy crust and include organics (e.g. Waite Jr. et al., 2006). This discovery has excited the field of planetary science due to its unexpected finding of a mass source and of a potentially life supporting environment in a system so far from the Sun (Porco, 2017).

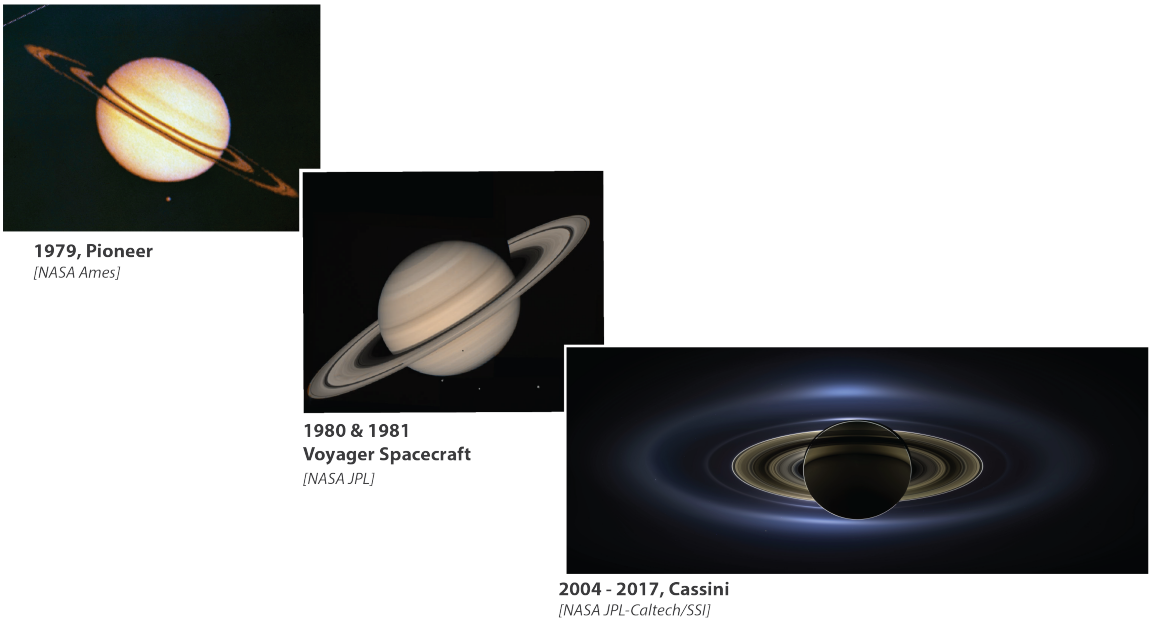

Figure 1.1: A timeline of Saturn system exploration. This image illustrates the history of all spacecraft missions sent to Saturn over the last half century. The most recent of which was the Cassini-Huygens mission which collected data over the Saturn system over multiple years, resulting in the back lit image shown within this figure. Images used in this figure are credited within.

1.2 A Neutral Dominated Magnetosphere

Saturn's magnetosphere is often called neutral dominated due to the effect of Enceladus plume material spreading out from 4 R_S to populate the expansive E-ring (stretching from 3 R_S outwards to near Titan at 20 R_S) (e.g. Srama et al., 2006). This dense material is primarily composed of H_2O ($\sim$91 $\pm$ 3% as compared to other molecular species) (Spahn et al., 2006; Waite Jr. et al., 2006). It is now understood that this neutral environment contains primary species of OH, H, and O in addition to H_2O (e.g. Dialynas et al., 2013; Esposito et al., 2005; Perry et al., 2010). This results in a neutral dominated region in the magnetosphere of Saturn with a minimum mean neutral-to-ion ratio of 60 within the equatorial 3–5 R_S region and increasing beyond (see review within Mauk et al., 2009; "The distribution of atomic hydrogen and oxygen in the magnetosphere of Saturn", 2009; Shemansky et al., 2009). For comparison Saturn's neutral to ion ratio is approximately 3 orders of magnitude higher than at Jupiter, another gas giant magnetosphere with mass sourced from a moon (Io in Jupiter's case) (Delamere et al., 2007). This complex mix of neutrals filling the magnetosphere, in addition to the unique presence of Cassini, makes Saturn an ideal location to study the effects of neutral and dusty plasma interactions.

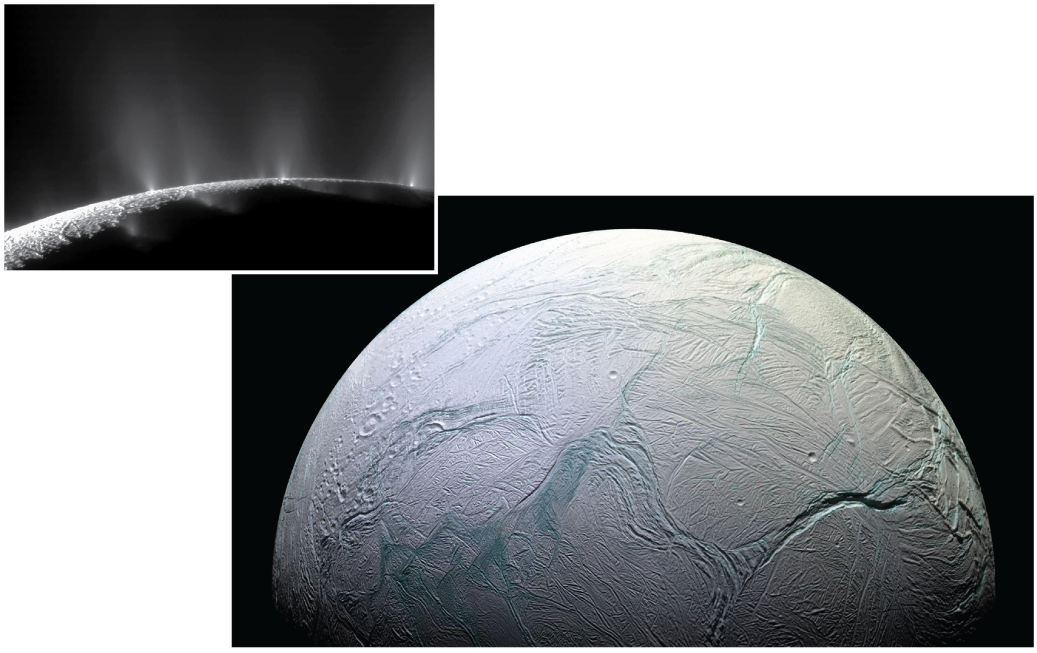

Figure 1.2: Enceladus' southern pole outgassing. The lower right photo shows a colorized image of Enceladus' south pole taken with Cassini in 2008, with the plume areas in blue. The upper left image shows active plumes outgassing from same region illuminated from the sun. Images used in this figure are credited within.

The dusty plasma environment around Saturn from its extensive ring system and Enceladus, impacts the dynamics of other particle and plasma populations (e.g. Wahlund et al., 2009; Morooka et al., 2018). This provides a unique test case to study other astrophysical systems, including planetary formation. Dusty plasma is considered a major stage for planetary formation from early nebula (Goertz, 1989; Birnstiel et al., 2016). From this source population of neutrals and dust a small amount undergoes ionization by impact ionization and charge-exchange, creating a dense and low temperature plasma population close to Saturn (Fleshman et al., 2013; Jurac & Richardson, 2005). This cold and dense plasma population's transition to the hotter tenuous plasma of the outer magnetosphere as observed through multiple Cassini passes has been termed a plasmapause (e.g. Thomsen et al., 2015; Young et al., 2005). This dense plasma is pushed against hot and less dense plasma, thought to be energized through tail reconnection processes (see Mitchell et al., 2015, for review of the energization process). The transition itself between these two plasma populations is often abrupt, and averages to near 10 R_S with significant variation in both time and space, with extensions at times of 15 R_S (Thomsen et al., 2015; Thomsen & Coates, 2019). Put into perspective, on the dayside of the planet, this dense water

rich population can extend to the magnetopause.

The transition from one population to another upon this plasmapause boundary are not always immediate. During certain Cassini orbits, alternating occurrences of these two plasma populations are observed before transitioning into the dominant population (Thomsen et al., 2015). Interchanging plasma populations are a necessary condition to transport cold plasma from the neutral dominated inner magnetosphere outwards, and subsequently from the energetic less dense populations inwards (see Thomsen, 2013, for a review). Interchange has long been proposed as a theoretical requirement of how mass must move around mass loaded magnetospheres (Southwood & Kivelson, 1987). The subsequent discovery of the unexpected water outgassing from Enceladus, shifted the understanding of mass transport around Saturn and brought the role of interchange to new importance.

This thesis uses large-scale statistics to fill in a new picture of interchange at Saturn. At the start of this work, how exactly these two plasma populations interchanged was unknown. Global understanding of the role of interchange in the Saturn system was limited. In Figure 1.3, an illustration of the interchange region in Saturn's magnetosphere is shown with limited mixing of the two plasma populations. The rest of this work investigates with the Cassini dataset, a new understanding of how interchange acts in Saturn's magnetosphere.

1.3 Interchange: A Critical Process in Transport

A magnetosphere can be considered the region in which particle motions respond to the magnetic field of the main body (Gold, 1959). At Saturn, the magnetosphere can be considered to extend on the dayside to the magnetopause, which nominally exists at 25 R_S but ranges between 17 and 29 R_S (Arridge, André, McAndrews, et al., 2011); occasionally leaving Titan at 20 R_S exposed to the solar wind. The dynamics of magnetospheres, or magnetic field and particle interactions, are responsible for the occurrence of the aurora at many planets, as well as the more damaging phenomena of space weather at Earth. How mass is circulated throughout a magnetosphere depends on both the internal (inside the magnetosphere), and external (most often referring to the solar wind) effects. One of the long standing questions of interest to magnetospheric studies has been to understand how mass is transported throughout a magnetosphere. Magnetospheres can be considered an interconnected system, in which the dynamics of the outer most reaches can affect observations at the upper atmosphere through complex interactions of magnetic fields and particle motion (e.g.

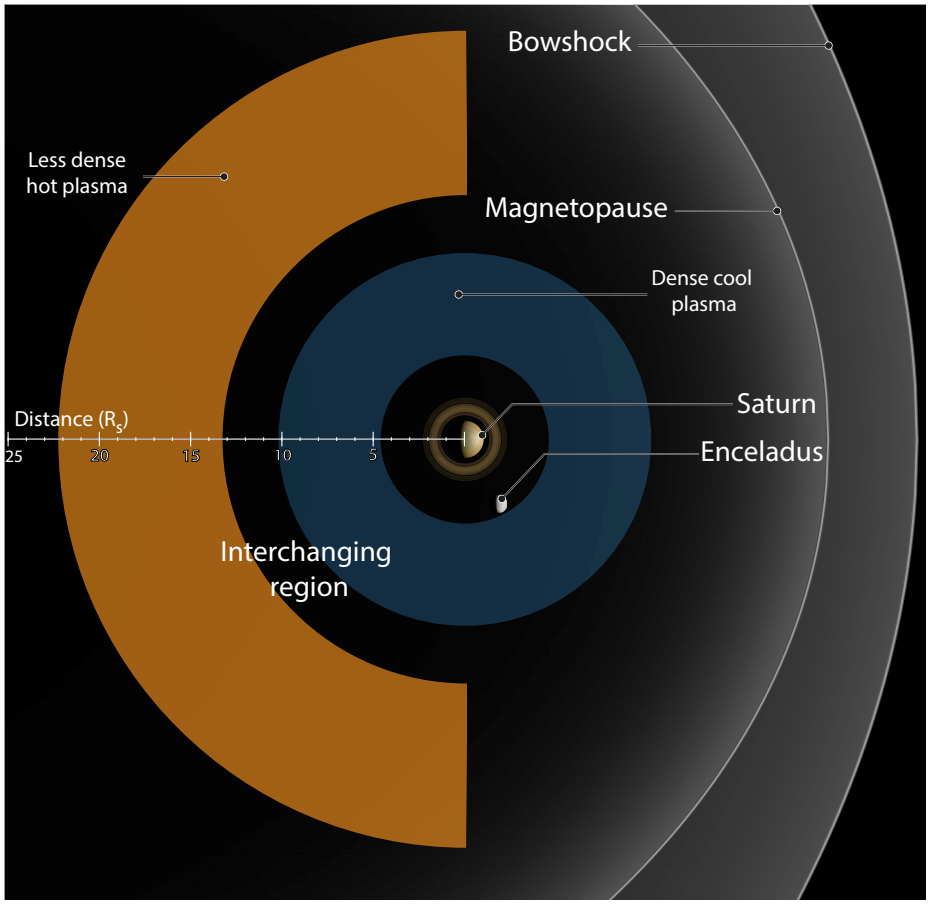

Figure 1.3: Schematic of interchange region at Saturn. This illustration provides a top down view of the two plasma populations acting in interchange. In blue is the Enceladus sourced cool plasma. In orange, a further distant hot plasma. Interchange occurs through mixing these two populations. This figure was created in consultation and with permission from Falconieri Visuals. Copyright held by Falconieri Visuals.

Borovsky & Valdivia, 2018). Studies into transport therefore, have been essential to understanding all parts of an interconnected magnetospheres.

How transport responds to internal or external influences categorizes a magnetosphere as either externally influenced or internally influenced. On one side of this classification, Mercury and Earth present as externally driven, where the magnetospheres respond to primary driving from mass, momentum, and energy from the solar wind. The circulation system for internally driven systems is the Dungey cycle, in which the solar wind triggers periodic mass release through magnetic reconnection from the tail, or far reaches of the magnetosphere (Dungey, 1961, 1963). Jupiter alternatively presents an internally driven system dominated by the mass loading of the inner magnetosphere from the moon Io, and the rapid rotation of the planet creates a situation known as the Vasyliūnas cycle (e.g. Bagenal, 2007; Krupp et al., 2004). In this mass release process, the primary driver is the rapid rotation of the planet itself, and internally generated mass loaded fielded lines are stretched downtail with the rapid rotation of the planet until magnetic reconnection occurs (Vasyliūnas, 1983). Saturn however breaks this traditional classification with presentation of both internal and external influences, and of both major mass transport processes (see reviews within Krupp et al., 2018; Thomsen, 2013).

These two main reconnection driven transport systems do not complete the full picture of mass transport in internally loaded systems. Interchange is traditionally considered an internal process, arising from the combination of mass loading and the rapid rotation of a planet (Southwood & Kivelson, 1987, 1989). Interchange fulfills the role of a bridge between the inner and outer regions of a magnetosphere. It transports plasma from the dense inner regions outwards, and similarly energized plasma inwards. Historically at Earth interchange was invoked as a description of inherent instability of the system, and more modernly, plasmapause evolution although evidence points toward convective erosion rather than interchange (e.g. Gold, 1959; Lemaire & Kowalkowski, 1981; Pierrard & Lemaire, 2004; Goldstein et al., 2003). This original concept was applied to the rapidly rotating outer planets by Hill (1976) (see Achilleos et al., 2015, for a review of the early history of interchange theory). At the outer planets, interchange is of greater importance due to higher mass loading and faster rotational rates. Interchange and its role in transport can now be studied in these systems due to modern observations.

Interchange itself can be considered most analogous to a Rayleigh-Taylor like instability, wherein a dense fluid is forced, usually by gravity, into a less dense fluid, creating a naturally dynamically unstable system. At Saturn, this is analogous to the

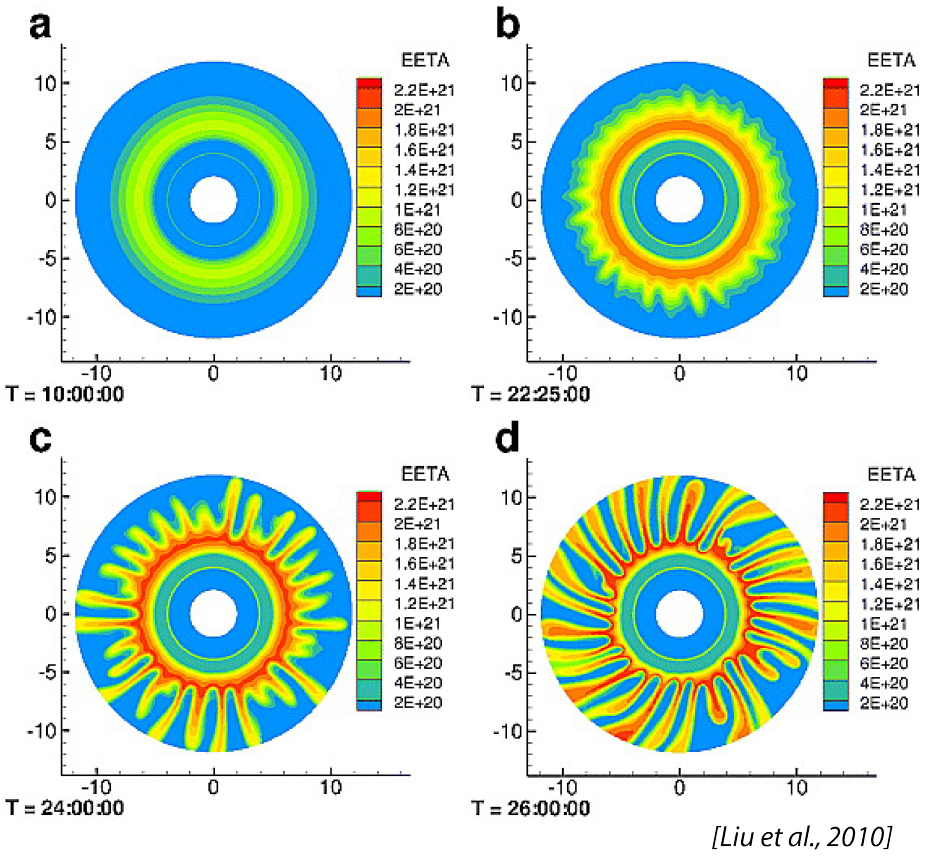

Figure 1.4: Magnetohydrodynamic simulation of interchange from Liu et al. (2010). The four panels represent a temporally evolving interchange unstable system using the Rice Convection Model. EETA represents flux tube ion content in ions per Weber. This represents the most cohesive system wide understanding of interchange at the start of this work. The reproduced figure is from an article within an American Geophysical Union (AGU) journal (see citation above and within). AGU does not request permission in use for republication in academic works.

rapid rotation of the planet at ∼10.7 hours imparting a centrifugal force outwards upon the plasma gradient between the cold dense plasma and the hot tenuous plasma of the outer magnetosphere (e.g. Delamere et al., 2015). Within this framework interchange motions would be considered to be respondent to the internal dynamics of the system and result in a system of interchange around Saturn shown in Figure 1.4. This series of magnetohydrodynamic simulations demonstrated the potential of interchange at Saturn for transporting plasma throughout the system by showing series of interchanging plasma populations (Liu et al., 2010; Liu & Hill, 2012). At the time of this thesis, these simulations presented the most complete system-wide understanding of Saturn's interchanging region. These results demonstrate the feasibility of the instability at Saturn. As discussed within Thomsen (2013), these simulations do not capture the observed rapid nature of injections. Additionally, observations from Cassini, and Galileo at Jupiter, began to bring into question the spatial locations of interchanging regions and interchange's response to external driving.

1.4 Observations of Interchange Injections

Previous to Cassini, the Galileo mission to Jupiter recorded observations of rapidly (∼100 km/s) traveling plasma toward the planet. These were identified as incoming interchange injections from at least 1 Jupiter Radii (R_J) if not more ("Galileo evidence for rapid interchange transport in the Io torus", 1997; Kivelson et al., 1997). Within these events significant changes in the pitch angle anisotropy hinted toward plasma heating, and interchange as a source of energetic particles in the inner magnetosphere ("Galileo evidence for rapid interchange transport in the Io torus", 1997). These incoming injections were most readily identified as enhancements of magnetic field upon the background magnetic field, thought to be from the requirement of magnetic and particle pressure balance within events (Kivelson et al., 1997; Lai et al., 2016; André et al., 2007, 2005). Similar to subsequent observations of injections by Cassini, the incoming interchange events, or injections, were much more readily identified than the equivalent outgoing drift. This created one of the first mysteries surrounded interchange injections as both the inflow and outflow should occur (seen in Figure 1.4). Evidence of outflow channels were not found until several years into the Cassini mission, in which Thomsen et al. (2015) identified an outflow region of the cold thermal plasma traveling outwards. Unfortunately, large-scale statistical studies of interchange were limited within Jupiter's system, as the Galileo mission suffered a catastrophic failure to deploy its high-gain antenna. As such the data return to

understand interchange was limited as only small amounts of the originally planned data was returned to Earth for analysis.

Within the Cassini observations, similar to Galileo, interchange injections can be identified through the suite of particle, wave, and magnetic field data. Within Figure 1.5 from Azari et al. (2018), a series of four incoming injections are presented in the Cassini data from the Cassini Magnetospheric Imaging Instrument: Charge Energy Mass Spectrometer (CHEMS), the Cassini Plasma Spectrometer (CAPS), and magnetometer (MAG). Within this Figure the four unique injections appear column like in the spectrometer data, with a corresponding enhancement of magnetic field upon the background. In terms of particle measurements, an inward moving interchange flux tube is normally characterized by its intensification of hotter plasma (>100 eV) and depletion of cold plasma. Since the arrival of Cassini at Saturn in 2004, interchange events have been observed with multiple sensors and thought to be the primary form of plasma transport from the inner magnetosphere to the outer magnetosphere at Saturn (e.g. André et al., 2005, 2007; Burch et al., 2005; Hill et al., 2005; Mauk et al., 2005; Rymer et al., 2009; Thomsen et al., 2014).

Interchange injections can be distinguished from the effects of large-tail related transport, also unfortunately called injections, from the primary location of these two effects and the energy range and scales of the incoming material. Compared to interchange events, larger scale flux transport events related to the Dungey and Vasyliūnas cycle occur predominantly within the night and morning sectors, as well as further outwards within the tail of the magnetosphere (> 15 R_S) lending credence to their relation to reconnection processes (Müller et al., 2010). Large-scale injections are associated with reconnection and follow particle acceleration and heating non-adiabatically from current sheet collapse, whereas interchange injections are expected to be primarily adiabatically energized (Mitchell et al., 2015). Within this work, interchange injections will be referred to as "interchange", or "injections", while tail-related processes will be referred to "large-scale injections" as much as possible. These larger scale injections are often discussed in relation to post-reconnection-driven transport, but their association with interchanging small events is not well constrained. Previous statistical studies with the Cassini mission have found varying local time and longitude organization of these small scale injections (Thomsen, 2013), leading to uncertainty in interchange's role in the Saturn system for mass transport and relation to external influences. These previous surveys however, all used different primary sensors for manual identification with little comparison between surveys. This suggested disagreement in the identification methods that impacted the scientific conclusions

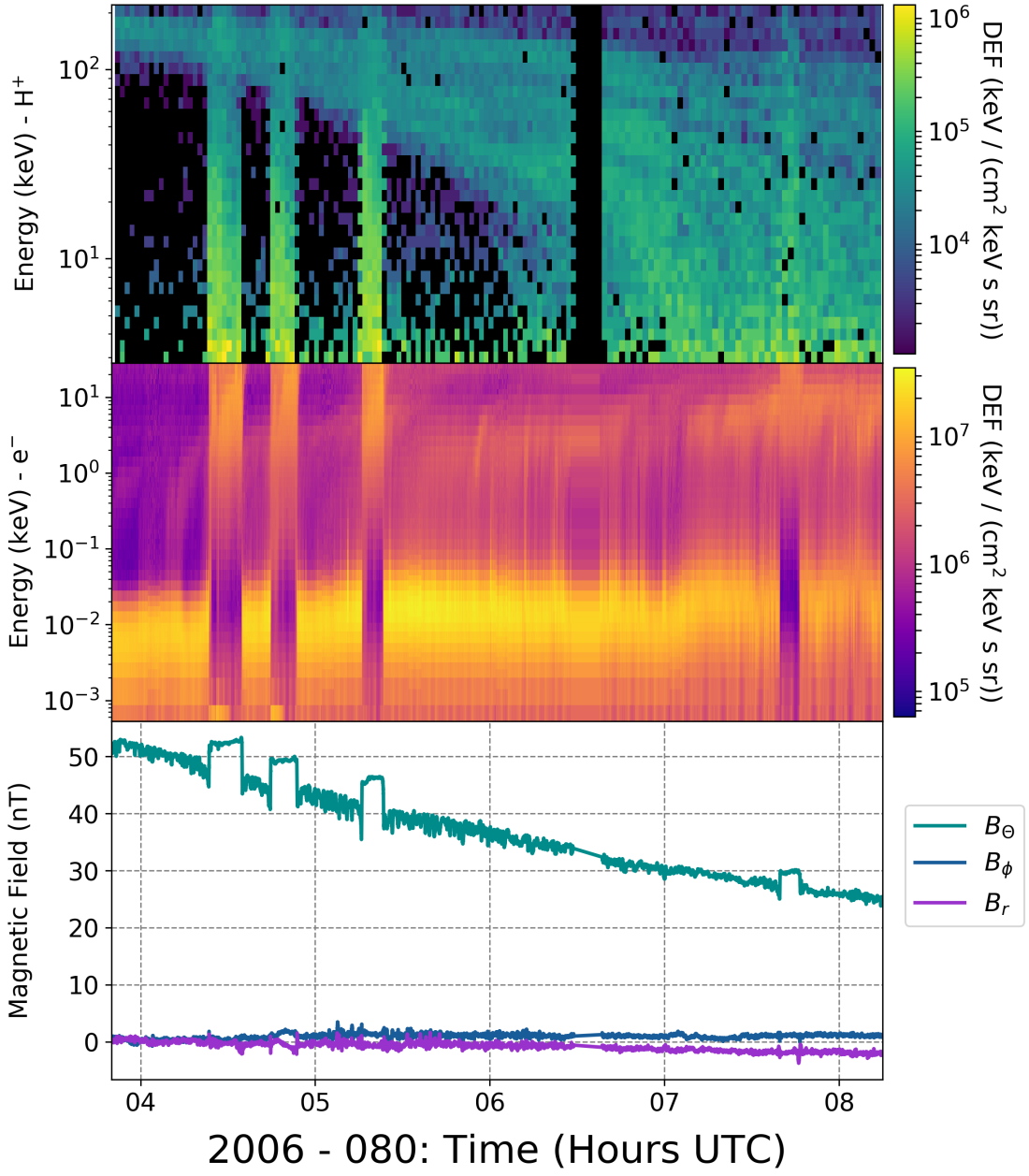

Figure 1.5: Series of interchange injections from Azari et al. (2018) on 2006 day of year 080. The top plot is the differential energy flux of H^+ as measured by CHEMS between 3 and 220 keV, followed by the CAPS ELS differential energy flux for electrons from Anode 4, and finally the magnetic field in KRTP (Kronocentric body-fixed, J2000 spherical coordinates). The reproduced figure is from an article within an AGU journal (see citation above). AGU does not request permission in use for republication in academic works.

gathered from these surveys. In addition, the majority of these surveys focused on the depletion of the thermal plasma and resultant signatures, such as plasma wave excitation, or magnetic field enhancement (Lai et al., 2016; Kennelly et al., 2013; Y. Chen & Hill, 2008), and the intensification of high-energy (keV) H^+ was often not included.

1.4.1 High-Energy Observations

The CHEMS high-energy sensor, presented in the top panel of Figure 1.5, clearly demonstrates an intensification of H^+ related to the transport of the material toward Saturn. It is expected that the thermal plasma should follow in greater agreement with the theory presented above. The high energy relation to the low energy signatures of interchange however is unclear. Müller et al. (2010) reviewed the high energy component of electron injections, but this study was pursued on a not yet complete Cassini mission and while their injection identification criteria is not a primary objective of the work, injections included were likely long-duration and related to tail processes. Interchange injections had not been examined statistically to understand high energy ion transport within the magnetosphere of Saturn, and this left conclusions about the system of transport incomplete. These questions included how the high energy regime related to the thermal plasma signatures, and to large scale injections and external influence. To understand the flow of mass around Saturn the creation of a standardized list of the high-energy ions was needed.

CHEMS was an active sensor onboard Cassini which collected pitch angle information and species resolved keV range particle data (Krimigis et al., 2004). Unlike the CAPS sensor, which was terminated mid-mission, CHEMS provides a mission long dataset of hydrogen and other ion information throughout the magnetosphere of Saturn. This allows for CHEMS to be used in statistical studies to evaluate the global system (e.g. Allen et al., 2017). Cassini's particle and field suite was designed with CAPS to be operational but due to technical difficulties the thermal dataset was limited after 2012. In one example, current calculations of equatorial plasma parameters inside of the magnetosphere can only be calculated for under 5% of the completed Cassini mission (Wilson et al., 2017). Nonetheless, CAPS informed a wide range of interchange surveys before 2012 which greatly advanced understanding of the thermal behavior of interchange. The difficulties encountered after 2012 created a need for other plasma instruments onboard Cassini for analysis. This included sensors which were originally unplanned to be used as the primary plasma sensors.

CHEMS for example, collects pitch angle information, which is critical to under-

standing the role of interchange within the system, but only for a distinct angular subset of the full available pitch angle space. A particle's pitch angle is the angle between its velocity vector and the magnetic field as it orbits around a magnetic field. A particle's pitch angle offers insight into plasma dynamics. On CHEMS this subset varies over the mission as the spacecraft rotates. Similarly, there are data gaps, both at single time points throughout the dataset, and over multiple sequential points in time (as can be seen within the CHEMS data in Figure 1.5). In addition to the inherent spatio-temporal nature of the satellite trajectory and dynamic system being measured, this creates a challenging task for automatic identification of interchange.

1.5 Context of Planetary Data for Machine Learning

Cassini was the first, and as planned, only long duration spacecraft to study Saturn's magnetosphere. Due to the recent occurrence of this mission arriving in 2004, statistical studies using machine learning on Saturn have been limited in comparison to other large-data communities. Studies using machine learning are particularly new to scientific analysis of planetary systems. Within other subsets of space physics, primarily space weather and solar physics, machine learning has shown promise in applications toward prediction (see relevant overviews within Camporeale, 2019; M. Bobra, 2017). Planetary science has also seen a surge of machine learning applications focused on environmental characterization such as change detection on planetary surfaces (e.g. Kerner et al., 2019) and for exoplanet detection (e.g. Millholland & Laughlin, 2017). Where does this leave applications of machine learning for understanding mass transport around Saturn? It makes sense to take advantage of the 635 GB collected from Cassini, but applications of machine learning for prediction are limited in planetary science. The main goal of this work is to understand and derive meaning from the observations within the context of the theoretical understanding of transport in planetary magnetospheres. In this context, the interpretability and explainability, or human understanding, of the machine learning model is critical.

Within the machine learning community incorporating knowledge that is specific to the application at hand, has been termed domain-knowledge. Within the physics community, this is known as physics-informed machine learning (e.g. Raissi et al., 2019). In the geosciences, such methods have advantages toward allowing scientists to interpret results, use existing knowledge, and to address specific issues in the nature of geoscience data that pose challenges to the applications of machine learning (Ebert-Uphoff et al., 2019). Geoscience data often has a spatio-temporal nature as

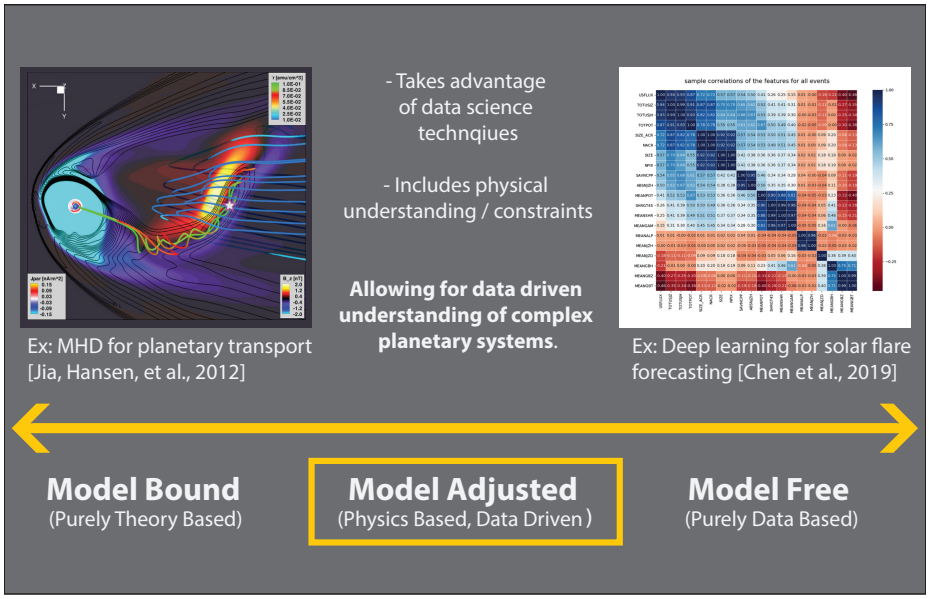

Figure 1.6: Model adjusted framework for machine learning in planetary sciences to gain physical insight. This diagrams a continuum moving from model bound, or purely theory bound, toward model free. The figure in model bound are from Jia, Hansen, et al. (2012), a magnetohydrodynamics simulation of Saturn's magnetosphere. The figure in model free is from Y. Chen et al. (2019), deep learning feature correlations for solar flare precursor identification. This figure contains subfigures from AGU journals. AGU does not request permission in use for republication in academic works but we do point readers toward the associated AGU works for citation.

well as rare events that scientists are interested in learning about (Karpatne et al., 2019). These challenges are only accentuated in planetary data, which not only has these aspects, but also from unexpected issues such as Galileo's transmission rate limitations, Cassini CAPS technical issues, or CHEMS' pitch angle resolution. The data from such planetary missions can be used, and these challenges addressed with machine learning by incorporating prior knowledge and pursuing model-adjusted applications. Figure 1.6 presents a proposed framework in this thesis of model-adjusted machine learning. In this framework, using domain knowledge specific to the planetary application, is used to address limitations of plaentary datasets and to increase interpretability and explainability. As planetary missions continue to collect large amounts of data, such methods will become essential tools for scientific analysis, but there are still many questions about best practices in applying these methods.

1.6 Guiding Questions

The Cassini mission presents an ideal dataset in which to apply and examine model-adjusted machine learning to understand the role interchange injections play in planetary magnetosphere. Presented here are the guiding questions for the following thesis.

1. **How are interchange injections distributed spatio-temporally and what implications does this have toward relation to large-scale dynamics of the Saturn system?**

2. **Are observed interchange injections sensitive to internal processes, such as ionospheric conductivity?**

3. **What role do interchange injections play in system wide transport for energization and loss?**

4. **When applying machine learning to answer planetary science questions, what considerations are needed?**

These questions address the role interchange plays as a major transport process at Saturn and provide paths forward toward completing understanding of planetary magnetosphere mass transport, and future work in applications of machine learning to understand physical systems.

1.7 Outline

In Chapter II, question 1 is addressed by identification and analysis of interchange injections through a supervised physics-based classification most similar to a logistic regression using the CHEMS high-energy H^+ flux data. In Chapter III, question 2 is addressed through reviewing organization of interchange with respect to longitude system which map into the ionosphere of the planet. In Chapter IV, question 3 is addressed by deriving a pitch angle parameter from the Cassini data to study how plasma is energized, and lost within the system, and compared to the system-wide distribution of energetic particles. In Chapter V, the original algorithm developed in Chapter II is evaluated against logistic regression and random forest models with varying data subsets to address question 4. As machine learning and even broader, large-scale statistics and visualization methods, are relatively new to the geoscience community, part of this thesis addresses developing educational material to train undergraduate and graduate students in application of statistical and visualization methods. This work is summarized in the Appendix. Finally, in Chapter VI the findings from these questions are discussed to provide a new picture of the Saturn system within the context of planetary magnetosphere mass transport, and comment on future directions of both the scientific pursuit of this topic and for applications of machine learning to other planetary science questions.

CHAPTER II

Automated Physics-Based Identification of Interchange from Energetic Protons

The chapter below details the development of a physics derived identification method for interchange injections based on the machine learning model of logistic regression. Using the identified events this chapter then pursues an analysis of the spatio-temporal locations of events within Saturn's system to understand the primary triggering mechanisms of interchange injections. The chapter was originally published in the Journal of Geophysical Research: Space Physics under the title of "Interchange Injections at Saturn: Statistical Survey of Energetic H^+ Sudden Flux Intensifications" in 2018 (Azari et al., 2018), and the produced interchange injection identification list is curated on University of Michigan's Deep Blue Data repository (Azari, 2018). The work is presented as published with minor formatting adjustments.

2.1 Introduction

The Cassini spacecraft routinely observed interchange injection events with multiple instruments since arriving at Saturn in 2004. Interchange injection events are thought to arise from a Rayleigh-Taylor like plasma instability driven by Saturn's rapid rotation (period ∼10.8 hr) and the dense plasma population that is created from Enceladus' plume neutrals. Strong centrifugal forces associated with the planetary rotation and internal neutral mass source from Enceladus result in a magnetosphere unstable to interchange (Hill, 1976; Michel & Sturrock, 1974; Southwood & Kivelson, 1987, 1989; Vasyliūnas, 1983).

The centrifugal force causes swapping between magnetic flux tubes containing dense and cold plasma originating in the inner magnetosphere and the relatively depleted flux tubes farther out, whereby dense, cold plasma is slowly transported

outward and less dense, hotter plasma is injected inward (e.g. Achilleos et al., 2015; Mauk et al., 2009; Thomsen, 2013). Such events are the primary source of mass transport in the inner/middle magnetosphere and play a critical role in plasma transport and dynamics within the Saturnian magnetosphere. Continuously supplied dense plasma must be transported outward, and to conserve magnetic flux, rapidly inward moving flux tubes of low density, energetic (>keV) plasma from the outer reaches of the Saturnian system also occur. These inward bound flux tubes are referred to as interchange injections. Since the arrival of Cassini at Saturn in 2004, interchange events have been observed with multiple sensors and thought to be the primary form of plasma transport from the inner magnetosphere to the outer magnetosphere (André et al., 2005, 2007; Burch et al., 2005; Hill et al., 2005; Mauk et al., 2005; Rymer et al., 2009; Thomsen et al., 2014).

In terms of particle measurements, an inward moving interchange flux tube is normally characterized by its intensification of hotter plasma (>100 eV) and depletion of cold plasma (see Figure 1.5 as originally presented within this work). The variations in plasma pressure often lead to measurable changes in the magnetic field consistent with injections being in pressure balance with the surrounding plasma. As such, interchange injection events can also be identified in magnetic field data (André et al., 2007, 2005; Lai et al., 2016). Compared to interchange events, larger scale flux transport events occur predominantly within the night and morning sectors lending credence to their relation to reconnection processes (Müller et al., 2010). It is probably true that events that occur on larger spatial scales carry with them a population of energetic charged particles, for example, in excess of hundreds of keV (Mitchell et al., 2009; Paranicas et al., 2007). It has been shown to be less likely for spatially localized (small) interchange to transport particles of hundreds of keV great distances inward, due to a drift out effect. Wherein energetic particles are preferentially lost due to their larger gradient-curvature drifts and exit the interchange structures as compared to lower energy, or 1 keV particles (Burch et al., 2005; Paranicas et al., 2016). While these large-scale injections are often discussed in relation to post-reconnection-driven transport, their association with the more ubiquitous small events is still a point of research for small-scale interchange injections. For example, there is a noticeable difference between triggering these large-scale events and smaller-scale events? Or can small-scale and large-scale events be thought of as a continuum? We know, for instance, that plasma must be shed, so the question is what magnetospheric factors, if any, lead to situations where heavy inner flux tubes are destabilized.

It has been suggested that after the occurrence of a large-scale injection, inter-

change occurrence rates would increase due to the enhanced flux tube gradient from the incoming plasma (Mitchell et al., 2015). This has been confirmed at a distance of $\sim$8.6 R_S to form a plasmapause with observed interchange injection activity (Thomsen et al., 2015). Within this paper, we will refer to interchange injections as "interchange" and tail-related processes as "large-scale injections."

Attempts to investigate interchange's dependence on other magnetospheric processes and plasma particle populations have resulted in several statistical survey analyses of the spatial dependence including radial and local time. Interchange occurs most often between at least 5 and 11 R_S, although not uncommonly extending beyond 11 R_S (e.g. Y. Chen & Hill, 2008; Thomsen, 2013, and references within) with a peak radial occurrence of $\sim$8.5 R_S (Kennelly et al., 2013).

By examining injections in Cassini Plasma Spectrometer (CAPS) data for the first two years of data after Saturn arrival, Y. Chen & Hill (2008) found preferential occurrence rates in the prenoon sector; however, their method of identification excludes very young (<1 hr old) events. A statistical survey by Kennelly et al. (2013) based on Radio and Plasma Wave Science (RPWS) identified injections from 2004 to 2011 targeted specifically young fresh events via enhanced wave activity associated with the contained hot electrons. The study found that the youngest interchange injections are preferentially located in the near-midnight and postnoon sector. Kennelly et al. (2013) accredits this difference to uncertainties associated with the back tracing method Y. Chen & Hill (2008) used in calculating the injection locations. The discrepancy in local time location has caused uncertainty in what if any local time distributions of injections exist, and the relation of interchange to plasmoid release downtail through reconnection or other triggering processes. One potential cause for this local time discrepancy beyond the identification disagreements is limited accounting for finite radial propagation time for incoming injections as suggested within Paranicas et al. (2016). These surveys have not been extended to the later years of the Cassini mission. But since CAPS returned no data after mid-2012, surveys have to rely on other data sets.

The intensification of 3–220 keV H^+ within interchange injection events has not previously been used as an identification method for a statistical survey of local time or radial distributions. A working definition of interchange events, let alone a detailed understanding of physical process, is not agreed upon in literature. This is due to the wide variety of methods pursued in event identification, gaps in survey results, and resultant disagreements in local time distribution. By pursuing a statistical survey of high-energy plasma measurements over the entirety of the Cassini mission, we can

complete the measurement set of Cassini observations related to interchange. Utilizing ion flux enhancement as our main identification criterion also allows us to observe different levels of intensification regimes and answer whether greater intensification events show different occurrence rates as compared to low intensification events.

We present an automated identification of interchange events using the Magnetosphere Imaging Instrument's (MIMI) CHarge Energy Mass Spectrometer (CHEMS) ion intensity data (Krimigis et al., 2004). CHEMS has near-continuous coverage during the Cassini mission, and pursuing the high-energy enhancement provides an opportunity to calculate particle pressure and intensity. We classify events by particle intensity increase above background flux levels and compare this new survey to previously published statistical interchange surveys to address the observed differences in these surveys. Such a computational classification and identification effort has never been pursued with ion intensity data, and we present similarities and differences to previous surveys.

We then evaluate interchange occurrence rates by local time and radial location, pressure, and intensity to answer our primary questions in this work: (1) do trends in local time and radial position persist over all phases of the mission/seasons of the planet and (2) are larger scale injections and ionospheric conductivity from the nightside of the planet playing a significant role for interchange occurrence rates?

2.2 Methods

2.2.1 Data

CHEMS obtains ion data by admitting a narrow energy per charge range into the device, then measuring the time of flight and energy deposited in the solid-state detector. The additional coincidence provided by the solid-state detector measurement is not available for all of the data (Krimigis et al., 2004). CHEMS has three separate telescope look directions each covering 53° in polar angle along the spacecraft's z axis, so it is often possible to sample different portions of the pitch angle distribution including measuring intensities near 90° pitch angle. For this reason we use CHEMS rather than the MIMI Low Energy Magnetospheric Instrument (LEMMS) instrument, as our primary energetic ion sensor as LEMMS is stuck since early 2005 at a single look direction and may not be sampling near 90° pitch angle as often as CHEMS. In addition, LEMMS's lowest energy for ions is 30 keV above our interest range between 3 and 22 keV. LEMMS is also sensitive to light contamination, making LEMMS difficult to use in an automated detection method (Vandegriff et al., 2013).

The sampling of CHEMS data utilized in this study is at no less than an ∼2 min cadence. The sampling varies to optimize for data quality and count rate. Inbound injections are represented in CHEMS H^+ data as a significant enhancement of energetic ions compared to the number local to the spacecraft without an injection event (Mauk et al., 2005). Inbound flux tubes are believed to come from a range of starting distances (Paranicas et al., 2016; Rymer et al., 2009). We expect the H^+/W^+ ratio to be significantly higher than back-ground values in the inner magnetosphere (Thomsen et al., 2014).

We use this energetic H^+ enhancement between 3 and 22 keV as the main identification criterion in our methodology. This measurement range is fortuitous because the highest energies in these discrete events tend to be in the tens of keV. This range allows for the classification of events by intensity, where we classify the most intense enhancements as the most severe. Dispersion signatures from older events and large-scale injections are seen to dominate spectrograms predominantly above 20 keV as compared to fresh event signatures, and this is an additional limiting factor for our energy range selection (see Figure 1.5).

In Figure 1.5 we present a selected grouping of interchange injection events. This series of events is of particular interest due to the bevy of previous studies on the pitch angle distributions, transport, and morphology of these interchange events (Mitchell et al., 2015; Paranicas et al., 2016; Rymer et al., 2009). In particular, this event shows particle energization dependence upon pitch angle (Mitchell et al., 2015). In this work we focus on all pitch angles, and we present in Figure 1.5 a comparison of CHEMS H^+ differential energy flux for all pitch angles sampled, the thermal electrons as measured through the CAPS electron spectrometer (ELS), and magnetic field from the MAG instrument. This figure demonstrates the flux drop-out discussed in the introduction within the thermal plasma and the intensification of the high-energy electrons, ions, and enhancement of magnetic field. The dispersion signatures discussed can be seen as the long curve in the CHEMS panel seen superimposed on the four fresh events. Our designed algorithm picks up each of these four fresh events, even though the fourth injection is particularly weak in CHEMS compared to the previous three.

We restrict our search for interchange events in the CHEMS H^+ data to the radial distances between 5 and 12 R_S, within the primary range of interchange occurrence rather than current sheet collapse events (Y. Chen & Hill, 2008; Mitchell et al., 2015; Thomsen, 2013). This satisfactorily avoids any effects from the warping of the plasma sheet with varying solar wind attack angle, which can reach up to $\pm 26.7^\circ$ at solstice (e.g. Arridge et al., 2008; Arridge, André, Khurana, et al., 2011; Carbary et al., 2008,

2015). Additionally, we limit our analysis to equatorial locations over the course of the mission, restricting the survey within 10° of the equatorial plane in the Saturn Equatorial System (SZS) to constrain our results to the plasma disk to allow for a buildup of background statistics within this dense region. We use CHEMS H^+ data primarily from equatorial passes of Cassini from between 2005 to mid-2016, excluding the beginning of the mission in 2004 and several high-latitude passes from the later months of the mission. These limitations still give us reasonable sample sizes from CHEMS H^+ data to test and run our identification criteria with a total of 68,090 data points totaling ∼172,980 minutes of sampling (see Figure 2.1).

In Figure 2.1 we present a diagram of Saturn by radial location and local time showing the total time the spacecraft spent in each location, after accounting for the restrictions described above on the CHEMS data set. The region between 5 and 12 R_S is reasonably well sampled, but by restricting our data to near equatorial (i.e., within 10° off the SZS equator), there are some gaps in local time, notably in the predusk and predawn sector. This is the primary rationale for presenting our results normalized to spacecraft dwell time to avoid sampling bias in our results.

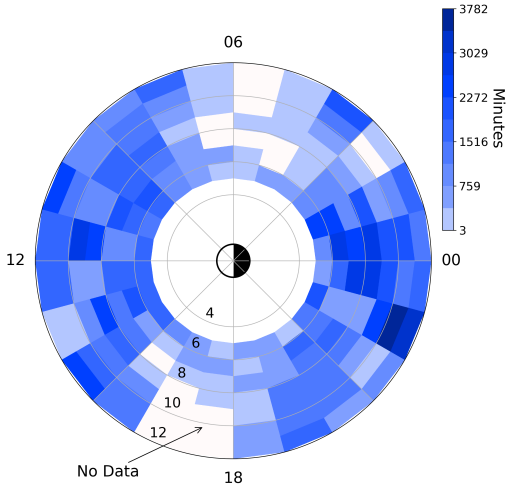

Figure 2.1: Cassini spacecraft equatorial plane sampling 2005 - 2016. Spacecraft dwell time representing the sample size of the CHEMS H^+ data set. Each region shows the total minutes occupied by Cassini that satisfy our selection criteria. This figure shows dwell time calculated from CHEMS timestamps of Cassini within the radial range of 5–12 R_S and at latitudes below 10° in SZS arranged by local time where noon is on the left of the figure. Bins with no data are shown in white.

We have designed and optimized an algorithm to automatically identify and rank events by H^+ particle intensity above the background plasma intensity. Additionally, this allows for a standardization of event identification and identification of categories of interchange intensity. This is extremely advantageous as we analyze the causation of the most intense interchange events as compared to less intense events and their respective influence from large-scale injection events. We discuss the algorithm development in sections 2.2.2 and 2.2.3.

2.2.2 Event Identification Procedure

The primary purpose of our designed algorithm is to identify, with reliability, and rank by their intensity, interchange events within the CHEMS H^+ equatorial data set between 2005 and 2016. Several critical design considerations were taken into account when developing this method, with the most critical being the distribution of plasma populations between 5 and 12 R_S. The Cassini trajectory had a range of periapsis distances and inclinations characterized by different particle populations. We address this by limiting our sampling to the primary region of interchange injection as dis-cussed above, but additionally, we subset our data set by season and then we weight high intensity values with respect to their radial and energy ranges as described in the flowchart of Figure 2.2. The weighting is discussed further in the following paragraphs and in Chapter V. Figure 2.2 represents a visual description of our algorithm procedure. Our identification method starts subsetting the equatorial CHEMS H^+ data between 5 and 12 R_S and partitioning into seasonal ranges of pre-equinox (2005–2008), equinox (2009–2011), and post-equinox (2012–2016).

There is evidence in the Cassini data set of seasonal variations so we pursued this subset in our methodology to allow for any seasonal effects to be captured in our analysis and in our results (Sergis et al., 2011). We also observed by dividing the data set in this manner our algorithm performance improved. Down sampling further into smaller time ranges (by year for example) did not produce significant improvement.Additionally, these ranges contain roughly equal data sampling with $\sim$760, 1,100, and 1,020 hr of data in the pre-equinox, equinox, and post-equinox date ranges above, providing a roughly equal sampling for our z-score calculations. Z-score, or standard score, is a commonly used term in statistics to refer to the number of standard deviations above a mean. Our pre-equinox data set is slightly smaller, but this is because of a small number of low inclination orbits in the pre-equinox date range. Our choice of these date ranges was influenced by the natural data gaps in the equatorial data between years and to achieve similar sample sizes and location coverage between the three partitions while still increasing performance. We use these samples to build up an aver-age with statistics and deviations from these averages through identification of outliers discussed in the next paragraph.

We further subset our seasonally separated data into 1 Rs bins between 5 and 12 R_S for the analysis as represented in Figures 2.2a–2.2c to address the variation in H^+ suprathermal plasma background with radial distance demonstrated in, for example, Sergis et al. (2017). Then for each 1 R_S subset within each seasonal selection, we calculate the distribution of the logged intensity values for each energy range. This

results in multiple distributions representing each season, radial location, and energy range between 3 and 22 keV. Using these distributions (see Figure 2.2a for an example distribution), we assign a z-score for each energy level between 3 and 22 keV (14 channels) for each CHEMS data point. This allows for addressing of any energy specific dependence within our data set by normalizing the value compared to the background (see Navidi, 2015). The z-scores are then summed and weighted as follows to obtain the variable S calculated in equation (2.1). S depends on each R value between 5 and 12, and can most accurately be thought of as a normalized value of the flux intensification above a variable background. Additional details on this procedure within the framework of machine learning is provided in Chapter V.

$$S = \sum_{E=0}^{14} 10^{Z_E - 2} \tag{2.1}$$

When S exceeds 0.9 standard deviations above the mean of S (dependent on radial distance and season, but not on energy), then we consider this to be an interchange injection event. We call 0.9 the threshold value. Within equation (2.1), there are two values, which can be adjusted: (1) the S base multiplier — currently set to 10 — will highlight extreme intensity values and scale S and (2) the Z power multiplier — currently set to 1 — is applied to the (Z_E - 2) as an exponentiation; this also will highlight extreme values. The current subtraction of 2 off of Z_E is for ease of calculation and does not have an effect on the classification of events. Subtracting 2 moves the lower bound of S values for positive z-scores close to 0, rather than 1. For example, a z-score of 0 (or a mean value) results in summing values close to 1 (10^0= 1), by subtracting 2, we now sum values close to 0 (10^{-2}= 0.01).

This expression (shown additionally in Figure 2.2b was chosen through comparing various functional forms to a pre-selected training set of interchange injection events. We discuss the optimization of this formula in section 2.2.3. The advantages of this particular formula are as follows: (1) it highlights high intensity outliers through exponentiation of the z-values and (2) it allows for natural data gaps or low intensity values at some but not all of the energy channels through a sum. This allows for flexibility in our algorithm by allowing any combination of high intensity values between energy channels 0 to 14 to obtain a large S value. These S values at each radial location are then used to identify an event and provide a statistically dependent ranking of how severe (intense compared to background) each event is.

We define intensity categories based on the S distributions as follows: category 1 (threshold for our event) from 0.9–1.5 standard deviations (σ) above the mean of

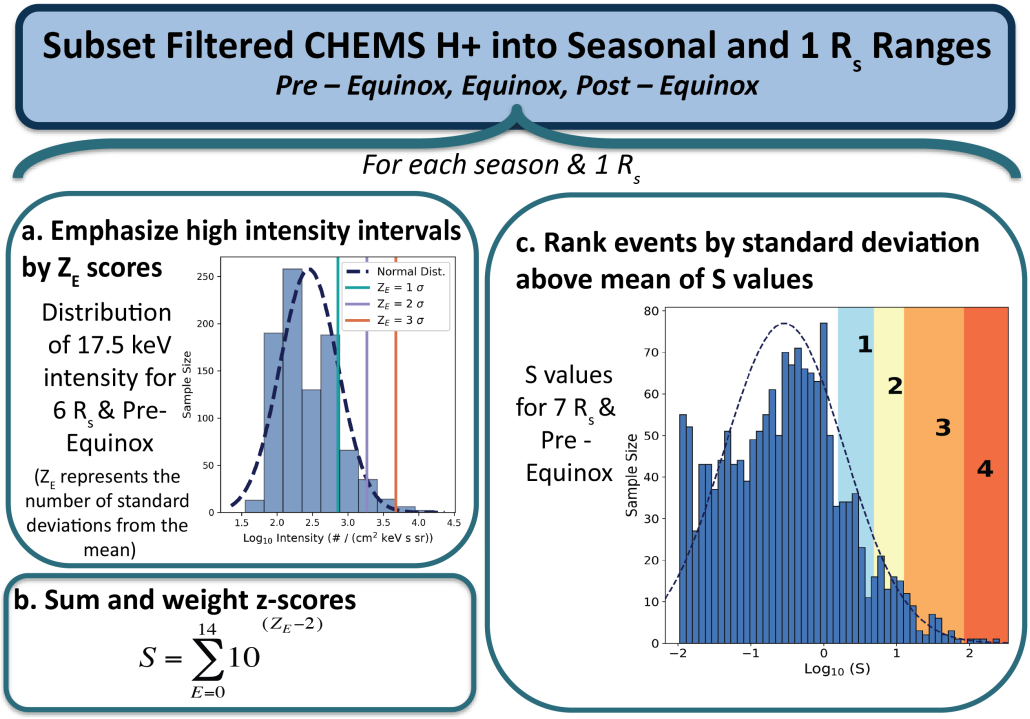

Figure 2.2: Diagram of CHEMS H^+ based event identification method. Within this diagram we present the algorithm procedure for event identification and seasonal subsetting procedure. (a) The plot is the distribution of the 17.5 keV data for 6–7 R_S within the pre-equinox date range. Each line represents standard deviations above the mean, known as a z-score in statistics, with the first line representing 1σ and so on. Z_E is the z-values. (b) The equation summarizes how to obtain the dimensionless S value using the Z_E scores obtained from panel (a). The Z_E values are summed for each energy channel to obtain S. (c) An example S value distribution for 7–8 R_S and the respective category breakdown from 1 to 4 with four representing the most extreme outliers. Categories are shown in the highlighted colors ranging from smallest intensity in pale blue, to largest intensity in red.

S, category 2 from 1.5 to 2σ, category 3 from 2 to 3σ, and category 4 from 3σ and above. As one might expect categories 1 and 2 represent the smallest intensity of all events, while categories 3 and 4 represent the most intense. The S values depend on radial distance. As a result, the absolute values of the categorical definitions depend on radial distance due to varying background, and therefore means, S, and σ. The relative (or normalized) thresholds of σ and categories are consistent with each radial distance.

We show in Figure 2.3 an example orbital segment for day of year 66–71 of 2005, with identified interchange injection events of these four categories in CHEMS data. We have also included the corresponding magnetic field variations. Within this figure there are magnetic field variations with no associated identified injection because of the lack of enhanced intensity of high-energy particles. This can be seen in the inbound orbital panel around time 22:30 UTC where the event in question shows significant dispersion and a lower signal at the lowest energy levels between 3 and 22 keV. This event is likely aged and thus does not trigger our algorithm. Since our method focuses on the enhancement of the hot particles compared to their average population in the area and energy range, the algorithm most readily captures young events. Similarly, we see events in the outbound panel that show differences in magnetic field signature. This is potentially a region where the internal pressure balance within the incoming flux tube varies, and thus, the magnetic field signature varies.

As illustrated in Figure 2.3 there are several events in quick succession. This method does not naturally group subsequent event identified time stamps into events for further analysis. To create groups of timesteps, or events, a three fold process was undertaken. First, subsequent timestamps which exceeded 0.9σ are grouped together. Second, if the event lasted for longer than 10 minutes, a check is undertaken to decipher if this long event is many events merged together. The category classifications are used to break merged events apart. If within an event of longer than 10 minutes, a decrease followed by an increase of a category threshold occurs then the larger event is reclassified as multiple short-duration events. This is robust against small fluctuations within categories, but enables large fluctuations to be recognized. This is most evident in the inbound panel around hour 23:00 UTC in which the first event is of a higher category than the second event but are located next to each other. The 10 minute check was chosen as manual review and comparison to previous surveys suggested that often events starting at 10 minute length were composite events. Third, and finally, the event is classified as the highest classification reached within. For example, if a timestamp within an event reached category 3, then the entire event

is considered a category 3 event.

2.2.3 Identification Optimization Procedure

We chose to develop an automated identification method rather than a by-hand identification to both reduce human bias in interchange injection identification and to enable a flexible novel categorization of interchange injection events by intensity. We used confirmed interchange injection events in 2005 for our test and training sets. These events were selected from comparisons between the lists of Lai et al. (2016), Kennelly et al. (2013), and Y. Chen & Hill (2008), and our own examination of CHEMS H^+ intensity data. Combined, the training and test sets represent 10% of our available data set (7,375/68,090 unique time points). To prevent any bias in our selection of training set data, the test and training sets are created by randomly selecting half of the available 7,375 points for each set. We optimize our algorithm on the training set,and then use the test set to estimate the error of our methodology. By splitting our test and training sets, we prevent any overfitting of the designed algorithm on our training set.

We optimized the form presented above in equation (1) through multiple iterations through the training set of events. For each time within the training set, we categorize the data point as event or nonevent manually and compare to the algorithm detection methods. This allows us to create a binary contingency table. The contingency table consists of four categories from comparing the predicted (algorithm determined) events to the true (by-hand identified) time periods as follows: hits (H), misses (M), false positives (F), and true negative (N). Hits are defined as both the algorithm and our by-hand set identify an event; misses are when the algorithm does not identify an event, but the by-hand set does; false positives are when our algorithm identifies an event, while our by-hand set does not identify one. Finally, negatives are when both the algorithm and the by-hand set do not contain events.

The algorithm's classification ability was then investigated using the Heidke Skill Score (HSS), the probability of detection (POD), and the probability of false detection (PFD), which can be calculated from the contingency table values of H, M, F, and N, as follows (Heidke, 1926):

$$HSS = \frac{2(HN - MF)}{(H + M)(M + N) + (H + F)(F + N)} \tag{2.2}$$

The HSS is a measure of correctly identified events compared to event predictions that are potentially correct from random chance. A perfect score is 1, while 0 in-

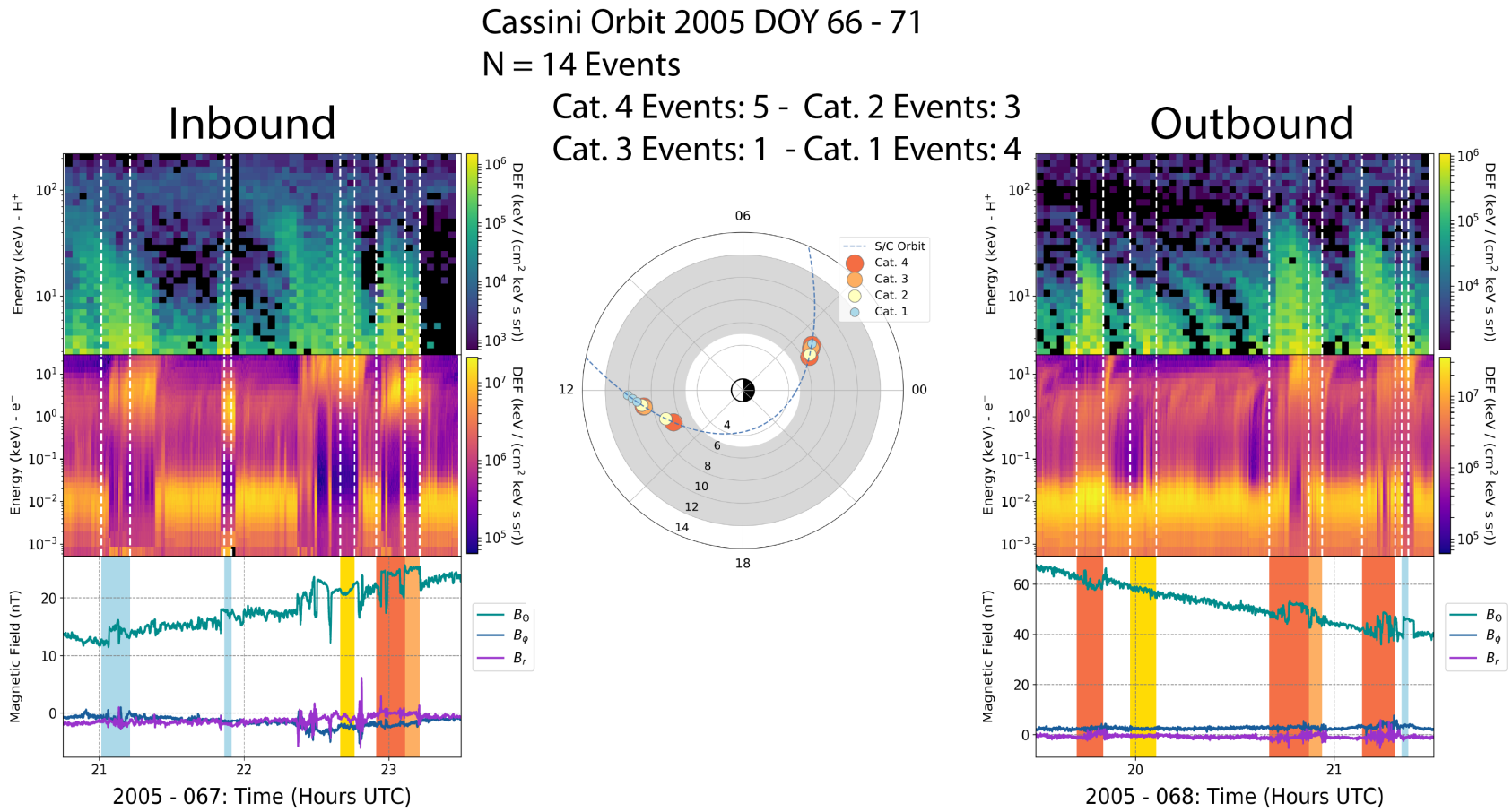

Figure 2.3: Demonstration of Cassini orbital pass algorithm identification. This figure demonstrates the different categories of events within one orbit pass in the beginning of 2005. The panels marked inbound and outbound represent selected portions of a single orbit trajectory, with the top subpanel displaying CHEMS H^+ differential energy flux between 3 and 220 keV, followed by the CAPS ELS differential energy flux for electrons from Anode 4, and finally the magnetic field components in KRTP (Kronocentric body-fixed, J2000 spherical coordinates). We did not use the MAG or ELS data to identify events but we do display it here for illustration purposes. In the outbound panel we can observe how injection events may or may not show a demonstrated magnetic field enhancement. The middle panel represents the orbit of Cassini, with the region allowable for the algorithm shaded in grey. The orbit of Cassini is the blue dashed line plotted in local time in hours and radial distance in units of Saturn radii. In the orbit and magnetic field plots the most intense events are marked with dark orange, with least intense in light blue. In the CHEMS and CAPS panels the event boundaries are marked with dashed white lines.

dicates that the prediction is as good as random, and negative values denote worse than random (Heidke, 1926; Pulkkinen et al., 2013; Stephenson, 2000). For reference, current estimations of active space weather models for predicting ground dB/dt measurements are on average <0.5 HSS for different latitude ranges (Pulkkinen et al., 2013). Similarly, evaluations of Inner Magnetosphere Particle Transport and Acceleration Model to nowcast electron fluxes have a maximum HSS of 0.17 (Ganushkina et al., 2015). Our selected algorithm has an HSS of 0.56 for the training set and 0.49 for the test set.

The POD represents the fraction of actual events that were correctly identified (Pulkkinen et al., 2013). POD ranges from 0 to 1 with 1, representing no misses. When calculating POD it is important to consider it in relation to the trade-offs with the PFD. A perfect POD is 1, but in addition, there could be many false positives.

$$POD = \frac{H}{H + M} \tag{2.3}$$

The PFD represents the fraction of incorrectly identified nonevents (Pulkkinen et al., 2013). Similar to POD, it ranges from 0 to 1, but in this case, 0 represents a perfect score. It can be thought of as the inverse of specificity (1 - specificity), with 0 being the most specific.

$$PFD = \frac{F}{F + N} \tag{2.4}$$

We performed a multivariate analysis of performance by varying three parameters in the above algorithm form. We found that upon this volume the maximum performance occurred while holding the other two parameters at their respective peak values and varying only one parameter. Figure 2.4 shows these performance curves. The set of criteria used in our final algorithm was based on maximizing the HSS while minimizing the PFD. To optimize equation 2.1, we tested a range of values for the (1) threshold value above which the dataset constitutes an event (set at 0.9σ mean of S), (2) the S base multiplier, and (3) the Z power multiplier. The panels shown in Figure 2.4 represent the performance of the event identification method compared to both the training (solid) and the test (dashed) sets. As expected, the test set shows slightly lower performance but similar shape and peak behavior.This demonstrates that the algorithm is not overfitted to the training set but reliable over a wide range.

In Figure 2.5 we present the receiver operating characteristic (ROC) curves for the three selected parameters presented above (threshold value, S base multiplier, and Z power multiplier). In order to create an ROC curve we vary a parameter in our

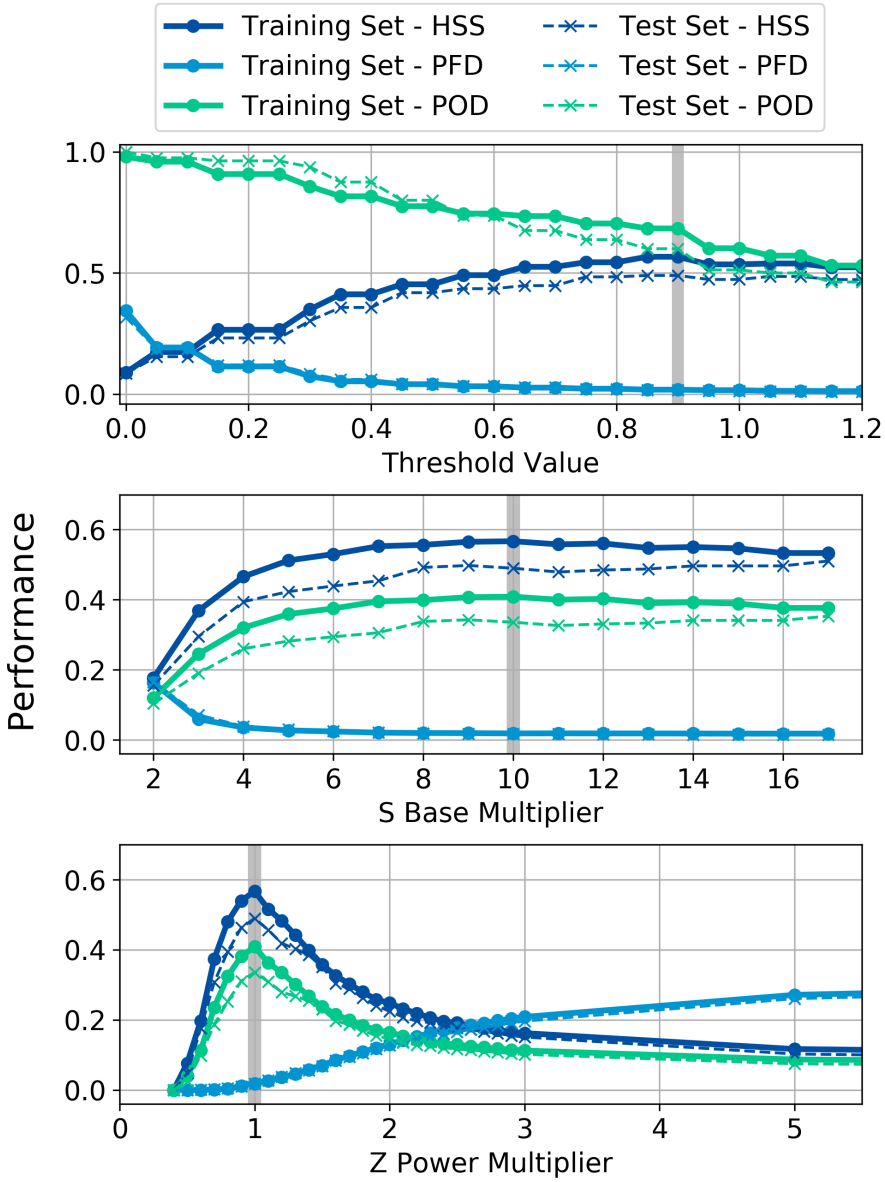

Figure 2.4: Performance curves of event detection algorithm for varying values of controlling parameters. These curves were created by holding the other two parameters constant at their optimized values of 0.9 for the threshold value, 1.0 for the Z power, and 10 for the S base while varying the singular selected parameter. The grey shaded region represents the chosen variable value for the finalized algorithm. The y axis represents the performance, or the value of HSS, POD, and PFD. The solid lines with circles represent the performance evaluated for the training set, while the dashed lines with cross markers represent the performance of the test set. The first panel represents the threshold value, with the best HSS found at 0.9, highlighted in grey. The second panel plots the S base multiplier. There is negligible improvement after a value of 10. The third panel displays the Z power multiplier, which shows the best performance at a value of 1 for HSS.

algorithm form and compare each output's PFD against the POD. This curve can be used to evaluate the performance of the algorithm form we designed and our chosen values by assessing its position on Figure 2.5, with the ideal position being in the upper left corner represented with 1 for the POD and 0 for the PFD, that is, a perfect classification. We designed our classifier algorithm to be limited in terms of the worst possible prediction and by maximizing our HSS; thus, our curve does not venture into the upper right corner of only false positives. Similarly, we opted to limit as much as possible the detection of false positives at the expense of detecting all possible events when choosing parameter values, as can be seen in the location of the grey shaded dots, which represent the final values chosen. Ideally, a classifier algorithm should be located above the grey dashed line as this represents random chance in ROC space (e.g. Fawcett, 2006; Mason, 1982, and references within). Because our chosen algorithm values product PODs significantly below the maximum sensitivity, it can be thought of as a conservative estimation of interchange as it has a high threshold of event identification to reduce false positives in our resultant set.

We examined our false positives from both the training and the test sets for any systematic errors that would affect our conclusions not covered in our previous methodology. We did not find any systematic errors in our local time distribution. However, by radial distance, there is a larger proportion of false positives beyond 11 R_S. We attribute this to the changing plasma population beyond 11 R_S from thermal, cool plasma of the inner magnetosphere to the less dense energetic plasma of the outer magnetosphere and where our methodology begins to identify more high intensity events, which are not attributed to interchange (e.g. Schippers et al., 2008; Thomsen et al., 2015). When analyzing our results we constrain our conclusions to be based only on the survey results between 5 and 10 R_S but we present the survey results beyond 10 R_S for comparative purposes. This methodology represents the first implementation of a classification algorithm developed for interchange events based on energetic particle data.

2.3 Results

We identified 816 interchange injections over the course of the Cassini mission between 2005 and 2016, 256 in the pre-equinox period (2005–2008), 303 in the equinox period (2009–2011), and 257 in the post-equinox period (2012–2016). The following sections analyze the occurrence of these events compared to previous surveys (section 2.3.1), in radial location (section 2.3.2), in local time (section 2.3.3), and finally

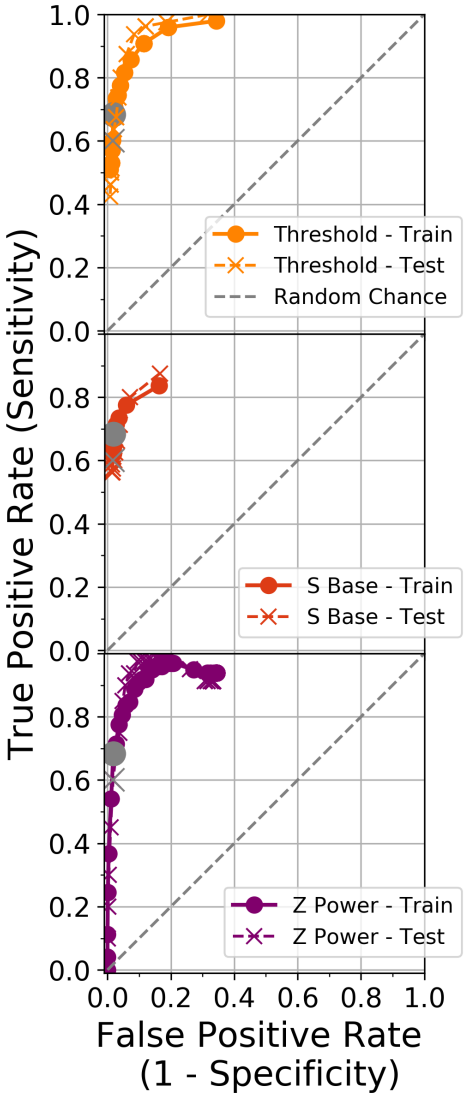

Figure 2.5: ROC analysis for event detection algorithm. These curves were created by holding the other two parameters constant at their optimized values of 0.9 for the threshold value, 1.0 for the Z power, and 10 for the S base while varying the singular selected parameter. The panels shown here represent the performance of the event identification method compared to both the training (solid) and the test (dashed) sets. The grey shaded values represent the chosen variable value for the finalized algorithm. All chosen values result in a less sensitive, but more specific algorithm. (a) ROC curve for threshold value. (b) ROC curve for S base multiplier. (c) ROC curve for Z power values.

characteristic scale sizes (section 2.3.4).

2.3.1 Comparison to Previous Works

Over the course of the Cassini mission, several large statistical studies have been conducted looking at the occurrence rates of interchange injection events. Each survey, however, focuses on investigating interchange from the viewpoint of one instrument. Lai et al. (2016), for example, examined the magnetic field data focusing on the enhancement and depletion of magnetic field pressure associated with the pressure balance of tangential discontinuities (see Figure 2.3 for demonstrated magnetic field perturbations). Kennelly et al. (2013) focused on the plasma wave emissions associated with interchange such as the upper hybrid emission, electron cyclotron harmonics, and whistler mode emissions. Y. Chen & Hill (2008), on the other hand, focused on CAPS ELS data. Because of these restrictions, and our particular focus on the high-energy H^+ particles of MIMI CHEMS, we do not expect a one-to-one matching between event lists. Rather, we investigate the similarity of these studies to our own, recognizing that all studies examine different physical changes manifested in interchange injection events.

To run a comparison between event lists, care must be taken to limit it to only those events that are eligible. For example, all studies vary in the range of dates, time resolution, spatial location, and methodology. We address this by limiting comparisons to events that occur within the same date and spatial range. This is most restrictive to the Lai et al. (2016) due to their additional examination of higher latitudes (i.e., off the magnetospheric equator). An event is counted as a match between lists if there is any overlap in identified time stamps. This is required to compare studies as the time resolution between chosen methodology varies—often with multiple MAG identified events located inside plasma data identified events. This is additionally why a one-to-one matching is not plausible where events in our study can match to more than one event in others and vice versa. This restricts our comparison-eligible events from 816 to 663, mostly due to the extension of our study to the post-equinox range.

In Figure 2.6 we present previous statistical studies compared to our identified list. We represent our comparison using the Circos tool more commonly used in genomics research (Krzywinski et al., 2009). This tool enables easy visualization of relational data wherein two objects are connected to each other in varying quantities especially when the data set in question has multiple characteristics. We find that our survey shares $\sim$30% of its events (187/663) with any of the lists of Lai et al. (2016), Kennelly

et al. (2013), or Y. Chen & Hill (2008). Of these 187 events ∼55% belong to category 3/4 and a slightly smaller amount, ∼46%, to category 1/2 events.

Of these 187 events, only 26 events are found shared between all of the event lists, including the current work. The events with no match to other lists (476) are primarily low intensity category 1/2 events (∼72%), while high intensity category 3 and 4 events represented only ∼28% of the unique-to-our-survey 476 events. We confirm that the most intense interchange events (higher categories) correlate between different instrument observations at higher rates than those of lower intensity.

Kennelly et al. (2013) has the most comparable list to that of our own, with 46% of their eligible comparison events finding a match within our list (121/262), followed by Lai et al. (2016) with ∼30% (145/455), and Y. Chen & Hill (2008) with ∼14% (67/417). This can be seen as the ribbons in Figure 7 leading to the nodes of the previous studies. About 187 unique events in total can be found in our list with matches in previous surveys. These consist of the following represented as the ribbons leading to the current node:

- 110 can be found within Kennelly et al. (2013).
- 135 can be found within Lai et al. (2016).
- 63 can be found within Y. Chen & Hill (2008).
- 8 can be found within Y. Chen & Hill (2008) and Lai et al. (2016).
- 2 can be found within Kennelly et al. (2013) and Y. Chen & Hill (2008).
- 84 can be found within Kennelly et al. (2013) and Lai et al. (2016).
- 26 can be found within Kennelly et al. (2013), Lai et al. (2016), and Y. Chen & Hill (2008).

We will be discussing the implications of this range in the following section. Our event list therefore captures a large percentage of Kennelly et al. (2013), but this only comprises a small part of our own list (∼30%)—confirming that while many of our events are unique, we reliably find previous studies.

We further compared our study to previous work by examining the partial particle pressure from interchange events from MIMI CHEMS H^+ between 3 and 22 keV, the primary region we used to identify interchange. To calculate the partial pressure from H^+ within our selected energy range, we used the methodology outlined in Krimigis et al. (1981) and additionally expanded on in Sergis et al. (2007).

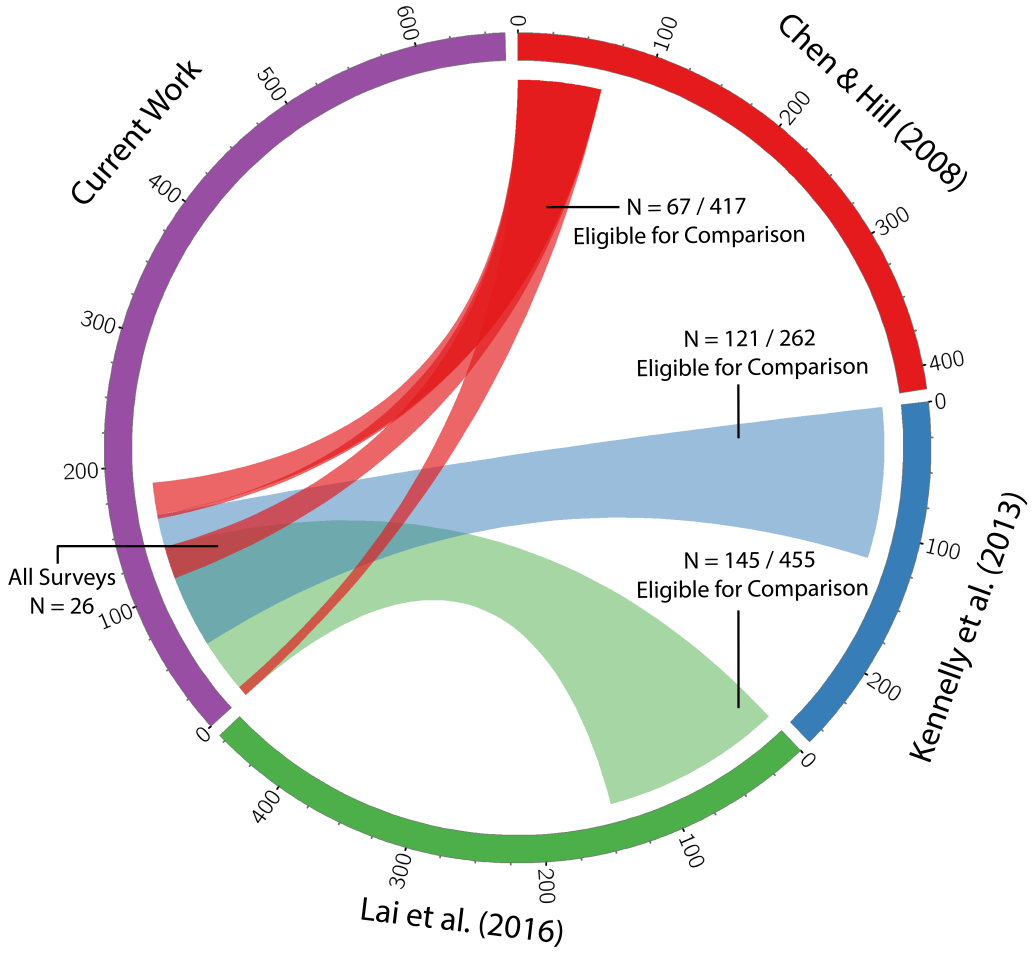

Figure 2.6: Comparison to previous surveys of interchange injection. Comparison between the current presented study from MIMI CHEMS H^+ data and events identified in statistical surveys from Lai et al. (2016), Kennelly et al. (2013), and Y. Chen & Hill (2008). The size of the ribbons connecting the nodes (colored arcs) represents the number of similar events between our list and others. Chen and Hill (2008) is represented with three ribbons to illustrate the shared overlap with other surveys. The ribbons are proportional to the number of shared events.

In Figure 2.7 we present the partial particle pressure distribution of H^+ between 3 and 22 keV for interchange injection events shared between our list and previous lists, and those unique only to our study. The pressures presented corresponds to the maximum reached pressure within the interchange event. This does not include W^+ group contribution but rather focuses on the physical quantity selected for our classification scheme.

As seen by a comparison of Figure 2.6a and 2.6b, the events within our list which are shared between studies and those unique to our study are of similar distribution. By comparing these panels, we see immediately that category 1 events are less likely to be shared between studies than events in categories 2, 3, and 4. Events with highest maximum partial pressure peak within the 6–9 Rs radial range. They do not, however, continue into 5 R_S, and these interchange events tend to cluster within 6–9 R_S, whereas other categories of events (lower pressures) are distributed over a wider range of radial distance with no clear peak. Event categories are based on particle pressure at each radial distance separately, thus becoming smaller nearer to Saturn, generally following the known suprathermal pressure profile (e.g. Sergis et al., 2017, and references within). We calculate the mean values of partial pressure for categories 1–4 within picopascals (pPa):

- Category 1: 7.1 ± 0.1 pPa
- Category 2: 8.3 ± 0.2 pPa
- Category 3: 9.7 ± 0.2 pPa
- Category 4: 13.5 ± 0.4 pPa

Within these means the errors are the standard error on the mean. The categories by pressure are distinct from each other, as their mean and standard errors do not overlap. We also find that the chosen algorithm form is able to capture the changes in background plasma population successfully. The gap region between 10 and 12 R_S is due to our limitations in cross comparing Y. Chen & Hill (2008) and Kennelly et al. (2013) as these surveys ended at 10 R_S and 11 R_S, respectively.

2.3.2 Radial Occurrence

We investigate the radial distribution of interchange injection between 5 and 12 R_S by overall occurrence rate and by intensity category. In Figure 2.8 we demonstrate the normalized occurrence (time spent within injection events/total observation time by

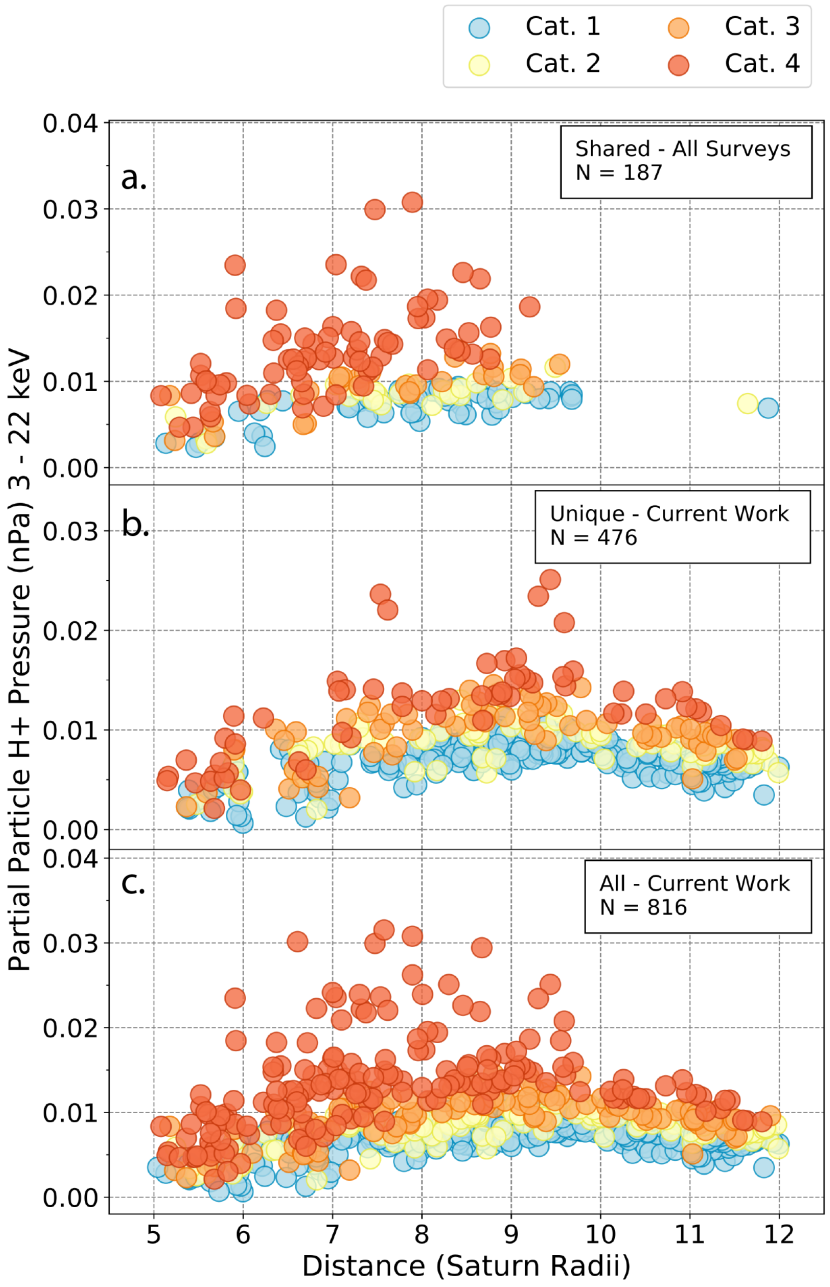

Figure 2.7: Radial distribution of partial plasma pressure within interchange events from 2005 to 2016. Comparison of identified event partial particle pressure (3–22 keV H^+) to previous surveys. (a) Partial particle pressure of interchange events cross listed in all surveys. This panel contains all cross-listed events, totaling 187 in total. (b) Partial particle pressure of interchange events only found in current work. This panel contains all of our events that could be compared, but are not found within another list (476 events). (c) Partial particle pressure of interchange events of all events in current work. This panel contains all of our events (816 total).

spacecraft within region) by radial location for the whole survey range, regardless of seasonal partitioning. We did not observe any significant deviation in radial location with season. As expected we observe a peak occurrence rate in the 7–9 R_S region from all our events, with 8–9 R_S demonstrating a slightly higher occurrence rate. This is similar to previous surveys, which find a peak around 8.5 R_S (Kennelly et al., 2013). By category, however, we observe our most intense events peak at 7 R_S while less intense events (categories 1 and 2) peak further out at 8–9 R_S and 11–12 R_S, respectively. As mentioned before, at 11 R_S we see the greatest occurrence of false positives, and thus, we do not conclude trends using this range. As discussed in section 2, 11 R_S is known to contain a large amount of false positives due to the large amount of highly energetic plasma and other tail-related processes. The secondary peak at 11 R_S we attribute to category 2 events and the presence of false positives beyond 11 R_S.

The peaks between 7 and 9 R_S can also be seen in our partial pressure distributions in Figure 2.7. In reviewing Figure 2.7 we note that our lower pressure events show less variation with in radial location, and in fact, the highest-pressure events show a distinctly different radial occurrence pattern than that of the bulk of events of lower pressure.

2.3.3 Local Time Occurrence

We examined the local time occurrence rates of interchange in order to resolve current disagreements in local time occurrence rates from Y. Chen & Hill (2008) and Kennelly et al. (2013) and to evaluate interchange occurrence rate dependence on large-scale injection events. In Figure 2.9 we present all event occurrence rates from 2005 to 2016. The occurrence rates are calculated from the total time spent in an interchange event divided by the total time spent observing within that location. The error bars calculated here and in the following figures are representative of the sampling error of $1/(\text{sample size})^{1/2}$ and propagated for both the numerator, and denominator. The error bars therefore increase in size when we have low representative samples or low event statistics.

Between 2005 and 2016 we observe a strong day-night asymmetry with a majority of events accounted for on the nightside of the planet ranging from $\sim$5 to 6 times higher occurrence rates. The dayside distribution in Figure 2.9 can be seen symmetrically located around noon with peaks in the prenoon and postnoon sectors with the lowest occurrence rates located at noon. This is most similar to Kennelly et al. (2013) due to the nightside dominance, but we find both the prenoon (0900)

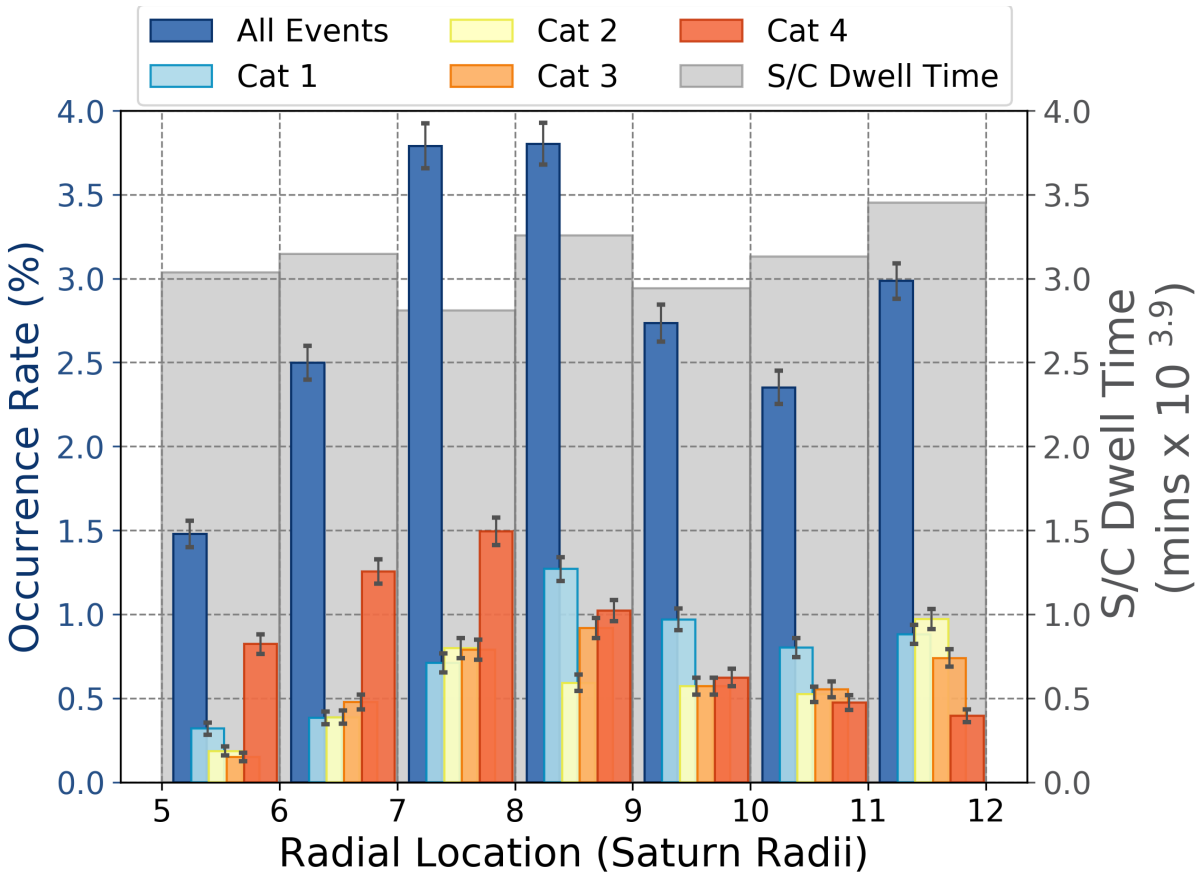

Figure 2.8: [Radial occurrence rates of interchange events from 2005 to 2016. Superimposed on the total sampling time the spacecraft spent in each radial bin of 1 R_S (the grey shaded region), we demonstrate by category of event the occurrence rates of interchange (the colored bars). We have binned our data by 1 R_S to prevent any sampling bias. Each bar plotted represents a 1 R_S range. The dark blue bars represent all categories combined.

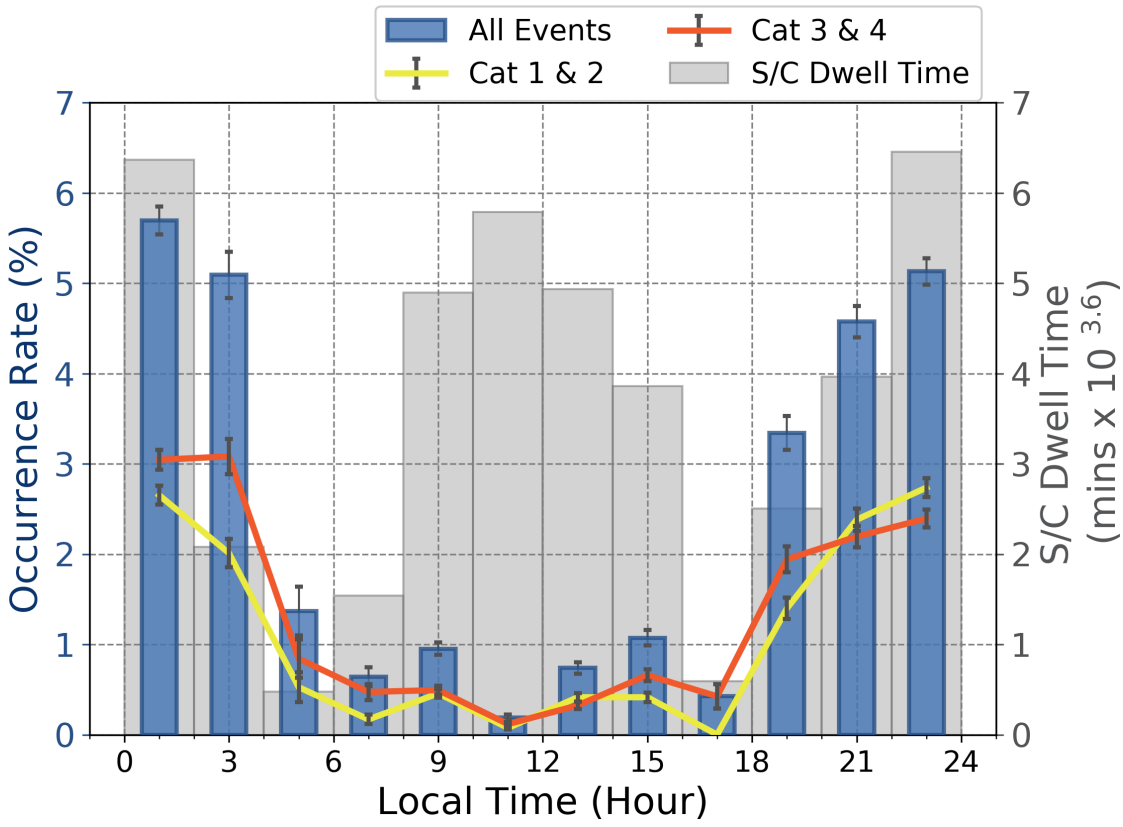

Figure 2.9: Local time occurrence rates of interchange events from 2005 to 2016. Superimposed on the total sampling time that the spacecraft spent in each local time bin of 2 hr (the grey shaded region), we present by grouped category of interchange the occurrence rates (time in event/total observation time) as a function of local time (blue bars and colored lines). The blue bars represent all interchange injections, while the yellow and orange lines represent the rates of low intensity (categories 1 and 2) and high intensity (categories 3 and 4), respectively

peak reported in Y. Chen & Hill (2008) and the postnoon peak (1500) reported in Kennelly et al. (2013). Additionally, we observe a slightly higher occurrence rate of more intense events (categories 3 and 4) on the dawnside of Saturn. We additionally investigated the local time distribution in our pre-assigned seasonal date ranges of pre-equinox, equinox, and post-equinox. We find that in all of these ranges, the nightside occurrence rates far dominate over the dayside occurrence rates.

2.3.4 Duration and Scale Size

We find that of the events identified, the majority are less than 15 min long (769 of 816 events or 94%). In Figure 2.10 we present the normalized distribution of durations of all identified events. The lower limit in event duration is due to CHEMS

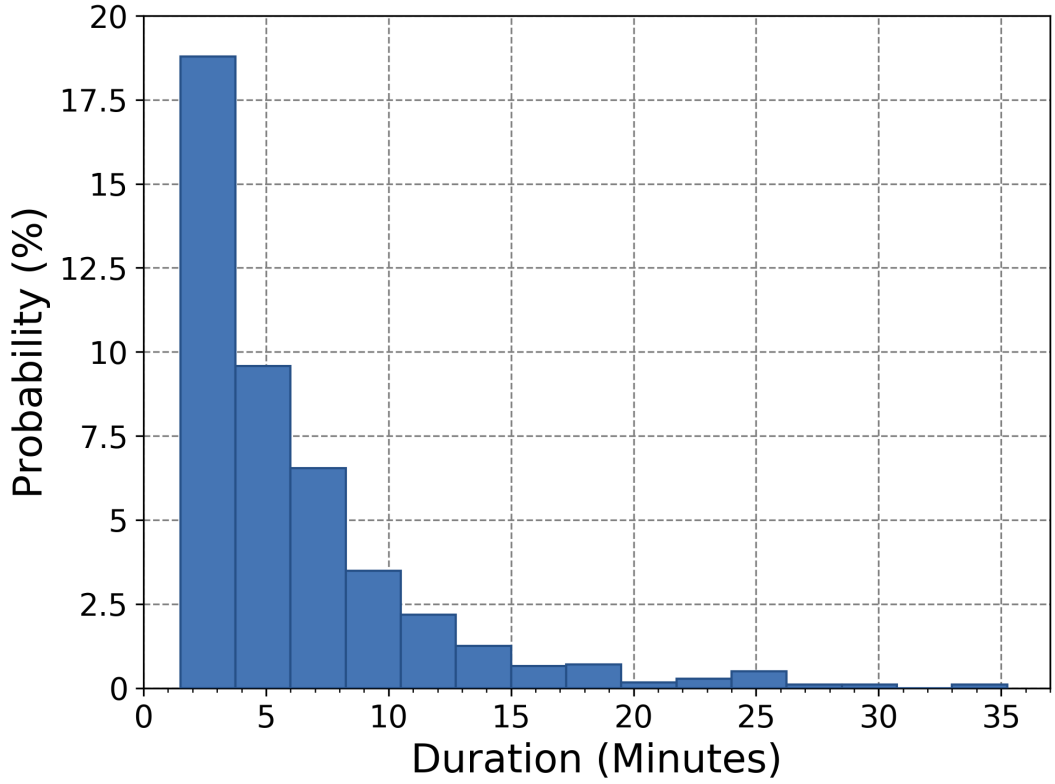

Figure 2.10: Normalized duration of interchange injections from 2005 to 2016. The normalized event distribution by duration is presented for all events (all intensity categories). There are 15 bins ranging from the lowest instrument resolution of ∼2 min to the longest event of ∼34 min.

time resolution, and it is likely that there are events occurring below our observed cutoff. Similarly we direct attention toward the previous discussion on the review of events greater than 10 minutes long in the methodology section. Shorter events are more commonly thought of as interchange, with fewer long (>15 min) events generally occurring at larger radial distances (Y. Chen et al., 2010; Thomsen et al., 2014). Our distribution is supported by previous studies evaluating the duration of magnetic field signatures of interchange events (Lai et al., 2016).

Based on the event durations, we calculated an estimated width of the interchange injection events. As the velocities of co-rotating particles in addition to their gradient-curvature drifts are much larger than the spacecraft velocity itself, we assume that the interchange event overtakes the spacecraft. Similar to the methodology employed in Y. Chen et al. (2010), we calculate the scale size of the interchange structure with equation (2.5). In which we find the width in R_S (W) by multiplying the average

radial location in R_S (60,268 km) of the interchange structure (R) by the duration in seconds, by the angular frequency of H^+ plasma at the location in radians/second (Ω). The angular frequency is obtained from the mean H^+ azimuthal flow velocities obtained in Thomsen et al. (2010); which surveyed the bulk ion parameters from the CAPS instrument, deriving estimates of the azimuthal flow velocities usually between ∼50 and 70% of solid co-rotation. This survey only extends to 6 R_S; to calculate the velocities of interchange events between 5 and 6 R_S we use estimated values at 6 R_S.

$$W = R\Delta T\Omega \tag{2.5}$$

We find that low intensity events are statistically smaller than high intensity events. Category 1 and 2 interchange structures (low intensity) have a mean width of 0.25 R_S, and category 3 and 4 (high intensity) events have a mean width of 0.41 R_S. The widths range from ∼0.04 to 1.72 R_S. We include the interchange widths in an associated Deep Blue Repository (Azari, 2018) along with error ranges propagated from the standard error on the mean azimuthal velocities included in Thomsen et al. (2010).

We additionally find a nightside/dayside asymmetry in the duration with long events (>15 min) more likely to be found on the nightside than on the dayside. We identified only 2 events on the dayside (out of 117 dayside events) >15 min long, while there were 45 events on the nightside (out of 699 nightside events) >15 min long.

2.4 Discussion

2.4.1 Comparison to Previous Works

In comparing our survey to published statistical surveys, we were careful to limit comparisons to the same date and space as discussed in section 2.3.1. We cannot, however, remove the influence from each survey's primary instrument identification choice and therefore do not expect interchange event lists to compare exactly to each other. We did find a greater correlation between previous surveys' events to high H^+ intensity interchange in our own. We suggest that these events would have a greater chance of being observed by each survey as suggested by Y. Chen & Hill (2008) as the decrease of low energy plasma observed by CAPS would potentially be more intense, by Lai et al. (2016) in MAG from an increase in resultant magnetic field signature from the depletion of low energy plasma, and by Kennelly et al. (2013) in enhanced plasma

wave activity due to perturbations in the electron density. Future work should analyze these instruments in aggregate to analyze these potential dependencies. Additionally, we designed our identification criteria for high intensity events, but still gather lower intensity events, so it is not unexpected to find this result. What is surprising, however, is the variation of our comparison to different surveys and subsequent small number of events found in all four lists.

We have found only 26 events to be correlated between all these lists. While this is limited to only events that can be compared, this is still a small subset of events. Additionally, our own survey correlates most highly with Kennelly et al. (2013) as compared to the surveys by Lai et al. (2016) and Y. Chen & Hill (2008). In the case of Y. Chen & Hill (2008) we attribute this difference to their study's focus on events of >1 hr old while the other surveys reviewed optimized for younger events. We suggest the greater match with Kennelly et al. (2013) as compared to the survey by Lai et al. (2016) is due to a potential underlying cause seen in multiple identification criteria. Our event identification requires a substantial increase of H^+ flux intensity above the average background. Kennelly et al. (2013) identified events through particular focus on the strength of signatures of upper hybrid waves, secondary plasma waves, and perturbations in the electron cyclotron frequency. We are curious as to the overlap between our surveys given the differences in event criteria. Lai et al. (2016) identified interchange on the equatorial plane through enhancements in magnetic field over the background that had a significant rise within a set time period. We expect their survey to contain events that might not have the plasma enhancement within the CHEMS energy range evaluated (3–22 keV) here. The differences between these surveys can also be observed in the presentation of CHEMS, CAPS, and MAG data within Figures 1.5 and 2.3.

Given the differences we have identified between published surveys to our own, however, we find such comparisons to be useful in evaluating the physical processes behind interchange injection events. There is a significant amount of interchange we observe only in certain measurements and not within others. This suggests that the underlying observation or occurrence mechanisms behind what we identify as interchange vary. Our analysis has not looked into comparisons between previous works, only comparisons of those works to our own. To fully evaluate the differences, we would need to compare each survey to each other, and this is not the focus of the present work. A deeper study of the identification is warranted. Additionally, our study has not evaluated contributions from W^+ or other ion species besides H^+ as this is the main species we expect to see in incoming interchange events (Thomsen

et al., 2014). Future work should consider the effect of additional criteria for both identification and for comparison of pressure within interchange events and between lists in order to address the underlying differences in the observed events.

2.4.2 Radial Occurrence

We observe the greatest occurrence of interchange to be located between 7 and 9 R_s which is a slightly more expanded range than the single peak at 8.5 R_s from Kennelly et al. (2013). We attribute this to the increased range of events we consider as compared to previous surveys. This location also coincides with the greatest observed partial high-energy H^+ pressure in events as discussed previously. Thus, we find that not only do events occur more frequently within this range but also the events that are most intense occur within this range.

The outer end of this range at 9 R_s correlates well with the location of a plasmapause-like boundary that separates incoming low density flux tubes arriving from reconnection processes downtail and inner magnetosphere rotating dense plasma (Thomsen et al., 2015). This boundary exhibits a large gradient in flux tube content, one of the major triggering processes of interchange signatures, and signatures were indeed observed to be forming in the event reported by Thomsen et al. (2015). We suggest that due to energization accompanying inward radial motion (e.g., within injection) competing with charge-exchange losses, the population of 3–22 keV protons maximizes between 7 and 9 R_s. This result confirms interchange's role as a major radial transport mechanism for high energy particles between 6 and 9 R_s, as previously discussed by DeJong et al. (2010), Thomsen et al. (2016), and Hill (2016b).

2.4.3 Local Time Occurrence

We find in section 2.3.3 the local time distribution from 2005 to 2016 that the interchange occurrence rate is ∼5–6 times higher on the nightside (1800–6 LT) than on the dayside (0600–1800 LT), supporting a significant potential triggering mechanism located on the nightside of Saturn. A similar nightside preference was observed by Kennelly et al. (2013), but they also observed a significant postnoon peak in occurrence rates. We expect the growth rate of the instability to inversely depend on the local Pedersen ionospheric conductivity (Southwood & Kivelson, 1989). We propose that as the nightside ionosphere would have a low conductivity, the local growth rates on the nightside would be higher than those on the dayside. So while the initiation does not depend on the conductivity, interchange could become more unstable and

potentially more detectable on the nightside from its growth.

As discussed above, Müller et al. (2010) identified 52 electron injection events observed with the MIMI LEMMS instrument most likely related to large-scale tail injections. They back traced dispersed injection events to their original local time location, which shows heavy nightside dependence with a slightly higher postnoon dayside sector. Our detection criterion is based on the lowest levels (0–14) of CHEMS or between ∼3 and 22 keV. We observe younger and lower energy events than Müller et al. (2010) but see a significant similarity to their local time results with a much larger sample size.

We also observed a slightly higher occurrence of intense events in the dawn sector (0000–0600). It is worth pursuing in a future work if there are noticeable differences between high intensity events in the dawn sector as compared to other sectors. Previous work has attributed interchange triggering to incoming flux tubes from large-scale injections, setting up the necessary flux tube content gradient as proposed by Mitchell et al. (2015) and demonstrated in the case study by Thomsen et al. (2015). Statistically, this preference seems small if existent, and it would be worth pursuing additional event studies within this region as compared to others.

In this analysis we focused on observation of injection events at the locations observed, rather than adjusting for the possibility of local time offsets due to both Coriolis force and finite radial propagation speed in order to compare to previous work. However, such effects can potentially adjust the local time location of interchange injection dependent on the inflow speed (Liu et al., 2010; Paranicas et al., 2016). Future work should investigate possible adjustments to the local time distributions in this and previously performed surveys.

2.4.4 Duration and Scale Size

We find the vast majority of events identified last for 15 min or less. This supports the idea of interchange as a process occurring in a narrow region (∼5–10%) of available longitude space as proposed and discussed in Y. Chen et al. (2010). Additionally, our distribution of duration is very similar to that of Lai et al. (2016) with the bulk of interchange events occurring on a short time scale.

We additionally observed a nightside asymmetry in duration (see section 2.3.4). This in addition to a higher occurrence rate of nightside interchange events. Both the duration and the occurrence rates peak on the nightside, suggesting that the nightside is the region with more intense and frequent interchange events.

From these durations, we calculated the width, finding that there is a difference in

widths between category 1 and 2 interchange structures (low intensity) and category 3 and 4 (high intensity) structures. We suggest that this is an observed effect of a larger intensity of events also resulting in larger scale sizes from the growth of the instability. These estimates have been updated from Y. Chen et al. (2010) by including the azimuthal velocity profile from Thomsen et al. (2010).

Our overall range between ∼0.04 and 1.72 R_S agrees with interchange injections as a "mesoscale" structure, limited to below many R_S (Hill et al., 2005). The mean estimated width and radial distribution for category 1 and 2 events of 0.25 R_S appears to be in the distribution within Y. Chen et al. (2010). The lower limit is approximately half of that reported within Hill et al. (2005). Hill et al. (2005) limited to observing interchange signatures with a clear dispersal; this is the most likely cause for the disagreements between these surveys as well as the updated azimuthal rotational profile from Thomsen et al. (2010). It is possible that as an interchange event sweeps over Cassini, the spacecraft only observes a part (random cross-section) of the event, not indicative to its true size. This limitation should be considered in further work to evaluate event size.

2.5 Conclusion

We have presented a novel method for identification and classification of interchange events based on the intensity of the 3–22 keV H^+ from CHEMS. The automated algorithm was robustly trained and tested to optimize selection of young injection events and is the first automated particle based classification algorithm developed for interchange injections. We have compared our survey to previous statistical surveys and investigated the dependencies of the occurrence rate and partial particle pressure on the radial distance, local time, and season. We have found the following:

1. Interchange occurrence rates peak between 7 and 9 R_S, and the maximum 3–22 keV partial pressure injections are limited to 6–9 R_S.

2. Local time occurrence rates of interchange between 2005 and 2016 are highest on the nightside and show slight preference for higher intensity events on the dawnside. This suggests a combined influence of the ionospheric conductivity in determining the growth rate of interchange instability and the large-scale tail reconnection in injecting hot and depleted flux tubes into the middle magnetosphere, which enhances the gradient in flux tube content relative to the inner

magnetosphere.

3. Most injection events last for 15 min or less in duration with a small trend toward longer events on the nightside rather than the dayside. Smaller intensity events have a mean width of 0.25 Rs, and high intensity events have a mean width of 0.41 Rs.

4. A comparison of events between this and three previous surveys showed relatively high overlap for some and low overlap with others, which can be explained by considering the selection criteria and the instrumentation used for each study. A surprising finding was the very small percentage of events (26 events) that were common to all four survey lists.

Our work has found that energetic proton injections are strongly organized by local time and radial distance. Future work should further investigate the underlying triggering mechanisms of interchange and how these influence plasma mass and transport within the Saturnian system. Further investigations should include study of the occurrence by different periodic fluctuation-based longitude systems such as the Saturn longitude systems and planetary period oscillation systems (e.g. Gurnett et al., 2011; Provan et al., 2016, and references within). Periodicities in the plasma properties and magnetic field have been observed at periods closely related to those of the emission power of Saturn kilometric radiation, leading to the hypothesis that the process controlling Saturn kilometric radiation modulation also controls aspects of magnetospheric physics (e.g. Carbary & Mitchell, 2013, and references within). Previous works have disagreed on interchange organization by longitude, and updating these results with this data set would be worthwhile (Y. Chen et al., 2010; Y. Chen & Hill, 2008; Kennelly et al., 2013). If interchange is organized by planetary oscillation phase, then interchange is a process propagating periodicities between the inner and outer magnetosphere of Saturn and should be investigated in future work.

CHAPTER III

Internal Driving Influences on Interchange

This chapter uses the previously identified list of interchange events to investigate the extent of ionospheric control, or internal processes, on the triggering process of the instability. It details an investigation to map interchange events into the available longitude systems of Saturn. The chapter was originally published in the Journal of Geophysical Research: Space Physics in 2019 under the title "Are Saturn's Interchange Injections Organized by Rotational Longitude?" (Azari, Jia, et al., 2019). The work is presented as published with minor formatting adjustments.

3.1 Introduction

The rotation rates of gas giant planets, such as Jupiter or Saturn, cannot be determined by tracking surface features; instead, periodic variations in the emission strength within the radio frequency band are used. Saturn's rotation rate has proven to be a difficult value to definitively quantify. Estimations of the period of Saturn's kilometric radiation (SKR) have shifted significantly from the Voyager era (10 hr 39 min 24 s $\pm$ 7 s), to Ulysses (10 hr 42 min 34.2 s), and finally to Cassini (10 hr 45 min 45 $\pm$ 36 s) (Desch & Kaiser, 1981; Galopeau & Lecacheux, 2000; Gurnett et al., 2005). The observed shifts in the SKR derived period are too large to represent changes in the rotation rate of the planetary body itself and must be produced by some other process yet undetermined (e.g., Cecconi & Zarka, 2005; Galopeau & Lecacheux, 2000; Stevenson, 2006). Further, adding to the mystery of Saturn's rotational period, the periodic nature of SKR is also observed throughout the magnetosphere in a range of plasma and magnetic field phenomena, including magnetic field perturbations near the equator and at high-latitudes, spoke formation in the rings, plasma density and pressure variations in the inner and middle magnetosphere, fluxes of energetic particles and energetic neutral atoms, the intensity of auroral hiss emissions, and location

of the auroral oval (e.g., Carbary & Mitchell, 2013; Carbary et al., 2007; Gurnett et al., 2007; Gurnett, Persoon, et al., 2009; Gurnett, Lecacheux, et al., 2009; Nichols et al., 2010; Paranicas et al., 2005; Porco & Danielson, 1982; Provan et al., 2012; Ramer et al., 2017; Ye et al., 2016). As the magnetic dipole and planetary spin axes are nearly aligned at less than 0.01° (Dougherty et al., 2018), the origin of these periodicities cannot be produced by a wobbling internal dipole as the planet rotates, as is the case for Jupiter. Many models have been proposed to explain the observed periodicities, including models that attribute the origin to processes occurring in the equatorial magnetosphere (e.g., Goldreich & Farmer, 2007; Gurnett et al., 2007; Khurana et al., 2009) and those that place the origin in the high-latitude atmosphere/ionosphere (e.g., Hunt et al., 2014, 2015; Jia & Kivelson, 2012; Jia, Kivelson, & Gombosi, 2012; C. G. A. Smith, 2006; Southwood & Cowley, 2014). A model that incorporates flow vortices in the upper atmosphere/ionosphere has been demonstrated to be able to account for many of the observed periodic phenomena with quantitative fidelity (e.g., Jia, Kivelson, & Gombosi, 2012; Jia & Kivelson, 2012).

For comparison, the rotation rate of Jupiter is relatively straightforward. Ground-based radio astronomers discovered and used periodic intensifications in the decametric radio frequency signals to determine a rotational rate of the planetary body itself of slightly less than 10 hr (Douglas, 1960; Franklin & Burke, 1958; Shain, 1955). The commonly used sidereal period, adopted by the International Astronomical Union, is 9 hr 55 min 29.7 s ± 0.04 s as discussed by Duncan (1975) and Seidelmann & Divine (1977). Subsequent work found the improvements from in situ measurements, for example, of the magnetic field, to be within expected error of this original estimation, and at this time there is good confidence in the rotational period of Jupiter (Yu & Russell, 2009).

Constraining Saturn's variable rotation rate is not so straightforward. In the course of this effort, magnetospheric processes have been linked to Saturn's variable planetary period, including coupling processes between the inner and outer magnetosphere. Given that many magnetospheric phenomena exhibit periodic variations, it is of particular interest to find out whether or not interchange also undergoes any periodic modulations in its occurrence rate. Similar to a Rayleigh-Taylor instability, centrifugally driven interchange is believed to be the primary process for plasma transport in the inner to middle magnetosphere (∼5–12 R_S) at Saturn (see Thomsen, 2013, for a review). Associated with the interchange process are injections of hot plasma from the middle into inner magnetosphere, which are often termed interchange injections. Interchange injections are typically characterized by an enhancement of

energetic (>100 eV) plasma and a depletion of low-energy plasma along with enhanced wave activity and magnetic field pressure (e.g., André et al., 2007, 2005; Azari et al., 2018; Burch et al., 2005; Y. Chen & Hill, 2008; Hill et al., 2005; Kennelly et al., 2013; Lai et al., 2016; Rymer et al., 2009). Within this very same spatial region in which interchange is occurring, modulations of the field and plasma conditions have been observed associated with rotational periodicities (e.g., Ramer et al., 2017). Are interchange injections similarly modulated with rotational periodicities?

A previous effort by Kennelly et al. (2013) investigated this question. They analyzed data from the Cassini Radio and Plasma Wave Science (RPWS) instrument for the first half of the mission (2004–2011) to identify interchange injection events based on the presence of strong upper hybrid emissions along with the lowering of the emission frequency. The authors investigated the occurrence rate of interchange injections identified in RPWS data as a function of the northern and southern phases of the Saturn Longitude System 4 (SLS-4). In SLS-4, there is a northern and southern phase system as the SKR period was shown to have two components, corresponding to the northern and southern latitude regions (Gurnett, Persoon, et al., 2009; Gurnett, Lecacheux, et al., 2009). Since this discovery, derived longitude systems have a northern and southern component, which differ in their period.

Kennelly et al. (2013) found a rather broad peak in the fresh interchange occurrence rate between local times of ∼19 and 03 LT with a secondary narrower peak between ∼12 and 17 LT. Furthermore, in the local time sector of 19 to 03, interchange was organized by the northern SLS-4 system for the pre-equinox interval (i.e., prior to August 2009) and by the southern SLS-4 system in the post-equinox interval. Theoretical work has tied the growth rate of interchange to ionospheric conductivity, wherein a larger conductivity suppresses interchange growth (Southwood & Kivelson, 1989). Kennelly et al. (2013) proposed that due to the seasonal differences in polar illumination, the conductivity changes drive the organization of interchange occurrence rates as organized by SLS-4. However, it is important to note that this result was obtained for the RPWS events through imposing a local time filter between 19 and 03 LT, omitting any injections at other local times. Such a result implies the requirement of a conductivity anomaly in each hemisphere that is fixed in longitude. Prior to this work, Y. Chen et al. (2010) found no systematic organization of interchange identified through Cassini Plasma Spectrometer data by SLS-3 (Kurth et al., 2008). However, the SLS-3 system was not defined separately for each hemisphere.

At the time of the Kennelly et al. (2013) work, the SLS-4 longitude system covered unequal time periods for the northern and southern components. Specifically SLS-

4 north was defined from April 5^{th}, 2006 to September 16^{th}, 2009, and SLS-4 south from September 2^{nd}, 2004 to January 9^{th}, 2011 (Gurnett et al., 2011). The SKR-based system has recently been updated to a SLS-5 longitude system with complete Cassini-mission temporal coverage (Ye et al., 2018). In addition, a longitude system termed the planetary period oscillation (PPO) system has been derived and continuously developed since the observation of these periodicities (see Andrews et al., 2012; Provan et al., 2013, 2014, , for detailed process on deriving PPO properties). The PPO system is based off the analysis of the magnetic field perturbations and has also yielded phases systems and periods that now extend to the end of the Cassini mission (e.g., Provan et al., 2018, , and references within). These magnetic field perturbations are quasi-sinusoidal oscillations in the magnetic field components that are periodic and closely related to the phase of SKR modulations (Andrews et al., 2008; Provan et al., 2009). It has been shown that both the SKR- and PPO-derived periods are very similar, but with some short intervals of deviation (e.g., Cowley & Provan, 2016; Fischer et al., 2015; Provan et al., 2016, 2014). Further analysis has associated periodicities in PPO with field-aligned currents flowing from Saturn's ionosphere through the magnetosphere (Hunt et al., 2014, 2015; Jia, Kivelson, & Gombosi, 2012; Jia & Kivelson, 2012; Ramer et al., 2017). In the PPO system $\sim$90° north and 270° south is the location of upward field aligned currents within the ionosphere of Saturn (Hunt et al., 2014, 2015). This has been discussed as associated with an inward displacement of the current system in the equatorial plane (Hunt et al., 2015). These efforts now represent two distinct rotational systems that can be used to study the entirety of periodic modulations of the Cassini data set.

Subsequent to the work by Kennelly et al. (2013), several studies have evaluated interchange distributions at Saturn, extending to close to the end of the Cassini mission in mid-September of 2017 (Azari et al., 2018; Lai et al., 2016). Azari et al. (2018) identified interchange injection events from 2005 to 2016 using a statistics-based algorithm applied to H^+ flux intensitifications from the Magnetosphere Imaging Instrument's CHarge Energy Mass Spectrometer (CHEMS) (Krimigis et al., 2004). In their work, interchange injections were found to be both more prevalent and more intense between 7 and 9 R_S. Further, interchange events were found to be primarily on the nightside of Saturn, rather than the dayside, similar to what has been found in previous work by Kennelly et al. (2013), and consistent with the idea that the growth rate of interchange is inversely proportional to the ionospheric Pedersen conductivity as first proposed by Southwood & Kivelson (1989). In addition to the broad nightside peak, Kennelly et al. (2013) also found a dayside, post noon peak, which does not

seem to fit this explanation of ionospheric conductivity. Beyond examining the local time and radial dependence of their identified injection events, Azari et al. (2018) also compared their interchange injection events found in the CHEMS data to previous interchange surveys that used different detection methods. They found only modest overlap between their high-energy ion event catalogue and prior lists, and similarly for the other lists to each other, with 26 events shared by all published surveys. The overlap with the event list identified by Kennelly et al. (2013) was somewhat better than with the sets of events identified by Y. Chen & Hill (2008) and Lai et al. (2016). With the newly updated SLS-5 and PPO-based longitude systems and the recent updated interchange lists, it is worthwhile to investigate whether or not the observed interchange injections at Saturn exhibit organization in longitude systems developed to characterize the periodic modulations of the SKR and magnetic perturbations.

In this study, we conduct an analysis similar to that of Kennelly et al. (2013) to evaluate the dependence of interchange injection, but with events identified by Azari et al. (2018) using high-energy H^+ intensifications on the SLS-5 and PPO longitude systems. We review if previously observed modulations can be observed in high-energy H^+ intensifications by first applying the same filtering method in time and local time used previously by Kennelly et al. (2013). We then extend our analysis to the full set of available mission data. We further review organization for different seasonal time ranges to identify potential seasonal trends in the occurrence of interchange injections. As discussed, a bevy of magnetospheric phenomena have been observed to modulate with these periodic systems and within this spatial region (e.g., Ramer et al., 2017). In addition, these modulations have been associated with current systems (e.g., Hunt et al., 2015). We ask if these modulations in the physical environment are affecting the occurrence of interchange at Saturn. If interchange injections are organized by longitude throughout the Cassini era (2004–2017), then the occurrence of interchange may be sensitive to periodicities between the inner and outer magnetosphere and a source of periodic and systematic mass transport at Saturn.

3.2 Methods

We use the interchange injection events identified by Azari et al. (2018) to investigate dependence on longitude for the pre-equinox, equinox, and post-equinox time range. We take the pre-equinox date range to be 2005–2008, equinox to be 2009–2012, and post-equinox to be 2013–2016. We choose 2009 through 2012 as equinox mainly because the periods of the northern and southern SKR or PPO systems within these

years are close to each other, whereas outside of these years they diverge (e.g., Lamy, 2017; Provan et al., 2016, and references within). We are interested in observing differences in northern and southern system dependency during different seasonal time ranges.

The interchange injection events presented in Azari et al. (2018) were selected from the entire Cassini mission's equatorial CHEMS database, using all measurements within $\pm 10^{\circ}$ of the Saturn Equatorial System equator and between 5 and 12 R_S. CHEMS sorts ion flux by energy per charge range, time of flight, and total energy (Krimigis et al., 2004). As we look at equatorial orbits, we would expect organization in both the southern and northern rotational systems. Events were selected through an automated detection algorithm that takes into account radial distance, energy range, and background values to identify sudden H+ intensifications. The algorithm was trained and tested on a subset of interchange injections identified through visual inspection and then applied to all of the Cassini CHEMS data between 2005 and 2016 to obtain the first computationally standardized and comprehensive list of interchange injection events (see Azari et al., 2018, , for more details). It is important to note that some of the CHEMS events in this study overlap with those RPWS events found within Kennelly et al. (2013), even though they were identified with different instruments and selection criteria.

We use the newly developed and updated SLS-5 and PPO longitude systems to evaluate periodicity dependence (Provan et al., 2018; Ye et al., 2018). SLS-4 was the first system that separated the northern and southern signals and extended the SLS identification to early 2011 using a tracking filter (Gurnett et al., 2011). SLS-5 was derived similarly and extends past 2011. To separate the northern and southern systems, Ye et al. (2018) used the polarization of the SKR signal to separate the components. In this work we use SLS-5, which now covers the whole period of the Cassini mission (see Ye et al., 2018, , for additional dsicussion on SLS-5 and previous SLS systems). In comparisons, we transform findings of the SLS-4 system to SLS-5 with care taken in regards to the differences in the time range.

The PPO phase/longitude systems are developed based on Cassini measurements of the quasi-periodic magnetic perturbations. For both the northern and southern PPO systems, 0° is where the perturbation field of the quasi-uniform equatorial field points radially outward (e.g., Provan et al., 2018). The PPO phases of the northern and southern systems then increase with time at a given spatial location at their respective rates, as the systems rotate in the same sense as the planet. Both SLS-5 and PPO have been converted in our analysis to represent the phase/longitudes of

the spacecraft using the methods detailed most recently in Provan et al. (2018) and Ye et al. (2018).

Several studies have undertaken comparisons between the SLS and PPO systems (e.g., Cowley & Provan, 2016; Fischer et al., 2015; Provan et al., 2016, 2014). Due to the recent advances in the development of these systems, including the update to SLS-5, we present in Figure 3.1 a comparison between SLS-5 and PPO phases inside of 25 R_S. We use these comparisons as a guide to interpreting the differences in interchange occurrence analyses in subsequent figures. In Figure 3.1, we can observe that during most of the time, the phase difference remains approximately constant, meaning closely similar periods, with actual values depending on the orientation of the magnetic systems at times of corresponding SKR maxima. During most of the interval studied, the phase difference of the northern systems is near zero, meaning the quasi-uniform field of the northern system points sunward at the times of northern SKR maximum. The phase difference of the southern systems, however, generally is $\pm 180°$, meaning that the quasi-uniform field of the southern magnetic systems points antisunward at times of southern SKR maximum. PPO and SLS-5 are derived from different measurements onboard the Cassini spacecraft, which helps to explain these differences. For this reason, we analyze the interchange on rotational phase using both the PPO and SLS-5 systems.

In this analysis, we focus on the locations of the interchange events as observed by Cassini, rather than backtracking them to their estimated onset locations. The events identified in the Azari et al. (2018) survey are relatively young events because the identification method was developed and optimized to avoid significant dispersion in the CHEMS energy spectra. Ideally, one would estimate the onset locations by accounting for the finite radial propagation time and corresponding azimuthal drift as discussed by Liu et al. (2010) and Paranicas et al. (2016). These effects would potentially affect both the local time location and the PPO and SLS-5 longitudes. Paranicas et al. (2016) estimated the radial propagation time for three dispersionless injection events. They found propagation times ranged between 1.2 and 2.4 hr. As discussed, the time an injection travels inward without showing significant dispersion governs the evolution of the injection event, but the radial velocity and starting radial distance cannot be determined independently. Paranicas et al. (2016) relied on measured phase space density using a similar methodology to Rymer et al. (2009) to obtain estimates of the starting radial distance and to derive the radiation propagation time. Paranicas et al. (2016) found a radial drift velocity ranging between $\sim$9 and 18 km/s. The primary radial range of the interchange events found in Azari et al.

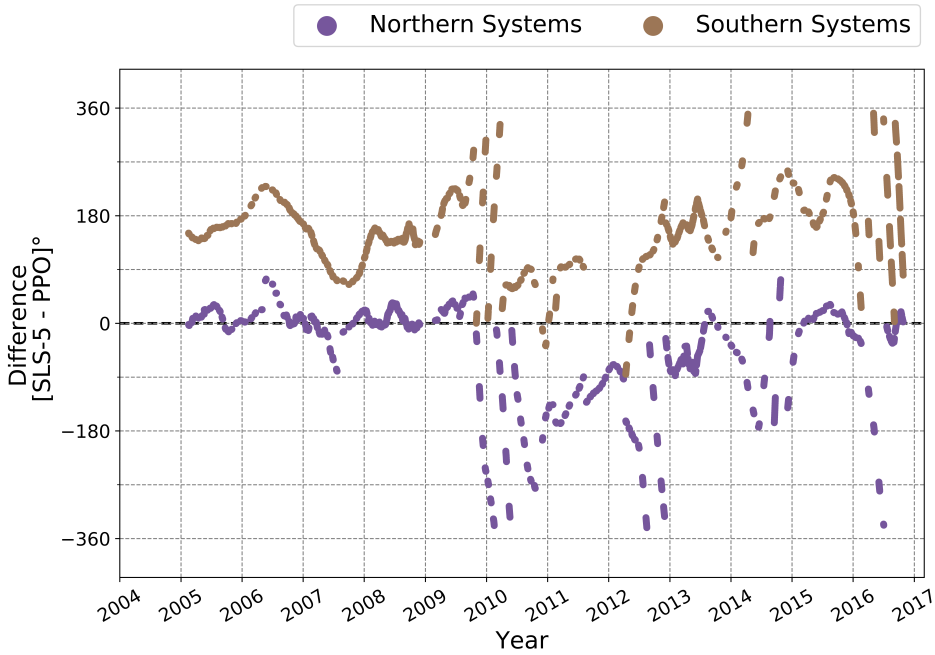

Figure 3.1: Difference in phase between the SLS-5 and PPO systems. The thick dashed line marks 0°, where the systems are in phase. The difference of the northern systems is represented in purple, while southern systems are represented in a light brown.

(2018) is between 7 and 9 R_S. If an event onset occurs at or beyond 9 R_S, then the maximum azimuthal drift speed in this range (between 9 and 10 R_S) is ∼0.69 of the rigid co-rotation speed with a standard error of 0.02 as estimated by Thomsen et al. (2010). Subsequent work by Wilson et al. (2017) estimated an azimuthal drift of ∼0.68 times rigid corotation between 9.5 and 10 R_S, within the error of the original work by Thomsen et al. (2010). We now estimate a maximum reasonable local time adjustment of the onset location of an interchange injection event. Taking the longer propagation time of 2.4 hr from Paranicas et al. (2016) at 0.68 of the rigid co-rotation velocity with a planetary rotational period of ∼10.7 hr, we predict an azimuthal propagation of ∼55° or of ∼3.7 hr in local time. At the lower limit of the radial propagation time of 1.2 hr, at a co-rotation velocity of only 0.61 rigid co-rotation a value more representative of an onset between 12 and 13 R_S based upon Wilson et al. (2017), we would expect ∼25° of azimuthal shift or <2 hour local time of azimuthal shift for an observed dispersionless event.

In our analysis, considering the available data coverage, we have chosen to organize our observed interchange events in 30° longitude bins, which are larger than the lower limit of the expected azimuthal offsets between the onset and the observer

location for the young injection events. We find that longitude bins of 30° present reliably consistent yet detailed results. We have also performed the statistical analysis (detailed below) with larger longitude bins but do not find any major differences in our results.

When calculating occurrence rates, we present sampling errors on all rates presented in this paper. Occurrence rates of interchange are calculated by normalizing by spatial sampling (e.g., radial location, local time, and SLS-5). More specifically, rates are calculated by taking the time Cassini spent within interchange and then dividing by the time Cassini spent in totality in that spatial region (e.g., radial location, local time, and SLS-5). This corrects for sampling bias in the Cassini orbits. We include on the occurrence rates propagated error. This is calculated from traditional propagation of error rules. The two sources of error are from the sampling error on time within interchange, and sampling error on time within spatial location, of the form $1/(\text{sample size})^{1/2}$.

3.3 Results and Discussion

We seek to determine whether or not interchange occurrence can be organized by either of these two longitude systems, that is, SLS-5 and PPO. In light of the previous findings of different relationships during pre-equinox and post-equinox (Kennelly et al., 2013), we examine the Cassini mission by analyzing the pre- equinox, equinox, and post-equinox time ranges separately. We begin by comparing results with the previous work by analyzing our events in SLS-5 for the same time and local time range used in Kennelly et al. (2013) (section 3.3.1). Section 3.3.1 is the only section in which we take a local time filter. We then use the updated SLS-5 and PPO systems for the whole pre-equinox time range 2005–2008 (section 3.3.2), the equinox time range 2009–2012 (section 3.3.3), the post equinox 2013–2016 (section 3.3.4) mission interval, and all 2005–2016 equatorial data (section 3.3.5) without restricting by local time.

3.3.1 Comparison With Previous Studies With Different Sampling Constraints

We first examine the dependence of occurrence rates of the Azari et al. (2018) interchange events on the SLS-5 longitudes for the same pre-equinox interval and local time range (19–03 LT) used by Kennelly et al. (2013). We compare the previous distribution found by Kennelly et al. (2013) in SLS-4 by transforming into SLS-5. SLS-4 north was defined from April 5^{th}, 2006 to September 16^{th}, 2009, and SLS-

4 south from September 2^{nd}, 2004 to January 9^{th}, 2011. Following Kennelly et al. (2013), who used August of 2009 as equinox, we evaluate our events in the pre-equinox time range for SLS-5 north between April 5^{th}, 2006 to August 2009 and SLS-5 south between the start of our own survey (2005) to August 2009. As a result, the total number of events available for evaluation of the northern phase becomes 100 while the southern phase event sample becomes 175. The limitation is discussed further in this section. More information on the valid date ranges for the SLS phase systems is available at the SLS-4 website (http://cassini.physics.uiowa.edu/sls4/).

As shown in Figure 3.2, our analysis confirms the original results of Kennelly et al. (2013) for the pre-equinox time range between 19 and 03 LT. Starting with the northern system (Figure 3.2, upper panel), the distribution of those events shared between the lists of Kennelly et al. (2013) and Azari et al. (2018) (magenta shading) shows a strong peak within the 60–90° northern longitude bin, very similar to the previous work. Further, the distribution of high-intensity events shows a similar peak in the 30–60° longitude bin. The distribution of all events identified in the Azari et al. study exhibit two comparable peaks within a broader longitude range of $\sim$ 30–180° that encompasses the peaks seen in the high-intensity events and the events shared with the Kennelly et al. study. Our full set of injection events exhibits another peak in the $\sim$300–330° SLS-5 north longitude bin. This peak is primarily due to events found at distances greater than 11 R_S. We discuss this radial bifurcation of our peaks in section 3.3.5. As the Kennelly et al. (2013) events are all within 11 R_S, we do not expect to see this peak in the overlapping data set. We also performed an analysis without this local time filter and find a similar distribution to that presented in Figure 3.2.

The total event distribution of events as function of the SLS-5 southern longitude (lower panel of Figure 3.2) shows an apparent preference centered on the 0° bin ranging between 240° and 120°. An additional secondary peak is in the 210–240° range. The primary difference between the northern and southern systems in our analysis however is the non-apparent organization of the events shared between the Kennelly and Azari lists and of the high-intensity events, in which the northern system showed a singular peak and the southern system has a lack of any apparent preference on a specific longitude bin. The lack of apparent organization by SLS-5 southern longitude for these high-intensity and overlap events is in agreement with the earlier results obtained by Kennelly et al. (2013). Interestingly, the distribution of all events in the Azari et al. list shows a different pattern in that there is a broad peak over the southern longitude range between 330° and 60°. However, the distribution of

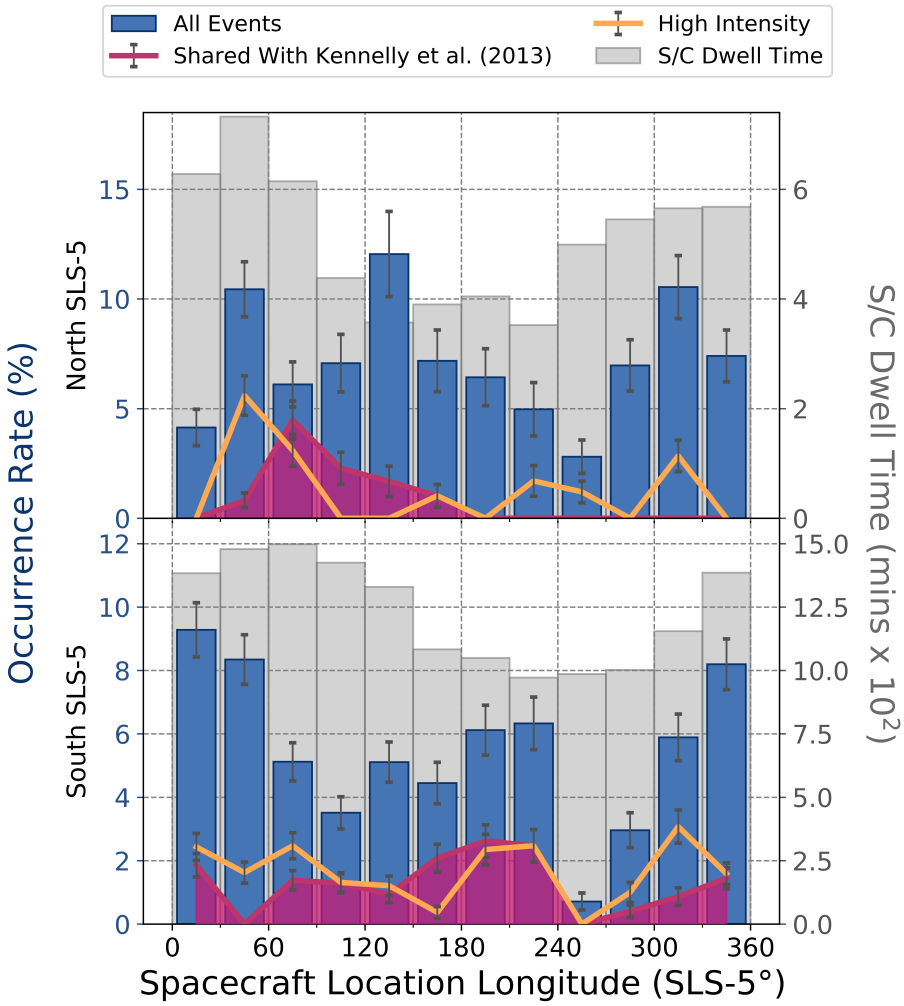

Figure 3.2: Pre-equinox interchange injection events normalized by spacecraft dwell time in SLS-5 between 19 and 03 LT. The top chart shows the normalized distribution of interchange events in SLS-5 north between April 2006 and August 2009 while the bottom chart shows the events in SLS-5 south between January 2005 and August 2009. The error bars are representative of the sampling error of 1/(sample size)$^{(1/2)}$ on the event and dwell time and propagated appropriately. The gray-shaded bars show the total sample size. The blue bars are the interchange events identified by Azari et al. (2018). The orange line represents the extremely high H^+ flux events of Azari et al. (2018) (>3 σ above background values). The magenta-shaded region represents events found by both Kennelly et al. (2013) and Azari et al. (2018).

all events (shown in blue) for both the northern and southern SLS-5 systems shows broad peaks within this time range. We cannot claim that the all event distribution of the northern system is more or less organized than the southern system for this time range.

Let us comment on the primary differences we have observed between the northern and southern SLS-5 systems within this sampling regime. This single-peaked distribution for the northern system is seen both with the events shared between Kennelly et al. (2013) and Azari et al. (2018) and our high-intensity events—also known as category 4 events, which have enhancements >3 standard deviations (σ) above background values in CHEMS as described in Azari et al. (2018). As can be seen in Figure 3.2, these two subsets of events show a similar distribution to each other. In the sections below, we use category 4 events as proxies for Kennelly et al. (2013) events, as their published list does not continue into the post-2012 date range.

As discussed above, applying the local time and time filters as required for direct comparison to previous works leads to different numbers of events for the northern and southern SLS-5 systems. There are a total of 100 events for evaluation of dependence of SLS-5 northern longitude, of which 12 events are shared with Kennelly et al. (2013) and 11 events are of high intensity. The 12 events shared with Kennelly et al. (2013) all come from just three orbits in the later half of 2007. Meanwhile, there are a total of 175 events for evaluation of dependence of SLS-5 southern longitude, of which 38 events are shared with Kennelly et al. (2013) and 30 events that are of high intensity. The 38 events shared with Kennelly et al. (2013) were observed during 12 orbits between 2005 and 2007. This difference between the northern and southern sample size is simply due to the availability of the SLS-4 system discussed above. In this previous analysis we used SLS-5 but applied the same time range restrictions that previous works had using SLS-4.

Restricting the local time and time range to compare to previous works yields three times as many high-intensity events in the SLS-5 south longitude system as compared to SLS-5 north. There are also nine more orbits in the southern system events, resulting in better spatial coverage. We are now able to confirm that the interchange events identified in the CHEMS data in SLS-5 show a single peaked distribution, primarily located in the high-intensity events. This is the very same peak that Kennelly et al. (2013) found in the pre-equinox period through identifying events with RPWS.

Therefore, we find that with the same sampling and restrictions, we are able to reproduce the dependence on the northern system in the pre-equinox period for

high-intensity events. The southern system does show disorganized behavior in the high-intensity events, which also agrees with previous findings. However, the overall distribution of all events appear similar between the northern and southern systems. The sampling restrictions primarily affected these high-intensity events of which are most similar to previous findings. Now we move on to expanding our sampling to all local times and available years to obtain equal sampling for time range and number of events between seasonal selections to evaluate the complete pre-equinox, during equinox, and post-equinox time periods.

3.3.2 Pre-equinox Distribution

Figure 3.3 shows the distribution of interchange occurrence rates from 2005 to 2008 as a function of the PPO and SLS-5 longitudes. The analysis in this section is not restricted by local time. Similar to Figure 3.2, we plot all events or the overall distribution in dark blue. Based on Figure 3.3 we note that the SLS-5 north and PPO north system distributions do show similar distributions for the high intensity and previously studied events, but there are also minor differences. This is to be expected because in Figure 3.1 we can see that between 2005 and 2008 the difference between PPO and SLS-5 north trends close to 0° with some deviations. We also note that the southern systems do show dissimilar patterns due to the offsets between these systems. As discussed previously the difference between the two southern longitude systems during the pre-equinox period centers around ∼180° due to the system definitions, and the distribution of injections as organized by the southern systems of SLS-5 and PPO does appear to be similar if shifted by ∼180°. We can observe this most easily for the total event distribution (blue shaded bars).

As noted in section 3.3.1, the northern system had markedly smaller sampling than the southern system. There are 256 events represented in this figure with 47 events shared with Kennelly et al. (2013) and 43 of high H^+ flux intensity (magenta-shaded regions and orange lines, respectively). While there are subtle rises and falls in the overall distribution with longitude in all northern and southern systems, we find that by introducing larger sample sizes (which also makes them roughly equal), the stark differences seen previously in Kennelly et al. (2013) are reduced. The results presented here are not filtered by local time, but we found no significant changes in the results with local time restricted to the nightside. As discussed above, the Azari et al. (2018) events are predominantly located on the nightside, and therefore, filtering by local time only slightly reduces the sample size but does not affect the overall longitude pattern.

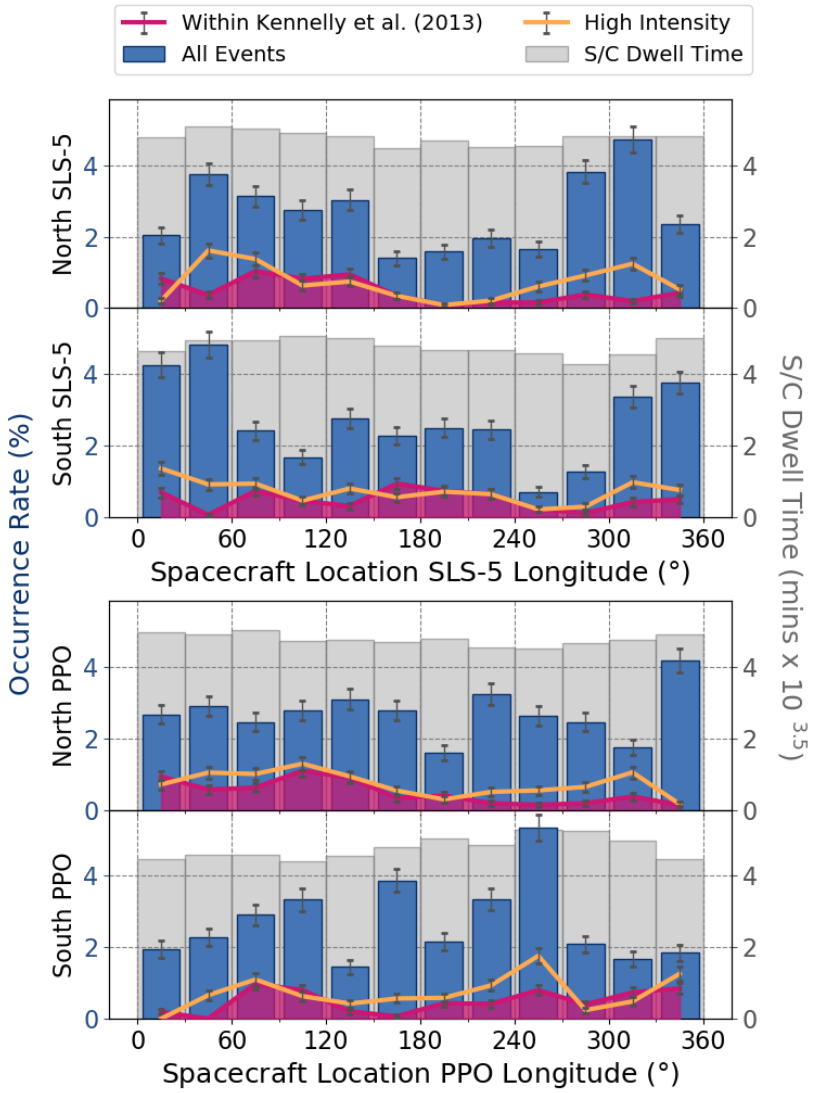

Figure 3.3: Interchange injection events normalized by spacecraft dwell time between 2005 and 2008 by SLS-5 and PPO. The top chart shows the normalized distribution of interchange events in SLS-5 north, followed by SLS-5 south, then PPO north, and PPO south. The error bars are representative of the sampling error of $1/(\text{sample size})^{(1/2)}$ on the event and dwell time and propagated appropriately. The gray-shaded bars show the total sample size. The blue bars are the interchange events identified by Azari et al. (2018). The orange line represents the extremely high H^+ flux events of Azari et al. (2018) (>3 σ above background values). The magenta-shaded region represents events found by both Kennelly et al. (2013) and Azari et al. (2018).

We find peaks in the injection occurrence rate in the SLS-5 north system for both overall events and for high-intensity events: There are two peaks: one centered between 0° and 120° and another between 300° and 330°. The 0–120° peak mirrors our previous finding in section 3.3.1, and by expanding the sampling we pick up additional patterns at other longitudes. In the PPO system, this trend is less clear, particularly when all events are included. In the southern SLS-5 system we observe a broad peak around 0° and in the southern PPO system multiple modest peaks, but in particular at 240–270°.

The difference between the northern and the southern system is small, and we cannot claim that in the pre-equinox period the northern system is more organized than the southern system. To confirm previous theories on systematic hemispheric seasonal dependence, we were expecting to observe an organization in the northern system as compared to an unorganized southern system due to different hemispheric illumination and therefore conductance during this time regions. But, in this comparison we have not observed a distinct change in organization with system.

In the PPO system 90° and 270° are of particular significance with respect to field aligned current systems since in the northern ionosphere parallel currents are directed outward at 90° and inward at 270° and reversed for the southern system (Hunt et al., 2014, 2015). We do observe small enhancements near these locations of interchange occurrence rates but only within the most intense of interchange events ($>3\ \sigma$ above background). We can say similarly for specific physical locations in the SLS-5 systems. These enhancements are small as compared to the values at other longitude locations and not reliably located in any singular hemisphere. We discuss this further in the following sections.

3.3.3 Equinox Distribution

We now analyze the equinox period between 2009 and through 2012. The analysis in this section is not restricted by local time. Figure 3.4 shows the occurrence rates of interchange within this period with no local time filters. There are 364 events represented in this figure with 63 events shared with Kennelly et al. (2013) and 92 of high H^+ flux intensity events. Overall, we do not observe a greater organization by the northern and the southern systems than seen in pre-equinox. However, within this time range we do not expect to see great organization due to the similarity of the ionospheric hemisphere illumination between 2010 and 2012.

In the SLS-5 charts we observe the northern system has greater occurrence rates again between 0° and 120° and around 270°. This is the same 0–120° as seen both

in the subset sampling (section 3.3.1) and in the full pre-equinox data set (section 3.3.2). For comparison, the northern PPO system shows peaks between 90–120° and 210–240°. Unlike the northern systems, the southern systems for both SLS-5 and PPO show different behavior from the pre-equinox period. SLS-5 shows enhanced occurrence rates between 60–90° and 270–300°, while PPO shows enhancements around 180–210°.

Comparing the results between equinox and pre-equinox, we find that the event distribution pattern in the southern system has undergone significant changes between the two seasonal phases, whereas in the northern systems interchange occurrence consistently exhibits enhancement around the ∼90° phase. This is unexpected as compared to the previous work by Kennelly et al. (2013).

3.3.4 Post-equinox Distribution

We now evaluate the post-equinox distribution of interchange by longitude for 2013–2016. The analysis in this section is not restricted by local time. Similar to previous sections, we present the distribution without filtering for nightside local time in order to maximize the sample size for our statistical analysis. In Figure 3.5, we present 196 events from Azari et al. (2018) of which 40 are of high intensity. We do not present our results for the category of events shared with Kennelly et al. (2013) because the Kennelly survey ends within this period and there are only a handful of events (i.e., not enough for statistical significance). However, we note that as shown in Figures 3.2 and 3.3, the distribution of our identified high-intensity events is very similar to that found in the shared-event set. Indeed, over all time, the highest intensity events find greater cross-correlation between lists than weaker intensity events (Azari et al., 2018). Similar to the equinox distributions, the northern and southern systems both show differences between SLS-5 and PPO. This is not unexpected, as there is more variability in the phases between SLS and PPO in the post equinox period (see Figure 3.1). Within Figure 3.5 we continue to observe an enhancement between 30° and 120° within the northern systems, but the secondary peak has decreased. The southern systems on the other hand show a large change from the pre-equinox and equinox periods, but not toward a more organized behavior as found within Kennelly et al. (2013). The post-equinox phases used by Kennelly et al. (2013) was only available between August of 2009 and January 2011—whereas the post equinox period used in this work is 2013–2016 (see section 3.2). We expect however that if a post-equinox organization of the southern system persists, it would be evident in 2013 and onward. Indeed, the peaks in the southern system are just as

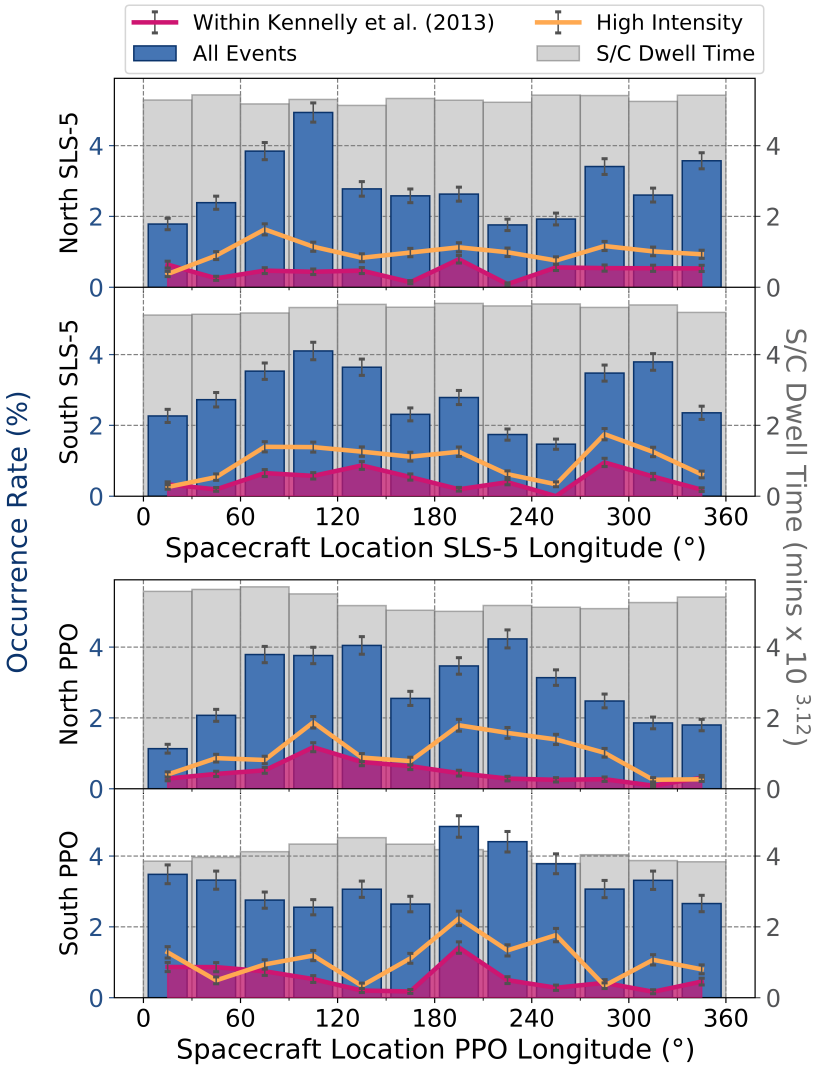

Figure 3.4: Interchange injection events normalized by spacecraft dwell time between 2009 and 2012 by SLS-5 and PPO. The top chart shows the normalized distribution of interchange events in SLS-5 north, followed by SLS-5 south, then PPO north, and PPO south. The error bars are representative of the sampling error of $1/(\text{sample size})^{(1/2)}$ on the event and dwell time and propagated appropriately. The gray-shaded bars show the total sample size. The blue bars are the interchange events identified by Azari et al. (2018). The orange line represents the extremely high H^+ flux events of Azari et al. (2018) (>3 σ above background values). The magenta-shaded region represents events found by both Kennelly et al. (2013) and Azari et al. (2018).

high, and indeed, the dips just as low, but they do not cluster in a broad region, nor remain consistent between pre-equinox, equinox, and post-equinox time periods.

We observe that the interchange event occurrence shows persistent enhancement within the ∼0–120° in the northern phase systems during the post equinox time period, just as seen in the pre-equinox and equinox time periods. The distributions are dissimilar to each other between the PPO and SLS-5 southern systems—not unexpectedly from the phase differences (see Figure 3.1). In previous works reviewing this interchange event list, occurrence rates were strongly organized in radial distance and local time (Azari et al., 2018). In section 3.3.5 we compare these statistics over all years combined as compared to local time and radial organization, having now found little difference in the northern systems with season.

3.3.5 Organization of Interchange Over All Years for Longitude, Local Time, and Radial Distance

Figure 3.6 shows the SLS-5, PPO, and radial and local time dependence of interchange occurrence rates for all the events identified in Azari et al. (2018). The right-hand panel of the figure shows the strongly nightside dominant local time organization discussed by Azari et al. (2018) with occurrence rates stronger by about 5–6 times on the nightside compared to the dayside. The left panels present the occurrence rates by rotational longitude and radial distance. In the northern systems, the small peak described within sections 3.3.2–3.3.4 between 30° and 120° clearly appears in both the SLS-5 and PPO plots. These panels all show that the injection events occur primarily near 8 R_S. The secondary peak present in the SLS-5 northern system around ∼300° is seen to be due to events outside of 11 R_S, which is outside the radial range included by Kennelly et al. (2013). This range was shown to have a larger proportion of enhancements due to tail effects (e.g., current sheet collapse) rather than interchange in the Azari et al. (2018) event list. We therefore focus on the peak located between 30° and 120° in this discussion rather than those between 11 and 12 R_S. As noted above, ∼90° north and 270° south in the PPO system is the location of upward field aligned currents within the ionosphere of Saturn (Hunt et al., 2014, 2015). This has been discussed as associated with an inward displacement of the current system in the equatorial plane (Hunt et al., 2015). The peak in our interchange distribution might suggest that there is a systematic effect at this location, potentially because (1) changing the curvature of the magnetic field affects Rayleigh-Taylor instabilities in curved magnetic field configurations (e.g., Komori et al., 1978) and/or (2) through magnetosphere-ionosphere coupling augmenting the

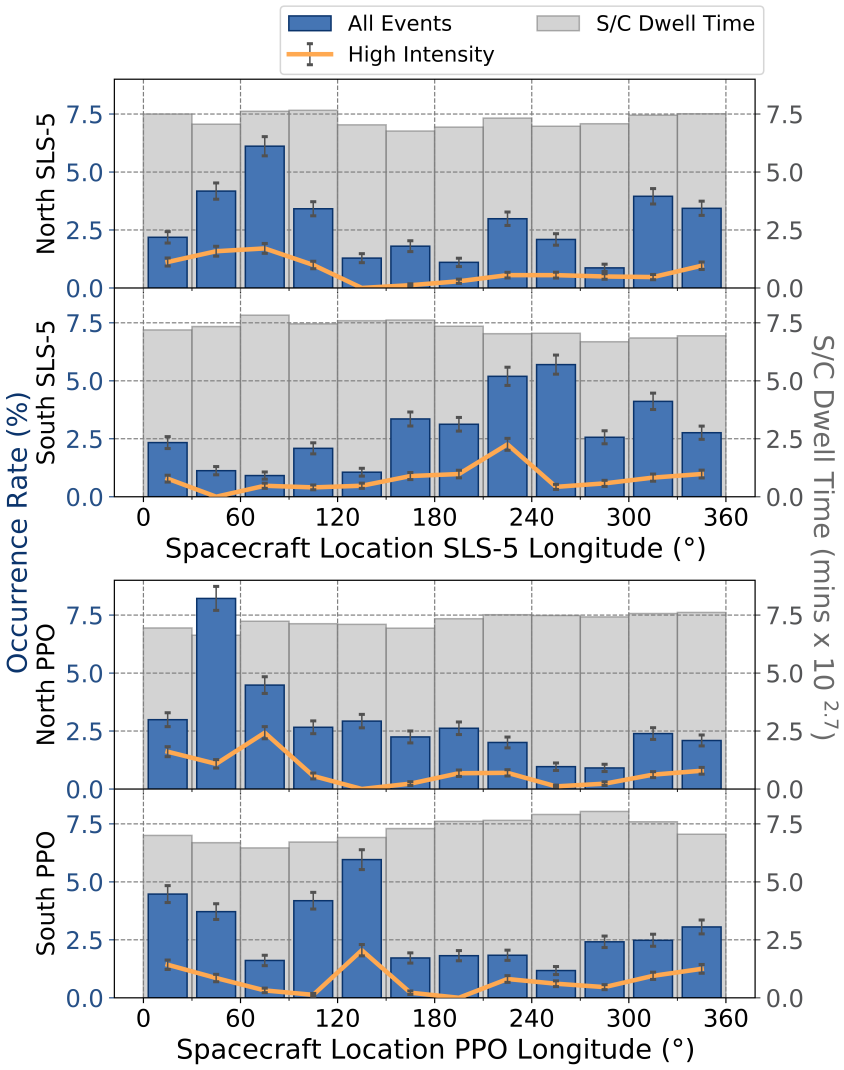

Figure 3.5: Interchange injection events normalized by spacecraft dwell time between 2013 and 2016 by SLS-5 and PPO longitude. The top chart shows the normalized distribution of interchange events in SLS-5 north, followed by SLS-5 south, then PPO north, and PPO south. The error bars are representative of the sampling error of 1/(sample size)$^{(1/2)}$ on the event and dwell time and propagated appropriately. The gray-shaded bars show the total sample size. The blue bars are the interchange events identified by Azari et al. (2018). The orange line represents the extremely high H^+ flux events of Azari et al. (2018) (>3 σ above background values).

instability criterion. Such upward field aligned currents are often associated with increase conductivity, which based on previous models are thought to suppress interchange (Southwood & Kivelson, 1987, 1989) whereas we observe an intensification in some, but not all of the upward field aligned regions. We stress that while the peak at $\sim$90° in the northern systems seems to persists throughout the Cassini era, the southern systems show no clear enhancement around 270°. Switching of ionospheric control of interchange dependent on Saturnian season, and hemisphere illumination, through analysis in rotating longitude systems is inconsistent with our results.

The white scatter plot points in Figure 3.6 show the locations of the events of highest intensity (>3 σ). The white dots exhibit little organization in the SLS-5 and PPO coordinate systems and instead occur at many different longitudes. According to Azari et al. (2018), these events correspond to those that are commonly shared among available surveys based on different identification methods. For a quantitative comparison, we calculate the maximum occurrence rate to minimum occurrence rate difference for SLS-5 north as compared to the same metric for local time distribution for all radial distances and years. We use SLS-5 north, as this shows the most extreme difference between the maximum and minimum values for all longitude systems.

For SLS-5 north, the peak occurrence rate over 2005–2016 occurs between 60° and 90° at 4.24% ± 0.17% and the minimum occurs at 240–270° at 1.90% ± 0.12%. The error calculated here is the error as described in the methodology section of propagated sampling error. At the maximum occurrence rate we therefore find an enhancement of $\sim$2 times as compared to the minimum without overlapping error calculations. Comparatively for the local time distribution over all years, which can be observed in Azari et al. (2018) and further reviewed in this present work, the peak occurrence rate occurs between 00 and 02 local time hours at 5.70% ± 0.15%, and the minimum occurs between 10 and 12 LT at 0.19%± 0.03%. The ratio between the maximum and minimum rate is $\sim$30. However, in our previous work we report the difference in rates as compared not to the minimum, as this value is rapidly approaching zero near noon, but the pre noon and post noon quadrants between 08–10 LT and 14–16 LT with occurrence rates of 0.95% ± 0.07% and 1.07% ± 0.08%, respectively. This results in a rate enhancement of $\sim$5–6 times.

The radial location and local time distribution have been extensively discussed in Azari et al. (2018). The predominant peak around 7–9 R_S has been attributed to the competition between energization of inward bound injections and charge-exchange losses. The dominant nightside occurrence rates are in good agreement with the local time distribution of suprathermal particles in the inner to middle magnetosphere (e.g.,

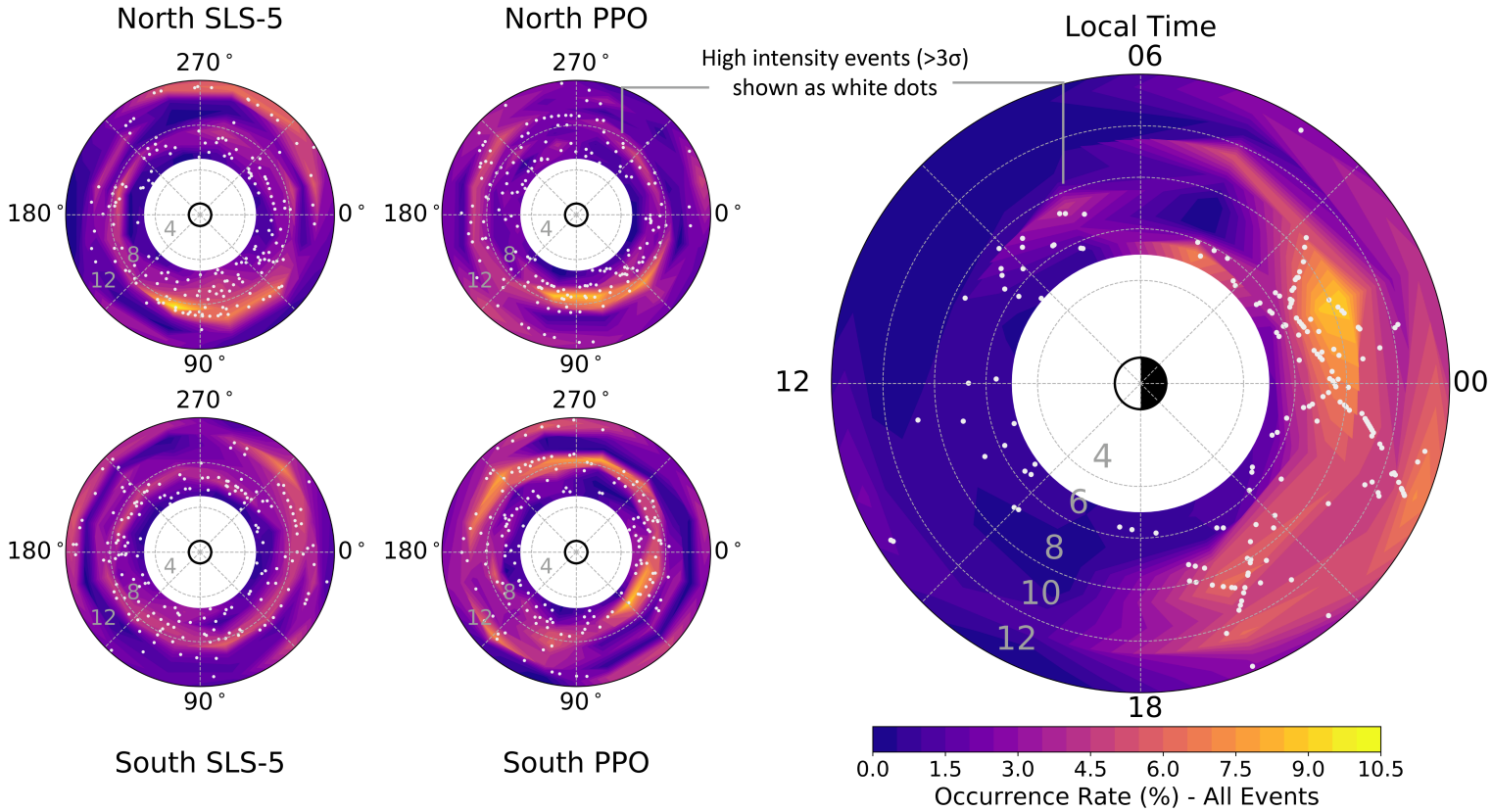

Figure 3.6: Interchange injection events normalized by spacecraft dwell time between 2009 and 2016 by SLS-5, PPO, and local time. The white dots represent extremely high H^+ flux events (>3 σ above background values) (Azari et al., 2018). All subplots share the same color bar.

Sergis et al., 2017; Thomsen et al., 2016). This is consistent with interchange as a primary radial transport mechanism additionally discussed by DeJong et al. (2010) and Hill (2016b). Examining the combined local time and radial distribution in Figure 3.6, we note a nightside asymmetry wherein the peak interchange occurrence rates are on the post midnight rather than pre midnight local time region, suggesting the triggering mechanisms of interchange is primarily intensified on the nightside, perhaps by large-scale tail injections or current sheet collapse. That is, large-scale tail injections form a fresh population of ∼keV ions just beyond 10 R_S in the midnight local time region. As these particles will drift eastward toward the dawn sector, there is a higher likelihood of interchange injection in the post midnight region, as seen in the right-hand panel of Figure 3.6.

The longitude enhancement is weak as compared to the local time enhancement. In addition, the northern system shows consistent enhancement, which does not change with season, and the southern system varies with season but not in a systematic manner. This is inconsistent with previous works and does not agree with current findings of interchange as responsive to seasonal differences in planetary period determinations. Instead, we interpret this result to suggest that the primary mechanisms behind interchange instability are strongly dependent on local time, with a weak enhancement due to physical mechanisms in the rotational phase systems.

3.4 Conclusion and Outstanding Questions

The dependence of the occurrence rates of interchange events identified by Azari et al. (2018) have been examined as a function of radial distance, local time, SLS-5 longitudes (north and south), PPO longitudes (north and south), and seasonal phases. Separate analyses were done for the full set of events and for the subsets of highest-intensity events (>3 σ above background of CHEMS) and events found also in a previous survey (Kennelly et al., 2013).

Within the same local time and date range examined by Kennelly et al. (2013), there is a distinct peak within the 30–120° range of SLS-5 north. This confirms their results, which were based on SLS-4 of an organized pre-equinox system. However, with a larger sample size the distribution shows multiple peaks at other longitudes in the northern system, and the single previously found organization diminishes, becoming comparable to the limited organization in the southern SLS-5 system. Further, we find that the northern longitude systems continue to show this 30–120° enhancement for the equinox and post equinox time ranges. The results of Kennelly et al. (2013)

suggest that this should not be the case, instead shifting to dominance by the southern longitude systems after equinox. This location of enhancement also shows distinct radial preference, located at $\sim$8 R_S, within the peak occurrence range of interchange injections at Saturn between 7 and 9 R_S (Azari et al., 2018). Our results show that interchange occurrence rates are not located in a singular longitude location by hemisphere or otherwise.

We find that there is a factor of 2 increase in occurrence at peak locations between 30° and 120° in the northern SLS-5 and PPO systems. We compare this to the enhancement found by Azari et al. (2018), which examined the local time distribution and found an enhancement of $\sim$5–6 times on the nighside as compared to the dayside. We further identify an asymmetry on the nightside, where peak interchange rates occur in the post midnight rather than the pre midnight sector, suggesting the triggering mechanisms of interchange are primarily intensified on the nightside, perhaps by large-scale tail injections or current sheet collapse.

The rather weak correlation between interchange occurrence and longitude systems suggests that rotational periodicities do not represent a primary mechanism influencing interchange injections. It is possible that periodicities and their causation through current systems could contribute through secondary effects such as the physical properties of interchange injection events (overall mass and energy transfer) or through other, still unexplored mechanisms in the middle magnetosphere of Saturn. Future work should consider investigation of solar influence on ionospheric conductivity through solar ultraviolet irradiance on the modulation of the occurrence rate of interchange as ultraviolet has been observed to affect the energetic environment (e.g., Kollmann et al., 2017; Roussos et al., 2014). We also note that interchange events used in this work are equatorial and subsequent work should additionally review high inclination injections for dependencies. The dependencies found in the present study do not totally preclude ionospheric control of interchange, but they show it to be at best a fairly weak influence.

Our results raise several questions in regard to interchange injection events. Given the previously found organization, limited when expanding the sample size as seen in this work, a revisiting of what physical mechanism could produce any dependence on longitude is worthwhile to re-investigate. This includes how the current systems associated with the PPO system could lead to interchange modulation. In this work limited organization is found in the northern systems (PPO and SLS-5), but this is weak compared to previous findings. Similarly, why is there then no such equivalent in the southern system for equatorial events? Why does the 90° peak in the north-

ern longitude system persist through all the seasons sampled? Additionally, these events studied were identified based on enhanced fluxes of high-energy ions; would interchange events identified using other instruments on-board Cassini show similar results? As shown by Azari et al. (2018), there are major differences in interchange surveys, and such efforts should be undertaken to continue identifying interchange injections in Cassini data. Future work should also investigate if interchange at Jupiter has any potential dependence on local time, radial distance, or longitude. As a gas giant with a similar mass transfer process, such a study would be essential in piecing together how rotational effects might affect the interchange process at rapidly rotating systems.

CHAPTER IV

The Role of Interchange in Energization and Loss

This chapter investigates the role of injections in contributing to hot ion energization and losses within the magnetosphere of Saturn. It details the development of a new parameter to identify energization of particles within the limited pitch angle resolution of Cassini data before comparing observations to expected energization and losses. The chapter is in preparation for submission for publication under the title "System wide evidence of particle loss and acceleration around Saturn" (Azari, Allen, et al., 2020).

4.1 Introduction

The magnetic environments, or magnetospheres of planets can be categorized into either externally influenced or internally influenced. Or more specifically, how sensitive the response of plasma and magnetic transport and flow around a planet are to external and internal drivers. Mercury and Earth present examples of externally driven magnetospheres with primary driving from mass, momentum, and energy the solar wind imparts to the planetary environment (see reviews by Borovsky & Valdivia, 2018; Slavin et al., 2018). For externally driven systems, the Dungey cycle is the primary large-scale circulation process (Dungey, 1961, 1963). A magnetosphere considered an internally driven system is Jupiter. Jupiter's system is dominated by the mass loading of the inner magnetosphere from the moon Io, and the rapid rotation of the planet itself (e.g. Bagenal, 2007; Fukazawa et al., 2006; Krupp et al., 2004). This leads to a process known as the Vasyliūnas cycle (Vasyliūnas, 1983) where internally generated mass loaded fielded lines are stretched downtail with the rapid rotation of the planet until magnetic reconnection occurs. Saturn, while commonly considered internally dominated, presents an in between, case with the presentation of both internal and external like behavior (see reviews within Krupp et al., 2018;

Thomsen, 2013). As shown through global magnetohydrodynamic modeling, Saturn's environment can respond to solar wind dynamics but has a consistent internally driven reconnection process (Jia, Hansen, et al., 2012). Saturn therefore represents a unique location for solar system studies of magnetospheres to study the interconnection of internally and externally driven systems.

One hallmark of an internally driven system is process known as interchange. This is a required mass transport system in the inner and middle magnetosphere at Saturn between ∼4 and 15 Saturn Radii (R_S). Interchange is most similar to a Rayleigh-Taylor like instability and are commonly associated with internal magnetospheric conditions. These are sourced from the cryo-volcanic outgassing of the moon Enceladus located at ∼4 R_S which creates a dense neutral population of primarily H_2O (∼91 ± 3% as compared to other molecular species) drifting to greater radial distances to form the extensive E-ring of Saturn (Spahn et al., 2006; Waite Jr. et al., 2006). A small amount of this neutral population then undergoes ionization by impact ionization and charge-exchange (Fleshman et al., 2013; Jurac & Richardson, 2005). This results in a neutral-dominated region in the magnetosphere of Saturn with a minimum mean neutral-to-ion ratio of 60 within the equatorial 3–5 R_S region and increasing beyond (see review within Mauk et al., 2009; "The distribution of atomic hydrogen and oxygen in the magnetosphere of Saturn", 2009; Shemansky et al., 2009). The dense resultant ions then undergo co-rotation from Saturn's rapid rotational rate of just under 11 hours per rotation, resulting in the dense ions experiencing centrifugal forcing into the less dense H^+ ions of the outer and middle magnetosphere. These energetic ions are found to peak in intensity near 10 R_S (Allen et al., 2018; Wilson et al., 2017). This physical situation is unstable against interchange instabilities. Interchange then acts as the primary mass transfer system in the middle magnetosphere, enabling the transfer of this dense population into the outer magnetosphere and returning energetic H^+ to the middle magnetosphere (Hill, 2016b; Thomsen et al., 2016).

The observation of the transport inwards of energetic (> 1 keV) H^+ due to this instability is called an interchange injection. This terminology is often confused with larger, downtail reconnection related injections from the Dungey and Vasyliūnas cycles (Mitchell et al., 2015; Thomsen, 2013). Interchange injections are distinct from large-scale tail injections in their primary triggering mechanisms, their spatial locations, and characteristic scale sizes. Within the Cassini data set, interchange is readily identified as an intensification of high-energy H^+, a corresponding altering of magnetic pressure, an evacuation of thermal plasma, and an enhancement of wave

activity (André et al., 2005, 2007; Azari et al., 2018; Y. Chen & Hill, 2008; DeJong et al., 2010; Kennelly et al., 2013; Lai et al., 2016). All these unique signals of interchange have led to a challenging issue when cross comparing interchange surveys, in which, depending on the primary identification metric, different events are identified as interchange injections.

Azari et al. (2018) developed an optimized automated identification of interchange based on statistical enhancements of the H^+ flux within the Charge Energy Mass Spectrometer (CHEMS) dataset. The automated method is most similar to a supervised logistic regression used within machine learning, but with physics based adjustments for consideration of radial and local time sampling constraints, potential seasonal variations, rare events, and energy-dependent flux asymmetries. This identification was created through a trained, tested, and automated process to identify interchange events by severity against the background high-energy H^+ plasma. This dataset provides the most complete detection and classification of interchange injection at Saturn to date.

It is important to consider the identification criteria when discussing interchange injections. In developing this automated list, it was found that only 30% of the automated events had a match within previous surveys, and only 26 events out of hundreds were shared between completed surveys (Azari et al., 2018). Through previous statistical surveys, it's understood that interchange is found primarily between 4 and 15 R_S, with peak occurrence rates and severity between 7 and 9 R_S (Azari et al., 2018; DeJong et al., 2010; Kennelly et al., 2013). By local time, surveys see a strong day-night asymmetry, with the nightside having stronger occurrence rates by 5 – 6 times and deeper radial range (Azari et al., 2018; DeJong et al., 2011; Müller et al., 2010). These surveys primarily focused on the high-energy signatures, and there is disagreement on the local time occurrence as surveys reviewing wave signatures and aged events have found a more azimuthally symmetric occurrence pattern (Y. Chen & Hill, 2008; Kennelly et al., 2013). This does still imply that at least for the high-energy (> 3 keV) interchange events, the nightside exhibits intensifications of the occurrence rate. This creates an entwined picture of large-scale and the smaller-scale, interchange injections. It has been proposed that large-scale injections can set up the necessary conditions to accentuate smaller scale interchange, through accentuating the plasma flux tube gradient on the nightside of Saturn (Azari et al., 2018; DeJong et al., 2011; Mitchell et al., 2015; Thomsen et al., 2015).

While it is observed that interchange appears to be sensitive to changing conditions in the tail region, it would also be expected to be sensitive to ionospheric

changes in conductivity, an internal process (e.g. Hill, 2016a; Southwood & Kivelson, 1989). Observations have found linkages between auroral activity and injections triggered by plasmoid release (Lamy et al., 2013). Interestingly for high-energy ions in interchange events, organization by longitude, and a marker of sensitivity to internal conditions in the ionospheric conductivity, is small compared to radial and local time organization, suggesting a lack of internal driver sensitivity (Azari, Jia, et al., 2019). However, surveys account for disparate findings in regards to ionospheric importance depending on their event selection and sample size, suggesting sensitivity to event definition. Most consistently found intensifications have been found near the $\sim$90° peak in northern longitude systems between 7 and 9 R_S, and show distinct trapped (perpendicular pitch angles) populations as compared to field aligned populations (Azari, Jia, et al., 2019; DeJong et al., 2010; Kennelly et al., 2013). Longitude systems at Saturn have undergone subsequent improvements over the Cassini mission and so while it can be difficult to compare statistical findings in previous systems, taken together, these surveys hint to a complex system. From these results, it appears that internal processes to the magnetosphere are limited and contribute a small accentuation on top of larger influences by tail and other in-situ dynamics.

This radial peak in particle populations is by itself, a long-standing mystery in the Saturn system with the very first Pioneer 11 observations noting ion temperature peaks between 7–8 RS (Frank et al., 1980). Now with additional measurements, it has become evident that this location in Saturn's magnetosphere is playing a key role in the system through interchange, particle dynamics, and ring current populations (see discussions within Azari et al., 2018; Sergis et al., 2017; DeJong et al., 2010). How interchange relates to system wide dynamics is an active question.

With the rise of statistical surveys from the Cassini mission dataset, findings suggest that interchange is sensitive to processes of external and local plasma condition forcing. Within Figure 4.1 we speculate based on previous findings the distribution and a picture of the day-night asymmetry for the high-energy H^+ signatures of interchange injections in the middle magnetosphere. Enceladus is illustrated as outgassing primarily water into the inner magnetosphere, which drifts and sets up a dense plasma population as discussed above. This then interchanges through Rayleigh-Taylor like instabilities with the less dense H^+ population. Interchange events range in size from $\sim$1.72 R_S down to, but not limited to, 0.04 R_S (Azari et al., 2018). This illustration represents a series of mid-scaled and large injections with respect to this size estimation. This scenario is based on the combination of several observations, and it is expected that the presence of injections is extremely dynamic in response to tail

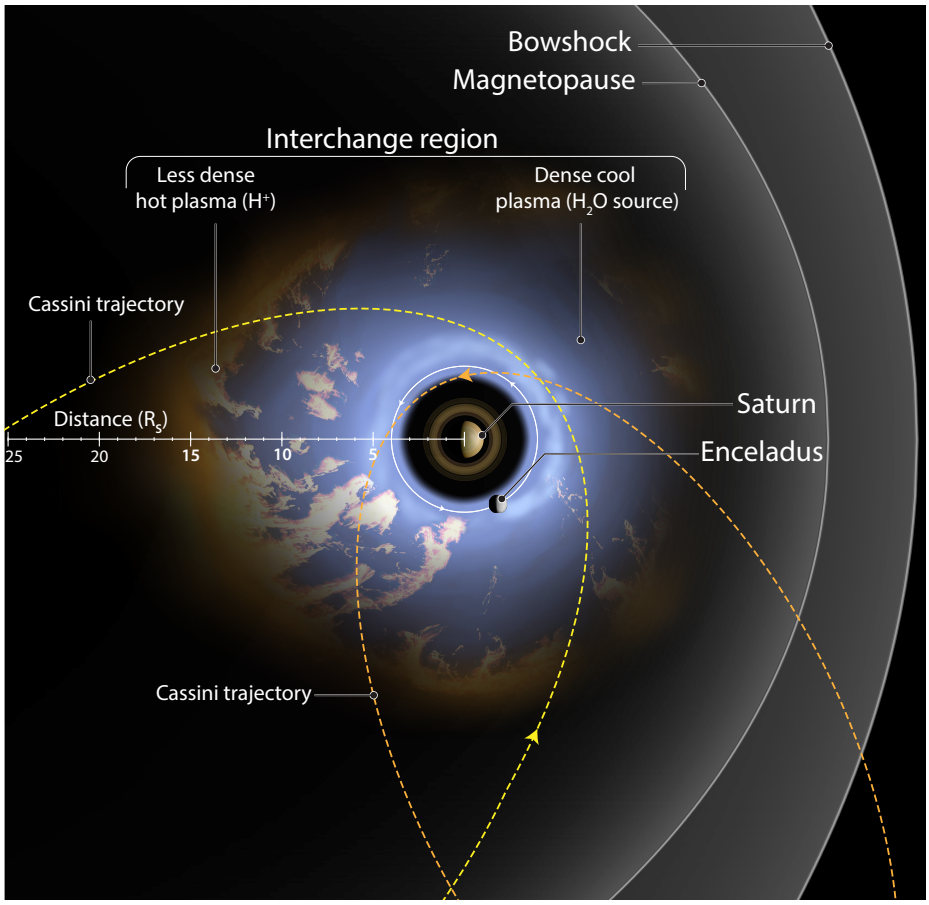

Figure 4.1: Illustration for several Cassini passes of the interchange region. High-energy interchange injections show prevalence on the nightside of the planet, as shown in pale orange. The Enceladus neutral torus is shaded in blue. Orbits illustrated are two equatorial orbits Rev 4 (2005 DOY 058 - 078) and Rev 22 (2006 DOY 068 - 099). Parts of this illustration are not to scale. This figure was created in consultation and with permission from Falconieri Visuals. Copyright held by Falconieri Visuals.

dynamics, plasmapause locations, and other internal and external factors and subject to rapid change (e.g. Azari, Jia, et al., 2019; Mitchell et al., 2015; Thomsen et al., 2015).

These statistical surveys from the Cassini mission open new questions about the role of interchange in the transport system around planetary bodies, not only to their sensitivity to triggering but also to their role in delivering energetic H^+ toward the planet. In particular, interchange occurrence rates vary widely over the course of the mission in time, and over the entire mission; even in the most prevalent radial region for interchange (7 - 9 R_S), interchange occurs <4% of the time (Azari et al., 2018). How does interchange then impact the background plasma conditions at Saturn?

As a primary transport process, the pitch angles of interchange injections convey

information about the transport of energetic particle populations in Saturn's magnetosphere. Interchange injection plasma is expected to be heated primarily through adiabatic conservation during inward radial transport (Mitchell et al., 2015; Paranicas et al., 2016). Rymer et al. (2009) found that distribution within interchange events evolves from isotropic to pancake (90° trapped) in agreement with adiabatic inward transport by evaluating the pitch angles of Cassini Plasma Spectrometer (CAPS) measured electrons. Mitchell et al. (2015) noted with the Magnetospheric Imaging Instrument (MIMI) suite including CHEMS a series of injections from 2006 day of year 080 energy dependent pitch angle behavior, hinting that ions with perpendicular pitch angles are energized more than those that are field-aligned. DeJong et al. (2011) noted that the perpendicular fluxes of CAPS electrons are higher on the nightside than the dayside and discussed the possibility that this is due to the asymmetry in interchange rates. Interchange prevalence on the nightside can also help explain the day-night asymmetry found within intensities of plasma within the middle magnetosphere (Kollmann et al., 2011; Paranicas, Mitchell, Roussos, et al., 2010). Unique to Saturn, these asymmetries are also potentially contributed to from the noon-to-midnight electric field (e.g. Andriopoulou et al., 2012; Paranicas, Mitchell, Krimigis, et al., 2010; Thomsen et al., 2012). Pitch angles distributions of injections, not only hint at the acceleration mechanisms but also reflect on the system wide pitch angles distributions at Saturn and outstanding questions of global configuration, including as a potential contribution to Saturn's variable ring current (Sergis et al., 2017).

Within this work we investigate sources and losses of high-energy (> 3 keV) ions in the inner and middle magnetosphere (focusing between 5-12 R_S) and the effect of interchange injection on the background distributions of energetic particles. We build off the events selected by Azari et al. (2018) using CHEMS data and develop a pitch angle analysis for both interchange events and the background plasma population within the $3 - 220$ keV energy range. Within this work we detail the development of new pitch angle analyses using CHEMS (Section 4.2), before analyzing the distributions of these pitch angles both within events, and globally, while comparing these results to modeled expectations (Section 4.3). Finally we comment on our conclusions on global mass transport and losses due to interchange influence, a long-standing area of research within mass transport (Section 4.4). As a major transport mechanism, interchange is a primary source of energetic material in the middle and inner magnetosphere. Investigating the pitch angles of interchange fills in the missing pieces of global transport, including sources and losses, between the mass loading of Enceladus and far tail loss.

4.2 Methods

4.2.1 Event Selection Criteria

All interchange events are identified based on the criteria described within Azari et al. (2018). In brief, events were identified in an automated fashion most similar to a supervised logistic regression, a type of binary classification algorithm most commonly used for categorical data in machine learning contexts. A set of training data was selected from the Cassini CHEMS H^+ flux to optimize thresholds of an optimized parameter to detect events. The method employed in Azari et al. (2018) differed from traditional machine learning and supervised logistic regression by taking into consideration radial variation, potential seasonal variations over the Cassini mission, and energy dependent flux asymmetries. In addition, by setting the optimization algorithm form but not the final threshold values, this method provided the ability to standardize the detection of events. Events are standardized so those within the final analyses are statistically meaningful enhancements of H^+ flux over the background data. The performance of this algorithm was then evaluated over a separate set of test data. The final optimization was performed on the Heidke Skill Score (HSS). Interchange injection events occur infrequently, and HSS, which depends on event frequency was used rather than other other types of machine learning optimization (Manzato, 2005). These physics-based adjustments address several outstanding issues in applying machine learning to geoscience datasets including those illuminated within Karpatne et al. (2019), such as spatio-temporal structure, high-dimensionality, lack of concise object definitions, and rare classes. As reported within Azari et al. (2018), the final form of the detection metrics obtained an HSS of 0.56 for the training set, and 0.49 for the test set. The false positives detected within this list are also guaranteed to be enhancements over the background of the CHEMS H^+ background and each event contains a standardized degree of physical information. We use the 816 events identified within this previous work.

4.2.2 Data Source: CHEMS Pitch Angles

CHEMS was a charge-energy-mass spectrometer within the MIMI suite on board the Cassini spacecraft that arrived at Saturn in 2004 and collected 13 years of data until 2017. CHEMS collected ion data by admitting a narrow energy per charge range followed by the time of flight and energy technique as described in Krimigis et al. (2004). This study is focused on: the H^+ equatorial flux, within 10° of the equatorial plane in Saturn Equatorial System (SZS), between 3 and 220 keV, and

between 5–12 RS. These are the same restrictions as the original event detection for interchange injection identification.

CHEMS is made up of three distinct telescopes, each one covering 53° in polar angle along the spacecraft's z-axis – and at times measuring different portions of the pitch angle distribution of incoming particles. For pitch angle analysis, flux from each telescope is assigned a pitch angle using the mid-point look direction of the telescope and the magnetic field direction from the magnetometer data. The Cassini spacecraft did rotate at specific times in its orbit and the pitch angle that a telescope was measuring can change due to changes in the direction of the magnetic field with respect to the spacecraft. To investigate statistical information on pitch angles, care must be taken on not assuming full pitch angle coverage at any single time as it is unknown. Additionally, grouping fluxes at a range of binned pitch angles can also be problematic. For example, a telescope that has been measuring pitch angles at 90° contains other pitch angle information which cannot be recovered. Therefore, if you compare the fluxes at 110° of any telescope to those at 90° there is an unknown amount of overlap. These two values are now no longer unique and pitch angle analysis becomes ambiguous. Additionally, at certain magnetic field orientations all three telescopes will be measuring the same near 90° pitch angle range. However, this is the only mission long dataset that provides pitch angle information for high energy H^+.

To address the limitations of the dataset we have developed a ratio that compares near-perpendicular fluxes with near-parallel and anti-parallel fluxes. The ratio is only calculated when one of the three telescopes is pointing in the near 90° pitch angle direction, and another in the near field-aligned or anti-field-aligned direction. We define an anisotropy ratio in which we can quantify the relative enhancement fluxes near 90° pitch angles as compared to field and anti-field aligned particle fluxes. The anisotropy ratio, A, is described mathematically as:

$$A(t, e) = \frac{F_{\perp}(t, e)}{F_{\uparrow,\downarrow}(t, e)} \tag{4.1}$$

Within equation 4.1, A is calculated at every time t that meets our pointing requirements. The variable e denotes each energy band between 3 and 220 keV. The numerator $F_{\perp}$ represents the flux in the perpendicular direction and the denominator $F_{\uparrow,\downarrow}$, represents the flux in either the parallel or the anti-parallel field direction. Because the field-aligned and anti-field-aligned flux are only very rarely both present simultaneously in the CHEMS data set, either is used, whichever exists for that time

interval (or both). This calculation assumes the fluxes along the parallel and anti-parallel direction are of equal value. We tested this assumption and found that the variation between parallel and anti-parallel is much less than the current calculated ratio. From these calculations we move toward treating parallel and anti-parallel directional flux similarly to increase the sampling.

We set a 45° range for classification of the telescope into perpendicular (67.5° - 112.5°), parallel (0° - 45°), or anti-parallel (135° - 180°). This removes data when telescopes were within the gap region of these bins but this selection gap provides an additional restriction that the populations will never overlap in their pitch angle fields of view. Smaller than 45° bins were attempted, but yielded significant data gaps that compromised statistical significance.

A series of injections previously described in associated interchange works and further detected by Azari et al. (2018) are presented as examples of the pitch angle anisotropy and ratio calculation for several distinct energy ranges over the CHEMS dataset (Mitchell et al., 2015; Paranicas et al., 2016; Rymer et al., 2009). Figure 4.2 demonstrates both a schematic of the CHEMS instrument (Figure 4.2a), as well as a series of energy per time flux spectrograms (Figure 4.2b-d) corresponding to the observed pitch angles of 40°, 90° and 140°. Figure 4.2e then demonstrates the calculated anisotropy ratio comparing near 90° fluxes to near parallel and anti-parallel fluxes. Within these events we present the first quantification of the scale of high-energy ion anisotropy within injections at Saturn. Similar to the observations previously reported by Mitchell et al. (2015) and Rymer et al. (2009), we find clear energy dependent behavior by particle pitch angle with clear perpendicular enhancements at >30 keV energies. Within Figure 4.2 we find a perpendicular flux enhancement of ∼40 times higher than non-perpendicular flux in the 47 – 71 keV energy range. This is likely to be an underestimation of the highest amount of enhancement at the near-perpendicular pitch angles as they have a sampling width of 45° of pitch angle, but this demonstrates a first estimation of the potential range of acceleration. At the lower energies, fluxes demonstrate either isotropic or non-perpendicularly dominated flux populations. Within the results section we propose and evaluate the cause of this difference as a result of betatron acceleration.

The 2006 DOY 080 events shown in Figure 4.2 and those discussed earlier within Mitchell et al. (2015) and Rymer et al. (2009), are all located within 7-9 R_S. As discussed within the Introduction, this region contains the most interchange injections, the most intense injections, and the most organization by Saturn longitude (Azari, Jia, et al., 2019; Azari et al., 2018). To accurately gain an understanding of the po-

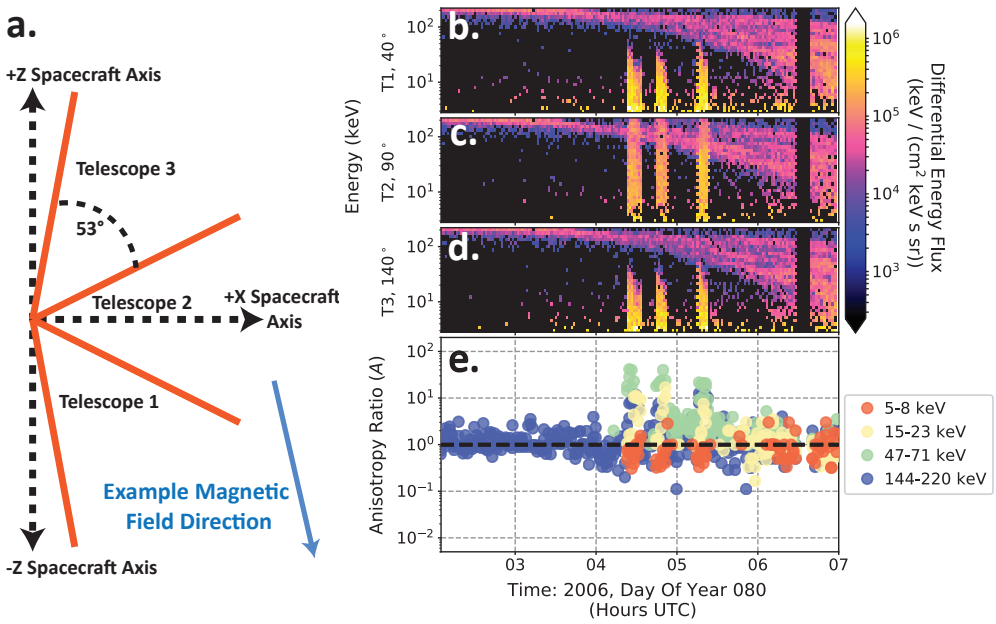

Figure 4.2: Schematic of CHEMS instrument pitch angle anisotropy within interchange. Part a demonstrates a schematic of the CHEMS telescope directions with a demonstrated magnetic field direction relating to the spectrograms observed in parts b – d with calculated pitch angles in the subtitles. Panel e highlights for 4 distinct energy ranges for CHEMS the behavior pitch angle dependent particles both before, during, and after the injection events.

tential role of adiabatic acceleration on these events, we will examine injections at all radial distances from 5-12 R_S. In the next section we use the anisotropy ratio defined to discuss the role of interchange events in system wide distributions.

4.3 Results and Discussion

4.3.1 Evidence of First Adiabatic Invariant Conservation Within Interchange

Within interchange injections, it's expected that adiabatic invariance related acceleration will result in observed energization. Mitchell et al. (2015) remarked on the intensification of >30 keV ion populations within injection events as evidence of an adiabatic acceleration process. At Saturn there are two categories of injections responsible for moving mass toward the planet: tail-reconnection-driven current sheet collapse and interchange injections. As described by Mitchell et al. (2015), a current sheet collapse event energizes and transports mass through non-adiabatic processes, while flux tube interchange is heated through adiabatic means. While triggered by

different mechanisms, interchange events have been shown to be sensitive to the effects of the former tail injections, potentially due to the intensification and accentuation of a plasmapause-like boundary from the large-scale nightside injections (Azari et al., 2018; Thomsen et al., 2015). The repercussions of this triggering on interchange is proposed to result in the situation is detailed in Figure 6.1.

It has not been shown statistically over many injection events the role adiabatic invariance plays on the energization of this transport process. Both betatron acceleration and Fermi acceleration are potential adiabatic processes that could be acting on incoming injections. Betatron acceleration results in enhancements within the perpendicular component of the particles' pitch angles as particles travel toward the planet and into regions of greater magnetic field strength. Fermi acceleration would enhance the parallel components of this flux, and have a limiting effect on the observed intensification of the anisotropy ratio of the particles' pitch angle distribution. Characteristic time scales can be calculated to estimate these two processes potential roles in energization of incoming injections.

The gyropoeriod and the bounce period are considered characteristic time scales for betatron and Fermi acceleration respectively. It can be expected then that the adiabatic invariant resulting in Fermi acceleration will not be conserved as compared to betatron acceleration from estimations of characteristic time scales. At Saturn for a 3 keV ion (H^+) at 7 R_S, the gyroperiod is $\sim$1 second. The bounce period of a 3 keV ion is $\sim$1000-2000 seconds (tens of minutes). In comparison to characteristic interchange time scales, previous works estimate the incoming velocity of injections ranging between 25 and 71 km/s (Burch et al., 2005; Y. Chen et al., 2010; Krupp et al., 2018; Rymer et al., 2009; Paranicas et al., 2016). Converting this to a time scale then results in an incoming injection able to travel 1 R_S on the order of a single bounce period. We predict that the primary acceleration mechanism describing the anisotropy ratio is betatron rather than Fermi acceleration. We expect for this situation, therefore, that when organized by radial distance, interchange events should demonstrate adiabatic conservation of phase space density following betatron acceleration. Studies investigating similar adiabatic conservation have through event studies have been seen within Paranicas, Mitchell, Roussos, et al. (2010) and Rymer et al. (2009).

We present in Figure 4.3a the radially binned anisotropy ratios within all our identified interchange injection events. We find greatly anisotropic values moving inwards from 12 R_S which peak within 7 – 8 R_S. Surprisingly this trend does not continue inside of 7 R_S. Below we discuss the potential causes of this enhancement

and subsequent depletion by evaluating a predicted effect of betatron acceleration and charge exchange. In Figure 4.3b we present the p-value of the distributions compared to the 7 – 8 R_S distribution using the two-sample Kolmogorov-Smirnov (K-S) statistic. The K-S quantity specifically tests for the likelihood that two data samples are obtained from the same distribution and does not require parametric or equal samples. The p-values shown in Figure 4.3b are calculated from testing the distribution of 7-8 R_S to other radial distributions. The p-value shows when comparing the distributions of 7-8 R_S to 8-9 R_S, or to 6-7 R_S the p-values drop quickly to well under 1%. From these values we can confirm that, within 1% p-value confidence, the distribution of 7 – 8 R_S is significantly different than at other radial distances. We now move to interpreting the anisotropy ratio for evidence of betatron acceleration.

In Figure 4.3a, we plot in the pale red, an envelope of an expected betatron acceleration for a particle population moving radially inwards at 11.5 R_S (pale red shaded region). The interquartile range (IQR) of the anisotropy ratio is shown in the figure with the colored boxes. From this we then developed a particle model, which calculates flux as a function of pitch angle given the conservation of the first adiabatic invariant. We do not include the second adiabatic invariant (Fermi acceleration) as this has a limiting factor on the anisotropy ratio we observe and, as discussed above, is unlikely a dominant effect given relevant timescales.

To calculate this expected envelope we first assume conservation of the first adiabatic invariant and a dipolar field. This results in equation 4.2 for the resulting perpendicular velocity of a particle at a future time as a function of its starting velocity.

$$v_{\perp,2} = v_{\perp,1}\sqrt{\frac{B_2}{B_1}} \tag{4.2}$$

The pitch angle of a particle can be written in equation 4.3 as a function of it's parallel and perpendicular velocity.

$$\alpha = \tan^{-1}\left(\frac{v_\perp}{v_\parallel}\right) \tag{4.3}$$

The pitch angle after injection then can be written by combining these equations as shown in equation 4.4.

$$\alpha_2 = \tan^{-1}\left(\frac{v_{\perp,1}}{v_{\parallel,2}}\sqrt{\frac{B_2}{B_1}}\right) \tag{4.4}$$

If then we assume the parallel velocity does not change during the injection process and violates the second adiabatic invariant, α_2 can be rewritten as shown in equation 4.5.

$$\alpha_2 = tan^{-1}\left(\sqrt{\frac{B_2}{B_1}}\tan(\alpha_1)\right) \tag{4.5}$$

It's important to note here, that by assuming violation of the second adiabatic invariant, equation 4.5 does not contain energy information at this point to govern the evolution of the particle's pitch angle. While the evolution in an injection event still does depend on the starting pitch angle distributions, how this evolves in time no longer contains an energy specific term.

Furthermore, by assuming a dipolar field, this equation may be rewritten as a function of starting and ending radial distance (r_1 and r_2, respectively) and the initial pitch angle (α_1).

$$\alpha_2 = \tan^{-1}\left(\sqrt{\frac{r_2^{-3}}{r_1^{-3}}}\tan\left(\alpha_1\right)\right) \tag{4.6}$$

This equation is then used to evolve a starting pitch angle distribution forward by assuming flux (j) as a function of pitch angle α. We assume flux initial values as represented by equation 4.7, as developed in previous works, which can be used to well describe pancake, isotropic, and field-aligned distributions (Allen et al., 2017; Clark et al., 2014; Kistler & Mouikis, 2016; Roeder et al., 2005; Rymer et al., 2008).

$$j(\alpha) = C\sin^n(\alpha) \tag{4.7}$$

The new pitch angle of a particle moving radially inward is dependent only on the change in magnetic field strength and starting pitch angle.

In equation 4.7, C designates the flux at 90° and n the anisotropy index. Since we are primarily interested in anisotropy (flux for ions with perpendicular pitch angles versus those with field-aligned and anti-field-aligned pitch angles) the choice of the C term will drop out when dividing, for example, $j(90°)$ / $j(0°)$. To compute values comprising the pale red region in Figure 4.3a, we assigned 10000 starting pitch angles, equally spaced between 0 and 180°, with a flux value from equation 4.7 that resulted in the IQR flux anisotropy values at 11.5 R_S. The pitch angles for the initial flux-pitch angle profiles were then recomputed for different radial distances using equation 4.6, and the re-binned flux-pitch angle profile was then used to re-compute the anisotropy.

A major limitation of the currently presented work, is that we assume the starting distribution for the same energy range as shown at each radial distance, instead of following along the expected contour of adiabatic invariance. This effectively provides a prediction of the likelihood of betatron acceleration for a near-isotropic distribution. Future work will take into account the distribution at a lower energy, and instead of following along a constant energy, will cut through energy and radial space along a preset adiabatic invariant contour. This will more effectively address the expectations of betatron acceleration.

From the present calculation and model we are able to predict, for a dipole configuration, the anisotropy ratio from a starting distance at 11.5 R_S. In Figure 4.3a, we observe that betatron acceleration accurately predicts the expected ratios we observe for the median from 12 until 7 R_S for an isotropic starting distribution. In particular, the predicted path of anisotropy always contains a large percentage of the observed interquartile range until inside of 7 R_S, at which it diverges. The marked departure inside of 7 R_S is a clear sign of another competing physical process depleting perpendicular fluxes. At 7 - 8 R_S the median of the model prediction is 2.35 with a standard deviation of 0.22 (calculated by averaging the model prediction between 7 – 8 R_S). The identified injection events have a median value of 2.42, within the range of expected values between 7 – 8 R_S predicted by the model. Note however, the range of values in the 7 – 8 R_S region (IQR: 1.30 – 14.1), well exceed the expected values of the model. This suggests that betatron acceleration alone is not sufficient to completely describe the extreme values. Fermi acceleration would limit the perpendicular enhancements. We propose that the most extreme outliers we observe could potentially be due to multiple injections interacting, such as tail injections and affecting interchange to build up to a large range of values at 7 R_S. A similar situation is discussed at Earth for multiple flux pileup events leading to observed large energization and possibly would result in the anisotropy calculations observed here (Gabrielse et al., 2017). Future modeling focused work in similar style would be beneficial to address how large-scale injections could be affecting, and energizing, localized interchange events. Additional contributions to the wide range of values observed at 7 R_S could partially be contributed to by variations in starting location as this is a composite analysis of multiple interchange identified events. Within this analysis we have focused on 47-71 keV. We now move to reviewing the anisotropy over the entirety of the CHEMS range (Section 4.3.2), before commenting on the observed losses in injection events (Section 4.3.2).

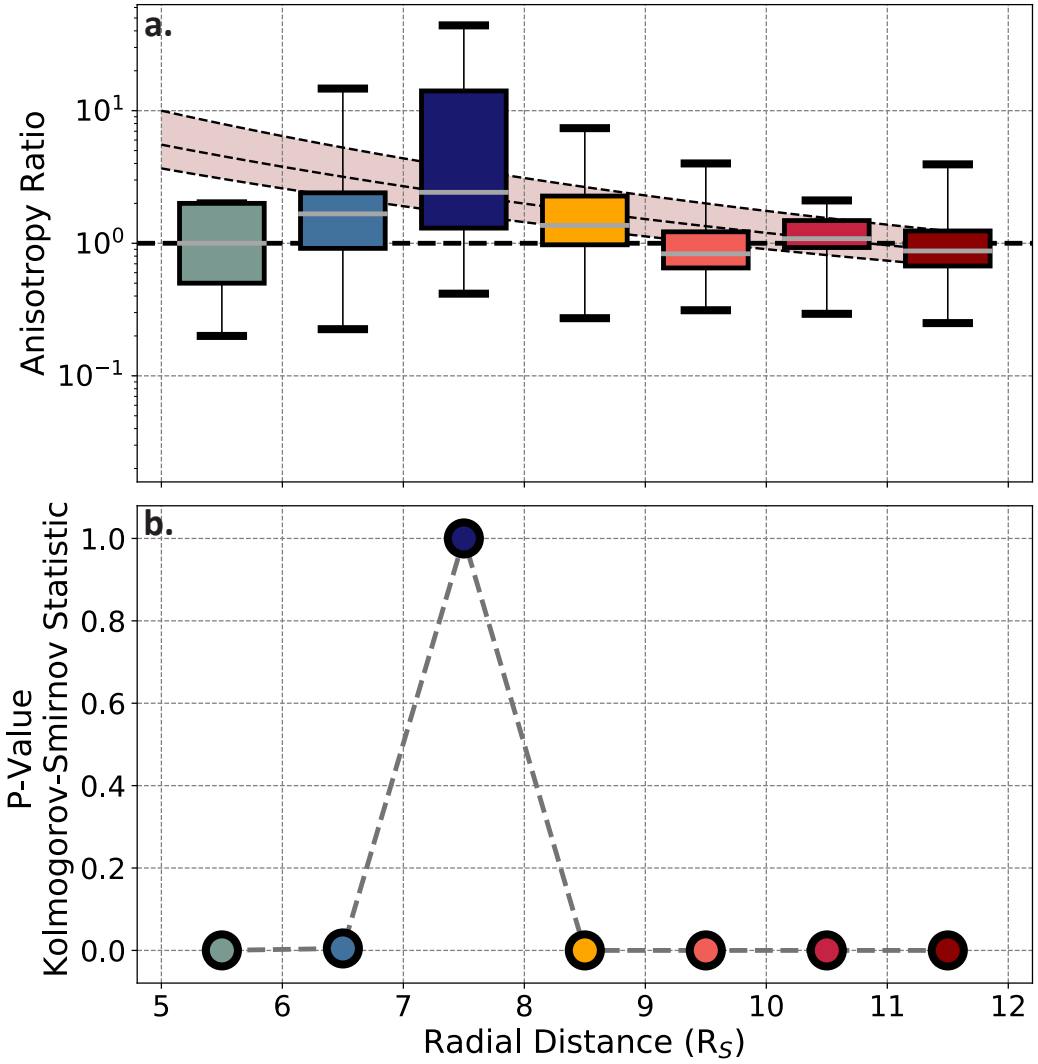

Figure 4.3: Anisotropy ratios between 47 – 71 keV of interchange and comparison to adiabatically conserved betatron acceleration. Panel a demonstrates the box-whisker distributions of anisotropy values of identified events, superimposed upon an evaluation of expected adiabatically conserved betatron acceleration in pale red. The boxes contain the interquartile range between quantiles 0.25 and 0.75, and the whiskers denote the maximum and minimum of the data. Panel b presents the p-values of the 2 sample Kolmogorov-Smirnov statistic calculating the likelihoods of a similar distribution to 7–8 R_S.

4.3.2 System Wide Dynamics of High Energy Hydrogen Ions

Interchange injections are a major form of transport of energetic material in the middle magnetosphere of Saturn and are a leading process for delivering the bulk of energetic (keV) electrons into the inner regions of Saturn's magnetosphere (Thomsen, 2013; Thomsen et al., 2016). Interchange events are highly dynamic with some Cassini orbits observing multiple events, and others with very little interchange activity. Interchange has been observed to deliver energetic electrons to differing distances in time periods of 10 hours or less ranging between from 4.7 – 8.4 R_S (Thomsen et al., 2016). For electrons, Thomsen et al. (2016) then found that this variable range and delivery is co-observed with global observations of energetic electrons, thereby supporting interchange as the primary source of this population. Energetic ions are expected to be similarly delivered to the inner regions of Saturn's magnetosphere by interchange events. The anisotropy observed in Section 4.3.1 for a single energy range of the CHEMS sensor is expected to be delivering a highly anisotropic population into these regions. Betatron acceleration is expected to act on all energy ranges, but as observed above there is a significant divergence from expected betatron acceleration inside of 7 R_S. How do interchange events display over all energy ranges? Similarly, what is their impact on the global dynamics and population? As discussed above, we examined one energy range with the greatly simplified model of conserving only the first adiabatic invariant and assuming an isotropic starting population. We now move toward a more accurate evaluation of the complete energy-radial space. Within this section we move beyond a single energy range to evaluate the global impact of interchange on the high-energy ion distributions.

The entire energy range of interchange injection anisotropy is shown in Figure 4.4. The three panels of Figure 4.4 represent the 25^{th}, 50^{th}, and 75^{th} quantiles, the same as the colored boxed in Figure 4.3 but over all energy and radial values. In this plot white designated isotropic, purple perpendicular, and orange parallel/anti-parallel. Grey designates missing values (no data). Figure 4.4b, the median values, or the 50^{th} quantile, shows a distinct non-perpendicular to perpendicular trend moving from lower right to upper left. The dashed lines represent the energy value of an ion starting at 12 R_S at 5 or 47 keV and moving inwards undergoing betatron acceleration. These curves will be used in future work to re-evaluate the effect of betatron acceleration in the previous figures. They are provided on this plot to guide the eye diagonally on reading these figures. Following along these expected paths, betatron acceleration would move a source population into increasingly perpendicular distributions. This would have the effect of a diagonally orange to purple represen-

tation in Figure 4.4b. However, similar to that seen in Figure 4.3, inside of 7 R_S, the highest energies return to a more isotropic (white) distribution, but more remarkably the lower populations trend to a non-perpendicular (orange) distribution. This was observed in Figure 4.3 and points to processes in the inner magnetosphere that are competing with the betatron acceleration expected from inward drifts. Figures 4.4a and 4.4c present the IQR of the anisotropies for interchange events. These panels provide additional information on the range and distribution of the observed median effects. The intense perpendicular population between 7 – 9 R_S is even more clearly observed in the 75^{th} quantile, with a still noticeable effect of the lower energy, non-perpendicular population in the lower left (inside of 7 R_S, and under 10 keV). Meanwhile the 25^{th} quantile shows a non-perpendicular population as to be expected. Figure 4.4 represents the material injected toward the planet from interchange. We move to now comparing this transient population to the global background.

Figure 4.5 shows, in similar style to Figure 4.4, the distribution of the entirety of the non-interchange equatorial CHEMS dataset. Figure 4.5 and Figure 4.4 are exclusive, in that the 816 interchange events are not included in Figure 4.5. At first glance these distributions are strikingly different from Figure 4.4. Again, remembering that white represents isotropic, the median shows the nominal behavior of the system is dominantly isotropic. Figure 4.5 can be interpreted as an end state, or a nominal state, of the system. From comparison between Figure 4.4 and 4.5, we can conclude, that non-isotropic particle distributions that come in from injection events are relaxed toward a more isotropic state over time. The biggest change being most evident inside of 9 R_S as 7-9 R_S demonstrates the biggest departure from betatron expectations. Outside of 9 R_S non-perpendicular populations are still prevalent as seen in the injection events themselves at the lowest energies. This mimics the electron pitch angles that have been previously observed to transition from field-aligned to perpendicular near 10 R_S (e.g. Carbary et al., 2011; Clark et al., 2014; DeJong et al., 2010). The original state of field-aligned populations is still a current topic of investigation in Saturn science. Rymer et al. (2008) further demonstrated through modeling comparisons that for thermal electrons from single injection events adiabatic energization was occurring to result in the perpendicular populations and proposed other loss terms, potentially from neutrals. Is a similar situation potentially occurring for the high-energy ions? In comparing the system wide background, the largest observable difference between Figures 4.4 and 4.5 is inside of 7 – 9 R_S. In Figure 4.3 and 4.4, this is the demonstrated location of divergence from expected betatron acceleration.

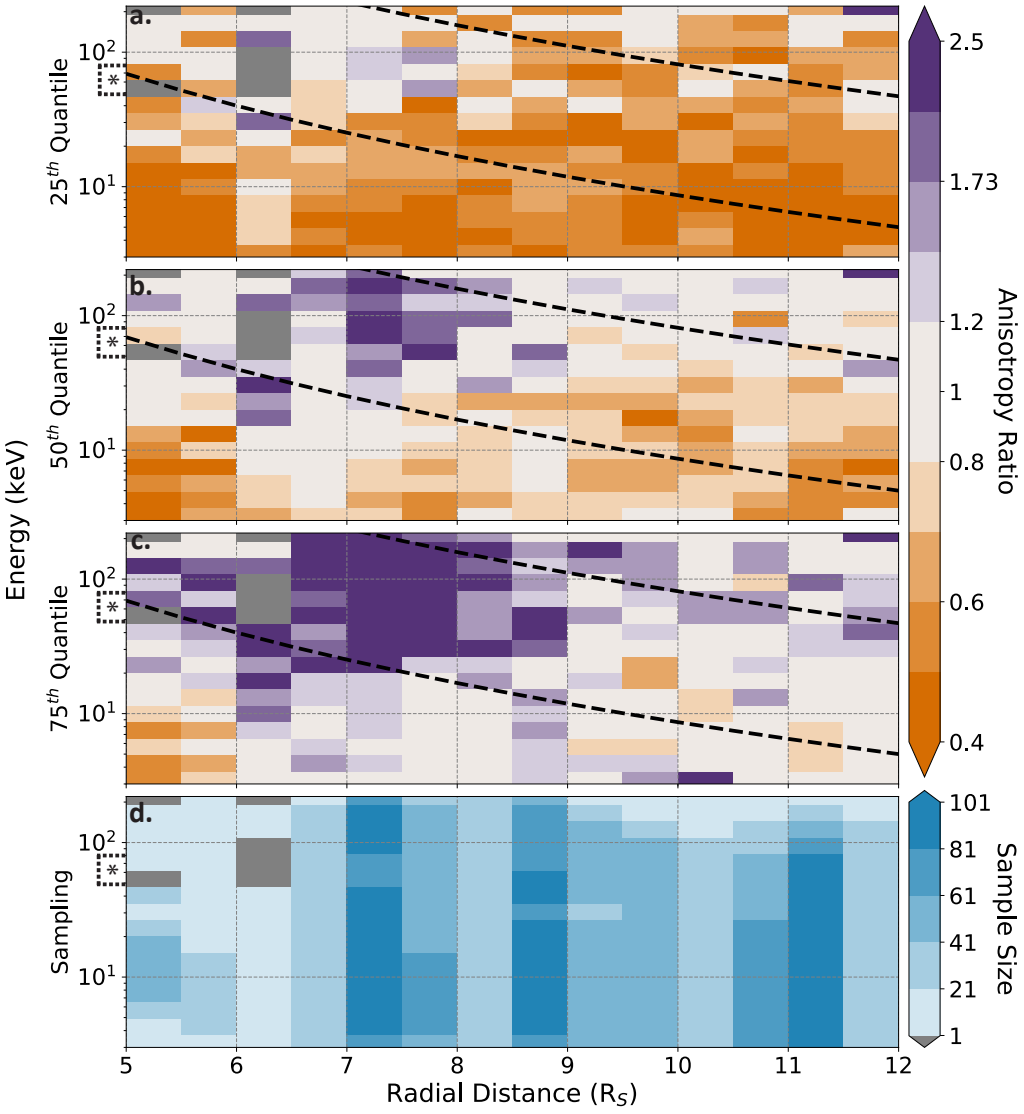

Figure 4.4: Interchange injection anisotropies for 3 - 220 keV ions. The top three panels (a-c) present the interquartile range of all observed interchange injection events presented over the CHEMS sensor energy range between 3 – 220 keV and radial distances between 5 and 12 R_S. The color ranges between orange and purple, representing perpendicular populations at the upmost purple range, and parallel or anti-parallel in the orange range. The black dashed lines in the top three plots represent expected energization curves of betatron acceleration, starting at 12 R_S and 5 or 47 keV. White represents near-isotropic populations, while gray represents a lack of sampling. The lower panel shows the sample size. The energy range starred on the left is 47 – 71 keV as presented in Figure 4.3.

The primary physics altering ion pitch angle distributions in a planetary magnetic environment include a range of processes. These can include effects of particle motion in various magnetic field configurations (e.g. betatron acceleration, wave-particle interactions) and environmental factors (e.g. pitch angle dependent sources and losses) (e.g. Wang et al., 2013). As shown in Figure 4.3, a particle motion specific effect, betatron acceleration, accounts for the observed anisotropy of ion populations from 12 to 7 R_S. However, inside of 7 R_S for the injection events, another process must be present because betatron no longer represents the correct anisotropy of the population. Inside of 7 R_S on the global scale also shows a markedly isotropic population, distinct from the injection events. This suggests that a competing process has influenced the injection events inside of 7 R_S and that globally, long after injection, the particles undergo additional pitch angle dependent processes. We next examine three potentially important effects influencing ions within the inner region of the magnetosphere: electro-magnetic ion cyclotron waves (EMIC), Coulomb collisions, and charge exchange.

4.3.3 Estimations of Particle Loss Processes Within the Inner Magnetosphere

4.3.3.1 EMIC Waves

EMIC waves are a commonly found plasma wave in magnetospheres and are a primary physical process to couple different aspects of a magnetospheric system together (see review by Borovsky & Valdivia, 2018). At Earth, EMIC waves have been associated with various processes and locations even in the outer magnetosphere at non-equatorial high latitudes (e.g. Allen et al., 2016; Vines et al., 2019). EMIC waves are generated from the instability of anisotropic hot population of ions (10-100 keV) and have been theoretically demonstrated to be more unstable in the presence of cold plasma and thus at Earth has been of interest related to plasmapause dynamics (e.g. Bashir & Ilie, 2018; de Soria-Santacruz et al., 2013; Kennel & Petschek, 1966; Tetrick et al., 2017). At Earth expected diffusion times for certain pitch angles and local times can reach <1 hour, or on the timescale of interchange injections to traverse 1 R_S (Kozyra et al., 1997). At Saturn, a plasmapause-like boundary is identified as the transition from cool dense plasma from the inner Enceladus dominated region to a tenuous hot plasma population from tail reconnection processes typically at 10 R_S (e.g. Thomsen et al., 2015; Thomsen & Coates, 2019). On this transition interchange is often associated, and the inherent instability assumed to be accentuated due to the

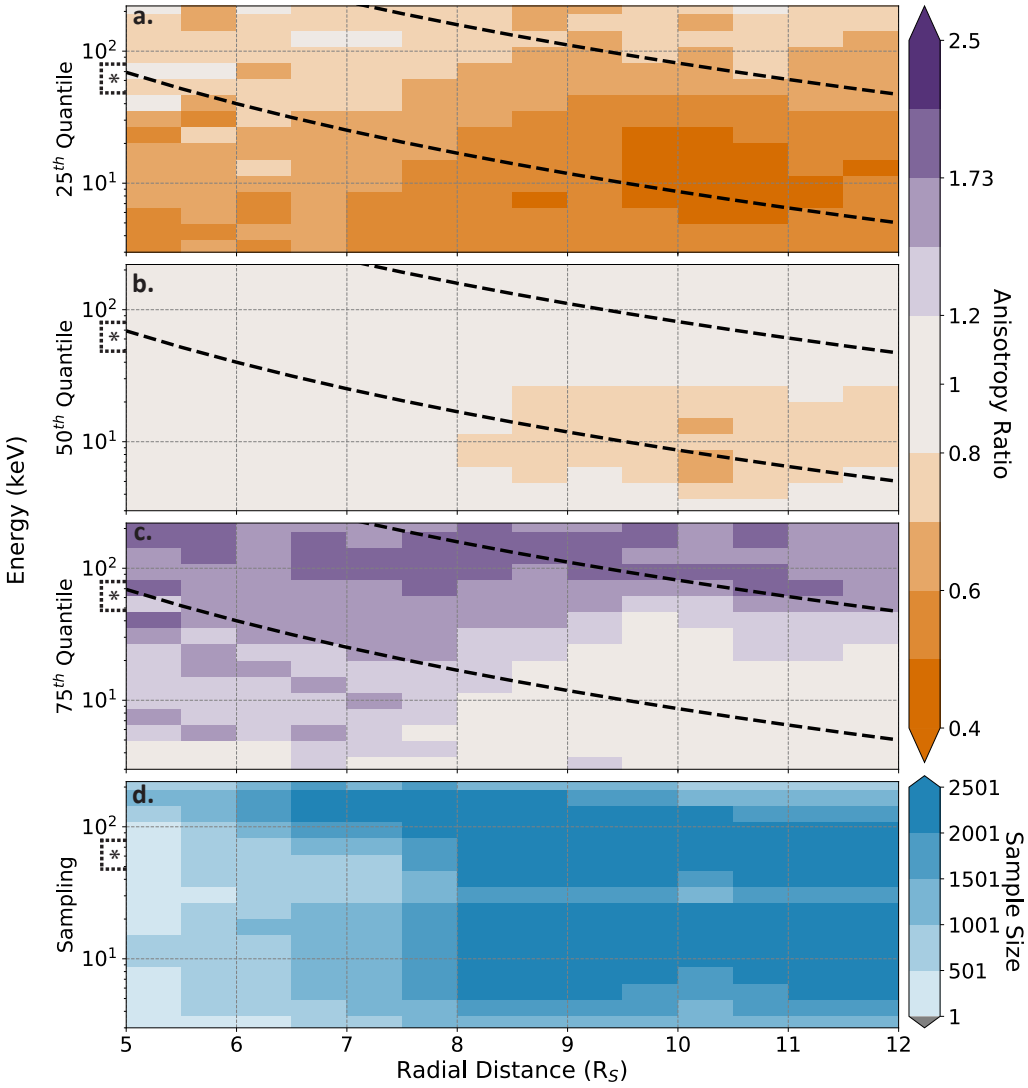

Figure 4.5: System wide background anisotropies for 3 - 220 keV ions. In similar style of Figure 4.4, this figure presents all of the CHEMS data of the Cassini mission near the equatorial plan (within ±10 degrees of the equatorial plane). The top three panels (a-c) present the interquartile range of all observed non-interchange over the CHEMS sensor energy range between 3 – 220 keV and radial distances between 5 and 12 R_S. The color ranges between orange and purple, representing perpendicular populations at the upmost purple range, and parallel or anti-parallel in the orange range. The black dashed lines in the top three plots represent expected energization curves of betatron acceleration, starting at 12 R_S and 5 or 47 keV. White represents near-isotropic populations, while gray represents a lack of sampling. The lower panel shows the sample size. The energy range starred on the left is 47 – 71 keV as presented in Figure 4.3.

steep gradient of the plasma population and relation to large scale or reconnection driven injections (Thomsen et al., 2015; Mitchell et al., 2015; Thomsen & Coates, 2019; Azari, Jia, et al., 2019). Young injection events themselves are associated with wave modes (Kennelly et al., 2013; Kumari et al., 2018). EMIC waves have been observed at Saturn with all missions which passed through the equatorial plane (Leisner et al., 2011), including Pioneer 11 and Voyager (e.g. Barbosa, 1993; E. J. Smith & Tsurutani, 1983). Within the equatorial region waves peak close to the planet at 4 R_S and decrease at larger distances, following a hyperbolic tangent out to 9 R_S (Meeks et al., 2016). The prevalence of interchange transporting highly perpendicular hot ions into cold and dense plasma could potentially trigger additional occurrence of EMIC waves in this region. As they do at Earth (e.g. Williams & Lyons, 1974), EMIC waves would have a pitch angle scattering effect on the perpendicularly peaked populations observed in Figure 4.4, and would lead to a more isotopic population and therefore to the observed global population in Figure 4.5. Interchange injections, we propose, could both be triggering EMIC waves, as well as undergoing scattering due to disturbing the background plasma populations. Further investigation into this potential and comparisons with former observations from the magnetic field and wave data is warranted. EMIC waves do not satisfactorily explain the prevalence of the field-aligned populations, or beyond isotropic, seen at lower energies in the injection anisotropy statistics.

4.3.3.2 Coulomb Collisions

Saturn's primary plasma component in the inner magnetosphere is cold dense thermal plasma, primarily of the water group (W^+) ions consisting of O^+, OH^+, H_2O^+, and H_3O^+ (Wilson et al., 2017). W^+ ions are the most prevalent species in the equatorial region around Saturn as compared to other major species of H^+ and H_2^+, before dropping to near unity between 17 and 20 R_S (Thomsen et al., 2010; Wilson et al., 2017). This thermal plasma controls the particle pressure distribution until 8 – 12 $_S$ where it is then controlled by hot ions (Sergis et al., 2017). However, these ion species are outnumbered by neutrals 12 to 1 (Bagenal & Delamere, 2011). Ions are sourced from the moon Enceladus deep within the magnetosphere at 4 R_S through a combination of impact ionization, charge-exchange, and transport (Cassidy & Johnson, 2010; Fleshman et al., 2013; Jurac & Richardson, 2005). Inside of 7 R_S chemical processes dominate as compared to transport. This forms the observed distribution of ions with observations of the plasmapause-like region extending to near 10 R_S on the dayside (Fleshman et al., 2013; Thomsen & Coates, 2019). Interchange

events carrying energetic ions are transported into an extremely dense plasma and cold neutral population as sourced from Enceladus.

This has two potential primary effects, first is the aforementioned EMIC waves, and second is the interaction of the hot ions with the neutrals and the thermal ions through collisions and charge exchange. Coulomb collisions pitch angle scatter anisotropic ion populations as they rapidly encounter the cold thermal plasma population. This is similar to the ring current interactions with the plasmasphere at Earth. At Earth, Coulomb collisions are important for the loss of particles below few tens of keV as compared to charge exchange (Fok et al., 1991). Charge exchange calculations at Earth are potentially under-constrained. Earth's neutral contribution to its near space environment under geomagnetic storm conditions is currently uncertain (e.g. Ilie et al., 2013; Krall et al., 2018; Østgaard et al., 2003). Given that Saturn has an additional source of neutrals charge-exchange losses may exceed other effects of the thermal population such as scattering from Coulomb collisions. Below we calculate the lifetimes for potential Coulomb collisions, as well as for charge exchange for Saturn's middle magnetosphere.

In plasma, particles can transfer energy through a series of interactions with particle-sourced electric fields, a process termed Coulomb collisions. After a Coulomb collision, particles will shift their trajectories and their pitch angles. Many collisions over a significant amount of time have the effect of isotropizing distributions and spreading particles into atmospheric loss cones. Coulomb collisions can transfer energy throughout a magnetosphere from plasma populations and at Saturn, equilibrate temperatures between ion and electrons (Rymer et al., 2007; Cravens et al., 2011). To estimate Coulomb processes for an interchanging hydrogen ion at 5 R_S we compare to a thermal electron, and a thermal higher mass ion. The first equation below is for an energetic ion interacting with the thermal electron (τ_{ei}, equation 4.8). The second is for interacting with a thermal high mass ion most similar to the water group constituents in this region (τ_{hw}), equation 4.9. In the second equation, the subscripts h and w represent the interacting species in question (H^+, W^+).

$$\tau_{ei} = \left(54.5 \frac{n_i Z_i^2}{T_e^{3/2}}\right)^{-1} \tag{4.8}$$

$$\tau_{hw} = \left(B_{hw} \frac{n_w}{T_w^{3/2}}\right)^{-1} \tag{4.9}$$

The numerical forms provided in equation 4.8 and 4.9 are from Schunk & Nagy (2009), in which these are derived by assuming a Coulomb logarithm value of 15. We

use a thermal O^+ as the hypothetical water group ion for collision as it's the closest species with a provided reaction rate. Future estimations for characteristic constants for the interaction rates for species more commonly found in Saturn's environment would assist in these interaction calculations as the most appropriate evaluations, as those used here, are by comparing to ionospheric analogs.

In equation 4.8, n_i represents the density of the ion species, in this case the high energy H^+ representing an incoming injection. We use an estimate from the calculations of partial densities from Allen et al. (2018) of 10^{-3} cm^{-3} for the energetic H^+. Z_i is the ion charge number, T_e is the electron temperature for the thermal cold plasma. Electron temperatures vary at Saturn near 5 R_S, but often are within the single (1-10) eV range (see Krupp et al., 2018, and relevant citations within). For an electron temperature value of 4 eV τ_{ei} is just over 2000 days at 5 R_S.

In equation 4.9, n_w represents the density of the water group species, and T_w the temperature. From the CAPS data over the course of the Cassini mission, Wilson et al. (2017) derived a W^+ composite density of 25 cm^{-3}, a perpendicular temperature of 93 eV, and a parallel temperature of 34 eV at 5 R_S. From Schunk & Nagy (2009) B_{hw} is 0.077 for a hydrogen and O^+ population. If we use purely the parallel temperature value, being generous, this results in a τ_{hw} approaching 1500 days. Both of these lifetimes mean that Coulomb collisions will not be a significant loss process for high-energy ions.

These calculations provide a scale of expectation for Coulomb collisions. The above equations assume a Maxwellian distributed plasma and do not fully represent the complex interactions between the non-Maxwellian interchange plasma and the multi-species nature of the thermal plasma. As a time scale estimate they provide insight. To calculate the full potential loss from Coulomb collisions a full treatment accounting for the non-Maxwellian nature of the incoming plasma along with the potential effects on the pitch angles of the plasmas, should be undertaken through physical modeling. Given these estimates energetic ions from interchange injections will not be lost through Coulomb collisions before undergoing other processes such as EMIC waves, or charge-exchange.

4.3.3.3 Charge Exchange

Charge exchange occurs when an interacting neutral donates an electron to an ion. For interchange this would result in low-energy ion and a now neutral high-energy hydrogen atom. Due to the high density of neutrals within the equatorial plane, charge-exchange will be most extreme on ions spending time within this region, or

perpendicular pitch angle distributions. Armstrong et al. (2009) observed with the MIMI Low Energy Magnetospheric Measurement System (LEMMS) instrument that below 5 MeV, proton pitch angle distributions are on average isotropic or depleted near perpendicular pitch angles, particularly at the lowest energies observed. This was proposed to be due to a combination of Coulomb scattering and charge exchange with the neutral gas. For the MeV particle range, charge exchange cross sections are particularly small, and charge exchange has not been invoked as a significant loss process for the radiation belt with exception to double (subsequent) charge exchange (e.g. Roussos et al., 2011; Paranicas et al., 2008). At lower keV energies charge exchange is expected to be a significant loss process (e.g. Kollmann et al., 2011, 2013). Enceladus' sourced neutral cloud and extended neutral environment has been imaged through the MIMI Ion Neutral Camera (INCA) instrument, and in conjunction with other observations from Cassini, has constrained the primary species to H_2O, OH, H, and O (e.g. Dialynas et al., 2013; Esposito et al., 2005; Perry et al., 2010; Waite Jr. et al., 2006). Building on these observations, subsequent observational and modeling efforts have been developed to derive the neutral densities present in the inner magnetosphere over a range of radial distances (e.g. Cassidy & Johnson, 2010; Hartogh et al., 2011; "The distribution of atomic hydrogen and oxygen in the magnetosphere of Saturn", 2009). Previous works reviewing the role of charge exchange in the Saturn system have focused on the thermal population of the Enceladus torus and tend to not extend into the energy range of interest in this work (e.g. Fleshman et al., 2013; Tadokoro et al., 2012; Holmberg et al., 2016). We estimate the charge exchange lifetimes for an energetic hydrogen ion of similar energy range for the CHEMS sensor, against the neutral background surrounding Saturn.

Charge exchange lifetimes for various reactions can be represented as seen in equation 4.10 below, in which n is the neutral density, v the relative velocity, and σ the species and energy dependent cross section of the reaction (F. F. Chen, 1974).

$$\tau_{ce} = \frac{1}{n\sigma v} \tag{4.10}$$

We focus on energetic H^+ charge exchange with primary neutral constituents of H, H_2O, and O sourced from Enceladus through the following reactions presented in equations 4.11 - 4.13. OH is additionally an important constituent, but due to limitations of measurements of cross section for energetic H^+ we focus on the aforementioned three components and their potential effect on injections. For comparison, the expected density of OH is most comparable to H, but less dense that H_2O as estimated in Fleshman et al. (2013).

$$H_2O + H^+ \rightarrow H_2O^+ + H \tag{4.11}$$

$$O + H^+ \rightarrow O^+ + H \tag{4.12}$$

$$H + H^+ \rightarrow H^+ + H \tag{4.13}$$

We estimate n_H from the analytic radial profile presented in Fleshman et al. (2013) based on previous work in Fleshman et al. (2012). Estimations of n_{H_2O} and n_O are obtained from (Fleshman et al., 2013) which are based on previous works in (Cassidy & Johnson, 2010) and (Fleshman et al., 2012). The velocities in lifetime calculations are taken to be the kinetic velocity of the energetic H^+. Cross sections (σ) depend on the species of the interacting particles, as well as the energy. We use cross section fits as calculated within Lindsay & Stebbings (2005) for σ_{O,H^+} and σ_{H,H^+}. The σ_{O,H^+} fit is only valid under 100 keV; we present the lower energy range for this calculation. We use the calculation in Rudd et al. (1985) for cross sections for σ_{H_2O,H^+}. The work by Rudd et al., has been expanded on in several works (Gobet et al., 2001, 2004; Lindsay et al., 1997). These calculations are primarily limited by the estimations of neutral densities as these are based off modeling outputs. However, estimating these quantities provides first look insights into the potential contributions of losses due to this important physical process at Saturn. Future efforts should undertake representing and capturing the non-Maxwellian behavior of these high-energy ions more extensively.

In Figure 4.6 we present estimations of charge-exchange lifetimes for the primary population in incoming interchange injections. The contribution of charge exchange to the loss of energetic H^+ can be attributed to interactions with the neutral H_2O as compared to O and H. The charge exchange lifetimes of this H^+ to H_2O become an important loss process by 6 - 7 R_S where lifetimes pass under 10 hours and by 4 - 5 R_S are <1 hour. Figure 4.6's radial dependence in the charge exchange will lead to a radially dependent loss process greatly affecting inside of 7 R_S. Charge exchange presents the most dominant loss mechanism as compared to other candidates including Coulomb collisions to affect incoming energetic H^+. EMIC waves, while only examined qualitatively, are expected to alter particle populations to near-isotropy, and can explain the overall isotropic background of the plasma population in Figure 4.5 and losses first observed inside of 7 R_S in Figure 4.3. EMIC waves are likely acting due to the accentuated perpendicular populations within injections and scattering the

particles into the atmospheric loss cone, but they are not expected to change pitch angle distributions into a field-aligned configuration.

At the lowest energy levels of CHEMS within the interchange events inside of 7 R_S field-aligned populations are found, this cannot be explained with EMIC waves. Coulomb collisions lifetimes are greatly in excess of a single Saturn rotational rate, and in comparison to charge exchange lifetimes are expected to be less critical in removing transient high energy H^+. Charge exchange lifetimes as discussed within the 4 - 7 R_S region quickly approach hours to sub-hours. This is well within the same time regime as a single co-rotational drift period around Saturn. The incoming speed of an injection discussed in Section 4.2.2 provides a travel time over 1 R_S within the tens of minutes range with total travel time estimates from Paranicas et al. (2016) in the hours range. Charge exchange lifetime estimations quickly approach estimations for characteristic time scales of fresh injections within 7 R_S. Charge exchange at Saturn is expected to affect perpendicular populations most drastically as compared to field-aligned particles. The primary location of dense neutrals will be in the equatorial region due to Saturn's fast rotation rate. Perpendicular populations will spend more time, compared to field-aligned pitch angle particles, in the equatorial region due to the particle motion (bounce motion) within a dipolar field. Strongly perpendicular populations will potentially cause excitation of EMIC waves as discussed above, but also be lost preferentially inside of 7 R_S. Charge exchange can result in the observed distributions and act on short enough timescales to affect incoming injections.

Through large-scale statistical review of the pitch angle distributions and loss processes at Saturn, charge exchange along with betatron acceleration offers a potential explanation to long standing observations of temperature extremes at 7 – 8 R_S first noted with Pioneer 11 (Frank et al., 1980). Future work deriving the full EMIC wave conditions in comparison to charge exchange would be beneficial both at Saturn, and other planetary bodies, as we have demonstrated the surprising potential for quick losses due to heavy neutral-plasma interactions.

4.4 Conclusion

The magnetosphere around Saturn presents an opportune region to study the complex interaction of plasma transport and neutral populations as a directly observable solar system object. In-situ studies of particle populations complement our broader understanding of planetary formation and evolution. Saturn's fast rotating region of neutral-plasma interaction can be considered as near to an analog as pos-

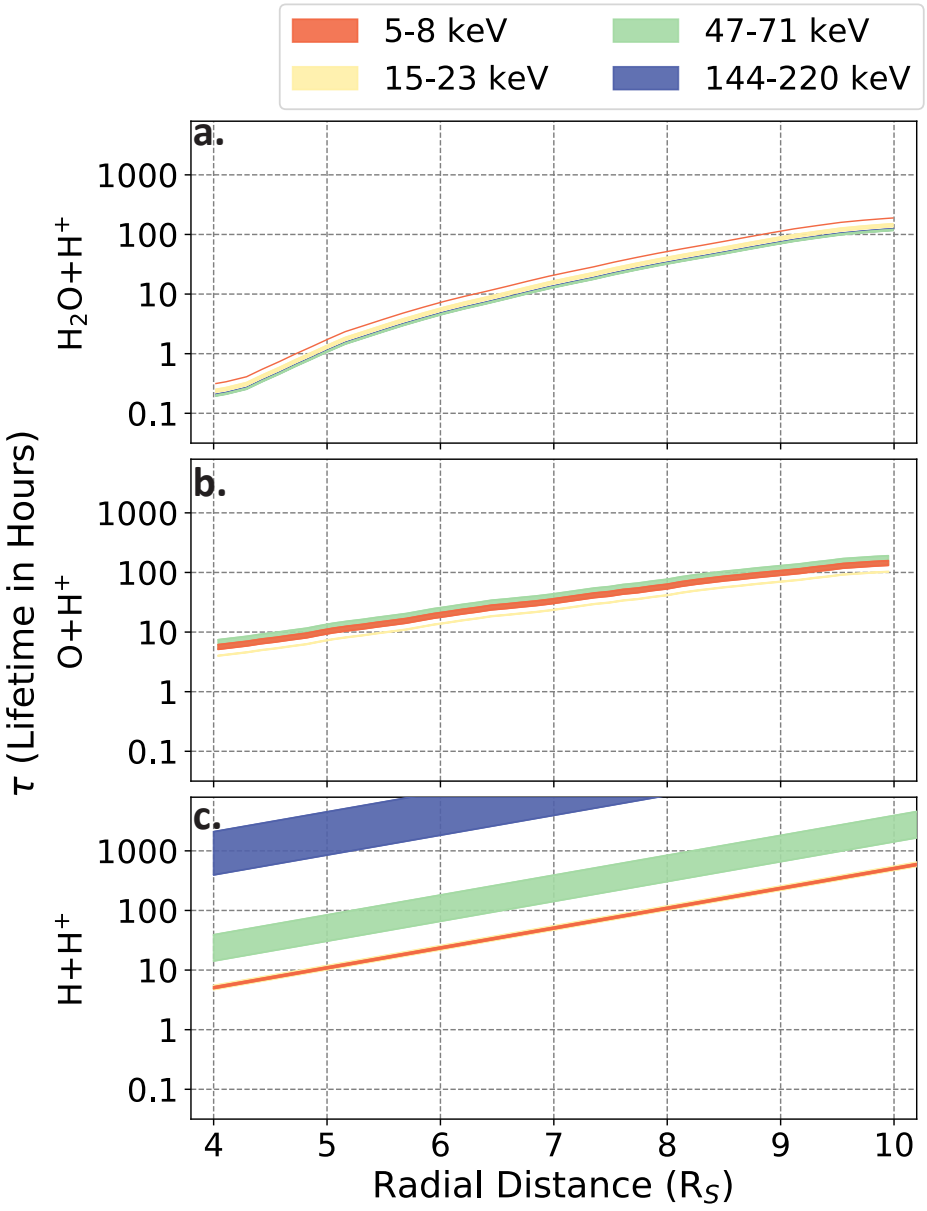

Figure 4.6: Charge exchange rates for incoming keV ions with dense neutral populations at Saturn. The three panels (a-c) present the expected lifetimes (τ) as a function of radial distance. The colors represent four energy ranges over the CHEMS sensor energy range. These are the same energies as presented in Figures 4.2 and 4.3.

sible of active planet formation. Within this work we presented the first large-scale statistical investigation of how interchange injections at Saturn are energized as well as lost. Until now, research at Saturn has not focused on the high-energy components of mass transport on a statistical level, which provide the unique signature of interchange injections, a Rayleigh-Taylor like instability at Saturn.

This work showed potential that betatron acceleration is the primary process resulting in the energization of interchange-associated ions in the keV energy range. This work has a planned extension toward a more accurate evaluation of betatron acceleration by taking into account different energy dependent starting distributions at 11 - 12 R_S and following along an expected adiabatic invariant through energy-distance space. The current presented work shows through the observation of perpendicular peaked populations, which follow the expected energization curves of betatron acceleration. Several interchange events did result in energization above the betatron acceleration modeled within this work. We propose this excess energization is associated with additional processes such as non-adiabatic energization from previous current sheet collapse events. This supports viewing interchange as a complex instability, sensitive to both internal and external effects. The field would benefit from additional modeling and parameter studies investigating the potential impacts of variable injections on Saturn's inner magnetospheric populations.

Energization of interchange potentially due to betatron acceleration competes with particle losses and scattering. We have found that inside of 7 R_S, losses overtake the enhancement of perpendicular flux. Of the leading loss processes that could result in this depletion, charge-exchange is considered most likely, in particular with water group neutrals from Saturn's moon Enceladus. Charge exchange lifetimes for energetic H^+ in particular decrease to under a single Saturn's rotational period within 7 R_S. They are fully capable of explaining the field-aligned pitch angle distributions observed at these radial distances. EMIC waves might also be scattering particles into the atmospheric loss cone, but they are expected to change the pitch angle distribution only as far as isotropy, not into a field-aligned configuration. It is concluded that while both EMIC waves and charge exchange may modulate the pitch angle distribution of the population, charge exchange is the most likely candidate contributing to the observed field aligned pitch angle distribution inside of 7 R_S. Future work investigating the role of EMIC waves during interchange events would be beneficial and inform current research at other planetary bodies. Through large-scale statistical review of pitch angle information, we have found that interchange plays a key role in resolving observations of energetic populations in the middle magnetosphere

of Saturn from Pioneer 11, Voyager, and now Cassini.

This creates a refined picture of mass transport at Saturn and explains previous observations. Interchange injection energization is clearly betatron as shown within this work. This results in a population of perpendicular energetic H^+ at 7-8 R_S. This finding allows constraints on our understanding of mass transport around Saturn and other interchange unstable planetary magnetospheres. We propose that additional energization could be due to previous injections, suggesting a tantalizing similarity to multi-energization phenomena at Earth and other externally driven systems. Saturn's energized populations are lost over longer time-scales, resulting in a near-isotropic background. We have found that the neutral background has extensive influence on the system-wide transport of Saturn, greatly limiting energization of particles around the planet.

As exoplanet characterization continues, findings are pointing toward complex plasma and neutral interactions with recent discoveries of exoplanets with moon-forming disks (Isella et al., 2019), along with estimations of magnetic fields (Cauley et al., 2019). From the present work it is predicted that neutral-plasma interactions will play a major role in shaping mass transport around these other planetary bodies. Future investigations into planetary environments should consider the roles of neutrals and look toward characterization studies of Saturn's neutral-plasma interactions as a valuable case for comparison and estimation for these interactions.

CHAPTER V

Incorporating Physical Knowledge into Machine Learning for Planetary Space Physics

This chapter addresses a path forward for applications of machine learning to understand complex planetary systems. It builds on the physics-based automated identification of interchange injections and details a comparison to machine learning models. This chapter is submitted to the Machine Learning in Heliophysics special issue in Frontiers in Astronomy and Space Physics (Azari, Lockhart, et al., 2020).

5.1 Introduction

Planetary space physics is a young field for large-scale data collection. At Saturn for example, it was only in 2004 that the first Earth launched object orbited this planet (Cassini) and landed on Titan (Huygens). After arriving Cassini collected data about Saturn and its near-space environment for 13 years, resulting in 635 gigabytes (GB) of scientific data (NASA Jet Propulsion Laboratory, 2017a). To put this into perspective, the Voyager I mission which flew by Saturn in 1980 had onboard $\sim$70 kilobytes (kB) of memory total (NASA Headquarters, 1980). The Cassini mission represents the first large-scale data collection of Saturn. This enabled the field of planetary science to apply large-scale statistics, including machine learning, to the most detailed spatio-temporally resolved dataset of the planet and its environment.

This surge of data is not unique to Saturn science. In planetary science broadly, Mars in 2020 has 8 active missions roving along the surface and orbiting (The Planetary Society, 2020). The Mars Reconnaissance Orbiter alone has already collected over 300 terabytes (TB) of data (NASA Jet Propulsion Laboratory, 2017b). It is expected that upcoming missions will face similar drastic advances in the collection of scientific data. Traditionally planetary science has employed core scientific meth-

ods such as remote observation and theoretical modeling. With the new availability of sampled environments provided by these missions, methods in machine learning offer significant potential advantages. Applying machine learning in planetary space physics differs from other common applications. Cassini's data is characteristic of other planetary and space physics missions like the Magnetospheric Multiscale Mission at Earth and the Juno mission to Jupiter. The plasma and magnetic field data collected by these missions are from orbiting spacecraft. This conflates spatial and temporal phenomena. This is a shared characteristic with the broader field of geoscience which often represents complex systems undergoing significant spatio-temporal changes with limitations on quality and resolution (Karpatne et al., 2019).

The desire to use these data is in order to better understand, or derive fundamental scientific theories. This requires the ability to back out meaning from applications of large-scale statistical methods. Unlike similar missions at Earth, machine learning for space physics data at Saturn has limited direct application to the prediction of space weather. As a result, machine learning applications require highly interpretable and explainable techniques to investigate scientific questions (Ebert-Uphoff et al., 2019). How to improve machine learning generally from an interpretability standpoint is itself an active research area in domain applications of machine learning (e.g. Molnar, 2019). In planetary science it's important to discern the workings of the model and understand the implications and results for physical systems. The two terms of interpretability and explainability have differing definitions within the machine learning community. Within this work we will use these two terms interchangeably to represent gaining scientifically actionable results from implementation of machine learning. The dual challenges of spatio-temporal data and interpretability are compounded for planetary orbiting spacecraft. Complications for orbiting spacecraft can range from rare opportunities for observation, and engineering constraints on spacecraft data transmission. How can machine learning be used within these constraints to answer fundamental scientific questions?

As a potential solution, attention has turned to physics-informed machine learning, of which a primary target has been physics-informed deep learning and discovery of physical concepts (e.g. Raissi et al., 2019; Iten et al., 2020; Ren et al., 2018). Within the space weather prediction community such integration has shown promise in improving the performance of machine learning models (Swiger et al., 2020). These efforts have focused on how to integrate or reveal physical and domain knowledge with machine learning. A long standing interest area is for the discovery of physical laws from machine learning (e.g. Kokar, 1986). For increasing physical understanding,

several fields including biology have argued for an equal value of domain knowledge and machine learning techniques (see discussion within Coveney et al., 2016). These discussions have culminated in several reviews for scientific fields on the integration of machine learning for data rich discovery (e.g. Butler et al., 2018; Bergen et al., 2019). Such merged methods underlie a trade between valuing increasing data and model freedom, or incorporating physical insight and model constraint. In Figure 5.1, we present a diagram for considering physical theory and machine learning within the context of theoretical constraints. The examples at either end of the continuum represent applications of traditional space physics from global theory driven modeling, to space weather and solar flare prediction. The model-adjusted center presented below takes advantage of data, but limits or constrains the application by merging with domain understanding. We argue that working within a model constrained environment can address both the dual aspects of data characteristics and desired use cases.

In the following work, we present comparisons between a range of data sizes and physics incorporation to classify unique plasma transport events around Saturn using the Cassini dataset. As a characteristic data set of space physics and planetary environments, this provides valuable insights toward future implementation of automated detection methods for space physics and machine learning. We focus on three primary guiding axes in this work to address implementations of machine learning. First, we address the performance and accuracy of the application. Second, we consider how to increase explainability of machine learning applications for planetary space physics. Third, we tackle how characteristics of spacecraft data change considerations of machine learning applications. All of these issues are essential to consider in applications of machine learning to planetary and space physics data for scientific interpretation.

To investigate these questions and provide a path toward application of machine learning to planetary space physics datasets, we compare and contrast physics-based and non-physics based machine learning applications. In Section 5.2, we discuss the previous development of a physics-based semi-supervised classification from Azari et al. (2018) for the Saturn system within the context of common characteristics of orbiting spacecraft data. We then provide an outline for general physics-informed machine learning for automated detection with space physics datasets in Section 5.3. Section 5.4 describes the machine learning model set up and datasets that we use to compare and contrast physics-based and non-physics based event detection. Section 5.5 details the implementation of logistic regression and random forest classification models as compared to this physics-based algorithm with the context of physics-

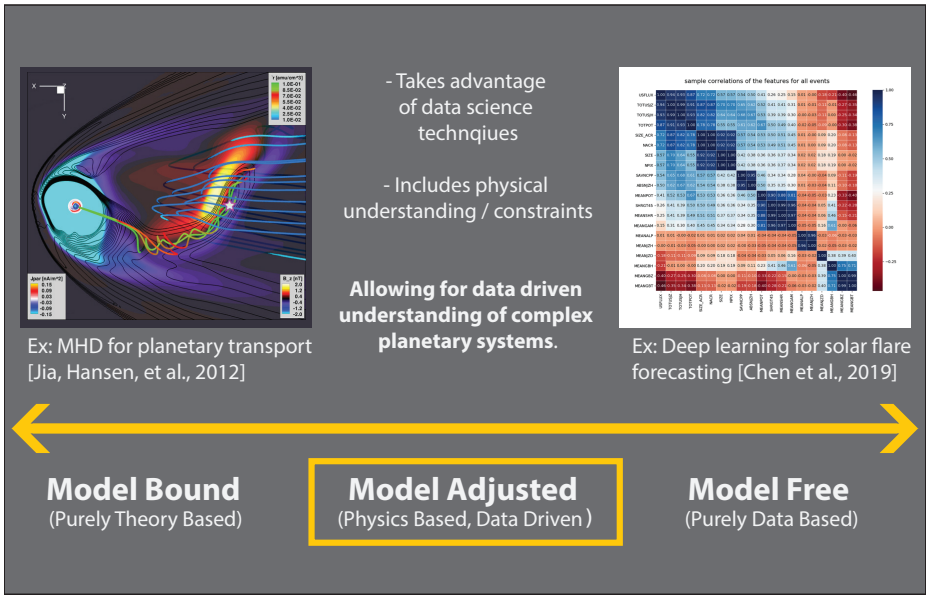

Figure 5.1: Framework for incorporating physical understanding in machine learning. This figure diagrams a continuum moving from purely theory bound, toward model free. The figure in model bound is from Jia, Hansen, et al. (2012), a magnetohydrodynamics simulation of Saturn's magnetosphere. The figure in model free is from Y. Chen et al. (2019), deep learning feature correlations for solar flare precursor identification. This figure contains subfigures from American Geophysical Union (AGU) journals. AGU does not request permission in use for republication in academic works but we do point readers toward the associated AGU works for citation and figures in Jia, Hansen, et al. (2012) and Y. Chen et al. (2019).

informed or model adjusted machine learning. Section 5.6 then concludes with paths forward in applications of machine learning for scientific insight in planetary space physics.

5.2 Background: Saturn's Space Environment and Data

Saturn's near space environment where the magnetic field exerts influence on particles, or magnetosphere, ranges from the planet's upper atmosphere to far from the planet itself. On the dayside the magnetosphere stretches to an average distance of 25 Saturn radii (R_S) with a dynamic range between 17 and 29 R_S (Arridge, André, McAndrews, et al., 2011) (1 R_S = 60,268 km). This distance is dependent on a balance between the internal dynamics of the Saturn system and the Sun's influence from the solar wind. Within this environment a complex system of interaction between a dense disk of neutrals and plasma sourced from a moon of Saturn, Enceladus, interacts with high-energy, less dense plasma from the outer reaches of the magnetosphere (see

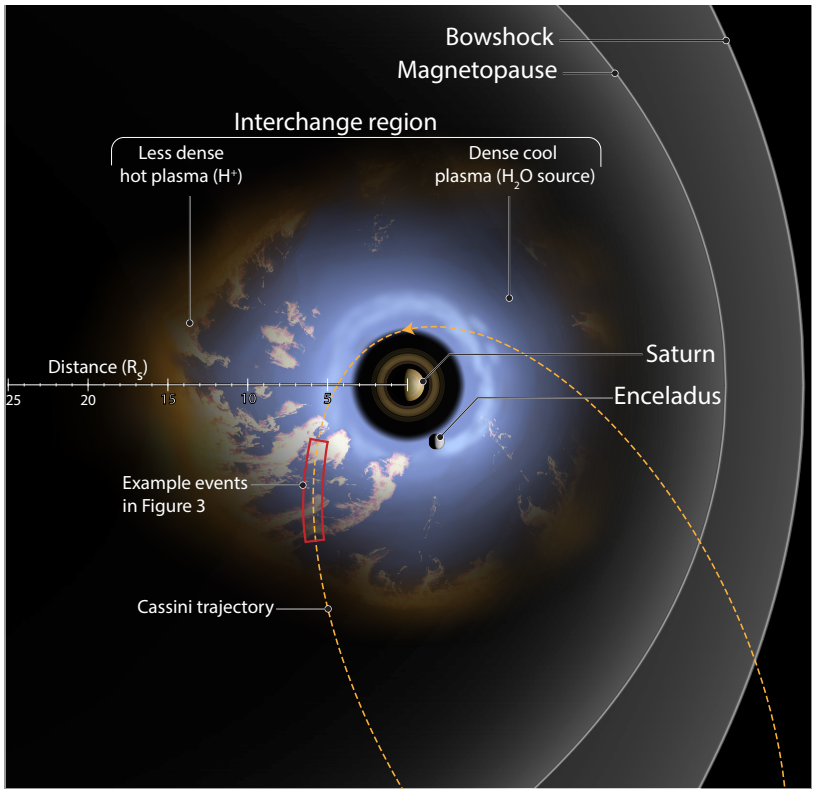

Figure 5.2: Diagram of interchange injection in the Saturn system. The illustrated orbit is an equatorial Cassini orbit from 2005. Injections are denoted by the pale orange material interspersed with the water sourced plasma from Enceladus. Along the example orbit the red box denotes a hypothetical segment of Cassini data discussed in Figure 5.3. The purpose of developing an automated event detection is to identify the pale orange material traveling toward the planet. This figure was created in consultation and with permission from Falconieri Visuals. Copyright held by Falconieri Visuals.

Figure 5.2).

This interaction, called interchange, is most similar to Rayleigh-Taylor instabilities and results in the injection of high-energy plasma toward the planet. In Figure 5.2, a system of interchange is detailed with a characteristic Cassini orbit cutting through the interchanging region. The red box in this figure is presented as an illustrative slice through the type of data obtained to characterize interchange. One of the major questions in magnetospheric studies is how mass, plasma, and magnetic flux moves around planets. At the gas giant planets of Saturn and Jupiter, interchange is thought to be playing a fundamental role in system-wide transport by bringing in energetic material to subsequently form the energetic populations of the inner magnetosphere, and to transport plasma outwards from the moons. Until Cassini, Saturn never had

a spacecraft able to develop large-scale statistical data to study this mass transport system.

The major scientific question surrounding studying these interchange injections is what role these injections are playing in the magnetosphere for transport, energization, and loss of plasma. To answer this question, it's essential to understand where these events are occurring and the dependency of these events on other factors in the system, such as influence from other plasma transport processes and spatio-temporal location. From Cassini's data, several surveys of interchange had been pursued by manual classification, but these surveys disagreed on both the identification of events and resulting conclusions (Kennelly et al., 2013; Lai et al., 2016; Y. Chen & Hill, 2008; Y. Chen et al., 2010; Müller et al., 2010; DeJong et al., 2010). This created a need for a standardized survey which was physically justified to allow for subsequent conclusions and comparisons. In Section 5.2.1 we discuss the Cassini dataset and summarize the previous development of a physics-based detection method in Section 5.2.2. We then provide a generalized framework in the following Section 5.3 for incorporating physical understanding into machine learning with the development of S as an example.

5.2.1 Cassini High-Energy Ion Dataset

Cassini has onboard multiple plasma and wave sensors which are in various ways sensitive to interchange injections. However, none of the previous surveys focused on high-energy ions, which are the primary particle species transported inwards during injections. In Figure 5.3 a series of injections are shown in high-energy (3-220 keV) ions (H^+) and magnetic field datasets. This figure shows three large injections between 0400 and 0600 UTC followed by a smaller injection after 0700 most noticeable in the magnetic field data. The top two panels detail the Cassini Magnetospheric Imaging Instrument: Charge Energy Mass Spectrometer (CHEMS) dataset while the last contains the Cassini magnetometer magnetic field data (Krimigis et al., 2004; Dougherty et al., 2004).

The CHEMS instrument onboard Cassini collected multiple species of ion data and finds the intensity of incoming particles in the keV range of data. This datastream can be thought of as unique energy channels, each with a spacecraft position and time dependence. In Figure 5.3b three unique energy channels are shown from the overall data in the top panel, to illustrate the nature of these high-energy data. This type of spatio-temporal data is often a characteristic of space physics missions.

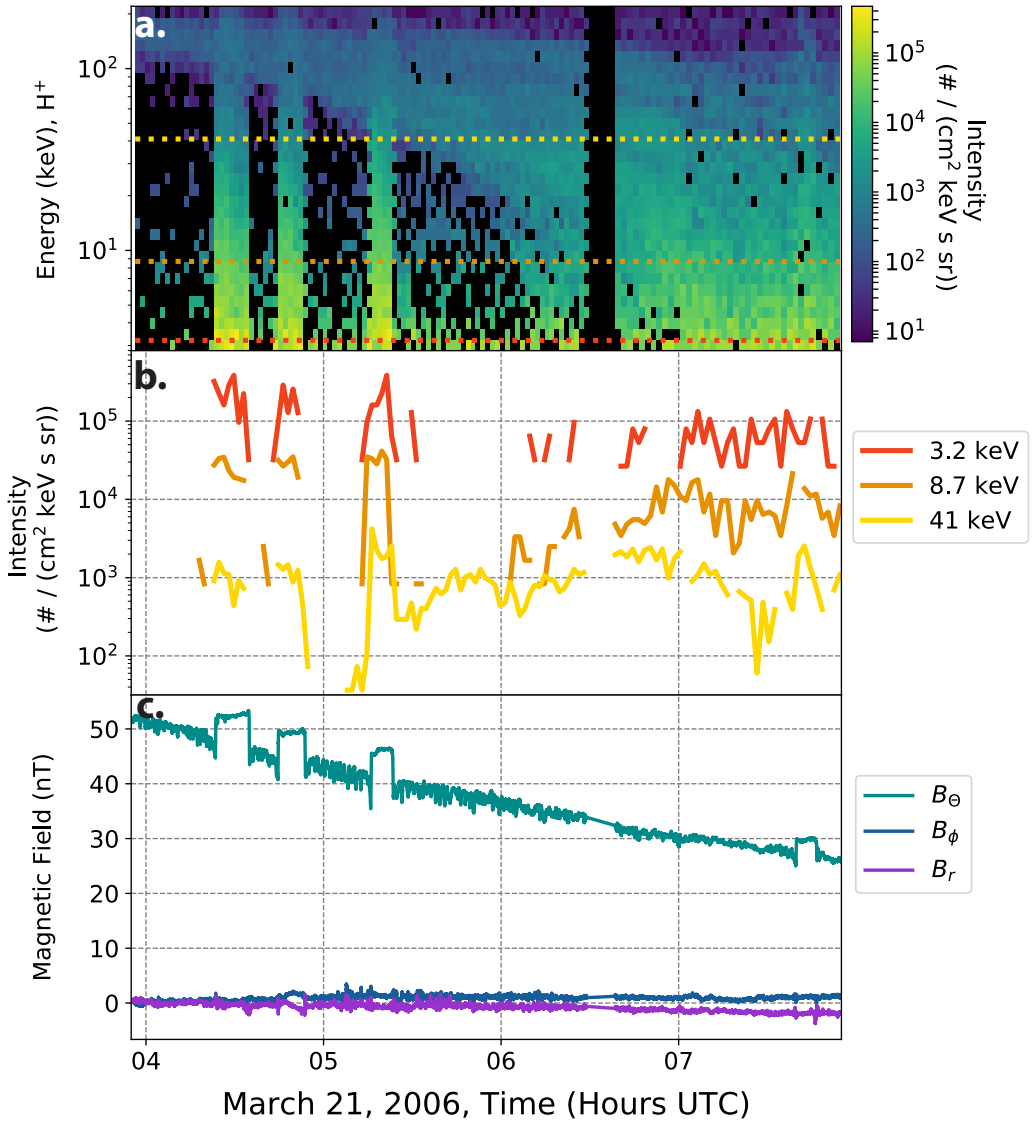

Figure 5.3: Series of interchange injections characterized by high-energy ions. Panel a details a energy time spectrogram of the intensity from the Cassini CHEMS sensor. The three lines are placed at the energy channels for the plot in panel b. Panel b shows the same CHEMS data, but split out into three characteristic energies over the entire CHEMS range. Panel c shows the magnetic field data in KRTP (Kronocentric body-fixed, J2000 spherical coordinates).

5.2.2 Incorporation of Space Physics into Automated Detection

When applying automated or machine learning methods, such data discussed above provides unique challenges and characteristics including: rare events (class imbalances), spatio-temporal sampling, heterogeneity in space and time, extreme high-dimensionality, and missing or uncertain data (Karpatne et al., 2019). These challenges are in addition to desired interpretability. It's essential that an interpretable model is used to learn substantive information about this application. One common use of machine learning is to input many values of interest into a black box model. However, as there are many inputs, and potentially many relationships within the model. A solution to this issue is to reduce dimensionality to fewer inputs. But at the same time, the model needs to be informative, and the inputs need to be meaningful. Incorporating domain knowledge and then letting the model determine their effectiveness in the system of study is a potential framework to consider.

For this reason, when developing a detection method to standardize, characterize, and subsequently build off the detected list, a physics-based method was chosen to address these unique challenges. This previous effort is discussed in Azari et al. (2018) and the resultant dataset is located on the University of Michigan's Deep Blue Data hub (Azari, 2018). We build on this effort in the present work to provide a new evaluation of alternative solutions for data-driven methods.

To develop this physics-based method, the common problems in space physics data described in Karpatne et al. (2019) were considered and addressed to develop a single dimension array (S). S was then used in a style most similar to a single dimensional logistic regression to find the optimum value for detecting interchange events. This classification was standardized in terms of event severity, as well as physically bound in definition of events. As a result, it was able to be used to build up a physical understanding of the high-energy dynamics around Saturn's magnetosphere including: to estimate scale sizes (Azari et al., 2018), demonstrate the influence of tail injections as compared to the ionosphere (Azari, Jia, et al., 2019), and derive the role of interchange in the energization and loss within Saturn's mass transport (Azari, Allen, et al., 2020). Following machine learning practices, S was designed through cross validation. It was created to perform best at detecting events in a training set and then evaluated on a separate test set. The test and training set were developed from 10% of the dataset (representing 7,375/68,090 time samples). The training set was used to optimize the final form of S and thresholds of detection. The test set was used to compare performance and prevent over fitting. The same test and training sets are used in the following sections.

S was developed to provide a single-dimension parameter which separated out the multiple dependencies of energy range and space while dealing with common challenges in space physics and planetary datasets. In mathematical form, S_r can be written as:

$$S_r = \sum_{e=0}^{14} w^{(Z_{e,r}-C)} \tag{5.1}$$

In the above equation, S is found by combining the normalized values of S_r over multiple radial distances between 5 and 12 R_S. The variables w and C represent weighting values and e and r represent energy channel and radial value. $Z_{e,r}$ represents a normalized intensity value observed by CHEMS. S can be thought of as a single number which describes the intensification of particle flux over a normalized background. Additional details on the development of S is described in Section 5.3 as an example of general strategies toward implementing physical knowledge and this equation is provided as a reference.

The final form of S depends non-linearly on the intensity values of the CHEMS sensor and radial distance. In Figure 5.4 we show the dependence of the finalized S value over the test set for the intensity at a single energy value of 8.7 keV and over all radial distances. Within this figure the events in the test set are denoted with dark pink dots. From panel d and e it's evident that S disambiguates events from underlying distributions, for example in panel b. By creating S it was possible to create a single summary statistic which separated events from a background population.

The strategies pursued in developing S are most applicable for semi-supervised event detection with space physics data. They can, however, prove a useful guide in starting to incorporate physical knowledge into other applications in heliophysics and space physics. Within the previous effort we used the model optimization process from machine learning to guide a physics incorporated human effort. This was a solution to incorporating the computational methods employed in machine learning optimization to a human-built model. The end result was optimized in a similar fashion as machine learning models but through manual effort to ensure physical-information preservation. Moving from this effort, we now present a framework for expanding the style of integrating human effort and physical-information into other applications for space physics data.

Below we provide a framework for incorporating physical-understanding into machine learning. In each strategy we discuss common issues in space physics data, using a similar phraseology as Karpatne et al. (2019). In addition to characteristics in the

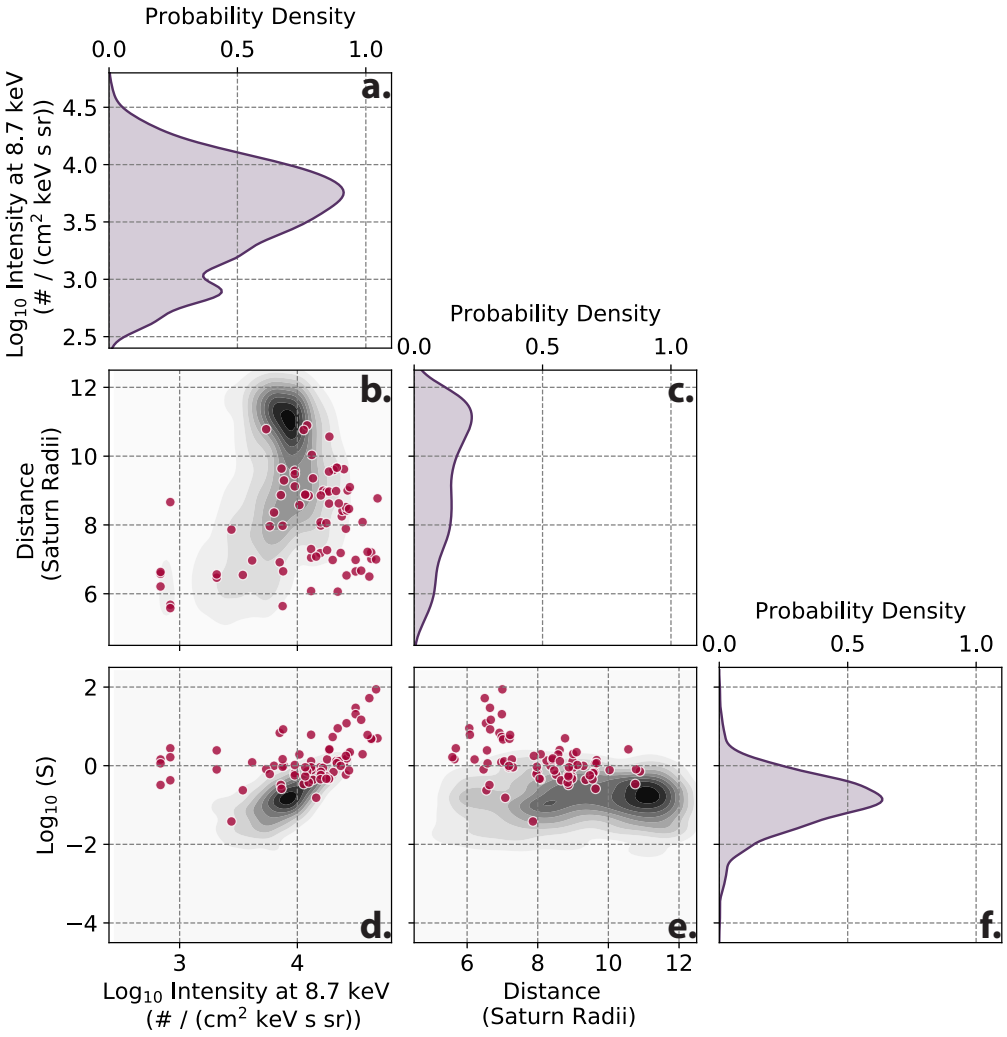

Figure 5.4: Distributions of S parameter developed in (Azari et al., 2018). This figure represents a subset of multiple dependencies of S from a kernel density estimation (kde). The data used in this figure is from the test set of the data. Events in this set are denoted in pink throughout the plot. Panels a, c, and f represent a single dimension kde of a CHEMS energy channel intensity, spacecraft location in radial distance, and of S. Panels b, d, and e represent two dimensional distributions. This figure was developed using the Seaborn statistics package's kde function (Waskom et al., 2020).

structure of geoscience data, we also add interpretability as a necessary condition. For space physics and planetary data, the challenges within Karpatne et al. (2019) are often compounded and where appropriate we note potential overlap. After each strategy, we provide a walk-through of the development of S employed in Azari et al. (2018).

5.3 Framework for Physics Incorporation into Machine Learning

This framework focuses on semi-supervised event detection with space physics data from orbiters for the end goal of scientific analysis. Depending on the problem posed certain solutions could be undesirable. For a similarly detailed discussion on creating a machine learning workflow applied to problems in space weather, see Camporeale (2019). The framework presented here can be thought of as a directed application of feature engineering for space physics problems, mostly for requiring interpretability. In general the strategies below provide a context for careful consideration of the nature of domain application which is essential for applications of machine learning models to gather scientific insights.

1. **Limit to region of interest.** Orbiting missions often range over many environments and limiting focus to regions of interest can assist in automated detection by increasing the likelihood of detection of events.

   Issues: heterogeneity in space and time, rare events (class imbalance)

   Example: The Cassini dataset represents a wide range of sampled environments, the majority of which do not exhibit interchange. In addition, the system itself undergoes seasonal cycles, changing in time, presenting a challenge to any long-ranging spatial or temporal automated detection. The original work targeted a specific radial region between 5 and 12 R_S in the equatorial plane. This region is known to be sensitive to interchange from previous studies. Similarly, each season of Saturn was treated to a separate calculation of S, allowing for potential temporal changes to the detection of interchange.

2. **Careful consideration of training and testing data.** Due to the orbiting nature of spacecraft, ensuring randomness in training and testing data is usually not sufficient to create a representative set of data for both sets across space and time. For event studies, considerations of independence for training and test set

while containing prior and post-event data (at times critical for event identification) are important. This is similar to recent strides in activity recognition studies with spatio-temporal data, in which training set considerations drastically affect the accuracy of activity classification (e.g. Lockhart & Weiss, 2014b,a).

Issues: heterogeneity in space and time, spatio-temporal data, rare events, small sample sizes

Example: While the test and training set represent 10% of the data for the worked example, the 10% was taken such that it covered the widest range of azimuthal and radial values, while still being continuous in time and containing a range of events.

3. **Normalize and/or transform.** Many space environments have a spatio-temporal dependent background. Normalizing separately to spatial or other variables will address these dependencies and can prove advantageous if these are not critical to the problem.

   Issues: heterogeneity in space and time, spatio-temporal sampling, multi-dimensional data

   Example: As seen Figure 5.4b flux values depend on radial distance and energy value. Similarly, flux exhibits log scaling, where values can range over multiple powers of 10 in the span of minutes to hours as seen in Figure 5.3. To handle the wide range of values from the CHEMS sensor, each separate energy channel's intensity was first converted into logarithmic space before then being normalized by subtracting off the mean and dividing by its standard deviation. Effectively, this transforms the range of intensities to a near-normal distribution dependent on radial distance and energy value (see $Z_{e,r}$ in equation 5.1). A similar treatment is performed on creating the final S from S_r. This is important due to the commonality of normalcy assumptions in which models can assume normally distributed data on the same scale across inputs.

4. **Incorporate physical calculations.** Space physics data can come with hundreds if not thousands of features. While many machine learning techniques are designed for just this kind of data, they do not typically yield results that are amenable to human interpretation and scientific insight into the processes of physical systems. They express a complex array of relationships among raw measurements that do little to help humans build theory or understanding. Summary statistics like summing over multiple variables, or taking integrals, can preserve a large amount

of information from the raw data for the algorithm while leaving scientists with smaller sets of relationships between more meaningful variables to interpret. For other fields rich in noisy and incomplete time-series data with a longer history of automated detection methods, summary statistic transformations have been a valuable way of handling this type of data for improved performance (e.g. Lockhart & Weiss, 2014b).

Issues: interpretability, multi-dimensional data, missing data

Example: To address missing values, not only does building up summary statistics help, but by summing over the energy channels intensity, this creates an integral calculation resembling particle pressure. This allows for the lower 14 energy channels to contribute without removing entire timepoints from the calculation where partial data is missing and also increasing interpretability of the end result (see sum in equation 5.1). Only the lower 14 channels are used as the higher energy channels also show long duration background from earlier events drifting in the Saturn environment (see Figure 5.3).

5. **Compare with alternate metrics.** Dependent on your use case, the trade-off costs between false positives and false negatives could be different from the default settings in standard machine learning tools. Investigating alternate metrics of model performance and accuracy are useful toward increasing interpretability.

   Issues: Interpretability, rare events (class imbalance)

   Example: In the training and testing sets only 2.4% of the data exist in an event state. This proves to be challenging for then finding optimum detection due to the amount of false positives and usage for later analysis. In equation 5.1 scaling factors of w and C are introduced. These scale factors are chosen by optimizing for the best performance of the Heidke Skill Score (HSS) (Heidke, 1926). HSS is more commonly used in weather forecasting than in machine learning penalty calculations but has shown potential for handling rare events (see Manzato, 2005, for a discussion of HSS). In Section 5.5 we evaluate how HSS performs as compared to other regularization schemes (final values: $w = 10$, $C = 2$).

6. **Compare definitions of events, consider grounding in physical calculations**. Much of the purpose of developing an automated detection is to standardize event definitions. Developing a list of events then can become tricky.

   Issues: Lack of ground truth, interpretability, rare events (class imbalance)

Example: At this point in the calculation of S, there is a single number, in units of standard deviations, for each time point. This represents, at its most basic, normalized flux intensifications of the lowest 14 energy channels of CHEMS above the plasma background. The final question becomes at which S value should an event be considered real or false.

Based on the training set, 0.9 standard deviations above the mean of S is the optimum parameter for peak HSS performance. Since S is in terms of standard deviations, additional higher thresholds can be implemented to sub-classify events into more or less severe cases with a physical meaning (ranking). This allowed for the application as a definition task with a physical justification.

7. **Investigate a range of machine learning models and datasets.** Incorporating a range of machine learning models, from the most simple to the most complex in addition to varying datasets, can offer insights in the nature of the underlying physical data.

   Issues: Interpretability

   Example: In developing S, alternative feature inclusions were considered. S was settled on for its grounding in physical meaning. A secondary major consideration was its accuracy compared to other machine learning applications. In the following sections we discuss additional models.

As similarly discussed within Camporeale (2019), the desire to incorporate physical calculations comes from an interest in using machine learning for knowledge discovery. In the use cases of interest here, both the needs for accuracy and interpretability are essential. These presented strategies are designed to improve the potential performance for semi-supervised classification problems and the interpretability for subsequent physical understanding. Creating the final form of S was a labor intensive process to create and then optimize. Due to S's non-linear dependence on the features shown in Figure 5.4, this was a non-trivial task. Similarly expanding S into additional dimensions is challenging. This is where the machine learning infrastructure offers significant advantages as compared to the previous effort. In the following sections we discuss alternative solutions to identification of interchange.

5.4 Methods: Models and Experimental Setup

In the previous physics-based approach, events were defined through intensifications of H^+ only, allowing for comparisons to other surveys and advancement of the

understanding of events. This was a non-intuitive approach as common logic in application of machine learning algorithms suggests that greater data sizes will result in additional accuracy given a well-posed problem. To explore both the potential accuracy as well as interpretability of the application, we compare the performance of two distinct machine learning models with access to varying data set sizes.

5.4.1 Models

Two commonly used machine learning models for supervised classification are logistic regression and random forest classification. Both are considered standard classification models when applying machine learning and performing comparative studies (Couronné et al., 2018). The original physics-based algorithm was designed with a logistic regression method in mind, but with significant adjustment. Comparisons to this model are directly informative as a result. Logistic regression categorizes for binary decisions by fitting a logistic form, or a sigmoid. Logistic regression is a simple, but powerful, method toward predicting categorical outcomes from complex datasets. The basis of logistic regression is associated with progress made in the 19^{th} century in studying chemical reactions, before becoming popularized in the 1940s by Berkson (1944) (see Cramer, 2002, for a review).

Random forest in comparison classifies by building up collection of decision trees trained on random subsets of the input variables. The predictions of all trees are then combined in an ensemble to develop the final prediction. Similar to logistic regression, the method of random forest has been built over time with the most modern development associated with Breiman (2001). While logistic regression requires researchers to specify the functional form of relationships among variables, random forests add complexity toward classification decisions, by allowing for arbitrary, unspecified nonlinear dependencies between features, also known as model inputs.

The models used within this chapter are from the scikit-learn machine learning package in Python (Pedregosa et al., 2011). Within the logistic regression the L2 regularization penalty is applied. Within the random forest a grid search with 5-fold cross-validation is used to find the optimum depth between 2 and 5, while the number of trees is kept at 50. These search parameters are chosen to constrain the random forest within the perspective of the noisy nature of the CHEMS dataset and to prevent over fitting. Alterations to this tuning parameter scheme are not seen to alter the results in the following section. Unless otherwise stated, models are used in conjunction with balanced class weights which adjusts event weighting to be proportional to the frequency of events and non-events. This results in events

weighted higher than non-events due to their rarity. Performance is shown in Section 5.5 against the test set defined above.

5.4.2 Dataset Definitions and Sizes

To explore the performance of logistic regression and random forest, four distinct subsets of the Cassini plasma and magnetic field data are utilized ranging in data complexity and size as follows:

1. S\C (Spacecraft) Location and Magnetic Field

   6 features, 68,090 time samples

2. S\C Location, Magnetic Field, and H^+ flux (3-220 keV)

   38 features, 68,090 time samples

3. Low Energy H^+ flux (3-22 keV)

   14 features, 68,090 time samples

4. Azari et al., 2018 (S Value)

   1 feature, 68,090 time samples

These subsets are chosen to represent additional features, complexity, and physics inclusion. All of these subsets should be sensitive in varying amounts toward identification of interchange injections as evidenced in Figures 5.3 and 5.4. The first two datasets are a comparison of increasing features that should assist in identification of interchange injection. The third dataset includes less features, but is the originator most similar to the derived parameter from Azari et al. (2018). The final dataset contains the single summary statistic array of the S parameter. In the following result section, these four dataset segments are used to evaluate the two models.

5.5 Results and Discussion

We are interested in evaluating how the former physics-based S parameter performs with other commonly used subsets of space physics data. We complete this through applying supervised classification models and evaluate the ease of explainability and their relative performance.

5.5.1 Supervised Logistic Regression Classification

In Figure 5.5 the ROC curve of a logistic regression for all four subsets of Cassini data is presented. Area under the curve, or AUC is presented as a metric to understand the overall performance of each logistic regression evaluation. AUC has the ideal parameters of ranging between 0 and 1, with 0.5 representative of random guessing, 1 representing perfect classification, and 0 as the inverse of truth. AUC can be thought of as an average accuracy of a model and isn't sensitive to class-balance and thresholds. The purple curve represents the logistic regression when evaluated with the derived physics-based S described in the above sections. This is provided as a benchmark as it results in the same performance discussed in (Azari et al., 2018). From this figure, this single summary statistic outperforms all other subsets of Cassini data with an AUC approaching near 1.0 (0.97).

Unexpectedly, it is not the largest dataset that has the second best performance. Instead, the red curve which contains only the low energy H^+ intensities shows the best performance of the non physics-adjusted datasets. The magnetic field is a useful parameter for the prediction of interchange as demonstrated in Figure 5.3 but the form of the logistic regression is unable to use this information successfully. This is possibly due to the higher time resolution needed for interchange identification from magnetic field data. The current dataset is processed such that each time point in the CHEMS set is matched with a single magnetic field vector. Normally within interchange analyses, the magnetic field information is of a much higher resolution. It is likely if a study pursued solely magnetic field data of higher time resolution and processed these data to represent pre and post event states dependent on time, the performance of the magnetic field data would be improved. It's evident from Figure 5.4 that S exhibits non-linear behavior from the distribution of S on intensity, distance, and energy. Similarly the magnetic field values likely range over a far range due to the background values, that the linear dependency requirements of logistic regression are unable to use this information. Without the flux data especially (the blue curve) logistic regression is unable to predict interchange as compared to the previous physics-based parameter.

The AUC doesn't capture the entire picture for our interest. While it shows the performance of the algorithm, it contains information for multiple final classifications of events. The grey dots on Figure 5.5 demonstrates the chosen cut-point for L2 regularization for class weighted events, or the final classification decision for an optimal trade between real events and false events. Within the previous section, the Heidke Skill Score or HSS was discussed as the final threshold separating events from

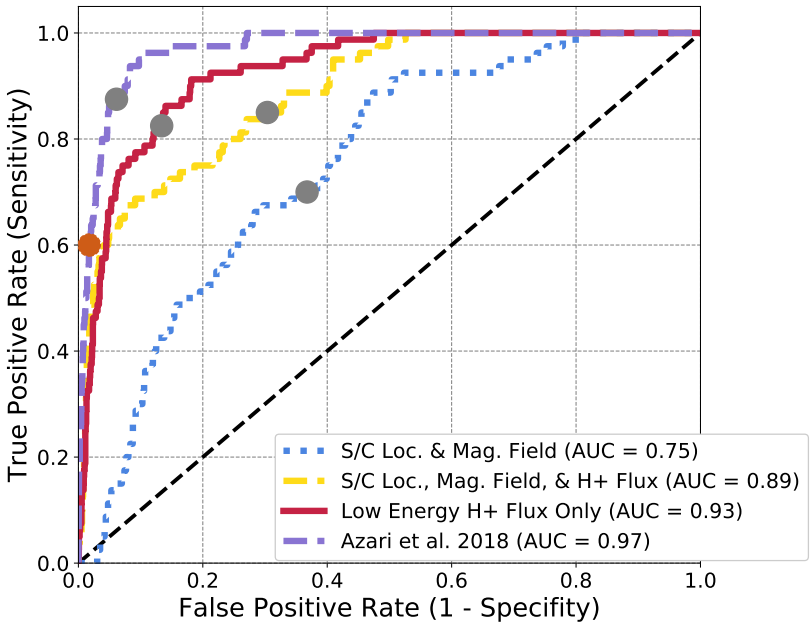

Figure 5.5: Logistic regression ROC diagram for Cassini data subsets. The grey dots represent the cut-off for L2 regularization for logistic regression. The orange dot represents the peak HSS value, used for optimization in Azari et al., 2018. The distinct curves represent separate ROC curves for each subset of data described in section 5.4.

non-events (denoted as the orange dot on Figure 5.5). Deciding the threshold of what separates an injection event from a non-event is critical for the implementation of statistical analysis on the results especially in this case, in which non-events outnumber events at a ratio of ∼50:1. One solution would be to rank events, in similar style of the previous work of S with categories of events (Azari et al., 2018).

5.5.2 Rare Event Considerations

We now move to evaluating the previous HSS optimization to the logistic regression L2 regulation for both class weighted and non-class weighted models. In Figure 5.6 the final forms of the weighted and non-weighted logistic regression for the trivial 1 dimensional array case of the S parameter are shown. The thresholds for the final decisions and for HSS are shown as vertical lines. Due to the extreme imbalance of non-events to events, implementing class weighting results in large shifts between what is considered an injection event or not. Between the two decision points of the blue and purple vertical lines there are 46 real events, but 202 non-events. This

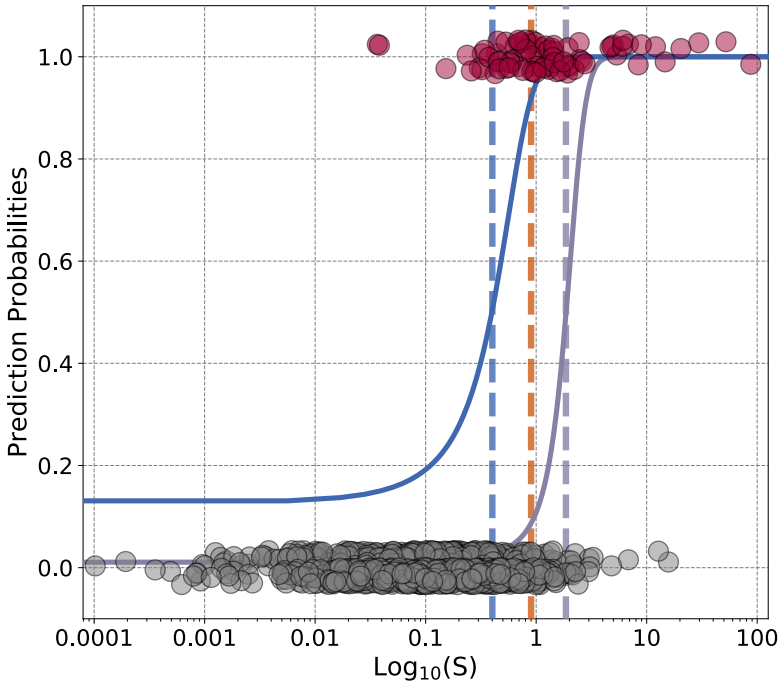

Figure 5.6: Finalized logistic regression against test set data. The grey dots represent the test set values of non-events, and the pink of events. The scatter in the dots around 0 and 1 are for aesthetic reasons and do not represent offset values. This figure contains logistic regressions performed on the physics-based parameter from Azari et al. (2018). The blue curve represents a class-weighted model and the purple without class weights. The x-axis is in logarithmic scale to demonstrate the range of the values, S itself does span both negative and positive values. The orange dashed line represents the HSS optimization used within Azari et al. (2018). From being presented in logarithmic space this gives the false illusion that the blue curve does not approach zero.

means that if using class-weighting in logistic regression for this problem, 202 non-events would be classified as events. Non-intuitively, for this application where the final events are used to understand the Saturn system, it's advantageous to use a non-class weighted model, as it limits the non-events. However the un-class-weighted model results in removing many real events as well as can be seen in the bulk of the pink events (real events) being misclassified by the purple vertical line.

The Heidke Skill Score provides an in-between choice of these by providing a higher threshold than the class-weighted, and lower than non-class weighted. The logistic regression for the S parameter shown here is easily intuited since the X-axis represents only one variable. The power of machine learning however is most advantageous in multiple dimensions. HSS has shown to be a more applicable metric for

rare events. Other skill scores, such as the True Skill Score have also shown promise in space physics applications (M. G. Bobra & Couvidat, 2015). For a discussion of additional metrics see Camporeale (2019). How can these traditional metrics for space applications be integrated into the regularization schemes? Future work in machine learning applications should consider shared developments between the physical sciences communities usage of skill scores and regularization of models.

5.5.3 Supervised Random Forest Classification

In Figure 5.7 the ROC diagram for the same subsets of data but for a random forest model are presented. In this case, unlike the logistic regression, other subsets of data can reproduce the same performance (or AUC) as the derived parameter. All curves, with the exception of the spacecraft location and magnetic field, quickly approach or slightly surpass the AUC of the physics-based parameter at 0.97, with small differences in the performance of the low energy H^+ flux (0.98) and of the combined spacecraft location, all flux, and magnetic field (0.97). The model form of random forest allows for non-linear behavior in the intensity and magnetic field data to find injection events. Increasing the features then helps in the case of random forest whereas it did not for logistic regression. Similar to the logistic regression, HSS results in a different ratio between true positive rate and false positive rate than the random forest model cut-off point with the grey dots.

Comparing back to logistic regression, even with a relatively complex model such as random forest, the AUC of the best ROC curves are near-identical. Given that S is an array, this is not that surprising. In both cases the physics-derived parameter outperforms or is effectively equivalent to all other data subsets, including those with access to a much richer information set and therefore more complex model. For the application of explainability for then gathering scientific conclusions, logistic regression is advantageous as it presents a much simpler model. However, random forest, has shown ability to mimic the underlying physics adjustments through selection of datasets.

Within these results, it's evident that the S parameter performs as well as simplistic machine learning models. Given that S is also grounded in a physics-based definition dependent on solely a variable flux background, this offers advantages to subsequent usage in scientific results. However, many of the adjustments in creating S can be implemented into other space physics data, and integrated into machine learning as evidenced here. In the description of the development of S, several challenges in geoscience data from the framework discussed in Karpatne et al. (2019),

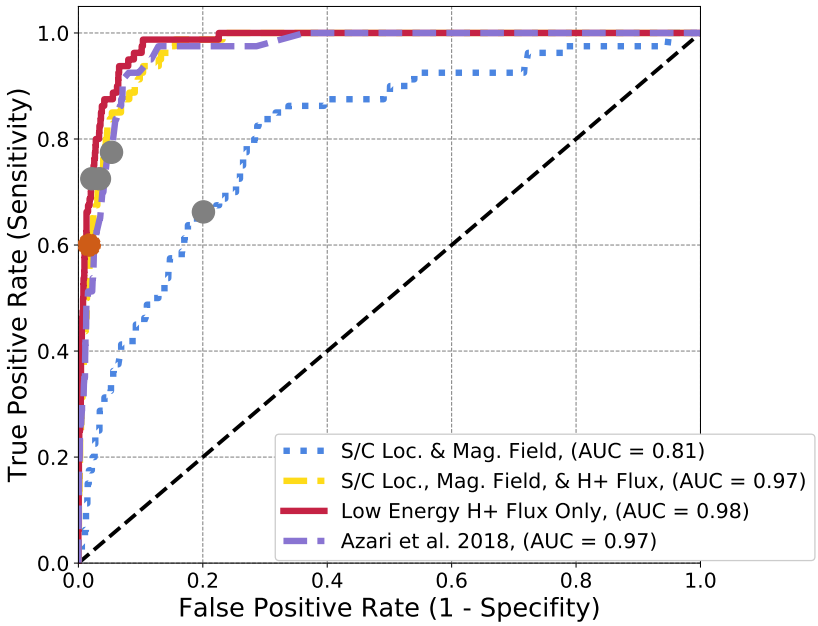

Figure 5.7: Random forest ROC diagram for Cassini data subsets. The grey dots represent the final optimization location for random forest classification. The orange dot represents the peak HSS value, used for optimization in Azari et al., 2018. The distinct curves represent separate ROC curves for each subset of data described in section 5.4.

and CHEMS specific solutions were presented. From the above evaluation, it is evident that applications of machine learning are useful to the task of automated event detection from flux data, but with diminishing explainability. A potential solution to both enhancing the explainability, similar to the S based parameter, but also incorporating the advantages of machine learning is presented in Figure 5.1. Rather than consider incorporation of physics-based information as deleterious to the implementation of machine learning, we have found that including this information simplifies the application, enhances the interpretability, and improves the overall performance.

5.6 Conclusion and Future Directions

Planetary space physics has reached a data volume capacity at which implementation of machine learning can address scientific questions. Within this work we addressed how machine learning can be used within the constraints of common characteristics of space physics data to investigate scientific questions. Care should be

taken when applying automated methods to planetary science data due to the unique challenges in spatio-temporal nature. Such challenges have been broadly discussed for geoscience data by Karpatne et al. (2019), but until now limited attention has been given toward planetary data.

Within this work we have posed three framing concerns for applications of machine learning to planetary data. First, it's important to consider the performance and accuracy of the application. Second, it's necessary to increase explainability of machine learning applications for planetary space physics. Third, it's essential to consider how the underlying issue characteristics of spacecraft data changes applications of machine learning. We argue that by including physics-based information into machine learning models, all three concerns of these applications can be addressed.

For certain machine learning models the performance can be enhanced but importantly in this application, the interpretability improves along with handling of characteristic data challenges. To reach this conclusion we presented a framework for incorporating physical information into machine learning. This framework targeted considerations for increasing interpretability and addressing aspects of spacecraft data into machine learning with space physics data. In particular, it addresses challenges such as the spatio-temporal nature of orbiting spacecraft, and other common geoscience data challenges (see Karpatne et al., 2019). After which we then cross-compared a previous physics-based method developed using the strategies in the framework to less physics-informed but feature rich datasets.

The physics-based semi-supervised classification method was built on high-energy flux data from the Cassini spacecraft to Saturn (see Azari et al., 2018). In investigating the accuracy of machine learning applications, we demonstrated this physics-based approach outperformed automated event detection for simple logistic regression models. It was found that traditional regularization through L2 penalties both under, and overestimated ideal cutoff points for final event classification (depending on class weighting). Instead, metrics more commonly used in weather prediction, such as the Heidke Skill Score, showed promise in class imbalance problems. This is similar to work demonstrating the applicability of True Skill Score in heliophysics applications (M. G. Bobra & Couvidat, 2015). Future work should consider shared developments between the physical sciences communities usage of skill scores and regularization of models.

While logistic regression is a more interpretable model, random forest proved that with the addition of more features from the Cassini mission the model could approximate the physics-based method successfully. From this evaluation it can be

gathered in this case physics-informed or model-adjusted machine learning, as defined within this work, can be approximated by different models but with less ability to then make further conclusions about implications of the results. For this application the interpretability is critical, and the simplistic model of logistic regression which results in the same performance is highly advantageous.

The framework and comparison presented here opens up avenues toward consideration of applying machine learning to answer planetary and space physics questions. In the future, cross-disciplinary work would greatly advance the state of these applications. Particularly within the context of interpretability toward scientific conclusions through physics-informed, or model-adjusted machine learning. The inclusion of planetary science and space physics domain knowledge in application of data science allows for the pursuit of fundamental questions. We have found that incorporating physics-based information increases the interpretability, and improves the overall performance of machine learning applications for scientific insight.

CHAPTER VI

Conclusions and Outlook

6.1 Summary

From Cassini, large-scale data analyses have fundamentally changed our understanding of Saturn's system, from identification of icy geysers on Enceladus, to the discovery of mysterious rotational periodicities. With the discovery of Enceladus' outgassing, we've learned that Saturn presents a strongly neutral dominated environment. This creates an ideal location to study neutral plasma interactions, as well as fundamental plasma instabilities arising from this internal mass source. As a highly sampled natural environment, Saturn can be used as a test case to expand our understanding of planetary environments, such as exoplanets, and for other neutral dominated astrophysical systems to inform formation theories.

How exactly, Saturn's magnetosphere transports plasma from Enceladus outwards, and from the outer regions inwards to form energetic populations close to the planet has long been a focus of the missions to Saturn. But until Cassini, long duration study has not been possible. This focus fits into a greater context, of how mass moves throughout planetary magnetospheres. As a system with evidence of both internally and externally driven dynamics, Saturn can greatly inform our understanding for all magnetospheres. As a theoretically predicted plasma instability, interchange instabilities have long held a critical role in understanding plasma transport in magnetospheres. With recent missions to the outer planets, where interchange is a dominant process in the inner and middle magnetospheres, data analysis studies have shed new light on the role of interchange in transport.

Data analysis is particularly critical for studying the high-energy signature of interchange, which are the primary inward transported mass, as this tenuous population is not expected to follow theoretical predictions of interchange. In Figure 1.4, a theoretical magneto-hydrodynamics model was presented of the interchange instability

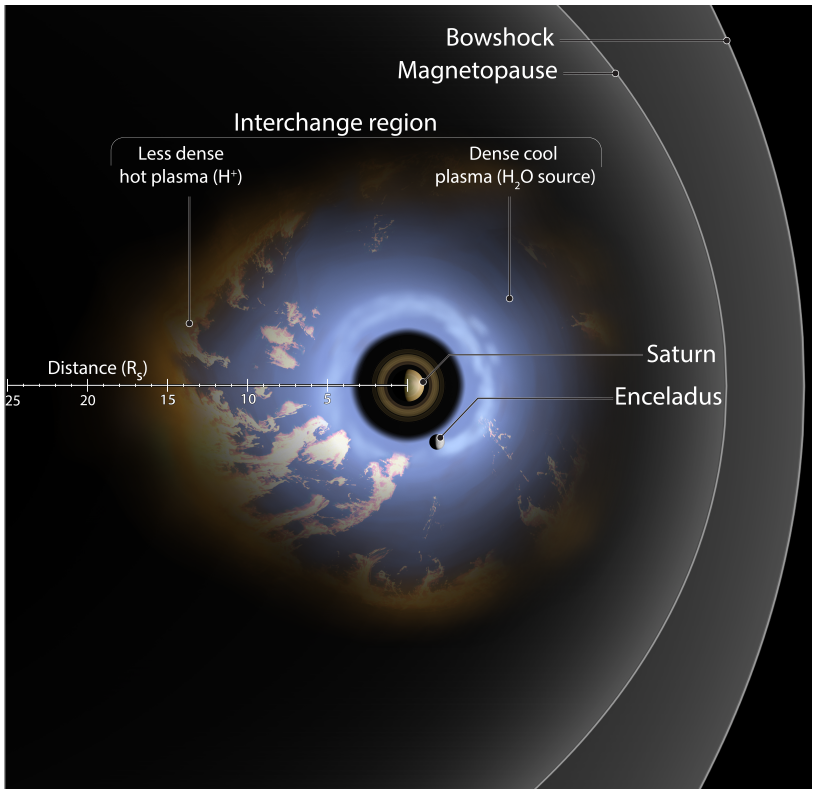

Figure 6.1: A detailed picture of the high-energy dynamics of Saturn's magnetosphere. This picture details the findings of this thesis from scale sizes and locations. This implies high-energy interchange's sensitivity to nightside conditions. This figure was created in consultation and with permission from Falconieri Visuals. Copyright held by Falconieri Visuals.

at Saturn. Within this thesis I have taken advantage of the rich Cassini dataset of interchange injections, to create a new data-driven picture of Saturn's environment (see Figure 6.1). This figure is comparable to Figures 1.3 and 1.4 which represent at the time of this thesis current global understanding of interchange at Saturn. Figure 1.3 showed a simplistic schematic of the interchanging plasma population. Figure 1.4 demonstrated through magnetohydrodynamic modeling a theoretical prediction of interchange.

Figure 6.1, building on the findings of this thesis, presents high-energy interchange injections at multiple scales and an asymmetric local time distribution, with a predominance on the nightside of the planet and superimposed with several Cassini orbits. This Figure suggests that the interchange triggering process is sensitive to nightside processes, including large-scale tail injections. This creates a more complex understanding of the Saturn system, where large magnetic reconnection driven injections of material, accentuate the plasma instability conditions of the interchange

process.

The chapters of this thesis are contributions to the field that enhance understanding of plasma transport around Saturn. This work has provided a new understanding of the high-energy ions within Saturn's magnetosphere, an often neglected regime of interchange studies. More broadly, this work provides a path toward implementing data-rich strategies through large-scale statistics and physics-informed machine learning. Below I detail the major findings of this work.

6.2 Discussion of Findings and Implications

This work was organized around four guiding questions and chapters, to advance understanding of the Saturn system through data-driven studies. Below are the primary contributions of this work toward filling in our understanding of mass transport in magnetized environments.

1. **How are interchange injections distributed spatio-temporally and what implications does this have toward relation to large-scale dynamics of the Saturn system?**

   Context

   At the start of this thesis, several surveys identified interchange injections over the course of the Cassini mission through manual identification methods (Lai et al., 2016; Kennelly et al., 2013; Y. Chen & Hill, 2008; Y. Chen et al., 2010). These surveys disagreed on the azimuthal location of events, leading to questions about the triggering process of injections. Theoretical expectations put interchange prevalence in all local time sectors (Liu et al., 2010; Liu & Hill, 2012) but these studies remained inconclusive. None of these efforts included the high-energy populations critical to energization of plasma in the environment with the exception of Müller et al. (2010), which when evaluating azimuthal distributions found evidence of these higher energy injections to be related to tail-reconnection processes further complicating the picture of interchange.

   To address this guiding question, a new survey was needed focusing on the higher energy components of interchange over the entirety of the Cassini mission. It was also critical that this list was standardized to advance our understanding of plasma transport. Chapter II discussed the creation the first injection related standardized identification of interchange through a physics-based supervised classification pursued in the style of a logistic regression with Cassini energetic ion data.

Findings and Implications

Chapter II showed that automated methods could be applied to the Cassini dataset grounded in physical meaning. In particular, a new distribution of interchange as nightside prevalent was found, hinting that interchange was related to repercussions from large-scale tail reconnection. This could have the effect of accentuating the instability condition through creating a steeper density gradient on the plasmapause boundary. This leads to a more complex understanding of how different types of injections interact with each other. This work constrained characteristic length scales and radial locations of events which are important parameters to understand further studies of system-wide plasma transport. By using a standardized method, it was also possible to compare this event list to others, demonstrating low overlap between previously identified lists. This can help explain how manual methods found major disagreements, but it also raises the importance for other standardized studies to pursue comparison to discuss the primary identification methods. This chapter focused on the first standardized characterization of the Saturn's interchange, but how these injections are controlled by different aspects of the planet was still an unconstrained question.

2. Are observed interchange injections sensitive to internal processes, such as ionospheric conductivity?

Context

Similar to the results in the local time locations of interchange, disagreements in the longitude of interchange events introduced uncertainty on if, or how, the ionosphere was influencing events (Kennelly et al., 2013; Y. Chen & Hill, 2008; Y. Chen et al., 2010). It is not unexpected that the ionosphere should conduct some control of interchange events due to expected system coupling from the ionosphere through to the magnetosphere (e.g. Hill, 2016a; Southwood & Kivelson, 1989). Chapter III undertook a study evaluating events against the available longitude systems which can be used to map into the upper atmosphere.

Findings and Implications

This Chapter represented a comparison between potential ionospheric control, and internal or in-situ control of interchange injections. Ionosphere control, at least through modulation of PPO and SLS systems, appears weakly and inconsistently over the entirety of the Cassini mission, especially as compared to influences from in-situ plasma conditions that can be accentuated from large-scale reconnection

driven injections. This finding was able to be shown, through careful analysis of the spatio-temporal aspects of the system and sample size constraints. It is still possible that ionospheric conducitvity plays a role, but this is unlikely modulated through the longitude systems. This finding suggested that new constraints in the theoretical underpinnings of ionospheric control of interchange should be investigated.

As an outcome of Chapters II and III, it became evident that the radial locations of interchange showed marked enhancements around 7-9 R_S for not only occurrence rates and severity, but also sensitivity to ionospheric organization. What exactly about this region made it so reactive? Chapter II suggested that potentially competing roles of loss and acceleration could lead to this intensified region, but such had not been quantified, leading to the following chapter.

3. What role do interchange injections play in system wide transport for energization and loss?

Context

Interchange plays a major role in accelerating particles in the inner magnetosphere. Pitch angle distributions can give clues to these acceleration processes occurring within the system. Within Chapter V a new parameter was derived to analyze particles' pitch angle information for this sensor. The rest of the chapter investigated with this parameter, how interchange injections are driving Saturn's magnetospheric energization, and responding to different loss processes.

Findings and Implications

Chapter IV suggested that injections can be thought of as an adiabatic process. Further work completing this estimation by following along the expected adiabatic invariant will be pursued prior to the final manuscript submission. This was long assumed, but never shown through large-scale statistical measurements. In investigating this, betatron acceleration was shown to be potentially counteracted inside of 7 R_S, meaning a competing process is limiting this acceleration. Through an estimation of potential loss processes, charge-exchange, or neutral-plasma interactions proved the most likely candidate. The neutral dominated magnetosphere of Saturn is therefore not only being one of the causes of interchange injections, but also to its limiting process in the inner magnetosphere. This Chapter illuminates Saturn's neutrals as an unexpectedly critical consideration for plasma transport both at Saturn, and elsewhere in astrophysical systems.

Throughout these chapters, we've seen applications of automated detection methods, large-scale statistics, and new instruments parameters to derive meaning from the complex plasma dynamics of Saturn's system. All these applications are within the restrictions that Cassini data, and more broadly planetary space physics data, often contain. These limitations include rare events, class imbalance, and the underlying spatio-temporal nature of the spacecraft trajectory and its collected data. With the rise of both data availability, and applicable methods in data science to planetary systems, this leads to the following, yet unexplored question.

4. **When applying machine learning to answer planetary science questions, what considerations are needed?**

   Context

   As planetary missions continue progressing forward in data collection, the importance of machine learning purely as a method to handle post-mission data analysis will become increasingly important. Planetary data however, contains several aspects that make applications of machine learning particularly challenging. In Chapter V I take the derived parameter from Chapter II and compare this with various models in machine learning, over different datasets, to discuss implementation of model-adjusted (or physics-informed) machine learning.

   Results and Implications

   In this comparison physics-based methods for identification of interchange outperformed or matched all other subsets of data for simple machine learning models including subsets that contained more information. This suggests that including physical information in machine learning can mimic large datasets. As such, increasing the dataset complexity, and the model complexity, can approximate the same performance as a simple physics-informed model, but then with less ability to interpret and understand the underlying event classifications. Moving forward, not only can such physics-informed models address the complex nature of planetary data, but also increase the ability to use machine learning to derive physical meaning about the system.

6.3 Future Directions

This thesis has expanded understanding of how plasma transport through interchange injection affects the plasma dynamics of Saturn's system. It has created a more nuanced understanding of the interaction between large-scale tail dynamic

driven injections, and interchange injections. It has shown that ionospheric control of interchange, long expected, is limited as compared to other plasma conditions in-situ to the instability. Through development of new parameters of the Cassini dataset, this work has shown that interchange provides a unique contribution to energetic particles at Saturn that maximize within the same region as the ring current, offering tantalizing insights into the role of these instabilities in driving energetic populations in the Saturn system. This contribution is limited due to extremely neutral environment of Saturn. The role of neutral-plasma interactions has been shown in this work to be critical in explaining the plasma environment of Saturn leading to far ranging repercussions for other neutral dominated astrophysical systems that do not have the same ability for in-situ studies. This has provided a new understanding of plasma dynamics in the system, but also led to several outstanding questions pertaining to space physics discussed below in section 6.3.1.

Throughout this work, a model-adjusted, or physics-informed algorithm was used to pursue identification of a standardized list of interchange injections which then led to the above contributions to the field's understanding of planetary magnetospheres. Through parameter studies, this thesis defined a new framework toward applications of machine learning for planetary science. This framework demonstrated incorporating physical knowledge can improve the performance of applications of simple and explainable machine learning and address limitations of the spatio-temporal nature of planetary data. This proof of concept opens up new avenues into exploration of applications, as well as best practices of machine learning to planetary datasets discussed below in section 6.3.2.

6.3.1 Toward Deeper Understanding of Plasma Dynamics

- **Interactions of large-scale reconnection injections and interchange**

  This work has seen some tantalizing hints of statistical distributions between large-scale injections and interchange. This offers evidence that the plasma density gradient set up by incoming large-scale injections can lead to an accentuation of the instability conditions upon the plasmapause. Recent works have proposed this (e.g. Mitchell et al., 2015; Thomsen et al., 2015) but the exact details of how these processes play together is unknown. For example, how does this transition occur? Is it only in Vasyliūnas or Dungey type reconnection that such interactions can be expected? Tail injections are more commonly seen to be organized in longitude studies (Bradley et al., 2018), and so is the organization

of tail injections the reason for the weak organization observed in interchange as a secondary process? This leads into the next outstanding question.

- **Role of ionospheric conductivity in injections**

  In reviewing potential ionospheric control of interchange injections in this work, a limited effect was found from evaluating the longitude systems. This effect was limited to the northern system. While this finding doesn't preclude all ionospheric influence on interchange, it does suggest that this influence is not carried through longitude system mapping. This is very surprising, and exactly how control from the ionosphere interacts with interchange is still an open ended question. For example, auroral activity has shown signs of injection processes and co-locate in the same region as interchange injections (e.g. Lamy et al., 2013; Grodent et al., 2010). How does the auroral activity relate to interchange processes? Similarly, how do high-altitude dynamics of interchange affect the ionosphere? Recently, the length of a Saturn day was constrained through ring seismology rather than plasma or field measurements (Mankovich et al., 2019), but the mystery of why these original longitude systems differ still stands. Reviewing how these new methods of longitude compare is worthwhile within reviews of ionospheric control. This work focused solely on the equatorial region, but Lai et al. (2016) has seen differences at higher latitudes in the magnetic fields of injections. At Earth, wave-particle interactions are an important consideration for these studies (e.g. Blum & Breneman, 2020), leading to the following study area.

- **Role of interchange in ring current populations and wave excitation**

  Interchange injections are associated with intensifications of plasma waves (e.g. Kennelly et al., 2013; Kumari et al., 2018). This thesis found that interchange injections accentuate asymmetric pitch angle distributions in areas of high density neutral populations, potentially leading to plasma wave intensifications. How these relate to Saturn's radiation belts, and observations of auroral dynamics, is an outstanding question that can inform not only Saturn studies, but also those of Earth and Jupiter.

- **Structure of injection events and role in mass balance of the system**

  Along with interchange's role in radiation belts, as well as potentially in wave dynamics, their role in balancing mass from the inner to the outer regions has not been quantified. The statistical characterizations pursued here found that

interchange events are extremely rare, and scale sizes are widely variable. Does this match with expectations of system wide mass, flow, and energy balance as discussed within Bagenal & Delamere (2011) for example? Extensions of the statistical studies within this thesis to understanding of mass balances within magnetic environments of the gas giants is warranted.

- **Neutral and dust interactions with plasma in astrophysical systems**

  A major finding of this work is the dominant role of neutral plasma interactions in limiting energetic particles near Saturn. How plasma, dust, and neutrals interact is not unique to Saturn and is a fundamental area of research in its own right. Dust is considered a necessary step for planetary formation (see reviews by Birnstiel et al., 2016; Testi et al., 2014). How magnetic fields and instabilities result in planetary formation is also a current theoretical field that can be greatly informed through cross-studies in current fast-rotating plasma systems (Turner et al., 2014, see review by). As exoplanet detection and more importantly for this work, characterization continues, findings are pointing toward complex plasma and neutral interactions. For example, exoplanets with moon-forming disks have been discovered (Isella et al., 2019), along with estimations of exoplanet magnetic fields (e.g. Cauley et al., 2019). This creates a natural extension of in-situ estimations from gas giant studies to broaden understanding of exoplanets.

6.3.2 Toward Machine Learning for Physical Insights

- **Physical reliability and explainability**

  One major reason for using logistic regression in this work as a base model was its simplicity as an explainable model and its ability to have a definable event metric based on a physical calculation. This worked well for interchange and more complex models were explored in Chapter V for performance. In this case, more complex models and greater data availability did not improve performance. How extendable is this finding to other applications? It is likely that future applications with increasing complexity will at times show greater performance with lower explainability and reliability. How these trade offs are captured within the overall context of then making scientific conclusions deserves additional reviews and should be considered in all applications.

- **Machine learning metrics for planetary science**

  The area under the curve (or AUC) is a common metric to describe classification algorithm ability. However, as seen in Chapter V, for class imbalances, as well as physical reliability, this does not present the entire picture toward usage in applications for planetary science and space physics. Class imbalance best practices have long been of interest to the machine learning community (see discussions in Haixiang et al., 2017; Chawla, 2005), but often in planetary applications rare events are also coupled with additional requirements. Future work should consider extensions of common machine learning metrics to adjust for the classic issues in planetary science data.

- **Considerations for future mission planning**

  In this application, increasing data availability was not found to increase algorithm performance regardless of model complexity. For mission planning, if machine learning is to be a major contribution of the post-data processing, greater spatio-temporal coverage, rather than in depth sampling, could prove useful. Exactly what the trade offs for in-depth sampling such as the current Magnetospheric Multiscale Mission, versus more widely distributed spatio-temporal coverage are worth considering. This of course depends on the scientific questions of interest (e.g. small scale physics versus global transport characterization) and planned usage of machine learning.

6.4 Outlook Moving Forward

In the world of big data, the 635 GB of Cassini data collected can seem insignificant. The Solar Dynamics Observatory alone collects per day more data than Cassini's total science relevant dataset. Compared to the history of exploration of the Saturn system however, this represents the first, and as planned only, mission to sample the entire Saturnian magnetospheric system from the ionosphere to the outer regions of Titan. Future studies delving into this rich dataset are critical to understand the Saturn system. The future directions proposed above are likely to be investigated not only with Cassini data analysis, but also with current missions such as the Juno mission to Jupiter. Modelling and theory efforts to capture the complex high-energy plasma populations in addition to the thermal background are essential to answering these questions in congruence with existing data observations of Saturn.

As future planetary missions expand toward planning to icy giant missions and potentially life supporting moons such as Europa and Titan, expected data return volumes are approaching realms at which manual identification methods become infeasible. Machine learning is not just a solution toward data volume management, but can also offer insights to these physical systems. Integrating studies between the machine learning and planetary science community is essential toward future understanding of planetary systems.

APPENDIX

APPENDIX A

Jupiter with Jupyter: A Growth Mindset Course in Data Visualization and Statistics for Geoscience

The following material is summarized from developed course materials which can be accessed on Github (Azari, Liemohn, & Swiger, 2019a). This work was presented (Azari, Liemohn, & Swiger, 2019b) at the American Geophysical Union 2019 Fall Meeting session on Jupyter (Moresi et al., 2019).

Background

Within the previous thesis, large-scale data analysis and techniques of machine learning have been applied to understand Saturn's mass transport. As planetary science moves from a data poor to a data rich field, educational programs in astronomy, geoscience, and physics are moving to rapidly include statistics and other core courses involving large-scale data analytics. Such course offerings coincide with the rise of data science opportunities outside of academia. This Appendix summarizes an effort to develop and offer a data rich course in the University of Michigan's Climate and Space Sciences and Engineering department to undergraduate and entry level graduate students.

The Case for Data Science in Undergraduate Geoscience Courses

Data science broadly has traditionally not been a targeted area for skillset development in geoscience courses. While certain subfields of geoscience have a long and rich history of data analysis, most often computational courses can be found with

computer science and statistics departments with limited if any physical science examples. In the last several years, educational offerings within this intersection have risen such as Stanford University's School of Earth Computational Geoscience degree program and data science courses (Than, 2014) and University of Colorado's EarthLab (Joseph & Wasser, 2020) through their publicly accessible education material and Earth Data Analytics Foundations Professional Certificate. These educational efforts coincide with the rise of a unified research community through efforts such as Pangeo, a community platform for big data geoscience (The Pangeo Team, 2018) and the Intelligent-Systems in Geosciences (IS-GEO) Research Coordination Network (Intelligent Systems for Geosciences (IS-GEO), 2018), (see overview of additional activities within Yue et al., 2016).

Pursuing data science within the geosciences requires interdisciplinary collaboration and skill acquisition as geoscience data provides unique challenges and use cases often differ (Ebert-Uphoff et al., 2019; Karpatne et al., 2019). This includes the spatio-temporal nature of geoscience data and a deeper understanding of inferring causation from large amounts of time series data (e.g. Runge et al., 2019). Coupled with the rise of open-data and ease of large-scale data computation data science driven geoscience skills needs are not only in academic research but also in private industry focused Earth analytics (Sand et al., 2019). This rise of Earth analytics both in and outside of research has not come without growing pains with recent developments in discussions cases of big data for oil extraction and private or pay for use climate services (Lee, 2020; Dembicki, 2019). To prepare students for future careers in both academia and industry, data science courses broadly have a role in engaging conversations on data ethics such as privacy, justice, fairness, and reproducibility (National Academies of Sciences, Engineering, and Medicine (NASEM), 2018). Courses preparing students then have a unique challenge of teaching both core data science skills including a range of technical and domain specific skills, but also evolving with the rapid rise of computational resources available to students (see Ma, 2018, for a review of computational strides in geoscience).

Targeting Visualization in Computational Courses

Mirroring developments in computational geosciences, a recent report by the National Academies recommends data science skills for all undergraduates, not just those within computational courses. As part of educating students, this core skillset should include grounding in domain specific examples, but also providing technical competencies in computing, visualization, data storage and access, and statistics (National

Academies of Sciences, Engineering, and Medicine (NASEM), 2018). Visualization methods are entwined with geoscience learning, but as a field in and of itself, are often neglected as a focus area in computational courses even as computationally heavy visualization focused courses have anecdotally shown increased student interest and are an essential part of geoscience (Hanrahan & Ma, 2005; Libarkin & Brick, 2002). Furthering the need for data visualization as a skill, visualization targeted job postings have increased by 1500% in the past decade (Ryan et al., 2019). By incorporating visualization into computational courses we can engage with student interest and leverage an already existing strength in geoscience.

A focus on visualization could also increase student interest and eventual comfort with computational concepts. The visualization community itself is positioned well to bring new approaches to diversity and inclusion as visualization becomes a needed skillset (Gaither, 2017). Student comfort with programming concepts varies widely dependent on their previous experience and can affect their experience in the classroom. Focusing on visualization is one potential avenue toward increasing student interest and experience with advanced programming concepts.

Diversity and Inclusion in Data Science for Geoscience

Student experience, including in the classroom, is essential to their sense of belonging in science, technology, engineering, or math (STEM) and eventual college major (e.g. Rainey et al., 2018; Good et al., 2012). As discussed within Foor et al. (2007), reconsidering traditional modes of curriculum development and classroom culture is necessary to addressing student experience. Computer science is particularly low in diversity and female representation amongst other technical fields. For example, in 2015 only 18% of undergraduate majors were women as compared to ∼40% for geoscience in the United States (National Science Foundation - National Center for Science and Engineering Statistics, 2019; Keane, 2016). For the computational sciences, this number is actually decreasing over time (see Sax et al., 2017, for a discussion on current trends). This is not to say that integrating geoscience into computational courses will increase diversity as geoscience itself has claim to the lowest diversity of all science, technology, engineering, and mathematics fields (see discussion in Huntoon et al., 2015). Within this light, developing courses that are acutely aware of these ongoing trends in both computer science and geoscience are essential.

Educational Research in Student Experience

Pennington et al. (2019) specifically calls for research development into effective pedagogies for developing interdisciplinary domain and data science skills. Within the discussion above, it's critical that along with strategies for focusing on content, student experience is of equal consideration. Canning et al. (2019) demonstrated that faculty mindset more than any other faculty characteristic (e.g. gender, race, age, experience) related to student motivation and achievement. Within this work, they additionally found that faculty with a growth mindset in STEM courses improved student's achievement (course grade) for all students and diminished gaps between white and underrepresented student grades.

Canning et al. (2019) specifically studied the difference between growth mindset and fixed mindset faculty. They defined fixed mindset to the belief that ability is innate and can not be changed much, whereas growth mindset focuses on ability as malleable. Fixed mindsets on innate ability can be especially negatively impactful to underrepresented student experience and success in courses. A growth mindset does not mean low expectations, instead growth mindsets in instructors can be encapsulated by high expectations and focus on guided improvement with mentoring (e.g. Rattan et al., 2012). In reality, not all people are one or the other type of mindset, and instructors can work toward creating a growth mindset through guiding achievement beyond simply rewarding effort (Dweck, 2015).

In enacting a growth mindset in the classroom, Dweck (2008) discusses engaging with students on learning from mistakes. This can be viewed in the light of Foor et al. (2007)'s discussion of Conefrey (2001)'s cultural myths of STEM. These include the myth that curriculum or pedagogy do not need change to accommodate different ways of learning and STEM environments, including courses, are beyond socio-cultural distinctions including gender, race, and class (Foor et al., 2007). We propose that purposeful restructuring of STEM educational environments, both in teaching mindsets and course structure, can address the aforementioned barriers to student experience in computationally rich courses.

Implementation

We developed a course in the University of Michigan's department Climate and Space Sciences and Engineering (CLaSP) department focusing on student competency in a three fold content of visualization, programming, and statistics. Content was grounded in content ranging from space physics and planetary science, to climate

change at the upper level undergraduate, early graduate level. Class time was split between statistics lessons and interactive computer labs. This course was offered in CLaSP starting in 2018 and each year afterwards and is part of the undergraduate core curriculum courses. Students from across the University, including outside of the College of Engineering, participated.

As the first iteration of this course, a careful consideration of the structure of this course within the context of a growth mindset was possible. We were particularly interested in providing experience with computational programming through visualization to students who had limited previous experience in coding. Programming and visualization are naturally iterative skills. Often the development of final products within either of these fields will occur over multiple iterations. Often times however the assessment of final assignments focus not on the process but the end result. It's not uncommon for computational assignments to be marked zero in the case of non-compiling or running programs. This does not reward any partial effort nor improvement toward developing computational skills within a growth mindset framework. Beyond addressing a growth mindset through student feedback and interaction, we wanted to develop a course in which the assignment structure built on an iterative learning approach.

The Jupyter Project

The Jupyter project is a wide spanning effort to develop a range of open-source computational resources and community including software and environments for interactive computing in many programming languages. The Jupyter environment has recently been bridged with other major geoscience efforts (Heagy & Pérez, 2019). Part of the Jupyter project includes Jupyter notebooks, in which text, multimedia, and code can be placed in a single environment together. This allows for students to immediately see the enactment of code, with the higher level context provided in the lesson. Notebooks can serve as self-contained reports to communicate presentation ready code and ideas between collaborators. As part of the notebook software, it's possible to run small and large amounts of code in the same document. This allows for rapid trial and error, and enables a style of try and learn programming. Jupyter provides easy access in the Python programming ecosystem, and with its rendering of visualization and equations has become a useful educational platform enabling visualization focused learning. All Jupyter notebooks were posted through the Github platform (Azari, 2018), for usage in other educational efforts outside of the University of Michigan.

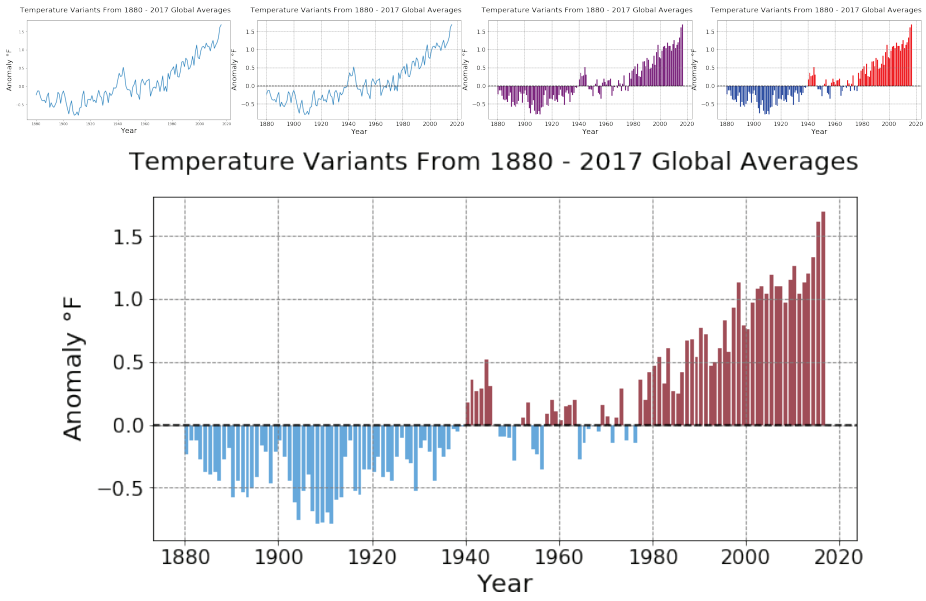

Figure A.1: Series of iterative visualization examples of NOAA NCEI data. Each iteration demonstrates an improvement discussed in classroom interaction with students. Data is sourced from National Oceanic and Atmospheric Administration - National Centers for Environmental Information (2020)

Within the course, we implemented interactive lessons using Jupyter notebooks as labs and also for assignments. The assignments themselves were assessed for partial completion grades and for if the notebook runs without errors. This allowed for assessment on student progress and guidance. Each submitted notebook was given feedback on student success on the assignment (such as style, overall notebook presentation) and then in addition directed places for improvement. This allowed a change from traditional assignment feedback to focus on guided student improvement. Within the course itself, students were also prompted through discussions of the iterative nature of coding.

Example of Iterative Learning Through Visualization

Each lab was coupled with examples of building up a statistical concept from the accompanying lectures with a visualization example, a computational method, and using a physically motivated dataset. In the first lab for example the NOAA National Centers for Environmental Information (NCEI) Climate at a Glance (National Oceanic and Atmospheric Administration - National Centers for Environmental Information, 2020) anomaly values were analyzed along with an introduction to data

analysis in Python and included concepts such as developing for loops and boolean indexing. Figure A.1 shows an example of an iterative process of using a visualization to develop student appreciation of iteration as well as computational concepts from the first lab experience within the course. Computational techniques and concepts such as boolean indexing and for loops were cross compared in this lab to generate the final figure. Throughout the process students were involved in collaboratively critiquing to obtain the final figure. Other lessons in the course involved using extreme heat days to develop an understanding of normal distributions, conveying multi-dimensional data through augmenting Juno data of Jupiter, and using linear regression to understand sea ice melting rates.

Discussion and Future Work

As part of the implementation of the course, students were prompted to assess times in which they struggled as well as how Jupyter notebooks in particular enabled learning from mistakes. Future work will discuss student feedback from this assessment. Geoscience data has entered a regime where courses bridging data science core concepts with geoscience are needed to prepare undergraduate students for industry and academic careers. With the low numbers of women and underrepresented students in geoscience and computer science, course development should actively consider improving the student experience as a necessary requirement. This can be considered through rethinking tools and assessment in courses STEM education that value a fixed mindset, or a value toward innate talent rather than developing active development. Jupyter notebooks provide a natural implementation and training tool that encourages iterative thinking in students, and teachers. This leads to valuing an iterative model of computational thinking. Visualization techniques can be integrated into Jupyter notebooks with ease, and provide a new perspective toward quantitatively rigorous courses. As discussed within Foor et al. (2007), a main tenet of the traditional academic environment is that changes in pedagogy and teaching are not required for student success. This and other myths Conefrey (2001) discussed have disproportionate impacts on disadvantaged students. Restructuring student feedback, engaging in developing a sense of student belonging in courses, and considering new computational tools show promise in addressing student experience. As new courses within the intersection of data science and geoscience are developed, they have an opportunity to reconsider new avenues toward learning.

BIBLIOGRAPHY

BIBLIOGRAPHY

Achilleos, N., André, N., Blanco-Cano, X., Brandt, P. C., Delamere, P. A., & Winglee, R. (2015). 1. Transport of mass, momentum and energy in planetary magnetodisc regions. *Space Science Reviews*, *187*, 229–299. doi: 10.1007/s11214-014-0086-y

Allen, R. C., Livi, S. A., Vines, S. K., Goldstein, J., Cohen, I., Fuselier, S. A., ... Spence, H. E. (2017). Storm time empirical model of O^+ and O^{6+} distributions in the magnetosphere. *Journal of Geophysical Research: Space Physics*, *122*, 8353–8374. doi: 10.1002/2017JA024245

Allen, R. C., Mitchell, D. G., Paranicas, C. P., Hamilton, D. C., Clark, G., Rymer, A. M., ... Vandegriff, J. (2018). Internal versus external sources of plasma at Saturn: Overview from Magnetospheric Imaging Investigation/Charge-Energy-Mass Spectrometer data. *Journal of Geophysical Research: Space Physics*, *123*, 4712–4727. doi: 10.1029/2018JA025262

Allen, R. C., Zhang, J.-C., Kistler, L. M., Spence, H. E., Lin, R.-L., Klecker, B., ... Jordanova, V. K. (2016). A statistical study of EMIC waves observed by Cluster: 2. Associated plasma conditions. *Journal of Geophysical Research: Space Physics*, *121*, 6458–6479. doi: 10.1002/2016JA022541

André, N., Dougherty, M. K., Russell, C. T., Leisner, J. S., & Khurana, K. K. (2005). Dynamics of the Saturnian inner magnetosphere: First inferences from the Cassini magnetometers about small-scale plasma transport in the magnetosphere. *Geophysical Research Letters*, *32*, L14S06. doi: 10.1029/2005GL022643

André, N., Persoon, A. M., Goldstein, J., Burch, J. L., Louarn, P., Lewis, G. R., ... Young, D. T. (2007). Magnetic signatures of plasma-depleted flux tubes in the Saturnian inner magnetosphere. *Geophysical Research Letters*, *34*, L14108. doi: 10.1029/2007GL030374

Andrews, D. J., Bunce, E. J., Cowley, S. W. H., Dougherty, M. K., Provan, G., & Southwood, D. J. (2008). Planetary period oscillations in Saturn's magnetosphere: Phase relation of equatorial magnetic field oscillations and Saturn kilometric radiation modulation. *Journal of Geophysical Research: Space Physics*, *113*, A09205. doi: 10.1029/2007JA012937

Andrews, D. J., Cowley, S. W. H., Dougherty, M. K., Lamy, L., Provan, G., & Southwood, D. J. (2012). Planetary period oscillations in Saturn's magnetosphere: Evolution of magnetic oscillation properties from southern summer to

post-equinox. *Journal of Geophysical Research: Space Physics*, *117*, A04224. doi: 10.1029/2011JA017444

Andriopoulou, M., Roussos, E., Krupp, N., Paranicas, C., Thomsen, M., Krimigis, S., ... Glassmeier, K. H. (2012). A noon-to-midnight electric field and nightside dynamics in Saturn's inner magnetosphere, using microsignature observations. *Icarus*, *220*(2), 503–513. doi: 10.1016/j.icarus.2012.05.010

Armstrong, T. P., Taherion, S., Manweiler, J., Krimigis, S., Paranicas, C., Mitchell, D., & Krupp, N. (2009). Energetic ions trapped in Saturn's inner magnetosphere. *Planetary and Space Science*, *57*(14), 1723–1731. doi: 10.1016/j.pss.2009.03.008

Arridge, C. S., André, N., Khurana, K. K., Russell, C. T., Cowley, S. W. H., Provan, G., ... Young, D. T. (2011). Periodic motion of Saturn's nightside plasma sheet. *Journal of Geophysical Research: Space Physics*, *116*, A11205. doi: 10.1029/2011JA016827

Arridge, C. S., André, N., McAndrews, H. J., Bunce, E. J., Burger, M. H., Hansen, K. C., ... Dougherty, M. K. (2011). Mapping magnetospheric equatorial regions at Saturn from Cassini Prime Mission observations. *Space Science Reviews*, *164*, 1–83. doi: 10.1007/s11214-011-9850-4

Arridge, C. S., Khurana, K. K., Russell, C. T., Southwood, D. J., Achilleos, N., Dougherty, M. K., ... Leinweber, H. K. (2008). Warping of Saturn's magnetospheric and magnetotail current sheets. *Journal of Geophysical Research: Space Physics*, *113*, A08217. doi: 10.1029/2007JA012963

Azari, A. R. (2018). *Event list for "Interchange injections at Saturn: Statistical survey of energetic H^+ sudden flux intensifications".* Retrieved from `https://deepblue.lib.umich.edu/data/concern/data_sets/3n203z679` doi: 10.7302/Z2WM1BMN

Azari, A. R., Allen, R. C., Liemohn, M. W., Jia, X., Dewey, R. M., Mitchell, D. G., ... Sergis, N. (2020). System wide evidence of particle loss and acceleration around Saturn. *In preparation for submission*.

Azari, A. R., Jia, X., Liemohn, M. W., Hospodarsky, G. B., Provan, G., Ye, S.-Y., ... Mitchell, D. G. (2019). Are Saturn's interchange injections organized by rotational longitude? *Journal of Geophysical Research: Space Physics*, *124*, 1806–1822. doi: 10.1029/2018JA026196

Azari, A. R., Liemohn, M. L., & Swiger, B. M. (2019a). *Data visualization and statistics in the geosciences.* Retrieved from `https://github.com/astro-abby/data_vis_statistics_geosciences`

Azari, A. R., Liemohn, M. W., Jia, X., Thomsen, M. F., Mitchell, D. G., Sergis, N., ... Vandegriff, J. (2018). Interchange injections at Saturn: Statistical survey of energetic H^+ sudden flux intensifications. *Journal of Geophysical Research: Space Physics*, *123*, 4692–4711. doi: 10.1029/2018JA025391

Azari, A. R., Liemohn, M. W., & Swiger, B. M. (2019b). Jupyter with Jupiter: Lessons from teaching data visualization and statistics in geosciences. In L. Moresi, R. Farrington, F. Perez, R. Schofield, L. J. Heagy, & S.-H. Shim (Eds.), *Linking Education and Research with Jupyter, 2019 Fall Meeting of the American Geophysical Union.* doi: 10.6084/m9.figshare.c.4783557.v3

Azari, A. R., Lockhart, J. W., Liemohn, M. W., & Jia, X. (2020). Incorporating physical knowledge into machine learning for planetary space physics. *Frontiers in Astronomy and Space Sciences, submitted*.

Bagenal, F. (2007). The magnetosphere of Jupiter: Coupling the equator to the poles. *Journal of Atmospheric and Solar-Terrestrial Physics*, *69*(3), 387–402. doi: 10.1016/j.jastp.2006.08.012

Bagenal, F., & Delamere, P. A. (2011). Flow of mass and energy in the magnetospheres of Jupiter and Saturn. *Journal of Geophysical Research: Space Physics*, *116*, A05209. doi: 10.1029/2010JA016294

Barbosa, D. D. (1993). Theory and observations of electromagnetic ion cyclotron waves in Saturn's inner magnetosphere. *Journal of Geophysical Research: Space Physics*, *98*(A6), 9345–9350. doi: 10.1029/93JA00476

Bashir, M. F., & Ilie, R. (2018). A new N^+ band of electromagnetic ion cyclotron waves in multi-ion cold plasmas. *Geophysical Research Letters*, *45*, 10,110–150,159. doi: 10.1029/2018GL080280

Bergen, K. J., Johnson, P. A., de Hoop, M. V., & Beroza, G. C. (2019). Machine learning for data-driven discovery in solid Earth geoscience. *Science*, *363*(6433), eaau0323. doi: 10.1126/science.aau0323

Berkson, J. (1944). Application of the logistic function to bio-assay. *Journal of the American Statistical Association*, *39*(227), 357–365. doi: 10.2307/2280041

Birnstiel, T., Fang, M., & Johansen, A. (2016). Dust evolution and the formation of planetesimals. *Space Science Reviews*, *205*, 41–75. doi: 10.1007/s11214-016-0256-1

Blum, L. W., & Breneman, A. W. (2020). Observations of radiation belt losses due to cyclotron wave-particle interactions. In A. N. Jaynes & M. E. Usanova (Eds.), *The Dynamic Loss of Earth's Radiation Belts* (pp. 49–98). Elsevier. doi: 10.1016/B978-0-12-813371-2.00003-2

Bobra, M. (2017). Machine learning in solar and space physics. In *National Academy of Science Space Studies Board Fall Meeting.* Ivine, CA. Retrieved from `https://sites.nationalacademies.org/cs/groups/ssbsite/documents/webpage/ssb_182877.pdf`

Bobra, M. G., & Couvidat, S. (2015). Solar flare prediction using SDO/HMI vector magnetic field data with a machine-learning algorithm. *The Astrophysical Journal*, *798*(2), 135. doi: 10.1088/0004-637x/798/2/135

Borovsky, J. E., & Valdivia, J. A. (2018). The Earth's magnetosphere: A systems science overview and assessment. *Surveys in Geophysics*, *39*(5), 817–859. doi: 10.1007/s10712-018-9487-x

Bradley, T. J., Cowley, S. W. H., Bunce, E. J., Smith, A. W., Jackman, C. M., & Provan, G. (2018). Planetary period modulation of reconnection bursts in Saturn's magnetotail. *Journal of Geophysical Research: Space Physics*, *123*, 9476–9507. doi: 10.1029/2018JA025932

Breiman, L. (2001). Random forests. *Machine Learning*, *45*(1), 5–32. doi: 10.1023/A:1010933404324

Burch, J. L., Goldstein, J., Hill, T. W., Young, D. T., Crary, F. J., Coates, A. J., ... Sittler Jr., E. C. (2005). Properties of local plasma injections in Saturn's magnetosphere. *Geophysical Research Letters*, *32*, L14S02. doi: 10.1029/2005GL022611

Butler, K. T., Davies, D. W., Cartwright, H., Isayev, O., & Walsh, A. (2018). Machine learning for molecular and materials science. *Nature*, *559*, 547–555. doi: 10.1038/s41586-018-0337-2

Camporeale, E. (2019). The challenge of machine learning in space weather: Nowcasting and forecasting. *Space Weather*, *17*, 1166–1207. doi: 10.1029/2018SW002061

Canning, E. A., Muenks, K., Green, D. J., & Murphy, M. C. (2019). STEM faculty who believe ability is fixed have larger racial achievement gaps and inspire less student motivation in their classes. *Science Advances*, *5*(2), eaau4734. doi: 10.1126/sciadv.aau4734

Carbary, J. F., & Mitchell, D. G. (2013). Periodicities in Saturn's magnetosphere. *Reviews of Geophysics*, *51*, 1–30. doi: 10.1002/rog.20006.1.

Carbary, J. F., Mitchell, D. G., Krimigis, S. M., & Krupp, N. (2007). Electron periodicities in Saturn's outer magnetosphere. *Journal of Geophysical Research: Space Physics*, *112*, A03206. doi: 10.1029/2006JA012077

Carbary, J. F., Mitchell, D. G., Paranicas, C., Roelof, E. C., & Krimigis, S. M. (2008). Direct observation of warping in the plasma sheet of Saturn. *Geophysical Research Letters*, *35*, L24201. doi: 10.1029/2008GL035970

Carbary, J. F., Mitchell, D. G., Paranicas, C., Roelof, E. C., Krimigis, S. M., Krupp, N., ... Dougherty, M. (2011). Pitch angle distributions of energetic electrons at Saturn. *Journal of Geophysical Research: Space Physics*, *116*, A01216. doi: 10.1029/2010JA015987

Carbary, J. F., Sergis, N., Mitchell, D. G., & Krupp, N. (2015). Saturn's hinge parameter from Cassini magnetotail passes in 2013–2014. *Journal of Geophysical Research: Space Physics*, *120*, 4438–4445. doi: 10.1002/2015JA021152

Cassidy, T. A., & Johnson, R. E. (2010). Collisional spreading of Enceladus' neutral cloud. *Icarus*, *209*(2), 696–703. doi: 10.1016/j.icarus.2010.04.010

Cauley, P. W., Shkolnik, E. L., Llama, J., & Lanza, A. F. (2019). Magnetic field strengths of hot Jupiters from signals of star–planet interactions. *Nature Astronomy*, *3*, 1128–1134. doi: 10.1038/s41550-019-0840-x

Cecconi, B., & Zarka, P. (2005). Model of a variable radio period for Saturn. *Journal of Geophysical Research: Space Physics*, *110*, A12203. doi: 10.1029/2005JA011085

Chawla, N. V. (2005). Data mining for imbalanced datasets: An overview. In O. Maimon & L. Rokach (Eds.), *Data Mining and Knowledge Discovery Handbook.* Boston, MA: Springer. doi: 10.1007/0-387-25465-X_40

Chen, F. F. (1974). *Introduction to plasma physics.* Plenum Press.

Chen, Y., & Hill, T. W. (2008). Statistical analysis of injection/dispersion events in Saturn's inner magnetosphere. *Journal of Geophysical Research: Space Physics*, *113*, A07215. doi: 10.1029/2008JA013166

Chen, Y., Hill, T. W., Rymer, A. M., & Wilson, R. J. (2010). Rate of radial transport of plasma in Saturn's inner magnetosphere. *Journal of Geophysical Research: Space Physics*, *115*, A10211. doi: 10.1029/2010JA015412

Chen, Y., Manchester, W. B., Hero, A. O., Toth, G., DuFumier, B., Zhou, T., ... Gombosi, T. I. (2019). Identifying solar flare precursors using time series of SDO/HMI images and SHARP parameters. *Space Weather*, *17*, 1404–1426. doi: 10.1029/2019SW002214

Clark, G., Paranicas, C., Santos-Costa, D., Livi, S., Krupp, N., Mitchell, D. G., ... Tseng, W.-L. (2014). Evolution of electron pitch angle distributions across Saturn's middle magnetospheric region from MIMI/LEMMS. *Planetary and Space Science*, *104*(Part A), 18–28. doi: 10.1016/j.pss.2014.07.004

Conefrey, T. (2001). Sexual discrimination and women's retention rates in science and engineering programs. *Feminist Teacher*, *13*(3), 170–192. Retrieved from `http://www.jstor.org/stable/40545972`

Couronné, R., Probst, P., & Boulesteix, A. L. (2018). Random forest versus logistic regression: a large-scale benchmark experiment. *BMC Bioinformatics*, *19*(1), 270. doi: 10.1186/s12859-018-2264-5

Coveney, P. V., Dougherty, E. R., & Highfield, R. R. (2016). Big data need big theory too. *Philosophical Transactions of the Royal Society A: Mathematical, Physical and Engineering Sciences*, *374*(2080). doi: 10.1098/rsta.2016.0153

Cowley, S. W., & Provan, G. (2016). Planetary period oscillations in Saturn's magnetosphere: Further comments on the relationship between post-equinox properties deduced from magnetic field and Saturn kilometric radiation measurements. *Icarus*, *272*, 258–276. doi: 10.1016/j.icarus.2016.02.051

Cramer, J. S. (2002). The origins of logistic regression. *Tinbergen Institute Working Paper No. 2002-119/4*. doi: 10.2139/ssrn.360300

Cravens, T. E., Ozak, N., Richard, M. S., Campbell, M. E., Robertson, I. P., Perry, M., & Rymer, A. M. (2011). Electron energetics in the Enceladus torus. *Journal of Geophysical Research: Space Physics*, *116*, A09205. doi: 10.1029/2011JA016498

DeJong, A. D., Burch, J. L., Goldstein, J., Coates, A. J., & Crary, F. (2011). Day-night asymmetries of low-energy electrons in Saturn's inner magnetosphere. *Geophysical Research Letters*, *38*, L08106. doi: 10.1029/2011GL047308

DeJong, A. D., Burch, J. L., Goldstein, J., Coates, A. J., & Young, D. T. (2010). Low-energy electrons in Saturn's inner magnetosphere and their role in interchange injections. *Journal of Geophysical Research: Space Physics*, *115*, A10229. doi: 10.1029/2010JA015510

Delamere, P. A., Bagenal, F., Dols, V., & Ray, L. C. (2007). Saturn's neutral torus versus Jupiter's plasma torus. *Geophysical Research Letters*, *34*, L09105. doi: 10.1029/2007GL029437

Delamere, P. A., Otto, A., Ma, X., Bagenal, F., & Wilson, R. J. (2015). Magnetic flux circulation in the rotationally driven giant magnetospheres. *Journal of Geophysical Research: Space Physics*, *120*, 4229–4245. doi: 10.1002/2015JA021036

Dembicki, G. (2019). *The multi-billion-dollar "climate services" industry is altering access to climate data.* Retrieved from `https://ensia.com/features/private-climate-services-industry-environmental-justice-corporations-inequity/`

Desch, M. D., & Kaiser, M. L. (1981). Voyager measurement of the rotation period of Saturn's magnetic field. *Geophysical Research Letters*, *8*(3), 253–256. doi: 10.1029/GL008i003p00253

de Soria-Santacruz, M., Spasojevic, M., & Chen, L. (2013). EMIC waves growth and guiding in the presence of cold plasma density irregularities. *Geophysical Research Letters*, *40*, 1940–1944. doi: 10.1002/grl.50484

Dialynas, K., Brandt, P. C., Krimigis, S. M., Mitchell, D. G., Hamilton, D. C., Krupp, N., & Rymer, A. M. (2013). The extended Saturnian neutral cloud as revealed by global ENA simulations using Cassini/MIMI measurements. *Journal of Geophysical Research: Space Physics*, *118*, 3027–3041. doi: 10.1002/jgra.50295

The distribution of atomic hydrogen and oxygen in the magnetosphere of Saturn. (2009). *Planetary and Space Science*, *57*(14-15), 1743–1753. doi: 10.1016/j.pss.2009.04.014

Dougherty, M. K., Cao, H., Khurana, K. K., Hunt, G. J., Provan, G., Kellock, S., ... Southwood, D. J. (2018). Saturn's magnetic field revealed by the Cassini Grand Finale. *Science*, *362*(6410), eaat5434. doi: 10.1126/science.aat5434

Dougherty, M. K., Kellock, S., Southwood, D. J., Balogh, A., Smith, E. J., Tsurutani, B. T., ... Cowley, S. W. H. (2004). The Cassini magnetic field investigation. *Space Science Reviews*, *114*(1), 331–383. doi: 10.1007/s11214-004-1432-2

Dougherty, M. K., Khurana, K. K., Neubauer, F. M., Russell, C. T., Saur, J., Leisner, J. S., & Burton, M. E. (2006). Identification of a dynamic atmosphere at Enceladus with the Cassini magnetometer. *Science*, *311*(5766), 1406–1409. doi: 10.1126/science.1120985

Douglas, J. N. (1960). *A study of non-thermal radio emission from Jupiter*. (Doctoral dissertation). New Haven, CT: Yale University.

Duncan, R. A. (1975). Jupiter's rotation period from dekametric observations 1951-1975. *Publications of the Astronomical Society of Australia*, *2*(6). doi: 10.1017/S1323358000014211

Dungey, J. W. (1961). Interplanetary magnetic field and the auroral zones. *Physical Review Letters*, *6*(2), 47–48. doi: 10.1103/PhysRevLett.6.47

Dungey, J. W. (1963). The structure of the exosphere or adventures in velocity space. In C. DeWitt, J. Hieblot, & L. LeBeau (Eds.), *Geophysics, the earth's environment* (pp. 503–550). New York: Gordon and Breach.

Dweck, C. (2008). Mindsets and math/science achievement. *Prepared for the Carnegie Corporation of New York, Institute for Advanced Study Commission on Mathematics and Science Education*. Retrieved from `https://www.growthmindsetmaths.com/uploads/2/3/7/7/23776169/mindset_and_math_science_achievement_-_nov_2013.pdf`

Dweck, C. (2015). Growth mindset, revisited. *Education Week*, *35*(5), 20–24. Retrieved from `https://www.edweek.org/ew/articles/2015/09/23/carol-dweck-revisits-the-growth-mindset.html`

Ebert-Uphoff, I., Samarasinghe, S. M., & Barnes, E. A. (2019). Thoughtfully using artificial intelligence in Earth science. *Eos*, *100*. doi: 10.1029/2019EO135235

Esposito, L. W., Colwell, J. E., Larsen, K., McClintock, W. E., Stewart, A. I. F., Hallett, J. T., ... Yung, Y. L. (2005). Ultraviolet imaging spectroscopy shows an active Saturnian system. *Science*, *307*(5713), 1251–1255. doi: 10.1126/science.1105606

Fawcett, T. (2006). An introduction to ROC analysis. *Pattern Recognition Letters*, *27*(8), 861–874. doi: 10.1016/j.patrec.2005.10.010

Fischer, G., Gurnett, D. A., Kurth, W. S., Ye, S.-Y., & Groene, J. B. (2015). Saturn kilometric radiation periodicity after equinox. *Icarus*, *254*, 72–91. doi: 10.1016/j.icarus.2015.03.014

Fleshman, B. L., Delamere, P. A., Bagenal, F., & Cassidy, T. (2012). The roles of charge exchange and dissociation in spreading Saturn's neutral clouds. *Journal of Geophysical Research: Planets*, *117*, E05007. doi: 10.1029/2011JE003996

Fleshman, B. L., Delamere, P. A., Bagenal, F., & Cassidy, T. (2013). A 1-D model of physical chemistry in Saturn's inner magnetosphere. *Journal of Geophysical Research: Planets*, *118*, 1567–1581. doi: 10.1002/jgre.20106

Fok, M.-C., Kozyra, J. U., Nagy, A. F., & Cravens, T. E. (1991). Lifetime of ring current particles due to coulomb collisions in the plasmasphere. *Journal of Geophysical Research: Space Physics*, *96*(A5), 7861–7867. doi: 10.1029/90JA02620

Foor, C. E., Walden, S. E., & Trytten, D. A. (2007). "I wish that I belonged more in this whole engineering group": Achieving individual diversity. *Journal of Engineering Education*, *96*, 103–115. doi: 10.1002/j.2168-9830.2007.tb00921.x

Frank, L. A., Burek, B. G., Ackerson, K. L., Wolfe, J. H., & Mihalov, J. D. (1980). Plasmas in Saturn's magnetosphere. *Journal of Geophysical Research: Space Physics*, *85*(A11), 5695–5708. doi: 10.1029/JA085iA11p05695

Franklin, K. L., & Burke, B. F. (1958). Radio observations of the planet Jupiter. *Journal of Geophysical Research (1896-1977)*, *63*(4), 807–824. doi: 10.1029/JZ063i004p00807

Fukazawa, K., Ogino, T., & Walker, R. J. (2006). Configuration and dynamics of the Jovian magnetosphere. *Journal of Geophysical Research: Space Physics*, A10207. doi: 10.1029/2006JA011874

Gabrielse, C., Angelopoulos, V., Harris, C., Artemyev, A., Kepko, L., & Runov, A. (2017). Extensive electron transport and energization via multiple, localized dipolarizing flux bundles. *Journal of Geophysical Research: Space Physics*, *122*, 5059–5076. doi: 10.1002/2017JA023981

Gaither, K. (2017). How visualization can foster diversity and inclusion in next-generation science. *IEEE Computer Graphics and Applications*, *37*(5), 106–112. doi: 10.1109/MCG.2017.3621230

Galileo evidence for rapid interchange transport in the Io torus. (1997). *Geophysical Research Letters*, *24*(17), 2131–2134. doi: 10.1029/97GL01788

Galopeau, P. H. M., & Lecacheux, A. (2000). Variations of Saturn's radio rotation period measured at kilometer wavelengths. *Journal of Geophysical Research: Space Physics*, *105*(A6), 13089–13101. doi: 10.1029/1999JA005089

Ganushkina, N. Y., Amariutei, O. A., Welling, D., & Heynderickz, D. (2015). Nowcast model for low-energy electrons in the inner magnetosphere. *Space Weather*, *13*, 16–34. doi: 10.1002/2014SW001098

Gobet, F., Eden, S., Coupier, B., Tabet, J., Farizon, B., Farizon, M., ... Scheier, P. (2004). Ionization of water by (20-150)-keV protons: Separation of direct-ionization and electron-capture processes. *Physical Review A*, *70*(6), 1–8. doi: 10.1103/PhysRevA.70.062716

Gobet, F., Farizon, B., Farizon, M., Gaillard, M. J., Carré, M., Lezius, M., ... Märk, T. D. (2001). Total, partial, and electron-capture cross sections for ionization of water vapor by 20-150 keV protons. *Physical Review Letters*, *86*(17), 3751–3754. doi: 10.1103/PhysRevLett.86.3751

Goertz, C. K. (1989). Dusty plasmas in the solar system. *Reviews of Geophysics*, *27*(2), 271–292. doi: 10.1029/RG027i002p00271

Gold, T. (1959). Motions in the magnetosphere of the Earth. *Journal of Geophysical Research (1896-1977)*, *64*(9), 1219–1224. doi: 10.1029/JZ064i009p01219

Goldreich, P., & Farmer, A. J. (2007). Spontaneous axisymmetry breaking of the external magnetic field at Saturn. *Journal of Geophysical Research: Space Physics*(A05225). doi: 10.1029/2006JA012163

Goldstein, J., Sandel, B. R., Forrester, W. T., & Reiff, P. H. (2003). IMF-driven plasmasphere erosion of 10 July 2000. *Geophysical Research Letters*, *30*, 1146. doi: 10.1029/2002GL016478

Gombosi, T. I., Armstrong, T. P., Arridge, C. S., Khurana, K. K., Krimigis, S. M., Krupp, N., ... Thomsen, M. F. (2009). Saturn's magnetospheric configuration. In M. K. Dougherty, L. W. Esposito, & S. M. Krimigis (Eds.), *Saturn from Cassini-Huygens* (pp. 203–255). Springer. doi: 10.1007/978-1-4020-9217-6_9

Good, C., Rattan, A., & Dweck, C. S. (2012). Why do women opt out? Sense of belonging and women's representation in mathematics. *Journal of Personality and Social Psychology*, *102*(4), 700–717. doi: 10.1037/a0026659

Grodent, D., Radioti, A., Bonfond, B., & Gérard, J.-C. (2010). On the origin of Saturn's outer auroral emission. *Journal of Geophysical Research: Space Physics*, *115*, A08219. doi: 10.1029/2009JA014901

Gurnett, D. A., Groene, J. B., Averkamp, T. F., Kurth, W. S., Ye, S.-Y., & Fischer, G. (2011). An SLS4 longitude system based on a tracking filter analysis of the rotational modulation of Saturn kilometric radiation. In H. O. Rucker, W. S. Kurth,

P. Louarn, & G. Fischer (Eds.), *Planetary Radio Emissions VII* (pp. 51–64). Austrian Academy of Sciences Press. doi: 10.1553/PRE7s51

Gurnett, D. A., Kurth, W. S., Hospodarsky, G. B., Persoon, A. M., Averkamp, T. F., Cecconi, B., ... Pedersen, A. (2005). Radio and plasma wave observations at Saturn from Cassini's approach and first orbit. *Science*, *307*(5713), 1255 – 1259. doi: 10.1126/science.1105356

Gurnett, D. A., Lecacheux, A., Kurth, W. S., Persoon, A. M., Groene, J. B., Lamy, L., ... Carbary, J. F. (2009). Discovery of a north-south asymmetry in Saturn's radio rotation period. *Geophysical Research Letters*, *36*, L16102. doi: 10.1029/2009GL039621

Gurnett, D. A., Persoon, A. M., Groene, J. B., Kopf, A. J., Hospodarsky, G. B., & Kurth, W. S. (2009). A north-south difference in the rotation rate of auroral hiss at Saturn: Comparison to Saturn's kilometric radio emission. *Geophysical Research Letters*, *36*, L21108. doi: 10.1029/2009GL040774

Gurnett, D. A., Persoon, A. M., Kurth, W. S., Groene, J. B., Averkamp, T. F., Dougherty, M. K., & Southwood, D. J. (2007). The variable rotation period of the inner region of Saturn's plasma disk. *Science*, *316*(5823), 442–445. doi: 10.1126/science.1138562

Haixiang, G., Yijing, L., Shang, J., Mingyun, G., Yuanyue, H., & Bing, G. (2017). Learning from class-imbalanced data: Review of methods and applications. *Expert Systems with Applications*, *73*, 220–239. doi: 10.1016/j.eswa.2016.12.035

Hanrahan, P., & Ma, K.-L. (2005). Teaching visualization. *Computer Graphics (ACM)*, *39*(1), 4–5. doi: 10.1145/1057792.1057798

Hansen, C. J., Esposito, L. W., Stewart, A. I. F., Colwell, J., Hendrix, A., Pryor, W., ... West, R. (2006). Enceladus' water vapor plume. *Science*, *311*(5766), 1422–1425. doi: 10.1126/science.1121254

Hartogh, P., Lellouch, E., Moreno, R., Bockelée-Morvan, D., Biver, N., Cassidy, T., ... Kidger, M. (2011). Direct detection of the Enceladus water torus with Herschel. *Astronomy & Astrophysics*, *532*, L2. doi: 10.1051/0004-6361/201117377

Heagy, L., & Pérez, F. (2019). Jupyter meets the Earth. *Jupyter Blog*. Retrieved from `https://blog.jupyter.org/jupyter-meets-the-earth-1b0eb33c83f`

Heidke, P. (1926). Berechnung des Erfolges und der Güte der Windstärkevorhersagen im Sturmwarnungdienst (Calculation of the success and goodness of strong wind forecasts in the storm warning service). *Geografiska Annaler Stockholm*, *8*, 301–349.

Hill, T. W. (1976). Interchange stability of a rapidly rotating magnetosphere. *Planetary and Space Science*, *24*(12), 1151–1154. doi: 10.1016/0032-0633(76)90152-5

Hill, T. W. (2016a). Magnetosphere-Ionosphere coupling at Jupiter and Saturn. In C. R. Chappell, R. W. Schunk, P. M. Banks, J. L. Burch, & R. M. Thorne (Eds.), *Magnetosphere-Ionosphere Coupling in the Solar System.* doi: 10.1002/9781119066880.ch24

Hill, T. W. (2016b). Penetration of external plasma into a rotation-driven magnetosphere. *Journal of Geophysical Research: Space Physics*, *121*, 10,032–10,036. doi: 10.1002/2016JA023430

Hill, T. W., Rymer, A. M., Burch, J. L., Crary, F. J., Young, D. T., Thomsen, M. F., ... Lewis, G. R. (2005). Evidence for rotationally driven plasma transport in Saturn's magnetosphere. *Geophysical Research Letters*, *32*, L14S10. doi: 10.1029/2005GL022620

Holmberg, M. K. G., Wahlund, J.-E., Vigren, E., Cassidy, T. A., & Andrews, D. J. (2016). Transport and chemical loss rates in Saturn's inner plasma disk. *Journal of Geophysical Research: Space Physics*, *121*, 2321–2334. doi: 10.1002/2015JA021784

Hunt, G. J., Cowley, S. W. H., Provan, G., Bunce, E. J., Alexeev, I. I., Belenkaya, E. S., ... Coates, A. J. (2014). Field-aligned currents in Saturn's southern nightside magnetosphere: Subcorotation and planetary period oscillation components. *Journal of Geophysical Research: Space Physics*, *119*, 9847–9899. doi: 10.1002/2014JA020506

Hunt, G. J., Cowley, S. W. H., Provan, G., Bunce, E. J., Alexeev, I. I., Belenkaya, E. S., ... Coates, A. J. (2015). Field-aligned currents in Saturn's northern nightside magnetosphere: Evidence for interhemispheric current flow associated with planetary period oscillations. *Journal of Geophysical Research: Space Physics*, *120*, 7552–7584. doi: 10.1002/2015JA021454

Huntoon, J. E., Tanenbaum, C., & Hodges, J. (2015). Increasing diversity in the geosciences. *Eos*, *96*. doi: 10.1029/2015EO025897

Ilie, R., Skoug, R. M., Valek, P., Funsten, H. O., & Glocer, A. (2013). Global view of inner magnetosphere composition during storm time. *Journal of Geophysical Research: Space Physics*, *118*, 7074–7084. doi: 10.1002/2012JA018468

Intelligent Systems for Geosciences (IS-GEO). (2018). *About IS-GEO.* Retrieved from `https://is-geo.org/about/`

Isella, A., Benisty, M., Teague, R., Bae, J., Keppler, M., Facchini, S., & Pérez, L. (2019). Detection of continuum submillimeter emission associated with candidate protoplanets. *The Astrophysical Journal*, *879*, L25. doi: 10.3847/2041-8213/ab2a12

Iten, R., Metger, T., Wilming, H., del Rio, L., & Renner, R. (2020). Discovering physical concepts with neural networks. *Physical Review Letters*, *124*(1), 10508. doi: 10.1103/PhysRevLett.124.010508

Jia, X., Hansen, K. C., Gombosi, T. I., Kivelson, M. G., Tóth, G., Dezeeuw, D. L., & Ridley, A. J. (2012). Magnetospheric configuration and dynamics of Saturn's magnetosphere: A global MHD simulation. *Journal of Geophysical Research: Space Physics*, *117*, A05225. doi: 10.1029/2012JA017575

Jia, X., & Kivelson, M. G. (2012). Driving Saturn's magnetospheric periodicities from the upper atmosphere/ionosphere: Magnetotail response to dual sources. *Journal of Geophysical Research: Space Physics*, *117*, A11219. doi: 10.1029/2012JA018183

Jia, X., Kivelson, M. G., & Gombosi, T. I. (2012). Driving Saturn's magnetospheric periodicities from the upper atmosphere / ionosphere. *Journal of Geophysical Research: Space Physics*, *117*, A04215. doi: 10.1029/2011JA017367

Joseph, M., & Wasser, L. (2020). *EarthLab - Free online courses, tutorials and tools.* Retrieved from `https://www.earthdatascience.org/`

Jurac, S., & Richardson, J. D. (2005). A self-consistent model of plasma and neutrals at Saturn: Neutral cloud morphology. *Journal of Geophysical Research: Space Physics*, *110*, A09220. doi: 10.1029/2004JA010635

Karpatne, A., Ebert-Uphoff, I., Ravela, S., Babaie, H. A., & Kumar, V. (2019). Machine Learning for the Geosciences: Challenges and Opportunities. *IEEE Transactions on Knowledge and Data Engineering*, *31*(8), 1544–1554. doi: 10.1109/TKDE.2018.2861006

Keane, C. M. (2016). U.S. female geoscience enrollments and degrees remain level in 2015. *Geoscience Currents*, *110*. Retrieved from `https://www.americangeosciences.org/sites/default/files/currents/Currents-110-GenderEnrollments2015.pdf`

Kennel, C. F., & Petschek, H. E. (1966). Limit on stably trapped particle fluxes. *Journal of Geophysical Research (1896-1977)*, *71*(1), 1–28. doi: 10.1029/JZ071i001p00001

Kennelly, T. J., Leisner, J. S., Hospodarsky, G. B., & Gurnett, D. A. (2013). Ordering of injection events within Saturnian SLS longitude and local time. *Journal of Geophysical Research: Space Physics*, *118*, 832–838. doi: 10.1002/jgra.50152

Kerner, H. R., Wagstaff, K. L., Bue, B. D., Gray, P. C., Bell, J. F., & Amor, H. B. (2019). Toward generalized change detection on planetary surfaces with convolutional autoencoders and rransfer learning. *IEEE Journal of Selected Topics in Applied Earth Observations and Remote Sensing*, *12*(10), 3900–3918. doi: 10.1109/JSTARS.2019.2936771

Khurana, K. K., Mitchell, D. G., Arridge, C. S., Dougherty, M. K., Russell, C. T., Paranicas, C., ... Coates, A. J. (2009). Sources of rotational signals in Saturn's magnetosphere. *Journal of Geophysical Research: Space Physics*, *114*, A02211. doi: 10.1029/2008JA013312

Kistler, L. M., & Mouikis, C. G. (2016). The inner magnetosphere ion composition and local time distribution over a solar cycle. *Journal of Geophysical Research: Space Physics*, *121*, 2009–2032. doi: 10.1002/2015JA021883

Kivelson, M. G., Khurana, K. K., Russell, C. T., & Walker, R. J. (1997). Intermittent short-duration magnetic field anomalies in the Io torus: Evidence for plasma interchange? *Geophysical Research Letters*, *24*(17), 2127–2130. doi: 10.1029/97GL02202

Kokar, M. M. (1986). Coper: A methodology for learning invariant functional descriptions. In T. M. Mitchell, J. G. Carbonell, & R. S. Michalski (Eds.), *Machine Learning. The Kluwer International Series in Engineering and Computer Science (Knowledge Representation, Learning and Expert Systems)* (pp. 151–154). Boston, MA: Springer. doi: 10.1007/978-1-4613-2279-5_34

Kollmann, P., Roussos, E., Kotova, A., Paranicas, C., & Krupp, N. (2017). The evolution of Saturn's radiation belts modulated by changes in radial diffusion. *Nature Astronomy*, *1*(12), 872–877. doi: 10.1038/s41550-017-0287-x

Kollmann, P., Roussos, E., Paranicas, C., Krupp, N., & Haggerty, D. K. (2013). Processes forming and sustaining Saturn's proton radiation belts. *Icarus*, *222*(1), 323–341. doi: 10.1016/j.icarus.2012.10.033

Kollmann, P., Roussos, E., Paranicas, C., Krupp, N., Jackman, C. M., Kirsch, E., & Glassmeier, K.-H. (2011). Energetic particle phase space densities at Saturn: Cassini observations and interpretations. *Journal of Geophysical Research: Space Physics*, *116*, A05222. doi: 10.1029/2010JA016221

Komori, A., Sato, N., & Hatta, Y. (1978). Excitation and Control of the Rayleigh-Taylor Instability in a Plasma with a Curved Magnetic Field. *Physical Review Letters*, *40*(12), 768–771. doi: 10.1103/PhysRevLett.40.768

Kozyra, J. U., Jordanova, V. K., Home, R. B., & Thorne, R. M. (1997). Modeling of the contribution of Electromagnetic Ion Cyclotron (EMIC) waves to stormtime ring current erosion. In B. T. Tsurutani, W. D. Gonzalez, Y. Kamide, & J. K. Arballo (Eds.), *Magnetic Storms* (pp. 187–202). doi: 10.1029/GM098p0187

Krall, J., Glocer, A., Fok, M.-C., Nossal, S. M., & Huba, J. D. (2018). The unknown hydrogen exosphere: Space weather implications. *Space Weather*, *16*, 205–215. doi: 10.1002/2017SW001780

Krimigis, S. M., Carbary, J. F., Keath, E. P., Bostrom, C. O., Axford, W. I., Gloeckler, G., ... Armstrong, T. P. (1981). Characteristics of hot plasma in the Jovian magnetosphere: Results from the Voyager spacecraft. *Journal of Geophysical Research: Space Physics*, *86*, 8227–8257. doi: 10.1029/JA086iA10p08227

Krimigis, S. M., Mitchell, D. G., Hamilton, D. C., Livi, S., Dandouras, J., Jaskulek, S., ... Williams, D. J. (2004). Magnetosphere Imaging Instrument (MIMI) on the

Cassini mission to Saturn/Titan. *Space Science Reviews*, *114*(1-4), 233–329. doi: 10.1007/s11214-004-1410-8

Krupp, N., Kollmann, P., Mitchell, D. G., Thomsen, M., Jia, X., Masters, A., & Zarka, P. (2018). Global configuration and seasonal variations of Saturn's magnetosphere. In F. M. Flasar, K. H. Baines, N. Krupp, & T. Stallard (Eds.), *Saturn in the 21st Century* (pp. 126–165). Cambridge: Cambridge University Press. doi: 10.1017/9781316227220.006

Krupp, N., Vasyliūnas, V. M., Woch, J., Lagg, A., Khurana, K. K., Kivelson, M. G., ... Paterson, W. R. (2004). Dynamics of the Jovian magnetosphere. In F. Bagenal, T. E. Dowling, & W. B. McKinnon (Eds.), *Jupiter: The Planet, Satellites and Magnetosphere.* Cambridge: Cambridge University Press.

Krzywinski, M. I., Schein, J. E., Birol, I., Connors, J., Gascoyne, R., Horsman, D., ... Marra, M. A. (2009). Circos: An information aesthetic for comparative genomics. *Genome Research*, *19*(9), 1639–1645. doi: 10.1101/gr.092759.109

Kumari, J., Kaur, R., & Pandey, R. S. (2018). Effect of hot injections on electromagnetic ion-cyclotron waves in inner magnetosphere of Saturn. *Astrophysics and Space Science*, *363*, 33. doi: 10.1007/s10509-018-3250-0

Kurth, W. S., Averkamp, T. F., Gurnett, D. A., Groene, J. B., & Lecacheux, A. (2008). An update to a Saturnian longitude system based on kilometric radio emissions. *Journal of Geophysical Research: Space Physics*, *113*, A05222. doi: 10.1029/2007JA012861

Lai, H. R., Russell, C. T., Jia, Y. D., Wei, H. Y., & Dougherty, M. K. (2016). Transport of magnetic flux and mass in Saturn's inner magnetosphere. *Journal of Geophysical Research: Space Physics*, *121*, 3050–3057. doi: 10.1002/2016JA022436

Lamy, L. (2017). The Saturnian Kilometric Radiation before the Cassini Grand Finale. In G. Fischer, G. Mann, M. Panchenko, & P. Zarka (Eds.), *Planetary Radio Emissions VIII* (pp. 171–190). Austrian Academy of Sciences Press.

Lamy, L., Prangé, R., Pryor, W., Gustin, J., Badman, S. V., Melin, H., ... Brandt, P. C. (2013). Multispectral simultaneous diagnosis of Saturn's aurorae throughout a planetary rotation. *Journal of Geophysical Research: Space Physics*, *118*, 4817–4843. doi: 10.1002/jgra.50404

Lee, T. B. (2020). *Amazon faces employee revolt over slow climate action.* Retrieved from `https://arstechnica.com/tech-policy/2020/01/hundreds-of-amazon-employees-blast-management-for-slow-climate-action/`

Leisner, J. S., Russell, C. T., Wei, H. Y., & Dougherty, M. K. (2011). Probing Saturn's ion cyclotron waves on high-inclination orbits: Lessons for wave generation. *Journal of Geophysical Research: Space Physics*, A09235. doi: 10.1029/2011JA016555

Lemaire, J., & Kowalkowski, L. (1981). The role of plasma interchange motion for the formation of a plasmapause. *Planetary and Space Science*, *29*(4), 469–478. doi: 10.1016/0032-0633(81)90090-8

Libarkin, J. C., & Brick, C. (2002). Research methodologies in science education: Visualization and the geosciences. *Journal of Geoscience Education*, *50*(4), 449–455. doi: 10.5408/1089-9995-50.4.449

Lindsay, B. G., Sieglaff, D. R., Smith, K. A., & Stebbings, R. F. (1997). Charge transfer of 0.5-, 1.5-, and 5-keV protons with H_2O: Absolute differential and integral cross sections. *Physical Review A*, *55*(5), 3945–3946. doi: 10.1103/PhysRevA.55.3945

Lindsay, B. G., & Stebbings, R. F. (2005). Charge transfer cross sections for energetic neutral atom data analysis. *Journal of Geophysical Research: Space Physics*, *110*, A12213. doi: 10.1029/2005JA011298

Liu, X., & Hill, T. W. (2012). Effects of finite plasma pressure on centrifugally driven convection in Saturn's inner magnetosphere. *Journal of Geophysical Research: Space Physics*, *117*, A07216. doi: 10.1029/2012JA017827

Liu, X., Hill, T. W., Wolf, R. A., Sazykin, S., Spiro, R. W., & Wu, H. (2010). Numerical simulation of plasma transport in Saturn's inner magnetosphere using the Rice Convection Model. *Journal of Geophysical Research: Space Physics*, *115*, A12254. doi: 10.1029/2010JA015859

Lockhart, J. W., & Weiss, G. M. (2014a). The benefits of personalized smartphone-based activity recognition models. *2014 SIAM International Conference on Data Mining*. doi: 10.1137/1.9781611973440.71

Lockhart, J. W., & Weiss, G. M. (2014b). Limitations with activity recognition methodology and data sets. *Proceedings of the 2014 ACM International Joint Conference on Pervasive and Ubiquitous Computing: Adjunct Publication*, 747. doi: 10.1145/2638728.2641306

Ma, X. (2018). Data science for geoscience: Leveraging mathematical geosciences with semantics and open data. In B. S. Daya Sagar, Q. Cheng, & F. Agterberg (Eds.), *Handbook of Mathematical Geosciences* (pp. 687–702). Springer International Publishing. doi: 10.1007/978-3-319-78999-6_34

Mankovich, C., Marley, M. S., Fortney, J. J., & Movshovitz, N. (2019). Cassini ring seismology as a probe of Saturn's interior. I. Rigid rotation. *The Astrophysical Journal*, *871*(1). doi: 10.3847/1538-4357/aaf798

Manzato, A. (2005). An odds ratio parameterization for ROC diagram and skill score indices. *Weather and Forecasting*, *20*, 918–930. doi: 10.1175/WAF899.1

Mason, I. (1982). A model for assessment of weather forecasts. *Australian Meterological Magazine*, *30*(4), 291–303.

Mauk, B. H., Hamilton, D. C., Hill, T. W., Hospodarsky, G. B., Johnson, R. E., Paranicas, C., ... Thorne, R. M. (2009). Fundamental plasma processes in Saturn's magnetosphere. In M. K. Dougherty, L. W. Esposito, & S. M. Krimigis (Eds.), *Saturn from Cassini-Huygens* (pp. 281–331). Dordrecht: Springer. doi: 10.1007/978-1-4020-9217-6_11

Mauk, B. H., Saur, J., Mitchell, D. G., Roelof, E. C., Brandt, P. C., Armstrong, T., ... Paranicas, C. P. (2005). Energetic particle injections in Saturn's magnetosphere. *Geophysical Research Letters*, *32*, L14S05. doi: 10.1029/2005GL022485

Meeks, Z., Simon, S., & Kabanovic, S. (2016). A comprehensive analysis of ion cyclotron waves in the equatorial magnetosphere of Saturn. *Planetary and Space Science*, *129*, 47–60. doi: 10.1016/j.pss.2016.06.003

Michel, F. C., & Sturrock, P. A. (1974). Centrifugal instability of the Jovian magnetosphere and its interaction with the solar wind. *Planetary and Space Science*, *22*(11), 1501–1510. doi: 10.1016/0032-0633(74)90015-4

Millholland, S., & Laughlin, G. (2017). Supervised learning detection of sixty non-transiting hot Jupiter candidates. *Astronomical Journal*, *154*(3). doi: 10.3847/1538-3881/aa7a0f

Mitchell, D. G., Brandt, P. C., Carbary, J. F., Kurth, W. S., Krimigis, S. M., Paranicas, C., ... Pryor, W. R. (2015). Injection, interchange, and reconnection. In A. Keiling, C. M. Jackman, & P. A. Delamere (Eds.), *Magnetotails in the Solar System.* doi: 10.1002/9781118842324.ch19

Mitchell, D. G., Carbary, J. F., Cowley, S. W. H., Hill, T. W., & Zarka, P. (2009). The dynamics of Saturn's magnetosphere. In M. K. Dougherty, L. W. Esposito, & S. M. Krimigis (Eds.), *Saturn from Cassini-Huygens.* Dordrecht: Springer. doi: 10.1007/978-1-4020-9217-6_10

Molnar, C. (2019). *Interpretable machine learning. A Guide for Making Black Box Models Explainable.* Retrieved from `https://christophm.github.io/interpretable-ml-book/`

Moresi, L., Farrington, R., Perez, F., Schofield, R., Heagy, L. J., & Shim, S.-H. (2019). Linking education and research with Jupyter. *Session at the Fall Meeting of the American Geophysical Union*. doi: 10.6084/m9.figshare.c.4783557.v3

Morooka, M. W., Wahlund, J.-E., Andrews, D. J., Persoon, A. M., Ye, S.-Y., Kurth, W. S., ... Farrell, W. M. (2018). The Dusty Plasma Disk Around the Janus/Epimetheus Ring. *Journal of Geophysical Research: Space Physics*, *123*, 4668–4678. doi: 10.1002/2017JA024917

Müller, A. L., Saur, J., Krupp, N., Roussos, E., Mauk, B. H., Rymer, A. M., ... Krimigis, S. M. (2010). Azimuthal plasma flow in the Kronian magnetosphere. *Journal of Geophysical Research: Space Physics*, *115*, A08203. doi: 10.1029/2009JA015122

NASA Headquarters. (1980). Voyager Backgrounder, Release No: 80-160.

NASA Jet Propulsion Laboratory. (2017a). Cassini Huygens by the numbers. Retrieved from `https://solarsystem.nasa.gov/resources/17761/cassini-huygens-by-the-numbers/`

NASA Jet Propulsion Laboratory. (2017b). Mars Reconnaissance Orbiter by the numbers. Retrieved from `https://mars.nasa.gov/resources/7741/mars-reconnaissance-orbiter-by-the-numbers/`

National Academies of Sciences, Engineering, and Medicine (NASEM). (2018). *Data Science for Undergraduates: Opportunities and Options*. The National Academies Press. doi: 10.17226/25104

National Oceanic and Atmospheric Administration - National Centers for Environmental Information. (2020). *Climate at a Glance: Global Time Series*. Retrieved from `https://www.ncdc.noaa.gov/cag/`

National Science Foundation - National Center for Science and Engineering Statistics. (2019). Women, Minorites, and Persons with Disabilites in Science and Engineering: 2019. Special Report NSF 19-304. Retrieved from `https://www.nsf.gov/statistics/wmpd`

Navidi, W. C. (2015). *Statistics for Engineers and Scientists*. New York, NY: McGraw-Hill Education.

Nichols, J. D., Cecconi, B., Clarke, J. T., Cowley, S. W. H., Gérard, J.-C., Grocott, A., ... Zarka, P. (2010). Variation of Saturn's UV aurora with SKR phase. *Geophysical Research Letters*, *37*, L15102. doi: 10.1029/2010GL044057

Østgaard, N., Mende, S. B., Frey, H. U., Gladstone, G. R., & Lauche, H. (2003). Neutral hydrogen density profiles derived from geocoronal imaging. *Journal of Geophysical Research: Space Physics*, *108*(A7). doi: 10.1029/2002JA009749

Paranicas, C., Mitchell, D. G., Krimigis, S. M., Carbary, J. F., Brandt, P. C., Turner, F. S., ... Burton, M. (2010). Asymmetries in Saturn's radiation belts. *Journal of Geophysical Research: Space Physics*, A07216. doi: 10.1029/2009JA014971

Paranicas, C., Mitchell, D. G., Krimigis, S. M., Hamilton, D. C., Roussos, E., Krupp, N., ... Armstrong, T. P. (2008). Sources and losses of energetic protons in Saturn's magnetosphere. *Icarus*, *197*(2), 519–525. doi: 10.1016/j.icarus.2008.05.011

Paranicas, C., Mitchell, D. G., Roelof, E. C., Brandt, P. C., Williams, D. J., Krimigis, S. M., & Mauk, B. H. (2005, nov). Periodic intensity variations in global ENA images of Saturn. *Geophysical Research Letters*, L21102. doi: 10.1029/2005GL023656

Paranicas, C., Mitchell, D. G., Roelof, E. C., Mauk, B. H., Krimigis, S. M., Brandt, P. C., ... Krupp, N. (2007, jan). Energetic electrons injected into Saturn's neutral gas cloud. *Geophysical Research Letters*, *34*, L02109. doi: 10.1029/2006GL028676

Paranicas, C., Mitchell, D. G., Roussos, E., Kollmann, P., Krupp, N., Müller, A. L., ... Johnson, R. E. (2010). Transport of energetic electrons into Saturn's inner magnetosphere. *Journal of Geophysical Research: Space Physics*, *115*, A09214. doi: 10.1029/2010JA015853

Paranicas, C., Thomsen, M. F., Achilleos, N., Andriopoulou, M., Badman, S. V., Hospodarsky, G., ... Sergis, N. (2016). Effects of radial motion on interchange injections at Saturn. *Icarus*, *264*, 342–351. doi: 10.1016/j.icarus.2015.10.002

Pedregosa, F., Varoquaux, G., Gramfort, A., Michel, V., Thirion, B., Grisel, O., ... Duchesnay, E. (2011). Scikit-learn: Machine learning in Python. *Journal of Machine Learning Research*, *12*, 2825–2830.

Pennington, D., Ebert-Uphoff, I., Freed, N., Martin, J., & Pierce, S. A. (2019). Bridging sustainability science, earth science, and data science through interdisciplinary education. *Sustainability Science*. doi: 10.1007/s11625-019-00735-3

Perry, M. E., Teolis, B., Smith, H. T., McNutt Jr., R. L., Fletcher, G., Kasprzak, W., ... Waite Jr., J. H. (2010). Cassini INMS observations of neutral molecules in Saturn's E-ring. *Journal of Geophysical Research: Space Physics*, *115*, A10206. doi: 10.1029/2010JA015248

Pierrard, V., & Lemaire, J. F. (2004). Development of shoulders and plumes in the frame of the interchange instability mechanism for plasmapause formation. *Geophysical Research Letters*, *31*(5). doi: 10.1029/2003GL018919

Porco, C. C. (2017). A community grows around the geysering world of Enceladus. *Astrobiology*, *17*(9), 815–819. doi: 10.1089/ast.2017.1711

Porco, C. C., & Danielson, G. E. (1982). The periodic cariation of spokes in Saturn's rings. *The Astronomical Journal*, *87*(5), 826. doi: 10.1086/113162

Porco, C. C., Helfenstein, P., Thomas, P. C., Ingersoll, A. P., Wisdom, J., West, R., ... Squyres, S. (2006). Cassini observes the active south pole of Enceladus. *Science*, *311*(5766), 1393–1401. doi: 10.1126/science.1123013

Provan, G., Andrews, D. J., Arridge, C. S., Coates, A. J., Cowley, S. W. H., Cox, G., ... Jackman, C. M. (2012). Dual periodicities in planetary-period magnetic field oscillations in Saturn's tail. *Journal of Geophysical Research*, *117*, A01209. doi: 10.1029/2011JA017104

Provan, G., Andrews, D. J., Arridge, C. S., Coates, A. J., Cowley, S. W. H., Milan, S. E., ... Wright, D. M. (2009). Polarization and phase of planetary-period magnetic field oscillations on high-latitude field lines in Saturn's magnetosphere. *Journal of Geophysical Research: Space Physics*, *114*, A02225. doi: 10.1029/2008JA013782

Provan, G., Cowley, S. W., Lamy, L., Bunce, E. J., Hunt, G. J., Zarka, P., & Dougherty, M. K. (2016). Planetary period oscillations in Saturn's magnetosphere: Coalescence and reversal of northern and southern periods in late northern spring. *Journal of Geophysical Research: Space Physics*, *121*, 9829–9862. doi: 10.1002/2016JA023056

Provan, G., Cowley, S. W. H., Bradley, T. J., Bunce, E. J., Hunt, G. J., & Dougherty, M. K. (2018). Planetary period oscillations in Saturn's magnetosphere: Cassini magnetic field observations over the northern summer solstice interval. *Journal of Geophysical Research: Space Physics*, *123*, 3859–3899. doi: 10.1029/2018JA025237

Provan, G., Cowley, S. W. H., Sandhu, J., Andrews, D. J., & Dougherty, M. K. (2013). Planetary period magnetic field oscillations in Saturn's magnetosphere: Postequinox abrupt nonmonotonic transitions to northern system dominance. *Journal of Geophysical Research: Space Physics*, *118*, 3243–3264. doi: 10.1002/jgra.50186

Provan, G., Lamy, L., Cowley, S. W. H., & Dougherty, M. K. (2014). Planetary period oscillations in Saturn's magnetosphere: Comparison of magnetic oscillations and SKR modulations in the postequinox interval. *Journal of Geophysical Research: Space Physics*, *119*, 7380–7401. doi: 10.1002/2014JA020011

Pulkkinen, A., Rastätter, L., Kuznetsova, M., Singer, H., Balch, C., Weimer, D., ... Weigel, R. (2013). Community-wide validation of geospace model ground magnetic field perturbation predictions to support model transition to operations. *Space Weather*, *11*, 369–385. doi: 10.1002/swe.20056

Rainey, K., Dancy, M., Mickelson, R., Stearns, E., & Moller, S. (2018). Race and gender differences in how sense of belonging influences decisions to major in STEM. *International Journal of STEM Education*, *5*, 10. doi: 10.1186/s40594-018-0115-6

Raissi, M., Perdikaris, P., & Karniadakis, G. E. (2019). Physics-informed neural networks: A deep learning framework for solving forward and inverse problems involving nonlinear partial differential equations. *Journal of Computational Physics*, *378*, 686–707. doi: 10.1016/j.jcp.2018.10.045

Ramer, K. M., Kivelson, M. G., Sergis, N., Khurana, K. K., & Jia, X. (2017). Spinning, breathing, and flapping: Periodicities in Saturn's middle magnetosphere. *Journal of Geophysical Research: Space Physics*, *122*, 393–416. doi: 10.1002/2016JA023126

Rattan, A., Good, C., & Dweck, C. S. (2012). "It's ok — Not everyone can be good at math": Instructors with an entity theory comfort (and demotivate) students. *Journal of Experimental Social Psychology*, *48*(3), 731–737. doi: 10.1016/j.jesp.2011.12.012

Ren, H., Stewart, R., Song, J., Kuleshov, V., & Ermon, S. (2018). Learning with weak supervision from physics and data-driven constraints. *AI Magazine*, *39*(1), 27–38. doi: 10.1609/aimag.v39i1.2776

Roeder, J. L., Chen, M. W., Fennell, J. F., & Friedel, R. (2005). Empirical models of the low-energy plasma in the inner magnetosphere. *Space Weather*, *3*, S12B06. doi: 10.1029/2005SW000161

Roussos, E., Krupp, N., Paranicas, C., Carbary, J. F., Kollmann, P., Krimigis, S. M., & Mitchell, D. G. (2014). The variable extension of Saturn's electron radiation belts. *Planetary and Space Science*, *104*, 3–17. doi: 10.1016/j.pss.2014.03.021

Roussos, E., Krupp, N., Paranicas, C. P., Kollmann, P., Mitchell, D. G., Krimigis, S. M., ... Jones, G. H. (2011). Long- and short-term variability of Saturn's ionic radiation belts. *Journal of Geophysical Research: Space Physics*, *116*, A02217. doi: 10.1029/2010JA015954

Rudd, M. E., Goffe, T. V., DuBois, R. D., & Toburen, L. H. (1985). Cross sections for ionization of water vapor by 7-4000-keV protons. *Physical Review A*, *31*(1), 1–3. doi: 10.1103/physreva.31.492

Runge, J., Bathiany, S., Bollt, E., Camps-Valls, G., Coumou, D., Deyle, E., ... Zscheischler, J. (2019). Inferring causation from time series in Earth system sciences. *Nature Communications*, *10*, 2553. doi: 10.1038/s41467-019-10105-3

Ryan, L., Silver, D., Laramee, R. S., & Ebert, D. (2019). Teaching data visualization as a skill. *IEEE Computer Graphics and Applications*, *39*(2), 95–103. doi: 10.1109/MCG.2018.2889526

Rymer, A. M., Mauk, B. H., Hill, T. W., André, N., Mitchell, D. G., Paranicas, C., ... Dougherty, M. K. (2009). Cassini evidence for rapid interchange transport at Saturn. *Planetary and Space Science*, *57*(14), 1779–1784. doi: 10.1016/j.pss.2009.04.010

Rymer, A. M., Mauk, B. H., Hill, T. W., Paranicas, C., André, N., Sittler Jr., E. C., ... Dougherty, M. K. (2007). Electron sources in Saturn's magnetosphere. *Journal of Geophysical Research: Space Physics*, *112*, A02201. doi: 10.1029/2006JA012017

Rymer, A. M., Mauk, B. H., Hill, T. W., Paranicas, C., Mitchell, D. G., Coates, A. J., & Young, D. T. (2008). Electron circulation in Saturn's magnetosphere. *Journal of Geophysical Research: Space Physics*, *113*, A01201. doi: 10.1029/2007JA012589

Sand, K., Wasser, L., & Herwehe, L. (2019). *Why Earth data scientists are in demand: A survey of hiring managers.* Retrieved from `https://www.earthdatascience.org/blog/earth-data-scientist-demand/`

Sax, L. J., Lehman, K. J., Jacobs, J. A., Kanny, M. A., Lim, G., Monje-Paulson, L., & Zimmerman, H. B. (2017). Anatomy of an enduring gender gap: The evolution

of women's participation in computer science. *The Journal of Higher Education*, *88*(2), 258–293. doi: 10.1080/00221546.2016.1257306

Schippers, P., Blanc, M., André, N., Dandouras, I., Lewis, G. R., Gilbert, L. K., ... Dougherty, M. K. (2008). Multi-instrument analysis of electron populations in Saturn's magnetosphere. *Journal of Geophysical Research: Space Physics*, *113*, A07208. doi: 10.1029/2008JA013098

Schunk, R., & Nagy, A. (2009). *Ionospheres: Physics, plasma physics, and chemistry* (2^{nd} ed.; J. T. Houghton, M. J. Rycroft, & A. J. Dessler, Eds.). Cambridge: Cambridge University Press. doi: 10.1017/CBO9780511635342

Seidelmann, P. K., & Divine, N. (1977). Evaluation of Jupiter longitudes in System III (1965). *Geophysical Research Letters*, *4*(2), 65–68. doi: 10.1029/GL004i002p00065

Sergis, N., Arridge, C. S., Krimigis, S. M., Mitchell, D. G., Rymer, A. M., Hamilton, D. C., ... Coates, A. J. (2011). Dynamics and seasonal variations in Saturn's magnetospheric plasma sheet, as measured by Cassini. *Journal of Geophysical Research: Space Physics*, *116*, A04203. doi: 10.1029/2010JA016180

Sergis, N., Jackman, C. M., Thomsen, M. F., Krimigis, S. M., Mitchell, D. G., Hamilton, D. C., ... Wilson, R. J. (2017). Radial and local time structure of the Saturnian ring current, revealed by Cassini. *Journal of Geophysical Research: Space Physics*, *122*, 1803–1815. doi: 10.1002/2016JA023742

Sergis, N., Krimigis, S. M., Mitchell, D. G., Hamilton, D. C., Krupp, N., Mauk, B. M., ... Dougherty, M. (2007). Ring current at Saturn: Energetic particle pressure in Saturn's equatorial magnetosphere measured with Cassini/MIMI. *Geophysical Research Letters*, *34*, L09102. doi: 10.1029/2006GL029223

Shain, C. A. (1955). Location on Jupiter of a source of radio noise. *Nature*, *176*(4487), 836–837. doi: 10.1038/176836a0

Shemansky, D. E., Liu, X., & Melin, H. (2009). The Saturn hydrogen plume. *Planetary and Space Science*, *57*(14-15), 1659–1670. doi: 10.1016/j.pss.2009.05.002

Slavin, J. A., Baker, D. N., Gershman, D. J., Ho, G. C., Imber, S. M., Krimigis, S. M., & Sunberg, T. (2018). Mercury's dynamic magnetosphere. In S. C. Solomon, L. R. Nittler, & B. J. Anderson (Eds.), *Mercury: The View after MESSENGER* (pp. 461–496). Cambridge: Cambridge University Press. doi: 10.1017/9781316650684.018

Smith, C. G. A. (2006). Periodic modulation of gas giant magnetospheres by the neutral upper atmosphere. *Annales Geophysicae*, *24*(10), 2709–2717. doi: 10.5194/angeo-24-2709-2006

Smith, E. J., & Tsurutani, B. T. (1983). Saturn's magnetosphere: Observations of ion cyclotron waves near the Dione L shell. *Journal of Geophysical Research: Space Physics*, *88*(A10), 7831–7836. doi: 10.1029/JA088iA10p07831

Southwood, D. J., & Cowley, S. W. H. (2014). The origin of Saturn's magnetic periodicities: Northern and southern current systems. *Journal of Geophysical Research: Space Physics*, *119*, 1563–1571. doi: 10.1002/2013JA019632

Southwood, D. J., & Kivelson, M. G. (1987). Magnetospheric interchange instability. *Journal of Geophysical Research: Space Physics*, *92*(A1), 109–116. doi: 10.1029/JA092iA01p00109

Southwood, D. J., & Kivelson, M. G. (1989). Magnetospheric interchange motions. *Journal of Geophysical Research: Space Physics*, *94*(A1), 299–308. doi: 10.1029/JA094iA01p00299

Spahn, F., Schmidt, J., Albers, N., Hörning, M., Makuch, M., Seiß, M., ... Grün, E. (2006). Cassini dust measurements at Enceladus and implications for the origin of the E ring. *Science*, *311*(5766), 1416–1418. doi: 10.1126/science.1121375

Srama, R., Kempf, S., Moragas-Klostermeyer, G., Helfert, S., Ahrens, T. J., Altobelli, N., ... Grün, E. (2006). In situ dust measurements in the inner Saturnian system. *Planetary and Space Science*, *54*(9-10), 967–987. doi: 10.1016/j.pss.2006.05.021

Stephenson, D. B. (2000). Use of the "Odds Ratio" for diagnosing forecast skill. *Weather and Forecasting*, *15*(2), 221–232. doi: 10.1175/1520-0434(2000)015<0221:UOTORF>2.0.CO;2

Stevenson, D. J. (2006). A new spin on Saturn. *Nature*, *441*(7089), 34–35. doi: 10.1038/441034a

Swiger, B. M., Liemohn, M. W., & Ganushkina, N. Y. (2020). Neural network performance of plasma sheet model improves with inclusion of physical knowledge. *In preparation for submission*.

Tadokoro, H., Misawa, H., Tsuchiya, F., Katoh, Y., Morioka, A., & Yoneda, M. (2012). Effect of photo-dissociation on the spreading of OH and O clouds in Saturn's inner magnetosphere. *Journal of Geophysical Research: Space Physics*, *117*, A09226. doi: 10.1029/2011JA017492

Testi, L., Birnstiel, T., Ricci, L., Andrews, S., Blum, J., Carpenter, J., ... Wilner, D. J. (2014). Dust evolution in protoplanetary disks. In H. Beuther, R. S. Klessen, C. P. Dullemond, & T. K. Henning (Eds.), *Protostars and Planets VI* (pp. 339–361). Univ. of Arizona, Tucson. doi: 10.2458/azu_uapress_9780816531240-ch015

Tetrick, S. S., Engebretson, M. J., Posch, J. L., Olson, C. N., Smith, C. W., Denton, R. E., ... Fennell, J. F. (2017). Location of intense electromagnetic ion cyclotron (EMIC) wave events relative to the plasmapause: Van Allen Probes observations. *Journal of Geophysical Research: Space Physics*, *122*, 4064–4088. doi: 10.1002/2016JA023392

Than, K. (2014). Training the next generation of computational geoscientists. *Computing in Science & Engineering*, *16*(6), 100–103. doi: 10.1109/MCSE.2014.130

The Pangeo Team. (2018). *About Pangeo.* Retrieved from https://pangeo.io/about.html

The Planetary Society. (2020). Missions to Mars. Retrieved from https://www.planetary.org/explore/space-topics/space-missions/missions-to-mars.html

Thomsen, M. F. (2013). Saturn's magnetospheric dynamics. *Geophysical Research Letters*, *40*, 5337–5344. doi: 10.1002/2013GL057967

Thomsen, M. F., & Coates, A. J. (2019). Saturn's plasmapause: Signature of magnetospheric dynamics. *Journal of Geophysical Research: Space Physics*, *124*, 8804–8813. doi: 10.1029/2019JA027075

Thomsen, M. F., Coates, A. J., Roussos, E., Wilson, R. J., Hansen, K. C., & Lewis, G. R. (2016). Suprathermal electron penetration into the inner magnetosphere of Saturn. *Journal of Geophysical Research: Space Physics*, *121*, 5436–5448. doi: 10.1002/2016JA022692

Thomsen, M. F., Mitchell, D. G., Jia, X., Jackman, C. M., Hospodarsky, G., & Coates, A. J. (2015). Plasmapause formation at Saturn. *Journal of Geophysical Research: Space Physics*, *120*, 2571–2583. doi: 10.1002/2015JA021008

Thomsen, M. F., Reisenfeld, D. B., Delapp, D. M., Tokar, R. L., Young, D. T., Crary, F. J., ... Williams, J. D. (2010). Survey of ion plasma parameters in Saturn's magnetosphere. *Journal of Geophysical Research: Space Physics*, *115*, A10220. doi: 10.1029/2010JA015267

Thomsen, M. F., Reisenfeld, D. B., Wilson, R. J., Andriopoulou, M., Crary, F. J., Hospodarsky, G. B., ... Tokar, R. L. (2014). Ion composition in interchange injection events in Saturn's magnetosphere. *Journal of Geophysical Research: Space Physics*, *119*, 9761–9772. doi: 10.1002/2014JA020489

Thomsen, M. F., Roussos, E., Andriopoulou, M., Kollmann, P., Arridg, C. S., Paranicas, C. P., ... Young, D. T. (2012). Saturn's inner magnetospheric convection pattern: Further evidence. *Journal of Geophysical Research: Space Physics*, *117*, A09208. doi: 10.1029/2011JA017482

Turner, N. J., Fromang, S., Gammie, C., Klahr, H., Lesur, G., Wardle, M., & Bai, X.-N. (2014). Transport and accretion in planet-forming disks. In H. Beuther, R. S. Klessen, C. P. Dullemond, & T. K. Henning (Eds.), *Protostars and Planets VI* (pp. 411–432). Univ. of Arizona, Tucson. doi: 10.2458/azu_uapress_9780816531240-ch018

Vandegriff, J., Difabio, R., Hamilton, D., Kusterer, M., Manweiler, J., Mitchell, D., ... Roussos, E. (2013). Cassini / MIMI instrument data user guide. Retrieved from http://cassini-mimi.jhuapl.edu/documents/mimi_user_guide_9_26_18.pdf

Vasyliūnas, V. M. (1983). Plasma distribution and flow. In A. J. Dessler (Ed.), *Physics of the Jovian Magnetosphere* (pp. 395–453). Cambridge: Cambridge University Press. doi: 10.1017/CBO9780511564574.013

Vines, S. K., Allen, R. C., Anderson, B. J., Engebretson, M. J., Fuselier, S. A., Russell, C. T., ... Burch, J. L. (2019). EMIC waves in the outer magnetosphere: Observations of an off-equator source region. *Geophysical Research Letters*, *46*, 5707–5716. doi: 10.1029/2019GL082152

Wahlund, J.-E., André, M., Eriksson, A. I. E., Lundberg, M., Morooka, M. W., Shafiq, M., ... Piskunov, N. (2009). Detection of dusty plasma near the E-ring of Saturn. *Planetary and Space Science*, *57*(14-15), 1795–1806. doi: 10.1016/j.pss.2009.03.011

Waite Jr., J. H., Combi, M. R., Ip, W.-H., Cravens, T. E., McNutt, R. L., Kasprzak, W., ... Tseng, W.-L. (2006). Cassini Ion and Neutral Mass Spectrometer: Enceladus plume composition and structure. *Science*, *311*(5766), 1419–1422. doi: 10.1126/science.1121290

Wang, C.-P., Zaharia, S. G., Lyons, L. R., & Angelopoulos, V. (2013). Spatial distributions of ion pitch angle anisotropy in the near-Earth magnetosphere and tail plasma sheet. *Journal of Geophysical Research: Space Physics*, *118*, 244–255. doi: 10.1029/2012JA018275

Waskom, M., Botvinnik, O., Ostblom, J., Lukauskas, S., Hobson, P., Gelbart, M., ... Evans, C. (2020). mwaskom/seaborn: v0.10.0 (January 2020). doi: 10.5281/zenodo.3629446

Williams, D. J., & Lyons, L. R. (1974). The proton ring current and its interaction with the plasmapause: Storm recovery phase. *Journal of Geophysical Research (1896-1977)*, *79*(28), 4195–4207. doi: 10.1029/JA079i028p04195

Wilson, R. J., Bagenal, F., & Persoon, A. M. (2017). Survey of thermal plasma ions in Saturn's magnetosphere utilizing a forward model. *Journal of Geophysical Research: Space Physics*, *122*, 7256–7278. doi: 10.1002/2017JA024117

Ye, S.-Y., Fischer, G., Kurth, W. S., Menietti, J. D., & Gurnett, D. A. (2016). Rotational modulation of Saturn's radio emissions after equinox. *Journal of Geophysical Research: Space Physics*, *121*, 11,714–11,728. doi: 10.1002/2016JA023281

Ye, S.-Y., Fischer, G., Kurth, W. S., Menietti, J. D., & Gurnett, D. A. (2018). An SLS5 longitude system based on the rotational modulation of Saturn radio emissions. *Geophysical Research Letters*, *45*, 7297–7305. doi: 10.1029/2018GL077976

Young, D. T., Berthelier, J.-J., Blanc, M., Burch, J. L., Bolton, S., Coates, A. J., ... Zinsmeyer, C. (2005). Composition and Dynamics of Plasma in Saturn's Magnetosphere. *Science*, *307*(5713), 1262–1266. doi: 10.1126/science.1106151

Yu, Z. J., & Russell, C. T. (2009). Rotation period of Jupiter from the observation of its magnetic field. *Geophysical Research Letters*, *36*, L20202. doi: 10.1029/2009GL040094

Yue, P., Ramachandran, R., Baumann, P., Khalsa, S. J. S., Deng, M., & Jiang, L. (2016). Recent Activities in Earth Data Science [Technical Committees]. *IEEE Geoscience and Remote Sensing Magazine*, *4*(4), 84–89. doi: 10.1109/MGRS.2016.2600528